STUDY OF RADIATIVE PROPERTIES OF THIN FILMS AND NEAR-FIELD RADIATION FOR THERMOPHOTOVOLTAIC APPLICATIONS

A Dissertation
Presented to
The Academic Faculty

by

Jesse I. Watjen

In Partial Fulfillment
of the Requirements for the Degree
Doctor of Philosophy in the
George W. Woodruff School of Mechanical Engineering

Georgia Institute of Technology
May 2016

STUDY OF RADIATIVE PROPERTIES OF THIN FILMS AND NEAR-FIELD RADIATION FOR THERMOPHOTOVOLTAIC APPLICATIONS

Approved by:

Dr. Zhuomin Zhang, Advisor
George W. Woodruff School of
Mechanical Engineering
Georgia Institute of Technology

Dr. Todd Sulchek
George W. Woodruff School of
Mechanical Engineering
Georgia Institute of Technology

Dr. Yogendra Joshi
George W. Woodruff School of
Mechanical Engineering
Georgia Institute of Technology

Dr. Martin Maldovan
School of Physics
Georgia Institute of Technology

Dr. Shannon Yee
George W. Woodruff School of
Mechanical Engineering
Georgia Institute of Technology

Date Approved: March 8, 2016

ACKNOWLEDGEMENTS

I would like to express my gratitude to Dr. Zhuomin Zhang for his guidance over the past six years of my Ph.D. study, without whom this work would have never been possible. I would like to especially thank him for the enlightening conversations, and the valuable insights he has given me relating to my academic, professional, and personal endeavors. I would also like to thank my Committee members: Dr. Yogendra Joshi, Dr. Shannon Yee, Dr. Todd Sulchek, and Dr. Martin Maldovan for their valuable feedback on my thesis work.

I would like to thank Dr. Christopher Muratore of the University of Dayton and Dr. Andrey Voevodin of the Air Force Research Laboratory, for their valuable input on crystallography, for the fabrication of the thin film tungsten samples. I would also like to thank Sampath Kommandur, Prabhakar Gulgunje, and Dr. Kan Wang of the Georgia Institute of Technology for their help with thermal property measurements of calibration materials. I would also like to thank the staff at the Georgia Tech Institute for Electronics and Nanotechnology for the advice and assistance with sample fabrication.

In addition, I would like to show my deepest appreciation to the current and former members of the Nanoscale Radiation Heat Transfer Group for their help and encouragement. In particular, I would like to thank Xianglei Liu for his help with the scattering theory coding for near-field grating simulations, and Dr. Trevor Bright for his help on the optical constant extraction and material characterization. I am also indebted to Bo Zhao whose tireless assistance with the near-field experimental work was invaluable, and the completion of this project would never have been possible without his help. I would like to thank all the other past and present group members for your friendship and support over these past few years.

Most importantly I would like to thank my wife Kaitlyn Watjen for her support throughout the years. Her bravery and strength have always been a source of inspiration

for me, and without her support through these years, I would never have been able to finish this work. Also, I would like to thank my parents, family, and friends for their understanding and encouragement throughout my graduate career.

Finally, I would like to thank the Department of Energy for partially supporting the work in this dissertation.

TABLE OF CONTENTS

LIST OF TABLES

LIST OF FIGURES

LIST OF SYMBOLS

Variables

a	particle diameter
A	amplitudes of forward wave or area
b	sagitta
B	amplitudes of backward wave
c_0	speed of light in vacuum
C	heat flux meter sensitivity or specific heat
d	vacuum gap spacing or thickness
$\mathbf{D}$	dynamical matrix
e	charge of electron 1.602×10^{-19} C
E	electric field
f	volume filling fraction or general function
FF	fill factor
$\overline{\overline{\mathbf{G}}}$	electric Green's function
h	heat transfer coefficient or Planck's constant 6.626×10^{-34} kg m^2 s^{-1}
$\hbar$	Planck's constant divided by 2π
H	grating height or magnetic field
i	index or $\sqrt{-1}$
I	signal intensity
$\mathbf{I}$	identity matrix
j	index
J	current
k	wavevector or index
k_0	magnitude of the wavevector

k_B	Boltzmann's constant, 1.3065×10^{-12} m^2 kg s^2 K^{-1}
Kn	Knudsen number
m	mass
M	number of Lorentz oscillators
$\mathbf{M}$	transfer matrix
n	refractive index or carrier concentration
N	number of elements, or diffraction orders
p	transverse magnetic polarization
P	grating period, pressure, or power
$\mathbf{P}$	propagation matrix
q	heat flux
Q	heat rate
r	Fresnel reflection coefficient, radius of curvature, or position
R	reflectance or thermal resistance
$\boldsymbol{R}$	reflection coefficient matrix
s	transverse electric polarization
S	Poynting vector, post spacing
$\mathbf{S}$	scattering matrix
t	Fresnel transmission coefficient or thickness
T	temperature or transmittance
U	uncertainty
V	voltage or volume
w	grating strip width or width
x	coordinate direction or general variable
y	coordinate direction
z	coordinate direction

Greek Symbols

α	thermal diffusivity, thermal accommodation coefficient, or weighting coefficients
β	radial wavevector or phase shift
γ	Lorentz scattering rate, or wavevector, or specific heat ratio
Γ	Drude scattering rate
$\overline{\overline{\mathbf{\Gamma}}}$	magnetic Green's function
δ	penetration depth, small change, Kronecker delta, or Dirac delta function
Δ	difference
ε	complex dielectric function, electrical permittivity, or emissivity
η	conversion efficiency
θ	angle
Θ	mean energy of Planck's oscillator
κ	extinction coefficient or thermal conductivity
λ	wavelength
Λ	mean free path
μ	magnetic permeability
ν	wavenumber
ξ	energy transmission coefficient
ρ	resistivity or reflectivity
σ	Stefan-Boltzmann constant
τ	relaxation time or transmissivity
ω	angular frequency or plasma frequency
Ω	plasma frequency or resistance

Subscripts/Superscripts

∞	high-frequency contribution
0	0^{th} index, ambient, or free space
1	forward moving or real component
-1	backward moving
2	imaginary component
a	incident from air or acoustic
atm	atmospheric
b	incident from substrate or boundary
BG	background
c	calculated, contact
calc	calculated
e	electrons
eff	effective
el	electrical
ew	evanescent wave
f	film
g	bandgap
H	high
i	index
j	index
k	index
L	low
m	measured
meas	measured
oc	open circuit

p	plasma, post, or pressure
ph	phonon
pw	propagating wave
TE	transverse electric
TM	transverse magnetic
s	substrate or source
sc	short circuit
sam	sample
SPP	surface plasmon polariton
v	volumetric
λ	varies with wavelength

LIST OF ABBREVIATIONS

AFM	atomic force microscopy
AMI	acetone methanol isopropanol
AWG	American wire gauge
bcc	body-centered cubic
CVD	chemical vapor deposition
D-Si	doped silicon
DC	Direct Current
DI	deionized
DTGS	deuterated tryglycine sulfate
EPA	error propagation analysis
fcc	face-centered cubic
FESEM	field-effect scanning electron microscope
FIR	far-infrared
FTIR	Fourier transform infrared spectrometry
FOM	figure of merit
GIXRD	grazing incidence x-ray diffraction
HFM	heat flux meter
HMDS	hexamethyldisilizane
ICDD	international center for diffraction data
IPA	isopropyl alcohol
IR	infrared
LC	inductor-capacitor
MEMS	micro electromechanical systems
MIR	mid-infrared
MP	magnetic polariton

NFTPV	near-field thermophotovoltaic
NIR	near-infrared
PDF	powder diffraction file
PECVD	plasma enhance chemical vapor deposition
PID	proportional integral differential
PM	particulate matter
PR	photoresist
PTFE	polytetrafluoroethylene
PV	photovoltaic
RBS	Rutherford backscattering
RCWA	rigorous coupled wave analysis
RIE	reactive ion etching
RMS	root mean square
RPM	revolutions per minute
RTD	resistance thermal detector
SEM	scanning electron microscope
SPP	surface plasmon polaritons
SPhP	surface phonon polaritons
TC	thermocouple
TE	transverse electric
TM	transverse magnetic
TPV	thermophotovoltaic
TTV	total thickness variation
UV	ultraviolet
XPS	x-ray photoelectron spectroscopy
XRD	x-ray diffraction

SUMMARY

Near-field thermophotovoltaic (NFTPV) devices have received much attention lately as attractive energy harvesting systems, whereby a heated thermal emitter exchanges super-Planckian near-field radiation with a photovoltaic (PV) cell to generate electricity. This work describes the advancement of NFTPV technology through both simulations of next-generation devices, and experimental research addressing the technical challenges faced by NFTPVs, including nanostructured material properties, and large-area near field heat transfer.

The first part of this proposed thesis seeks to improve the performance of a possible NFTPV device by using a periodic tungsten grating as the thermal emission source. The effects on the electrical power generation and the conversion efficiency are investigated via simulations with different grating geometries. It is found that by using the selected grating geometry the power output and efficiency could be increased by 40% and 6%, respectively, over a flat tungsten emitter. The reasoning behind the enhancement is attributed to a plasmonic resonance that shifts towards lower frequencies at large wavenumbers.

In the second part, extensive experimental research is undertaken to investigate the technical challenges in NFTPVs. The optical properties of thin tungsten films, which may serve as an emitter material, are extracted through spectroscopic measurements, and are found to be significantly different from reported bulk values due to a wide range of crystal structures that are present in sputtered films. Furthermore, a heat transfer experiment is designed and built to measure near-field radiation between two doped-silicon slabs separated by a submicron vacuum gap. The details of this system and the sample fabrication show a robust and straightforward method of measuring large-area near-field radiative heat transfer at distances below 200 nm and extend to distances up to 780 nm. Rigorous uncertainty analysis is performed to validate the results of this

measurement. These results show the largest energy throughput of submicron near-field heat transfer to date, and serve to address technical challenges behind practical near-field thermophotovoltaic technology.

1: INTRODUCTION

Near-field radiation heat transfer has been an exciting research avenue especially during the past decade [1]. Fluctuation-dissipation theorem describes that as two media with different temperatures are brought very close together, photon tunneling can greatly enhance the radiation heat transfer. One promising application of near-field radiation is in thermophotovoltaic (TPV) energy conversion devices [2]. With this technology, a high-temperature source radiates electromagnetic thermal energy toward a photovoltaic (PV) cell and electrical current can be generated by photons whose energy is above the bandgap of the PV material. Being small solid-state energy generation devices with no moving parts, TPVs can be used to recover waste heat from other energy generation technologies, such as fuel cells or combustion chambers [3, 4].

Near-field thermophotovoltaics (NFTPVs) have been considered to address the issue of low power throughput with thermal radiation. Using near-field radiation, the heat flux can increase by orders of magnitude higher as the distance between the emitter and the PV cell decreases well below the characteristic thermal wavelength [5]. Due to photon tunneling, radiation with very large wavevectors can travel across the vacuum gap, resulting in tremendous amounts of energy transported into the PV cell for the generation of electron-hole pairs [6]. There are still significant drawbacks to using this technology, and the focus of this work is to address some of these issues. Many of the topics presented are not exclusively limited to NFTPVs but do effectively help to overcome the hurdles that limit near-field thermophotovoltaic technologies. Some of the problems addressed are the lack of detailed simulations for elective NFTPV emitters, the properties of high temperature thermal emitter materials, and the physical realization of near-field heat transfer with high power throughput.

1.1 Design of High Performance Near-Field Thermophotovoltaic Emitters

Compared to solar PV cells, TPV devices have an advantage whereby the heated source can be a micro/nanostructured material, and the emissivity can be tuned to align with the bandgap of the receiver. Thus, only above-bandgap radiation leaves the source and the overall energy efficiency can be very high. Periodic grating structures have been proposed to control thermal emission including tungsten gratings [7], deep gratings [8], and two-dimensional gratings [9, 10] with great success. Work has been done to focus TPV emitter radiation to the cell bandgap as well by using thin films [11] and experimentally using a microcavity emitter [12]. While these devices may be able to tune the radiation such that the efficiency exceeds solar PV devices, the power throughput per unit area is still quite low.

Recently, much attention has been going to optimizing the radiative exchange in NFTPV devices by using a backside mirror [13], thin films [14], graphene [15, 16], and nanowires [17]. Thus far the analysis of NFTPV devices using structured emitters, especially gratings, is lacking. Furthermore, the role of gratings in the near-field regime is not well understood, behaving differently than far-field gratings [18-20].

This work describes the use of a grating structure to enhance the power throughput of NFTPV devices, while increasing thermal efficiency by ensuring that a large portion of the radiation entering the PV cell is above the bandgap. The device is modeled as a one-dimensional high-temperature tungsten grating on a tungsten substrate transferring energy to a room-temperature $In_{0.18}Ga_{0.82}Sb$ PV cell through a vacuum gap of several tens of nanometers. Scattering theory is used along with rigorous coupled-wave analysis to calculate the radiation exchange between the grating emitter and the PV cell. A parametric study is performed by varying the grating depth, period, and strip width in the range that can be fabricated using available fabrication technologies. By optimizing the grating parameters, it is found that the power output can be improved by 40% while

increasing the energy efficiency by 6% as compared with the case of a flat tungsten emitter. Explanations for the enhancement mechanisms are investigated and found to be a surface plasmon polariton resonance that shifts towards lower frequencies. This work shows a possible way of improving NFTPV and sheds light on how grating structures interact with thermal radiation at the nanoscale.

1.2 Analysis and Characterization of High-Temperature Thermal Emitter Materials

Thermophotovoltaic devices and particularly NFTPVs require very high operating temperatures (typically nearing 2000 K) to have acceptable throughput and efficiencies. This is partly due to the lack of high-efficiency PV materials capable of energy conversion of low-energy photons, and also due to the T^4 scaling of thermal radiative power. Thus it is critical to employ and understand emitter materials capable of operating as such extreme temperatures.

Tungsten has been used as a high-temperature thermal emission source because of its good thermal and chemical stability with a melting temperature near 3400°C [21-24]. Tungsten thin films allow for a reliable, high-temperature emission source integrated into a nanofabricated package. Tungsten gratings or microcavities [25-28], photonic crystals [29-31], thin-film multilayers [30], and hybrid micro/nanostructures [7] have recently been proposed as thermal emission sources for energy harvesting applications including thermophotovoltaic power generation. While some of these use tungsten films as a thermal emission source and others use them as a metal layer, prior knowledge of the optical properties is required for all applications. Therefore, it is critically important to understand the optical and radiative properties of tungsten, particularly in relation to the effect of microstructures.

Earlier, De Vos [22] measured the spectral emissivity of bulk single-crystal tungsten from 0.23 to 2.7 μm at temperatures from 1600 to 2800 K. Larrabee [23]

reported the spectral emissivity of tungsten in a similar temperature range up to 5 μm, considering the effects of polarization for various emission angles, and the optical constants (i.e., complex refractive index) of tungsten were obtained. The total hemispherical emissivity of tungsten was also measured using a calorimetric technique [24]. Roberts et al. [32] postulated a superposition formula that includes a summation of Drude terms and Lorentz terms to obtain the optical constants of tungsten based on the reflectance measurements in the wavelength region from 0.365 to 2.56 μm. Nomerovannaya et al. [33] determined the dielectric function from 0.265 to 20 μm using one Drude term and several additional Lorentz terms to describe the interband transitions. These interband absorption mechanisms have been validated through theoretical energy-band calculations [34, 35].

Weaver et al. [36] presented the dielectric function of tungsten from 0.15 to 33 eV using the Kramers-Kronig relation based on the absorptance (0.15-4.4 eV) and reflectance (4-33 eV) measurements. Additional high-energy data were used from another study along with an extrapolation. A Drude term was used to extend the optical properties to the far-infrared region beyond 8.3 μm wavelength [36]. The room-temperature optical constants of crystalline bulk tungsten were compiled by Palik [37], which is based on the results from Weaver et al. [36] from the ultraviolet to the far-infrared. Rakić et al. [38] used an optimization procedure to fit the data presented in [37] with an optical dispersion that includes contributions from both free and bound charges. Not only can the parameterized formulation capture the fundamental physics, but it can also facilitate numerical simulations using a smooth curve without the need of interpolation from discrete data points. Very few studies dealt with the optical properties of tungsten thin films, which can have very different characteristics compared with single-crystal tungsten [39-42].

Deineka et al. [39] used spectral ellipsometry in the visible to near-infrared region to study ultrathin (2 to 8 nm) tungsten films deposited by radio-frequency magnetron sputtering and analyzed the inhomogeneities with an effective medium theory. Davazoglou et al. [40] determined the dielectric function of a 200-nm-thick tungsten film at wavelengths from 0.19 to 0.82 μm and found large disagreement with the bulk values reported in [33, 36]. Gravier et al. [41] extracted the thickness and optical conductivity of several transition metals with body-centered-cubic (bcc) crystal structures at wavelengths from 0.22 to 3.9 μm. They measured the transmittance and reflectance at oblique incidences of films with thicknesses on the order of 30 nm and explained the spectral variation in the ultraviolet and visible regions by interband transitions. Nestell et al.[42] and Nestell and Christy [43] investigated the optical properties of different types of evaporated metal films, including tungsten, with thicknesses from 20 to 200 nm in the wavelength region from 0.19 to 2.5 μm. They report that the optical constants of polycrystalline thin films are akin to the corresponding bulk values with microstructural effects factored in. All of the above studies are for the stable tungsten phase (bcc α-W) and none of them extend to wavelengths longer than 4 μm.

Tungsten will in general form a polycrystalline film when it is deposited, although amorphous tungsten films have also been observed in as-deposited films [21, 44]. In principle, tungsten can be annealed to crystallize into a single crystal, but the annealing temperature would have to reach about 2400°C [22, 23], which is much higher than the melting point of most substrates. Alternatively, single crystal tungsten can be fabricated at lower temperatures, but the film would need to be extensively worked via rolling, drawing, or mechanical deformation [21]. This is impractical for thin-film applications. Since tungsten films have been considered as an interconnect material in microelectronics, the structural and electrical properties have been extensively studied

[45-47]. The density, resistivity, and other properties of the film vary greatly with deposition methods and conditions [44-50].

Tungsten films may exhibit three distinct crystal phases [21, 51-54]. The most stable one is the α-W bcc phase, with the highest density and lowest resistivity, as in most studied bulk tungsten and tungsten films. There also exist two metastable phases that can occur at low deposition temperatures and with small film thicknesses. The β-W phase is an A-15 type bcc crystal (W_3W), which was initially thought to be a W_3O compound due to the similar X-ray diffraction patterns [51, 53]. The γ-W phase, which can only exists in thin films, has a face-centered cubic (fcc) structure and the lowest density [21, 52-54]. The resistivity values for β-W are generally more than an order of magnitude higher than that of the bulk tungsten [45, 46]. These metastable crystal phases will transform irreversibly to α-W at elevated temperatures [21, 49, 54, 55]. At present, the infrared optical properties of thin-film tungsten are not well understood, particularly for the metastable phases.

The present work focuses on the radiative and optical properties of thin tungsten films at wavelengths from 1 to 20 μm (wavenumbers from 10,000 to 500 cm^{-1}), considering microstructural variations. Four films of a nominal thickness of 70 nm were deposited on silicon substrates using DC magnetron sputtering, and the effect of pre- and post-deposition treatments was investigated. Several analytical instruments were used to characterize the crystalline phases and microstructures, including X-ray diffraction, Rutherford backscattering, X-ray photoelectron spectroscopy, and scanning electron microscopy. The transmittance and reflectance of the film-substrate composites were measured at room temperature using a Fourier-transform infrared (FTIR) spectrometer. The dielectric function of each sample was obtained by fitting the measured radiative properties using the Drude-Lorentz dispersion model. The difference in the radiative

properties between samples was analyzed and related to the crystalline phases and density.

1.3 Experimental Investigation of Near Field Heat Transfer

Near-field radiation heat transfer has been an exciting research avenue over the past several years. Fluctuation-dissipation theorem describes that as two media are brought closer together, evanescent waves are able to couple, and photon tunneling can greatly enhance the heat transfer [56]. This allows for us to shatter the previous blackbody radiation limit by a factor of ten times at spacings significantly lower than the characteristic wavelength of radiation. Near-field technology has a lot of potential applications such as high-resolution imaging [57], near-field thermophotovoltaic systems [56], near-field cooling [58], and near-field thermal rectification [59]. While the theory and applications of near-field heat transfer are well established, experimental work is lacking. Several groups have demonstrated the existence of near-field heat transfer between an AFM tip and a flat surface [60-62], and have achieved gap spacings down to 100 nm. However, this is fundamentally limited for applications due to the low power throughput. Near-field effects between large planar areas have also been investigated [63, 64] but the improvements over blackbody radiation have been modest. Recently, Ito [65] has measured planar near-field radiation at gap spacings of 500 nm, and Lim [66] used a MEMS device to measure radiation at a 400 nm spacing. However, it is essential to demonstrate near-field radiation between even lower spacings with high heat fluxes.

The objective of the present work is to obtain experimental evidence of near room temperature near-field radiation between planar geometries with an area of 1 cm^2 at submicron gap spacing. The specimens used in this study are fabricated using conventional photolithography techniques such that two pieces of silicon wafers are suspended by a sparse array of silica nanoposts. This method can create a controllable vacuum gap between the two pieces of silicon with minimal conduction heat transfer

contributions. Through careful sample preparation, the flatness of each piece is assured, and a nanoscale vacuum gap can be achieved across the entirety of the 1 cm^2 area. This is measured and confirmed using a Fourier transform infrared spectrometer (FTIR) according to the effect of wave interference caused by the gap. The sample fabrication process will be elaborated on with extensive characterizations performed using techniques such as confocal microscopy, laser profilometry, scanning electron microscopy (SEM), and FTIR. Furthermore, the silicon wafers may be doped or coated with another thin film, or replaced by silica plates.

A high-vacuum thermal measurement setup has been developed. This steady-state system is capable of measuring a temperature drop using differential thermocouples and the heat flux across a test specimen independently using a heat flux gage to determine the thermal properties. By modeling the heat transfer phenomena, clear evidence of near-field radiation heat transfer far exceeding the blackbody limit is anticipated even above room temperature. The details of the experimental apparatus will be discussed, including the design, instrumentation, data acquisition, and calibration procedures. Measurements of the radiative heat flux between submicron vacuum distances will also be presented.

1.4 Outline

This thesis is divided into seven chapters. Chapter 2 goes through the detailed theoretical background needed for modeling throughout this work. The chapter begins with the calculation of reflection and transmission through thin films, and the modeling of optical properties of multiple layers of thin films on coherent and incoherent substrates will be shown. Next, an introduction to near-field thermal radiation is given, which will be an important topic throughout most of this thesis. Several formulations will be shown including heat transfer between semi-infinite media, a Green's function formulation for modeling finite layers, and scattering theory with rigorous coupled-wave analysis for modeling grating structures. Chapter 3 will detail the major instrumentation used and

developed in this work. This begins with the usage of FTIR spectroscopy for the measurement of optical properties of thin films, and the measurement of a near-field vacuum gap. The main topic in Chapter 3 is the development of a heat transfer experiment for near-field radiation measurements, and this will cover the design, analysis, construction, and calibration of the equipment with detailed uncertainty analysis.

Chapter 4 begins the main body of this work, with the design of a near-field tungsten grating emitter for near-field thermophotovoltaics. This begins with the numerical analysis required and covers a broad parametric sweep of emitter geometries. One emitter geometry has been chosen to investigate further, and the details of the enhancement mechanisms are investigated. Chapter 5 describes the extraction of the complex refractive index of thin tungsten films in the infrared region. Measurements are shown to determine the morphology and crystal structure of the films, and FTIR measurements are analyzed to produce a continuous refractive index for each film. Chapter 6 studies the measurements of near-field thermal radiation. The sample design and fabrication is discussed, followed by detailed analysis of all of the samples that showed near-field radiation with some uncertainty analysis. Finally, Chapter 8 outlines the main conclusions found in this thesis with avenues for the continuation of this research.

2: THEORETICAL BACKGROUND

This chapter seeks to lay out the theoretical background required to reproduce the results in this work, which focuses on investigating and exploiting the subtle ways in which thermal radiation changes behavior as length scales decrease. This begins with the formulation necessary to model the effects of constructive and deconstructive interference within a thin coherent film as explained in Section 2.1. The next several formulations will be detailed in Section 2.2 to describe the nature and methods of modeling near-field thermal radiation as it applies to multilayered structures, semi-infinite plates, and periodic gratings.

2.1 Radiative Properties of Thin Films

2.1.1 Reflection and Transmission within a Thin Film

For light incident on a plane parallel surface, the reflectance and transmittance of a plane wave can be calculated through the complex Fresnel coefficients. Here, light incident from medium 1 with an oscillating electric and magnetic field will have some energy transmitted into medium 2 and some energy reflected back to medium 1 [67]. This is found through knowledge of the z-component of the wavevectors and the properties of the media. For nonmagnetic media with a unity magnetic permeability, the Fresnel reflection coefficients can be written as

$$r_{12,\mathrm{TE}} = \frac{E_r}{E_i} = \frac{k_{1z} - k_{2z}}{k_{1z} + k_{2z}} \tag{2.1}$$

$$r_{12,\mathrm{TM}} = \frac{H_r}{H_i} = \frac{k_{1z}/\varepsilon_1 - k_{2z}/\varepsilon_2}{k_{1z}/\varepsilon_1 + k_{2z}/\varepsilon_2} \tag{2.2}$$

where k_z is the wavevector perpendicular to the plane of incidence and ε is the complex dielectric function of the medium. Here the transverse electric (TE) component (also

referred to as s-polarization) is found through the ratio of the reflected to incident electric fields while the transverse magnetic component (TM or p-polarization) is found through the ratio of the reflected to incident magnetic fields. A similar formulation for the complex transmission coefficients can be used to find

$$t_{12,\mathrm{TE}} = \frac{2k_{1z}}{k_{1z} + k_{2z}} \tag{2.3}$$

$$t_{12,\mathrm{TM}} = \frac{2k_{1z}/\varepsilon_1}{k_{1z}/\varepsilon_1 + k_{1z}/\varepsilon_1} \tag{2.4}$$

These equations form the basis of the optical formulations used here, however these only predict the optical properties at a single interface. To model the reflection and transmission through a free standing film as shown in Figure 2.1, the reflection and transmission through the bottom layer must be modeled as well. If the film thickness is on the order of the wavelength of the incident radiation, the phase of the light will be preserved within the film.

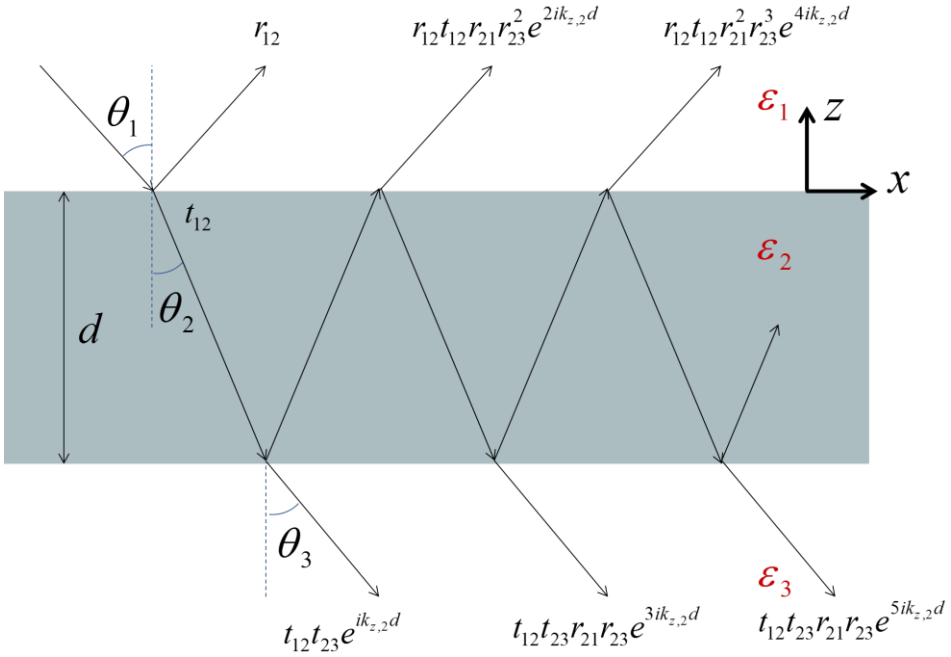

Figure 2.1. Illustration of reflection and transmission through a thin coherent film with multiple reflections shown.

Since the radiation is a propagating wave, the phase of the electric and magnetic fields will acquire a shift of

$$\beta = \frac{2\pi d}{\lambda}\sqrt{n_2^2 - n_1^2 \sin^2\theta_1} \tag{2.5}$$

Here the thickness of the film is, d, the wavelength in vacuum is λ, and the incident angle is θ. The complex refractive index $n = \varepsilon^2$ is used, and it should be noted that both the refractive index and complex dielectric function are strong functions of the wavelength or frequency. At the bottom interface, the wave will be partially reflected again, and acquire a further phase shift. When this reaches the first interface, there is the potential that this reflected wave can be in-phase or out-of-phase with the incident light, causing constructive or destructive interference. This causes interference fringes in either the reflected waves or the transmitted waves. Even if the refractive index is constant, this effect will cause a period variation in the reflection and transmission with the frequency. This can be predicted using the free spectral range

$$\Delta\nu = \frac{1}{2nd} \tag{2.6}$$

This predicts the frequency or wavenumber difference between one full period of the interference fringe.

Here the transmission and reflection coefficients for the film can be found as

$$r = r_{12} + \frac{t_{12}t_{21}r_{23}e^{2ik_{z,2}d}}{1 - r_{21}r_{23}e^{2ik_{z,2}d}} \tag{2.7}$$

$$t = \frac{t_{12}t_{21}e^{ik_{z,2}d}}{1 - r_{21}r_{23}e^{2ik_{z,2}d}} \tag{2.8}$$

Here the Fresnel reflection coefficients are found for the correct polarization. Finally the spectral directional reflectance and transmittance can be found.

$$R = rr^* \tag{2.9}$$

$$T_{\mathrm{TE}} = \frac{\mathrm{Re}\left(k_{3z}^*\right)}{\mathrm{Re}\left(k_{1z}^*\right)} tt^* \tag{2.10}$$

$$T_{\mathrm{TM}} = \frac{\mathrm{Re}\left(k_{3z}/\varepsilon_1\right)}{\mathrm{Re}\left(k_{1z}/\varepsilon_3\right)} tt^* \tag{2.11}$$

For thermal radiation the polarization is random, and the reflectance and transmittance should be averaged over both polarizations.

It should be noted that the interference pattern will become more closely spaced as the film thickness decreases, and this does not have a physical lower limit. For a very thick film, clear interference patterns can be seen as long as the surfaces do not have significant scattering. However, the free spectral range may be too small to be resolved by most instruments. Unfortunately, calculations of the optical properties are not subject to resolution limitations and spectral averaging must be used. Here the spectrally averaged transmittance can be found through

$$\bar{T}\left(\nu\right) = \frac{1}{\delta\nu}\int_{\nu-\delta\nu}^{\nu+\delta\nu} T\left(\nu'\right) d\nu' \tag{2.12}$$

where the integral average over a small range $\delta\nu$ can be found. This range must be large enough such that multiple interference fringes are included, and can lead to limitations on the resolution of the computation.

2.1.2 Multiple Coherent and Incoherent Layers

A free-standing thin film is generally not of any use, and must be placed on a substrate or in a stack. This section will outline the methodology to find the reflectance and transmittance that arises from a thin film on a thick incoherent substrate as well as an arbitrary stack of films.

Ray tracing allows for the determination of the reflectance and transmittance through a standing film as discussed above, but a similar formulation can be used to find the transmittance and reflectance through a thick incoherent slab by ignoring the phase information through the layer. This treatment can be extended by considering a thin coherent film on the top and/or bottom of a thick incoherent substrate, as shown below in Figure 2.2.

In this formulation, ray tracing is used to preserve the phase information for calculation of constructive and destructive interference within the thin films, but eliminates the need for spectral averaging in a thick substrate. This is a relatively common physical model and is used extensively in Chapter 5. Here, the reflectivity ρ and transmissivity τ can be found depending on the situation. If the layer is a thin film, or a thin film stack, then Equations 2.9 through 2.11 should be used in place of these values for the correct bounding media. If there is no film, and the interface is only between the substrate and air or vacuum, then Equations 2.1 through 2.4 should be used to find the reflectivity and transmissivity. Here it should be noted that the subscripts ‘a’ and ‘b’ refer to incidence from the air or substrate, respectively, while the subscript ‘s’ refers to interactions at the bottom interface where there is no incident radiation.

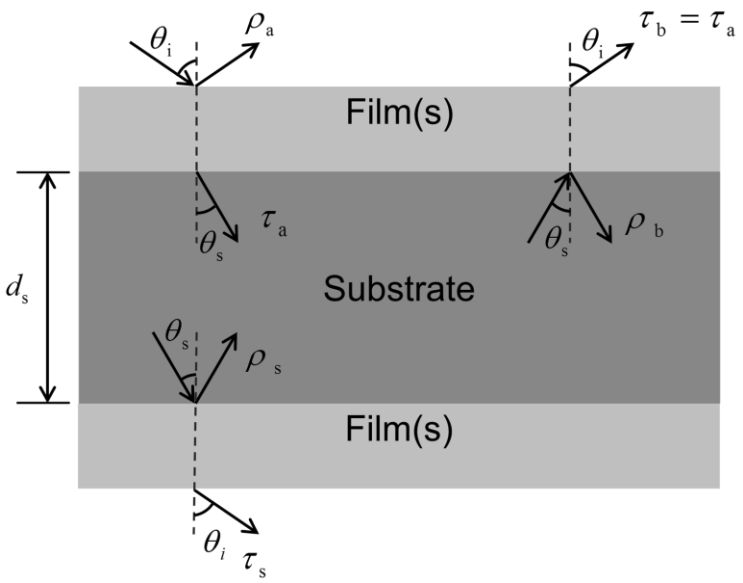

Figure 2.2. Schematic showing the reflectivities and transmissivities for a thin film on thick substrate model.

With the reflectivities and transmissivities calculated for all of the pertinent interfaces, the total transmittance and reflectance can be found. Note that these must be calculated individually for TE and TM waves.

$$R = \rho_a + \frac{\rho_s \tau_a^2 \tau^2}{1 - \rho_s \rho_b \tau^2} \tag{2.13}$$

$$T = \frac{\tau_b \tau_s \tau}{1 - \rho_s \rho_b \tau^2} \tag{2.14}$$

It should be noted that the transmittance is the same regardless of whether radiation is incident from the top or the bottom; however the reflectance does change if the top and bottom layers of films are not the same. This case will be important for modeling a single thin film on a silicon substrate in Chapter 5, and the reflectance will be broken down into two values, R_f and R_s representing the reflectance from the film-side or the substrate side. To solve for the substrate-side reflectance, the same formulation is used, though the location of the film is switched in Figure 2.2.

This methodology requires a single layer to be incoherent, but a stronger method, the transfer matrix method allows for the prediction of the reflectance and transmittance of any number of layers by assuming they are all coherent. It is through this method combined with the thin film on thick substrate model that multiple layers of films can be incorporated into Figure 2.2.

The transfer matrix method separates the electric and magnetic fields into forward and backwards propagating waves through an arbitrary layer, and the amplitudes are solved for. Eventually the ratios of the incident, reflected, and transmitted amplitudes are found which represent the overall transmittance and reflectance. TE and TM waves must be considered separately, but the electric field in any layer for a TE wave is given by

$$E_i(z) = A_i e^{ik_{iz}(z_i - z_{i-1})} + B_i e^{-ik_{iz}(z_i - z_{i-1})} \tag{2.15}$$

By preserving the boundary condition that the tangential component of the electric and magnetic fields must be continuous across an interface, the amplitude in any layer *i* can be related to the amplitude in the next layer *i*+1 through

$$\begin{bmatrix} A_i \\ B_i \end{bmatrix} = \mathbf{P}_i \mathbf{D}_i^{-1} \mathbf{D}_{i+1} \begin{bmatrix} A_{i+1} \\ B_{i+1} \end{bmatrix} \tag{2.16}$$

Here the propagation matrix preserves the phase within the layer and can be found as

$$\mathbf{P}_i = \begin{bmatrix} e^{-ik_{iz}d_z} & 0 \\ 0 & e^{ik_{iz}d_z} \end{bmatrix} \tag{2.17}$$

for any layer except the first, where the propagation matrix is simply the identity matrix. The dynamical matrix captures the change in wavevector across the interfaces and can be found as

$$\mathbf{D}_i = \begin{bmatrix} 1 & 1 \\ k_{iz}/\mu_i & -k_{iz}/\mu_i \end{bmatrix} \tag{2.18}$$

Here, the possibility of a magnetic material is considered as the magnetic permeability μ factors into the dynamical matrix.

The matrix multiplication in Equation 2.16 can be repeated to find the field amplitudes of any layer, and when this is applied to all *N* layers of the thin film stack, including the first and last semi-infinite layer, the incident amplitudes can be related to the transmitted amplitudes through the transfer matrix **M**.

$$\begin{bmatrix} A_1 \\ B_1 \end{bmatrix} = \prod_{i=1}^{N-1} \mathbf{P}_i \mathbf{D}_i^{-1} \mathbf{D}_{i+1} \begin{bmatrix} A_N \\ B_N \end{bmatrix} = \mathbf{M} \begin{bmatrix} A_N \\ B_N \end{bmatrix} = \begin{bmatrix} M_{11} & M_{12} \\ M_{21} & M_{22} \end{bmatrix} \begin{bmatrix} A_N \\ B_N \end{bmatrix} \tag{2.19}$$

This can then be solved for the reflectance and transmittance through

$$R = \left| \frac{M_{21}}{M_{11}} \right|^2 \tag{2.20}$$

$$T_{\mathrm{TE}} = \frac{\mathrm{Re}(k_{Nz} / \mu_N)}{\mathrm{Re}(k_{1z} / \mu_1)} \left| \frac{1}{M_{11}} \right|^2 \tag{2.21}$$

The TM waves are handled slightly differently, where the magnetic permeability μ in Equations 2.18 and 2.21 is swapped for the dielectric function ε, and the amplitudes of the magnetic fields are solved for instead of the electric fields.

While this method has the strength to handle transmission and reflection from any situation of plane layers there are drawbacks in terms of computational time and preserving coherence. A very common physical situation is to have a thick substrate for mechanical support, which when modeled with the transfer matrix method will show interference fringes every 6 cm^{-1} for a 500 μm thick silicon substrate. This completely obscures any important spectral variations and spectral averaging must be used in order to make sense of the optical properties. This formulation is used in Chapter 6 to model a thin film of air between two thick layers.

2.2 Near Field Thermal Radiation

The emission of radiative power is typically formulated from an indirect method. In this, the emittance of a material is found from Kirchoff's law equating the emissivity and absorptivity in thermodynamic equilibrium [68]. This emittance can then be used to find the emissive power as a proportion of Planck's blackbody distribution. For a diffuse grey surface this reduces to the well-known formula

$$Q = \varepsilon \sigma A T^4 \tag{2.22}$$

where the heat rate can be found as a function of the temperature to the fourth power. This sets a fundamental limit for radiation as the emittance ε cannot exceed unity.

In reality, thermal radiation is the excitation of electric and magnetic fields caused by minute oscillations of charge carriers that are vibrating due to thermal motions. Through simulating these fields, the true nature of radiation is made clear, and it is found that improvements over the blackbody limitation can be made when the fields are very close to the emitting body. Consider a transverse electric field acting in the *y*-direction crossing the interface between an optically dense medium to an optically rare medium. The electric field can be expressed as

$$\mathbf{E} = \hat{y} E \exp(i k_z z + i k_x x - i \omega t) \tag{2.23}$$

Note that *i* represents the imaginary number in this case, and the bold typeface for ***E*** denotes a vector quantity. Here the boundary conditions require that the wavevector component in the *x*-direction remains constant after crossing the interface, and the *z*-component of the wavevector will change according to the magnitude of the wavevector.

$$k_z{}^2 + k_x{}^2 = k_0{}^2 = n^2 \frac{\omega^2}{c_0{}^2} \tag{2.24}$$

If k_x is large in the emitting medium where *n* is large there is the potential that k_z must be imaginary after entering the medium with a smaller refractive index. In this case

Equation 2.23 shows that the electric field should be exponentially decaying with the *z*-direction. This is referred to as an evanescent wave, and is shown in Figure 2.3.

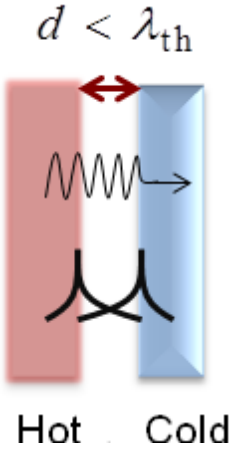

Figure 2.3. Schematic showing near-field radiation between a hot and cold body.

For thermal radiation, this electric or magnetic field only extends a few microns from the surface. However, if a third medium is brought close enough to the first, then the electric field can tunnel across the vacuum gap. Furthermore, the evanescent magnetic fields excited from the third medium can couple with this wave to create a real-valued Poynting vector defined by

$$\left\langle \mathbf{S}_{\omega}\left(\mathbf{r},\omega\right)\right\rangle = \frac{1}{4}\mathrm{Re}\left[\mathbf{E}\left(\mathbf{r},\omega\right)\times\mathbf{H}^{*}\left(\mathbf{r},\omega\right)\right] \tag{2.25}$$

at some position vector **r** and frequency ω. The asterisk here represents the complex conjugate operator. Here the magnetic and electric fields can have large imaginary components and the cross product yields a real value. The component of the Poynting vector in the *z*-direction is used to find the power transmission through a medium.

This is known as near-field thermal radiation, and can exceed blackbody radiation by orders of magnitude. The following subsections handle the treatment and formulation necessary to simulate the electric and magnetic fields to be used in Equation 2.25.

2.2.1 Fluctuation-Dissipation Theorem

To account for the fluctuations in the electric and magnetic fields, Ampere's Law needs to be modified slightly [69]

$$\nabla \times \mathbf{H}(\mathbf{r},\omega) = -i\omega\varepsilon\mathbf{E}(\mathbf{r},\omega) + \mathbf{J}_{\mathrm{r}}(\mathbf{r},\omega) \tag{2.26}$$

From here, the theory of fluctuational electrodynamics put forth by Rytov [70] predicts the ensemble average of thermally driven currents at any position **r** through all positions **r'**

$$\left\langle J_{\mathrm{r},i}(\mathbf{r},\omega) J^{*}_{\mathrm{r},k}(\mathbf{r}',\omega) \right\rangle = \frac{\omega\varepsilon_0}{\pi}\varepsilon''(\mathbf{r},\omega)\Theta(\omega,T)\delta_{ik}\delta(\mathbf{r}-\mathbf{r}') \tag{2.27}$$

where $\Theta(\omega,T)$ is the mean energy of the Plank oscillator at temperature T, ε_0 is the permittivity of free space, ε'' is the imaginary component of the dielectric function at spatial coordinate **r**, δ_{ik} is the Kronecker delta, and $\delta(\mathbf{r}-\mathbf{r}')$ is the Dirac delta function. The energy of Planck's oscillators is found

$$\Theta(\omega,T) = \frac{\hbar\omega}{\exp(\hbar\omega/k_{\mathrm{B}}T)-1} \tag{2.28}$$

where $\hbar$ is Plank's constant divided by 2π and k_{B} is the Boltzmann constant.

At this point, Equations 2.27 and 2.26 along with Maxwell's Equations can be used to find the electric and magnetic fields in the medium, and Equation 2.25 can find the power. Unfortunately, further treatment is needed to handle crossing an interface. Following treatment by Sipe and Francoeur [71, 72] the electric and magnetic fields in a multilayered structure can be found using Green's functions.

$$\mathbf{E}(\mathbf{r},\omega) = i\omega\mu\int_{V_{\mathrm{S}}} \overline{\overline{\mathbf{G}}}(\mathbf{r},\mathbf{r}_{\mathrm{S}},\omega)\cdot\mathbf{J}_{\mathrm{r}}(\mathbf{r}_{\mathrm{S}},\omega)\,d^3\mathbf{r}_{\mathrm{S}} \tag{2.29}$$

$$\mathbf{H}(\mathbf{r},\omega) = \int_{V_{\mathrm{S}}} \overline{\overline{\mathbf{\Gamma}}}(\mathbf{r},\mathbf{r}_{\mathrm{S}},\omega)\cdot\mathbf{J}_{\mathrm{r}}(\mathbf{r}_{\mathrm{S}},\omega)\,d^3\mathbf{r}_{\mathrm{S}} \tag{2.30}$$

This uses the dyadic Green's function for the electric field, $\overline{\overline{\mathbf{G}}}$, and magnetic field, $\overline{\overline{\mathbf{\Gamma}}}$, integrated over the entire volume containing the source current to find the electric and magnetic field in any layer. The details on how to evaluate the dyadic Green's functions are long and complicated and can be found from [72].

2.2.2 Heat Transfer Between Semi-Infinite Plates

While the method of solving the electric and magnetic fields through the Green's functions is general, the computation is extensive and prone to numerical errors. As such, a simpler formulation is desired when considering two opaque or semi-infinite surfaces separated by a vacuum gap, as shown in Figure 2.3. Following the approach set by Polder and Van Hove [73, 74], the Poynting vector can be simplified through the use of fluctuational electrodynamics and the Green's functions to yield a form

$$q'' = \frac{1}{8\pi^3}\int_0^\infty \left[\int_{-\infty}^{\infty}\int_{-\infty}^{\infty} \xi\left(\omega,k_x,k_y\right)dk_x dk_y\right]\left[\Theta\left(\omega,T_1\right)-\Theta\left(\omega,T_2\right)\right]d\omega \qquad (2.31)$$

Where the heat flux can be found from the integration of the *z*-component of the Poynting vector over all frequencies. This is found through the integration of an energy transmission coefficient $\xi\left(\omega,k_x,k_y\right)$ which depends on the in-plane wavevectors. This formulation will be modified as needed in this section and the next, but the transformation into a form that can be quantified using a single value is important.

If only semi-infinite isotropic media are considered as shown in Figure 2.4, the energy transmission coefficient can be simplified and recast in terms of the Frensel coefficients given in Section 2.1.1. Here the two semi-infinite media, 0 and 2 are separated by a non-absorbing gap of thickness *d.* Note here that the wavevector has been shown in cylindrical coordinates since the properties are assumed to be isotropic in the plane of incidence.

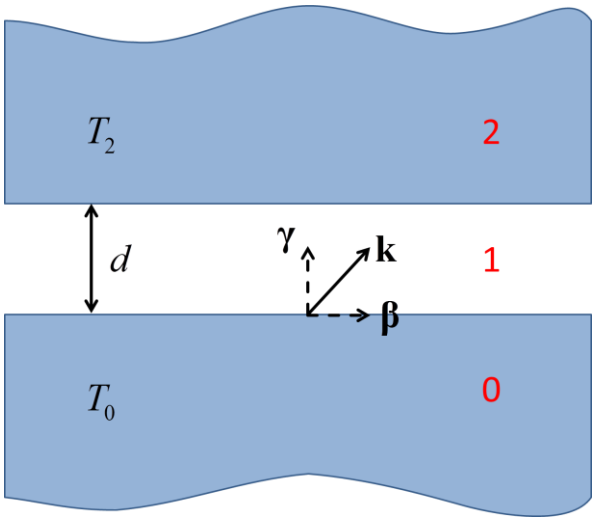

Figure 2.4. Illustration showing the conventions for near-field radiation between semi-infinite and a nanoscale vacuum gap.

$$q''_{\omega} = \frac{\Theta(\omega,T_0)-\Theta(\omega,T_2)}{\pi}\left\{\int_0^{k_0}\frac{\beta}{4}\left[\frac{\left(1-|r_{10}|^2\right)\left(1-|r_{12}|^2\right)}{\left|1-r_{10}r_{12}e^{2i\gamma_1' d}\right|^2}\right]d\beta + \int_{k_0}^{\infty}\beta\left[\frac{\mathrm{Im}(r_{10})\,\mathrm{Im}(r_{12})}{\left|1-r_{10}r_{12}e^{2i\gamma_1' d}\right|^2}\right]d\beta\right\} \tag{2.32}$$

Equation 2.32 gives the heat flux as a function of the spectral variable, and requires integration over the frequency to give the heat rate. Otherwise, the form is very similar to Equation 2.31, though the wavevector integration is broken into two cases. The first integration between 0 to k_0 represents radial wavevectors that do not necessarily create an evanescent wave, and this integration should be thought of as the integration of propagating waves. The second integration is for waves that are necessarily evanescent. While separate treatment is not required for these two cases, the simplifications arise from the evanescent integration. An interesting consequence of this formulation is that the calculation only involves Equations 2.1 and 2.2, and the computational time is very much reduced from the method in Section 2.2.1.

2.2.3 Scattering Theory

Aside from thin film stacks and bulk materials, micro and nanostructured materials are important for near-field heat transfer. In this case, a periodic one-dimensional grating geometry can be used to increase the heat transfer in a tunable frequency range depending on the geometry of the grating. The near-field heat transfer can be obtained between a periodic grating and a flat slab as seen in Figure 2.5 through the framework of scattering theory [75, 76].

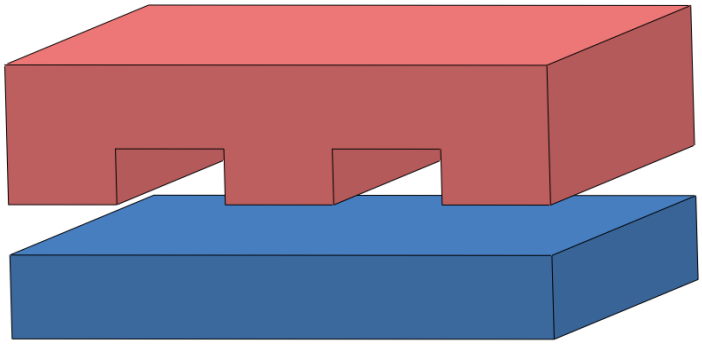

Figure 2.5. Desired geometry to simulate.

Here, the integration limits on Equation 2.31 are changed slightly because the k_x wavevector will only be considered in one period of the grating.

$$q'' = \frac{1}{8\pi^3}\int_0^\infty \left[\int_{-\infty}^{\infty}\int_{-\pi/P}^{\pi/P} \xi\left(\omega,k_x,k_y\right)dk_x dk_y\right]\left[\Theta\left(\omega,T_1\right)-\Theta\left(\omega,T_2\right)\right]d\omega \qquad (2.33)$$

Again, the function $\Theta\left(\omega,T\right)$ represents the average energy from Planck's oscillator at a given angular frequency and temperature, and $\xi\left(\omega,k_x,k_y\right)$ is the energy transmission coefficient. Scattering theory allows the expression of the transmission coefficient as [20]

$$\xi\left(\omega,k_x,k_y\right) = \mathrm{Tr}\left(\mathbf{D}\mathbf{W}_1\mathbf{D}^{\dagger}\mathbf{W}_2\right) \qquad (2.34)$$

Here the operator † represents the Hermetian adjoint. The scattering matrices can be evaluated from

$$\mathbf{D} = \left(\mathbf{I} - \mathbf{S}_1\mathbf{S}_2\right)^{-1} \tag{2.35}$$

$$\mathbf{W}_1 = \sum\nolimits_{-1}^{\mathrm{pw}} - \mathbf{S}_1 \sum\nolimits_{-1}^{\mathrm{pw}} \mathbf{S}_1^{\dagger} + \mathbf{S}_1 \sum\nolimits_{-1}^{\mathrm{ew}} - \sum\nolimits_{-1}^{\mathrm{ew}} \mathbf{S}_1^{\dagger} \tag{2.36}$$

$$\mathbf{W}_2 = \sum\nolimits_{1}^{\mathrm{pw}} - \mathbf{S}_2^{\dagger} \sum\nolimits_{1}^{\mathrm{pw}} \mathbf{S}_2 + \mathbf{S}_2^{\dagger} \sum\nolimits_{1}^{\mathrm{ew}} - \sum\nolimits_{1}^{\mathrm{ew}} \mathbf{S}_2 \tag{2.37}$$

Here $\mathbf{S}_1 = \mathbf{R}_1$ and $\mathbf{S}_2 = e^{ik_{z0}d}\mathbf{R}_2 e^{ik_{z0}d}$ where, $\mathbf{R}_1$ and $\mathbf{R}_2$ are the reflection matrices for the interfaces between the vacuum gap and medium 1 and medium 2, respectively. These are obtained by using rigorous coupled-wave analysis (RCWA). In RCWA the optical properties of the grating region which is necessarily composed of solid and vacuum are expressed as an infinite series to remove discontinuities. The incident wave is also transformed in such a way, and the boundary conditions whereby the tangential electric and magnetic fields are equal across the interface can obtain the unknown Rayleigh terms which constitute $\mathbf{R}_1$ and $\mathbf{R}_2$. The operators $\sum_1^{\mathrm{pw}}$ here identify propagating and evanescent modes with the superscript pw and ew, respectively, and travelling forwards or backwards waves with the subscript 1 and -1. The definitions of these operators and the reflection matrices are presented in [20, 77].

3: INSTRUMENTATION

Much of the work presented in this thesis is based on experimental measurements, and Chapter 3 seeks to describe the major instruments and techniques that are important. For instrumentation that is novel to this work, the design methodology as well as the implementation will be detailed, along with the procedures for data acquisition and refinement. This chapter will detail the procedure of obtaining accurate FTIR measurements in Section 3.1 along with describing the design and usage of a custom reflectance accessory to measure the spectral infrared reflectance of samples under a spring load. Section 3.2 describes the design and development of a one-dimensional thermal resistance measurement. Details on the individual components will be given and the operating procedure will be detailed. A detailed calibration has been conducted with this system, and from this the accuracy of the measurements are obtained. While much of the experimental work detailing sample fabrication and characterization is important, these topics will be discussed in the appropriate chapters.

3.1 Fourier Transform Infrared Spectrometry

An ABB FTLA-2000 FTIR was used for spectroscopic measurements in the spectral range from 500 to 10000 cm^{-1} (corresponding to the wavelength region from 1 to 20 μm). A globar source was used for the far-infrared signal with a separate near-infrared source, and a pyroelectric DTGS (deuterated tryglycine sulfate) detector was used for signal collection. A ZnSe window limits the lowest wavenumber to 500 cm^{-1}, while the strength of the signal is the limiting factor for high-wavenumber measurements, and useful data up to 14000 cm^{-1} can be obtained. The minimum resolution of the machine is 1 cm^{-1}, though this resolution is not used in this work due to the unwanted measurements of interference in the substrate media.

This instrument was used for the determination of the complex refractive index for thin tungsten films in Chapter 5, as well as the determination of vacuum gap spacing for mated samples used in Chapter 6. This section will highlight some of the salient and important characteristics of this machine, as well as the modifications made.

3.1.1 Measurement of Tungsten Film Reflectance and Transmittance

Nitrogen gas was introduced to purge the optical compartment to reduce the absorption due to CO_2 and water vapor. This was allowed to stabilize in the machine for at least 30 minutes prior to operation. Samples were inspected for dust and cleaned as needed using compressed air or isopropyl alcohol before measurement. Each measurement consisted of 256 scans to reduce signal noise with a spectral resolution of 8 cm^{-1}. Background signals to establish the initial intensity as well as to remove the gas absorption signals from carbon dioxide and water vapor were repeated every half hour to prevent changes in the gas absorption.

Normal incidence transmittance was measured using a sample holder with an aperture of 6 mm perpendicular to the beam. This allows for a half-cone angle of 6°, though for reasonably isotropic materials, the radiative properties should be invariant below 20° [67]. Measurements were made three times for each sample, taking measurements incident on both the film and substrate side, and these three measurements were averaged. The sample was removed and replaced in between each of these measurements. These measurements are compared against a background spectrum as the transmittance is necessarily a ratio of incident versus transmitted radiation. The background was taken with the sample holder creating the same reduced aperture with no sample. Then the transmittance can be found as from the ratio of the measured sample and background signal intensities.

$$T = \frac{I_{\text{sam}}}{I_{\text{BG}}} \tag{3.1}$$

The near-normal reflectance was measured with a Pike Technologies 10-spec 10° incidence reflectance accessory, using a gold mirror as the background reference. The reflectivity of this mirror is calculated from optical constants of Au presented in Palik [37]. From this, the reflectance can be determined for each measurement as

$$R = R_{\mathrm{Au}} \frac{I_{\mathrm{sam}}}{I_{\mathrm{BG}}} \tag{3.2}$$

The aperture of the sample holder was 9.5 mm with the 25 mm sample placed centered over the opening. Each measurement was repeated three times, and the averaged results are presented here. Again, the sample was either removed or flipped between measurements to include any potential alignment errors. It has been seen that the placement of the sample and the mirror can create errors of up to 10% if the placement is not correct. For this reason, the measurements of the film-side and substrate-side are individually averaged. The accuracy of the background gold mirror measurement was checked before and after each sample to ensure the integrity of the background. When this signal was off by more than 2% from the previous background measurements, the results may be untrustworthy, and the previous sample was remeasured. The estimated uncertainty in the measurements is 0.01 for transmittance, and 0.03 for reflectance. However, for transmittance less than 0.1, a relative uncertainty of 10% may be used as long as the transmittance is greater than 0.005. A more detailed description of the setup can be found in [78, 79].

3.1.2 Reflectance for Vacuum Gap Determination

Chapter 6 will detail the design, creation, and measurement of silicon samples that have a plane-parallel vacuum gap for photon tunneling. The thickness of this vacuum gap is validated using FTIR spectroscopy prior to the heat transfer measurement. The sample behaves as though it has two incoherent doped-silicon layers 500 μm thick sandwiching a

thin coherent layer of air or vacuum. The thickness of this layer will create a unique interference pattern, as shown below in Figure 3.1.

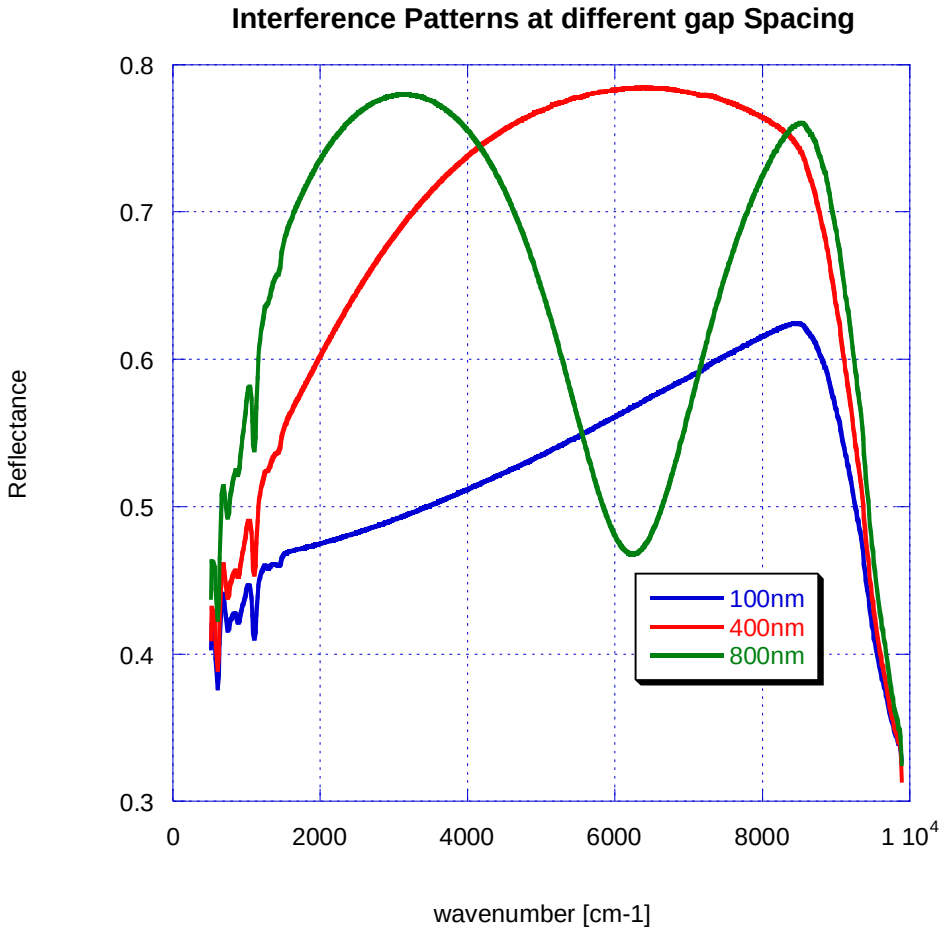

Figure 3.1. Reflection spectra for vacuum gaps sandwiched between undoped silicon. The interference patterns caused by the gap spacing are clearly seen.

Here the power of this technique is clearly seen, as the gap spacing can be clearly delineated between 100 nm, 400 nm, and 800 nm based on the interference fringe spacing. However, for the distinction of smaller increments, the difference is less obvious, and a high degree of accuracy is required. It is shown somewhat in Figure 3.1 for the 100nm and 400 nm calculations, but low gap spacings will not show multiple interference fringes like is seen with the 800 nm signal. In some cases the location of the reflectance peak can determine the gap spacing, however for accurate determination within 20 nm, accurate numerical comparison over the entirety of the signal is required.

For this reason, extra optical metrology equipment was designed and implemented to give more concrete numerical analysis.

One immediate challenge with this technique versus the previous FTIR measurements is that only one measurement is available. Since the sample is symmetric about the vacuum gap, the front-side and back-side reflectances will be the same (as opposed to the film-side and substrate-side reflectances). If the transmittance could be measured, then two independent curves can be used to determine the gap spacing. Unfortunately, the transmittance sample holder used in Section 3.1.1 could not be used as it placed too much lateral force on the samples, causing the samples to break. Since the two samples are held together only through weak Van der Waal's forces, they are very fragile, and any force acting parallel to the gap (i.e. shear forces or force applied to the sample sides) will cause the two Si pieces to delaminate and fall apart. When this happens outside of a cleanroom fume hood, the chance of a single piece of dust entering the sample is very high, causing the sample to fail.

A transmittance accessory was designed to hold the sample between two zinc selenide windows. Zinc selenide was chosen because it is transparent in the entire relevant spectral range. This technique failed for two reasons. Most importantly, the mechanism created too much shear stress at the ZnSe-Si interface, causing a very good chance to break the samples. Furthermore, modeling these two interfaces proved to be very difficult. Since the interfaces will not necessarily be perfectly plane-parallel due to dust, bowing, or surface roughness, a small air gap will form. Depending on the thickness and area of this gap, the overall transmittance can vary significantly. To alleviate this, the interface gap thickness can be reduced by applying force to the sample-window system. This was done using four springs in parallel on the metal plate holding the ZnSe window. While it did make the spectral measurement more reliable, the increased forces caused

every sample measured to break during the measurement. As such, measurements of the transmittance were abandoned.

The reflectance accessory needed to be modified as well. Since the aperture of the reflectance sample holder is a 9.5 mm diameter circle, and the samples were only 1 cm squares, the aperture needed to be reduced. The reason for this is that any incorrect placement of the sample, or incorrect mating of the sample can create a situation where part of the FTIR signal is not measuring the gap, and accurate determination is impossible. Furthermore, some degree of non-uniformity of the vacuum gap is expected due to bowing, and this tends to be more extreme very close to the sample edge. For a large-area FTIR measurement, this bowing can show up as a non-parallel gap, which is difficult to determine.

The optics of the reflectance accessory are still very useful, so only the removable sample holder plate needed to be redesigned. A simple flat plate with a 3 mm diameter aperture was machined out of low-carbon steel to match the dimensions of the original sample holder. This also gives the advantage of being able to measure at several different locations across the sample, and the smaller sampling area makes determination of small amounts of non-parallelism possible. Unfortunately, the data analysis needs to be modified for this hole size because of the spot size of the FTIR. The signal incident on the backside of the sample holder has a spot size of about 10 mm diameter, which means that a significant portion of the incident intensity will be directly reflected off of the sample holder and collected by the DTGS detector.

Typically, the measurement of the reflectance requires the use of equation 3.2, however this needs to be modified to account for the sample holder reflected intensity.

$$R = R_{\mathrm{Au}} \frac{I_{\mathrm{sam}} - I_{\mathrm{SH}}}{I_{\mathrm{BG}} - I_{\mathrm{SH}}} \tag{3.3}$$

In this case a measurement of the open sample holder needs to be made along with a background measurement. However, the strength of this sample holder signal needs to be as small as possible, otherwise any uncertainties in the sample holder measurement will overpower the sample measurement, and the reflectance will tend towards unity regardless of actual sample reflectance. To do this, the back of the sample holder was coated with carbon black using a lit candle. This was repeated as necessary if the maximum value of the sample holder signal became more than 10% of the intensity of the actual measurement.

Should the samples have any appreciable amount of bowing changing the gap spacing, force was typically applied to reduce this during the thermal measurements. However, this change in gap spacing with force needs to be quantified. As such, a modification to the reflectance accessory was developed such that force can be applied to the top of the sample, where the FTIR can determine the change in gap spacing the sample will experience under different loads. A picture of this is shown in Figure 3.2.

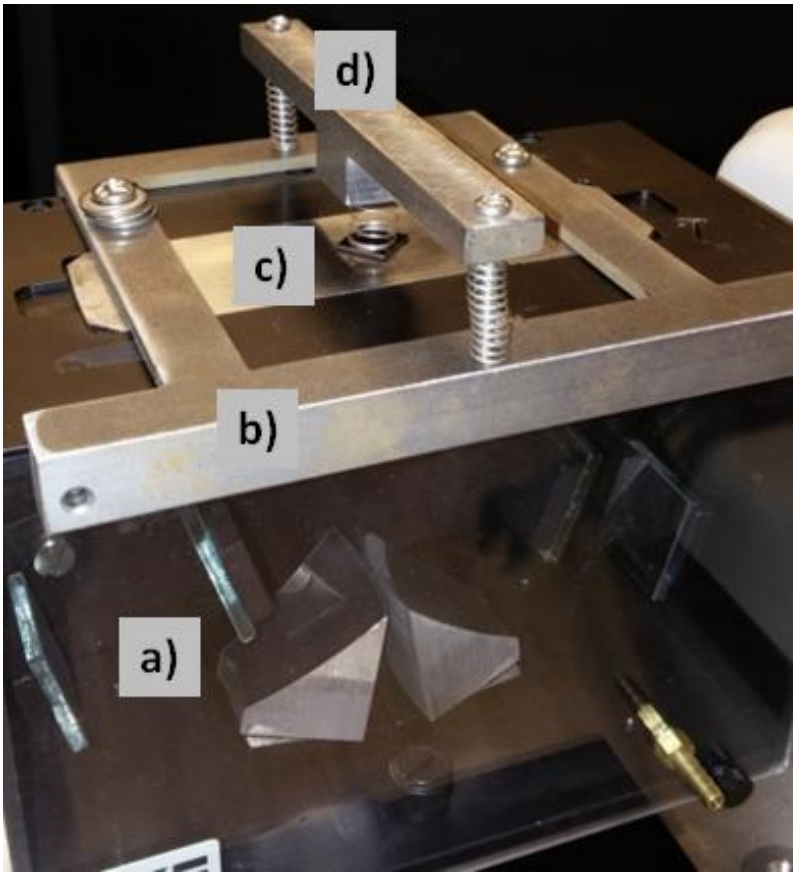

Figure 3.2. Picture of the reflectance accessory with the added components: a) Pike 10-spec, b) mounting bracket, c) 3 mm aperture sample holder, d) support bar. The sample and springs can also be seen.

Here, the equipment described earlier can be seen in Figure 3.2 with the original reflectance accessory shown as a) and the sample holder shown as c). To apply force to the sample shown just to the right of c), a spring is in contact with the sample and the support bar d). The mounting bracket b) secures this all together. All of the components were machined from low-carbon steel and fit with the existing threads in the reflectance accessory.

By measuring the height of the support bar, the amount of deflection and thus force can be found in the spring, which can vary between 0 to 50 grams for the spring shown, or 0 to 500 grams for a separate plastic spring. The spring shown has a very weak spring constant, 0.26 lbf/inch, so accurate determination of the force is fairly easy.

Without much effort the distance between the sample and support bar can be set within 0.01”, which corresponds to roughly 1 gram. It should be noted that the spring is not completely centered on the sample so that the force is delivered more to the center. The support bar has two springs on either end to remove the weight of the bar. These two springs are significantly more rigid than the spring contacting the sample, so the force on the sample due to the weight of the bar is negligible.

With this system, accurate determinations of the vacuum gap spacing can be made before the heat transfer measurements are performed. Measurements were made with large resolutions, typically 16 or 32 cm^{-1} spectral resolution and a large number of scans, up to 512 per measurement to reduce noise. A measurement of the open sample holder was made first, followed by a background measurement using a gold mirror. Samples were carefully placed over the aperture and the reflectance was measured. Since the yield is fairly low on these samples, this served as a preliminary measurement. A computer calculation matched the corrected reflectance as described in equation 3.3 and found the best fit gap spacing. Should a sample have a reasonable result, then further testing would occur.

Though not all samples presented in Chapter 6 were measured in every way, measurements at different positions with no force, and measurements of the center with applied force were very useful. For samples that showed higher gap spacing than desired, a position-resolved measurement was conducted. In this, the sample was measured at 5 positions in a line from one corner to the other, including the center, and then measured in 5 positions between the other two corners. Through this, a rough map of the deflection could be seen and any pitfalls could be avoided. One such problem that may arise is contact at the edges, which acts as a thermal short for the heat transfer coefficient and causes the temperature drop across the sample to disappear.

Samples that have a higher gap that appeared to be due to bowing were measured versus force. In this case only the center position was considered, and measurements started with the predicted spring force at 0 grams and were checked with the previous measurements. The bar was lowered by 0.02” on each side, as measured with a caliper, until the bar was parallel and at the next desired force. After each measurement, the force would be increased. This would typically go until 30-50 grams, as the heat transfer force cannot be set to higher values without the sample breaking. Results for individual samples will be shown in Chapter 6.

3.2 Development of a High-Vacuum Heat Flux Measurement

This section describes the design, development, and implementation of a room temperature thermal resistance measurement to take place under high vacuum conditions. The objective of Chapter 6 is to show strong evidence of near-field heat transfer, and requires a system to measure the temperature drop and heat flux across a sample. Based on the characteristics of the sample, especially the vacuum gap spacing described in Section 3.1.2, the amount of heat passing through the sample will increase or decrease. The results of these tests will be given in Chapter 6, though the design and testing of the heat transfer systems will be given here.

3.2.1 Overview

A schematic of the heat transfer system can be seen in Figure 3.3a, with a picture of the system in Figure 3.3b. To give scale, the dimensions of the PTFE calibration sample seen in Figure 3.3b seen in white is 1 cm by 1 cm by 1 mm. Here a heater will create a temperature drop across the sample, and the temperature drop as well as the heat flux over the sample will be measured. Accuracy of the absolute temperatures above and below the sample is very important, as is the accuracy of the heat flux. For this, a thermopile heat flux meter is used, and is calibrated in this system.

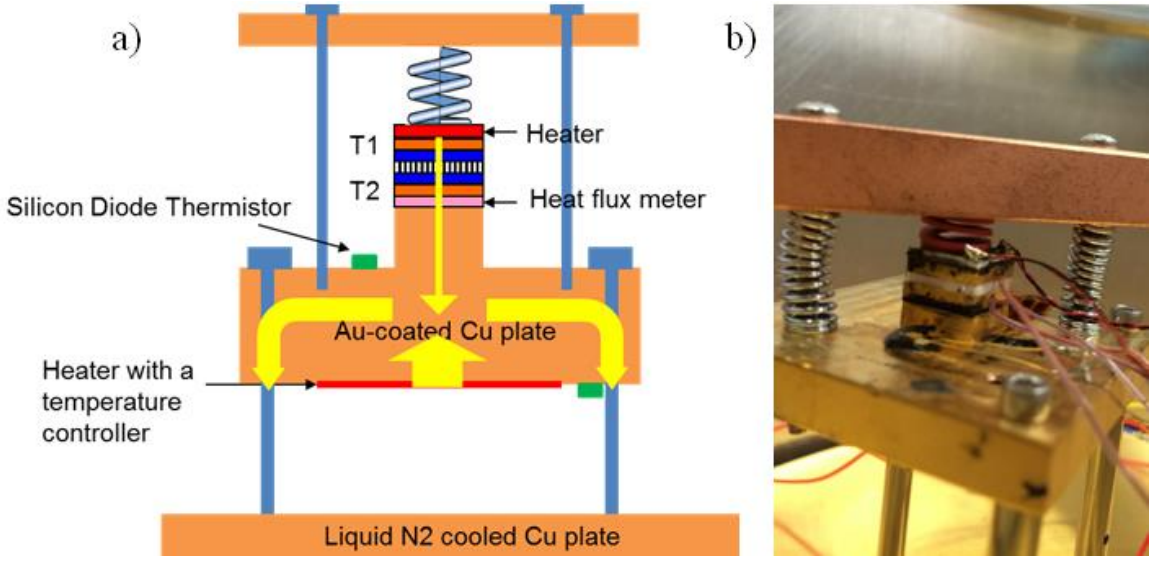

Figure 3.3. a) Schematic of heat transfer system with important components labeled. The sample is shown in blue. b) Picture of the system with a calibration sample in place.

In Figure 3.3a the path of the heat from the top to bottom is important, creating one-dimensional heat transfer across the sample. The heat passes from a resistance heater through a copper block with an embedded thermocouple, through the sample, and through another thermocouple block. Finally, the heat passes through a heat flux meter for measurement, and into the gold-coated copper base plate. Below the base plate is a thin film heater capable of delivering up to 5 W to raise the base temperature. This is to measure at elevated temperatures and to control the temperature with liquid nitrogen cooling. This heater is connected to a Lakeshore 325 temperature controller capable of setting the absolute temperature of the base plate with a PID loop, however this functionality is not used in the present work.

Aside from the sample, all components are secured with Stycast vacuum epoxy. The base plate is connected to the copper plate of the cryogenic dewar with screws and stainless steel spacers to ensure a tight and secure stage. Above the top heater is a spring in contact with a copper bar, referred to as the spring bar. This is to function identically to the force-controlled FTIR reflectance measurements in Section 3.1.2. Using the same spring, the height of the two ends of the bar can be measured with a caliper versus the

base plate. With all of the other geometries known the amount of force applied to the sample can be calculated. It should be noted that the two springs pushing the bar up make the weight of the copper bar negligible, and the total weight of the components above the sample is approximately 1 gram. The difficulty in measuring the height of the bar means that the height can be controlled accurately to within 0.01". As such, the uncertainty in the force applied to the sample will be less than 2 grams.

3.2.2 Cryogenic Dewar and Vacuum System

In order to show accurate near-field radiative heat transfer, the entire experiment must be conducted within vacuum. This is due to the fact that thermal conduction through a layer of air 200 to 1000 nm thick will have a thermal resistance of roughly 0.2 K/W versus the expected thermal resistance of the samples near 50 K/W. Thus, the gas must be rarefied, whereby the heat conduction is transported by individual non-interacting particles known as the free-molecular regime [67]. The low-pressure effective thermal conductivity in the free molecular regime decreases proportionally to the pressure [80], so measurements need to be under 10^{-4} torr (roughly 10^{-2} Pa) to effectively ignore gas conduction.

The entire system mounts to an Infrared Laboratories ND8 dewar with the screws shown. This not only allows for vacuum pressures to be achieved, but allows the entire vacuum chamber to act as a room-temperature thermal reservoir, ensuring that the flow of heat will be down through the sample and heat flux meter. Additionally, an aluminum foil radiation shield surrounds the entire system to help minimize side losses. The vacuum inside the chamber is controlled with an Agilent TPS compact vacuum pumping system. This uses a scroll pump and a turbomolecular pump to reach levels down to 10^{-5} Pa (10^{-8} Torr) as measured with an inverted-magnetron gage. Although this pump is capable of evacuating the dewar to 10^{-4} torr within a few hours to satisfy the gas thermal

conductivity requirement, all measurements were allowed to come to pressure for at least 10 hours, and all measurements took place at pressures lower than 2×10^{-6} torr.

Additionally, this system is capable of cryogenic temperatures, where near-field heat transfer can be stronger. At lower temperatures, the characteristic wavelength of thermal radiation shifts to longer wavelengths, and the necessary vacuum gap requirement for exceptional near field heat transfer can increase substantially, though the overall power throughput will drop significantly. This system has been tested in this capacity and was found to perform well. The dewar was cooled with liquid nitrogen under vacuum conditions. The sample stage was maintained at a constant temperature of 0°C to prevent damage to the sensing equipment which is not rated for liquid nitrogen temperatures, however a thermocouple measured the temperature of the dewar walls to be near 77K. The chamber was able to maintain this temperature for 10 hours without refilling the reservoir, and the vacuum pressure reached levels as low as 8×10^{-9} torr. While the ability to control the temperature to any point is useful, the dewar is designed such that the system must be inverted to hold liquid nitrogen, and leads to a high likelihood that the fragile sample will be damaged.

3.2.3 Thermal Metrology Components

Figure 3.4 shows an illustration of the heat transfer measurement system with an emphasis on the thermal metrology and control equipment. A schematic of the sample is also blown up to show the nanopillar geometry, though not to scale. A $1cm^2$ printed resistance heater from Thick Film Technologies with a resistance of 26Ω supplies heat to the top of the geometry, and the amperage, and thus the power is controlled using a Hewlett-Packard E3632A DC power supply. The input power to this heater is generally controlled between 20 mA and 300 mA. The heater is epoxied to a copper plate, referred to as the thermocouple block, 1mm thick with a thin hole drilled halfway through the side to allow a thermocouple to be inserted. Below the thermocouple block, the sample is

installed, with a thin layer of Aremco Heat-Away 641-EV silver grease to ensure good thermal contact. Silver compound joins the bottom of the sample to second thermocouple block. This is then epoxied to a Captec Enterprises thermopile-type heat flux meter (HFM). On the base plate, as close to the raised area as possible, a LakeShore DT-670 Silicon Diode thermistor is mounted to measure an accurate temperature reading. Between the thermocouples placed above and below the sample and the heat flux meter, both the heat rate and the temperature drop can be independently measured and compared to simulations to show the importance of near-field thermal radiation across the sample.

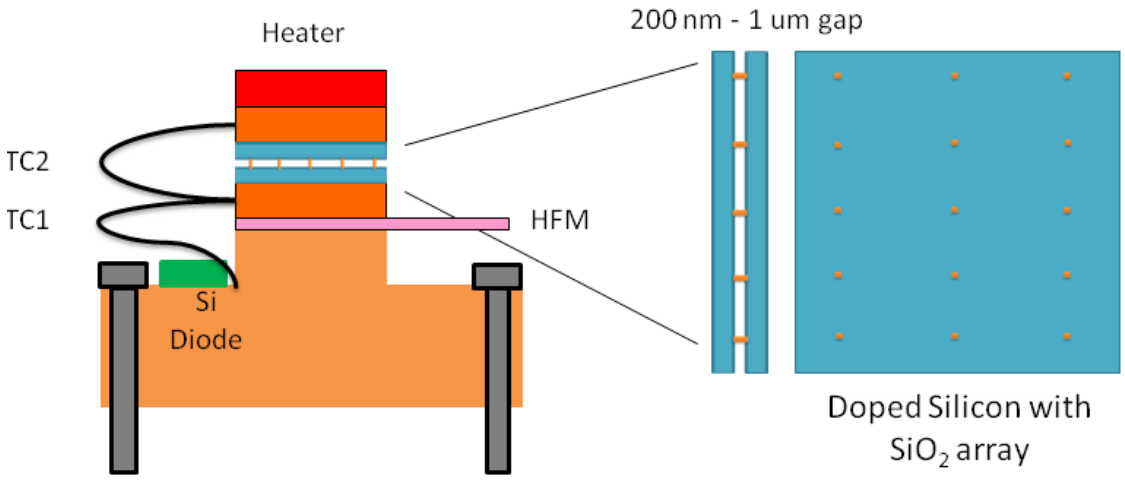

Figure 3.4. Schematic of the important heat transfer measurement components with an illustration of the sample geometry. Shown are the resistance heater, top and bottom thermocouples, heat flux meter, and silicon diode thermistor.

The HFM is epoxied to the base plate, a larger copper block that serves as a staging area for the measurement equipment. The base plate has is raised $1cm^2$ area to match the other equipment geometry. This helps to maintain the one-dimensional heat flow as heat spreading to the base plate will not create a nonuniform temperature within the sensing area. The entire system relies on maintaining one-dimensional heat flow across the sample, with a uniform temperature in the perpendicular plane. There will of course be some amount of heat lost to the sides, but this is not a significant problem for several reasons. The temperature uniformity only needs to be maintained across the

sample, which will have a very small amount of area on the sides. Each silicon piece that the samples are made from is approximately 500 μm thick, giving a surface area of 0.4 cm^2. Furthermore, the silicon and the copper pieces above and below have a high thermal conductivity, versus the high thermal resistance caused by the vacuum gap. As such, the temperatures above and below the vacuum gap should be very uniform.

While heat may radiate through the sides of the other components, or even from the top or through the spring above the heater, none of this is important. From all of the calibration tests and measurements, it is found that generally 35% of the heat input to the heater does not pass through the sample. For this reason, the input power to the heater is controlled, though is only used as a set point. Regardless of the amount of heat passing through, the HFM will determine the correct value independent of the thermocouple temperature readings. The HFM needs to be individually calibrated for this setup, as the vacuum pressures change the heat transfer coefficient to values different than what the manufacturer calibrated for, and this will be discussed in the following section. In this case, the total amount of side heat leakage does not affect the results, as the calibrated values account for this, however it must be maintained constant. Should the relative amount of heat leak change, the calibration will not hold anymore.

For this reason, the amount of heat leak has been minimized at every opportunity. At these vacuum pressures, the heat transfer out of the sample stage can only be through radiation or conduction, and the majority of heat is removed through the screws connecting the base plate to the dewar. Conduction through the wires connecting all of the equipment is believed to have very little impact. The wire material and gauges used were chosen to be very highly thermally resistive to prevent unwanted conduction. Only the heat flux meter, bottom control heater, and top heater have wires that could potentially conduct heat, and these are all outside of the measurement heat path. The

thermocouples used are teflon-coated 40 AWG wires, and excess conduction through these is negligible.

The spring to control the applied force to the sample was chosen for low thermal conductivity. Two sets of springs were used during this experiment, a plastic resin spring and a low gauge stainless steel spring. The plastic resin spring has a spring constant of 2.65 lbf/inch, was used largely for calibration experiments where the desired force was high to reduce contact resistance. The stainless steel spring has a spring constant one-tenth of the plastic spring, making this ideal for finely tuned force measurements. It was found to be very difficult to control the plastic spring to forces lower than 30 grams. The amount of heat flux through the springs was measured for identical test situations, and both springs were found to have negligible conduction when not significantly loaded. When the compression of the springs reached roughly 15-20% of the maximum deflection, the heat rate passing through the sample decreased, showing heat being conducted through the spring. At first this was attributed to the force, as this manifested more with the plastic spring. However, stronger springs made from a similar resin material and with the same geometry were tested. It was found that the change in the heat rate was not a function of the applied force, but of the compression in the spring. Only when the spring was sufficiently compressed would the spring come in contact with itself reducing the distance that the heat would travel in the spring, and thus the thermal resistance. With this in mind, the springs were never allowed to be compressed more than 70% during measurements.

Finally, the overall radiation heat leak was minimized. Except for the bar above the heater that holds the spring, all of the copper pieces used were electroplated with gold, approximately 50 μm thick to reduce surface radiation. Since gold is a highly conductive metal, the absorptivity and thus emissivity is very low, reducing the overall radiative losses. Additionally, a radiation shield was used to minimize the side heat

transfer. This was made of ultra-high vacuum aluminum foil and was molded around the staging area. The methodology behind a radiation shield is to use a low-emissivity material at an intermediate temperature between the thermal source and surroundings to increase the radiative thermal resistance. In this case, the radiation emitted by the sample stage is able to reflect back to itself, reducing the overall amount of heat transfer. Attempts were made to maintain the foil radiation shield at the same temperature as the base plate by maximizing the contact with the base plate and spring bar, however great care was taken to not contact any of the wires for the sake of mechanical stability of the system.

The thermocouples used to measure the temperatures above and below the sample, T_{H} and T_{L} respectively, are Omega 40AWG E-type thermocouples that were purchased pre-bonded. However, the accuracy of thermocouples is insufficient for this application. As seen in Figure 3.5a a thermocouple is made by joining two dissimilar metal wires, in this case constantan and Chromel for types 1 and 2, respectively. Since these wires have different values of thermal and electrical conductivity, the thermal transport of heat carried by electrons should be different in each wire. However, the temperature drop is maintained the same between the junction between the two wires and the connection to an electrical lead wire, and to resolve this, a potential voltage is generated. This voltage can be used to find the temperature difference between the lead and junction.

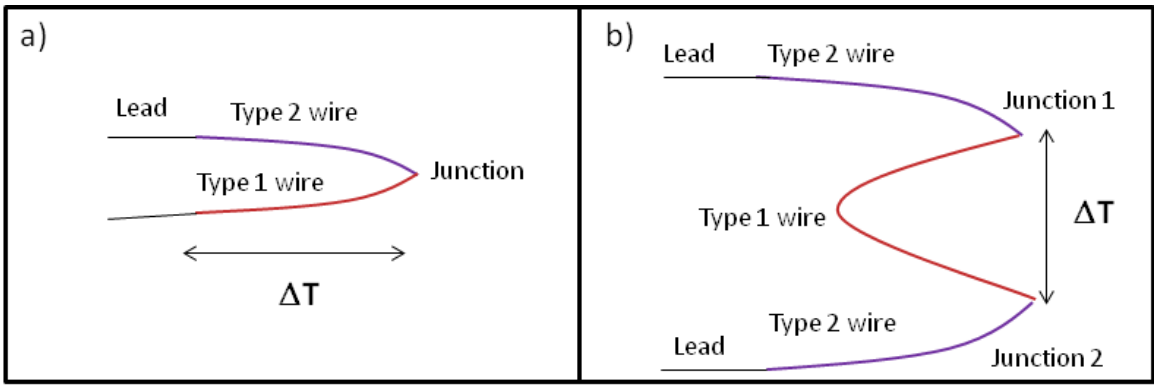

Figure 3.5. Thermocouple configurations where the relevant measured temperature drop is shown. a) single thermocouple, b) duplexed thermocouple.

However, there is a major flaw in this measurement: the absolute value of the lead temperature must be known. In many cases this is either poorly controlled with a thermocouple reader, or is left to be the ambient temperature, and both cases generate a good deal of uncertainty in the junction temperature. Especially in this case, the electrical lead connections may be any temperature between the base plate temperature and the temperature of the dewar, which may be as high as a 10°C difference. For this system, duplexed thermocouples are used, as demonstrated in Figure 3.5b. Here, two premade thermocouples are used, but instead of connecting the type 1 constantan wire to the lead, the two constantan wires are connected together. In this configuration the constantan wires are bonded together using a thermocouple arc welder such that the output voltage is the difference in voltages between the two normal chromel-constantan junctions. This is very useful for this case, as the temperature of the lead connection is not required, only the temperature of one junction. Thus, the low-temperature junction for the bottom thermocouple, denoted as TC1 in Figure 3.4, is placed immediately next to the Si diode thermistor, which gives an absolute temperature calculated with a LakeShore 325 temperature controller. With the lower temperature known, the voltage output of the thermocouple is measured with an Agilent 34401A multimeter, and the temperature just below the sample is known. A second thermocouple, referred to as TC2, measures the

temperature difference across the samples, giving an accurate measurement of the absolute temperatures above and below the sample.

However, while this configuration does remove the uncertainties associated with knowing the lead temperatures, there are still challenges associated with relative temperatures. The thermocouples as described output a potential voltage according to the temperature difference between the two junctions, however, because of the slight nonlinearities in the thermocouple sensitivities, the absolute temperatures of both junctions have an effect on the output voltage. For this reason, the temperature drop cannot be measured directly, but the temperatures above and below the sample can be found.

As seen in Figure 3.4 there is a silicon diode thermistor near one of the junctions to thermocouple TC1. This LakeShore DT-670 Silicon Diode thermistor is individually calibrated to give accurate absolute temperature readings within 37 mK. This device has a nominal 100 Ω resistance, and the temperature-dependent resistance is measured in a four-wire configuration to remove the resistance of the lead wires, and a calibration curve set by the manufacturer determines the absolute temperature. Immediately epoxied next to this is the cold junction for the first thermocouple, and it is assumed that it is the same temperature as measured by the thermistor.

Due to the nonlinearities in the temperature-voltage relationship for the thermocouples and the reference temperature of 0°C, the temperature of the cold junction of TC1, T_0, affects the potential voltage. To find the temperatures from the thermocouple, the thermistor temperature is converted to the corresponding voltage for the thermocouple for the temperature difference between T_0 and 0°C. The output voltage from the thermocouple is added to this, and the resulting voltage is used to find the temperature difference between T_L and 0°C. Here both of the absolute temperatures T_L and T_H, corresponding to the temperatures below and above the sample, respectively, can

be found. The copper block that holds the hot junction for TC1 also contains the cold junction for the second thermocouple, TC2. Using the same methodology, and assuming the two contacting junctions are the same temperature, the absolute temperature above the sample is obtained.

These thermocouples allow for accurate measurement of the absolute temperatures above and below the sample, and the accuracy of these devices will be discussed in Section 3.2.5. Along with the temperatures of the sample, the heat rate or heat flux is necessary to determine the near-field heat transfer performance. This is possible through the use of a thermopile heat flux meter that is calibrated for this measurement system, as described in the next section.

3.2.4 Heat Flux Calibration

The heat flux meter outputs voltage to a multimeter, and this in turn determines the heat flux passing through it. The manufacturer has calibrated each HFM individually, however, a precise calibration is needed since the manufacturer did not calibrate for vacuum conditions. Figure 3.6 shows the heat flux meter, showing the 1 cm square sensing area encased in copper. Though it is difficult to see from this picture, the thickness of the copper area is less than 1 mm. Next to the sensing area is a fairly large section of lead wires encased in kapton for insulation. Because of the relatively large surface area of the leads, the heat transfer from the surface can be significant. This problem is typically alleviated by the manufacturer through a calibration; however, since this measurement takes place in high vacuum, the heat transfer coefficient should be roughly half of the calibration value. This will undoubtedly affect the response between the voltage and heat rate.

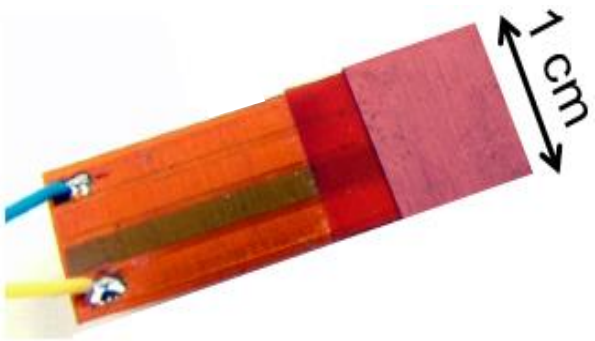

Figure 3.6. Heat flux meter used in this work.

The premise behind the operation of a heat flux meter is measuring a temperature drop over a material of known thermal resistance. The embedded thermopile measures the voltage, which is linearly proportional to the temperature drop. Through the use of a calibration constant, the heat rate can be found $Q_{\mathrm{HFM}} = V / C$ as the ratio of the output voltage and the sensitivity C. The sensitivity of this device changes slightly because of the decrease in heat leaving the side lead area. Thus for a given voltage (temperature drop), the sensitivity should be smaller to account for a larger amount of heat passing through the sensing area. It is difficult to predict this amount of change, so a calibration is needed in the same conditions that it is to operate under.

To determine the calibration constant, measurements were made with natural virgin PTFE pieces approximately 1 mm and 2.5 mm thick. These experiments were conducted in the same manner as the real samples, with everything fully installed. PTFE was chosen because it has similar thermal resistances with the sample predictions, and also for the ease of installation and the vacuum compatibility. The thermal conductivity was given by the manufacturer as 0.20 W/m-K, however extruded or formed plastics may have very significant differences in the thermal properties between manufacturers, or even between batches of material. As such, measurements were done to investigate the thermal conductivity of the samples. It should be noted that the 1 mm and 2.5 mm thick PTFE samples were cut from two different sheets. It is not known if these sheets were

created during the same batch, and it is expected that the thermal properties may differ between the thicknesses. The sheets were approximately 18” square, and samples were cut via a razor blade. Though it is possible that the thermal properties vary across the sheet, this will not be considered. As such, properties for the thick and thin sheets will be found independently, and the correct properties will be used in the calibration experiments.

A three-omega technique developed by a colleague at the Georgia Institute of Technology for thermal conductivity measurements of polymers was used. In this, interdigitated metal heater and sensor lines are deposited using electron-beam evaporation directly onto the sample [81]. Only the thin set of samples was measured here, though nine samples were measured. While this technique often requires the use of photolithography for pattern transfer using a lift-off technique, the metal pattern is large enough to simply evaporate onto the sample using a mask. A pulsed heat input is used to generate a temperature difference, which can be measured and used to find the thermal conductivity. Because of the nature of this measurement, the effects of the specific heat of the sample are removed from the measurement, and the thermal conductivity can be found directly. Using this technique, the thermal conductivity of the thin PTFE was found to be 0.27 W/m-K with an uncertainty of 5%.

Because of the significant disagreement between the measured thermal conductivity and the given thermal conductivity, a second set of measurements were made. Another colleague at the Georgia Institute of Technology measured the thermal diffusivity using a Netzsch LFA 467 Hyperflash laser flash measurement system. Here both the thin and thick samples were measured over a temperature range from 25°C to 55°C in intervals of 5°C. Two samples of each thickness were measured and four measurements were taken at each temperature. Samples were cut very carefully using razor blades and tested in the sample holder to make sure that there was no excess light

bleeding from the sides, and then were coated in aerosol graphite to promote absorption. In laser flash measurements, the thermal diffusivity can be determined by applying heat to the top surface of the sample using a pulsed laser beam. An infrared pyrometric detector measures the temperature of the bottom surface of the sample, and the time lag can be used to find the thermal diffusivity, α. This can be used to find the thermal conductivity from

$$\kappa = \rho C_p \alpha \tag{3.4}$$

Thus the density ρ, and specific heat C_p are required to determine the thermal conductivity. The density was measured simply by measuring the volume and mass of several samples. Two samples of each thickness were cut to approximately 1 inch squares, and the dimensions were measured using calipers and a micrometer to find the volume. Since the samples were not perfectly square, several measurements of the length and width were made and average values were used. The mass was measured using a precision scale, and the density was found to be 2.17 g/cm^3 for all four samples. A differential scanning calorimeter was used to measure the specific heat. A TA Instruments Q100 Differential Scanning Calorimeter was used to measure one sample of each thickness. In this measurement, a small chunk of material (less than 100 mg) was cut and weighed, then placed in an aluminum crucible. A precise amount of heat is added to the sample and the temperature rise is measured. This is compared to a reference crucible with no sample to remove the specific heat of the pan. This measurement was conducted between temperatures of 20°C and 55°C, and the results are shown in Figure 3.7.

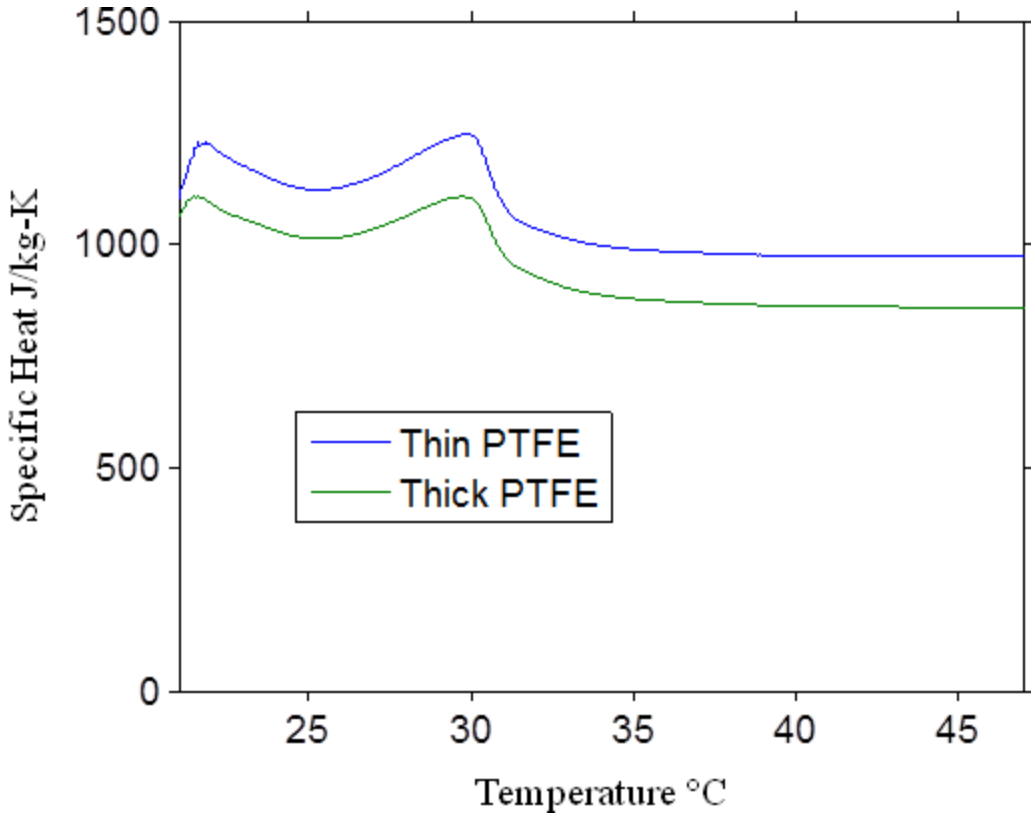

Figure 3.7. Measured specific heats for the thin and thick PTFE samples. Note the bump near 30°C corresponding to a change in the crystal phase.

Here the differences between the thick and thin PTFE samples are apparent. Furthermore there is an increase in the specific heat near 30°C associated with the transition from a hexagonal crystal to a pseudo-hexagonal crystal structure [82]. While this will affect the thermal properties of this material, is it clear that the temperature-dependent properties must be used in any case.

From this the temperature-dependent thermal conductivity is found for both thicknesses. The values for the thick and thin PTFE samples between 25°C and 55°C are shown in Figure 3.8. The change in specific heat shown in Figure 3.7 causes a decrease in thermal conductivity past 30°C, however it is very interesting to note that the shapes of the two curves are dissimilar before this point. There is a difference in the thermal diffusivities between the two thicknesses. While both samples show a decrease in thermal diffusivity at 30°C (versus the high temperature diffusivity) to offset the specific heat

spike, the measurements at 25°C are notably different. With the thick samples, the diffusivity is larger at 25°C than it is at 30°C; however the thermal diffusivities for 25°C and 30°C are the same in the thin samples. Since the specific heat is lower at 25°C, this gives a lower thermal conductivity.

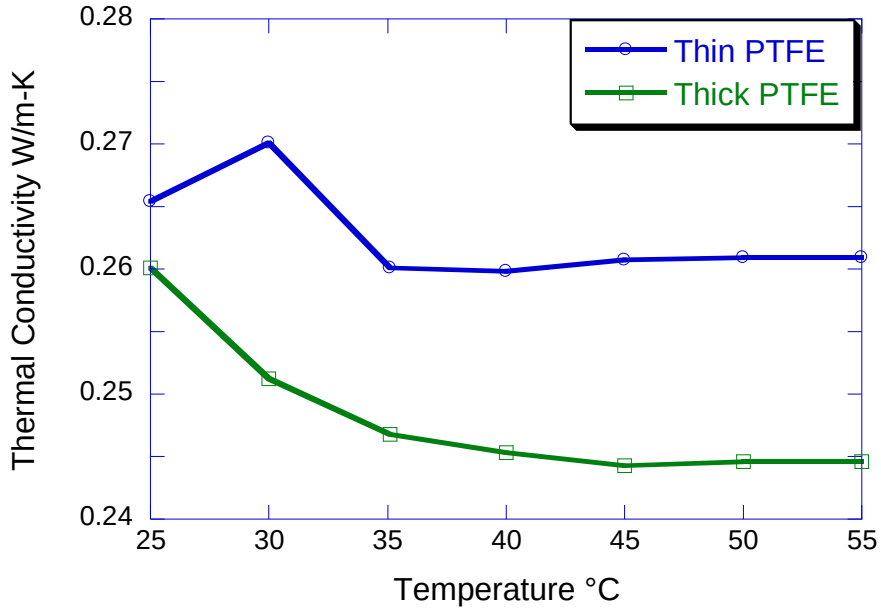

Figure 3.8. Thermal conductivities for both PTFE sizes

It should be noted that this trend is not from an isolated measurement. Another set of laser flash measurements were taken with three thin PTFE samples, however there were problems with light leaking through the edges of the samples during the measurement, and the accuracy could not be trusted. However, all three of these samples, as well as the single thick sample showed the same trends between 25°C and 30°C, giving some validity to the measurements. Furthermore, as will be discussed in Section 3.2.5, the relative uncertainty of these measurements spans the potential discrepancy. However, the uncertainty found is only 3.3%, and does not explain the differences between the thin and thick samples. As such, the temperature dependent thermal conductivities of the appropriate sample thickness shown in Figure 3.8 will be used for the heat flux meter calibration, with interpolation used when necessary, however a rough

value for the thermal resistances of these sample is approximately 40 K/W for the thin samples, and 100 K/W for the thick samples.

The heat flux meter calibration consisted of 12 measurements of PTFE samples, along with 2 measurements of silicon samples. The samples were installed onto the sample stage in the same location as the sample in nearly identical fashion as described in Section 3.2.3. The samples were cut from sheets using a razor blade into 1 cm square pieces. The dimensions were measured using calipers and a micrometer. Two measurements were taken for each side and the average was used to find the area of the square. Five measurements were made of the thickness, and the average is used. Adequate thermal contact is required for the repeatability of the measurements. Contact resistance for an area this size can be as high as 10 K/W, while the thin samples only have a thermal resistance of 40 K/W. To alleviate this, Aremco Heat-Away 641-EV silver grease was used to decrease the contact resistance. Additionally, due to difficulties in predicting the contact resistance, measurements of 1 cm square silicon pieces 500 μm thick were measured. Using a thermal conductivity of 140 W/m-K, the thermal resistance of the silicon samples is negligible, and any thermal resistance found in the measurement can be prescribed to contact resistance.

Thermal compound was applied above and below the sample, and the whole stack was compressed to ensure good thermal contact between the thermocouple blocks and the sample. It was common that thermal compound would spill out of the stack during compression, and the excess was wiped away using a low-particulate wipe. The sample was visually inspected and checked for rotation, and corrected if necessary. To ensure good repeatable contact resistance, a large amount of force was placed on the sample with a plastic spring, ranging between 150 grams to 500 grams. This is far in excess of what the fabricated samples can safely tolerate, however the contact resistance for those fabricated samples will be independently measured. A radiation shield was employed to

reduce side leakage, and the vacuum was left to run for at least 10 hours. The heat rate through the sample was controlled by adjusting the input power to the top heater. Each measurement had at least three different power settings between 50 mW and 300 mW, and the system was allowed to come to steady state for at least 1 hour before the power changed. A Labview program was created to handle the transient data acquisition.

With all measurements taken, the heat flux meter sensitivity can be found. As expected, there are differences between the sensitivity as determined for each measurement, so only one value for the sensitivity was fit, along with a single value for the contact resistance. Six data points were taken from each measurement for fitting: one from the beginning of each power setting once steady state had been reached, and one from the end of each power setting immediately before the power was changed. These points were chosen to represent a difference in temperatures, as the base plate temperature, T_0 would steadily rise over the course of the experiment. The total thermal resistance of the installed sample can be found from

$$R(T) = \frac{t}{A\kappa(T)} + R_c \tag{3.5}$$

where the thermal conductivity κ is a function of the PTFE temperature. Here, the temperature is found as an average between the top and bottom of the sample. The contact resistance R_c is added to this, and represents both interfaces as well as any extra thermal resistance.

At this point, the heat rates through the sample can be determined using the heat flux meter and the sample temperature drop. The heat rate through the sample can be determined as $Q_{sam} = \Delta T / R(T)$ where this depends on a variable contact resistance. The heat rate can also be found as $Q_{HFM} = V_{HFM} / C$ with a variable sensitivity. With twelve measurements of PTFE samples and two measurements of silicon samples, both the sensitivity and contact resistance can be fit. A guess value for the sensitivity and contact

resistance were first chosen. The root-mean-square (RMS) error between the heat rates found from the heat flux meter and the temperature difference was compared at each of the six points of each PTFE measurement, and the sensitivity was adjusted until the RMS error was minimized. The RMS error for the silicon samples was then calculated, and the value of the contact resistance was changed to minimize the error in the silicon samples only. Since the heat rate agreement depends on both the contact resistance and sensitivity, the sensitivity would need to be re-optimized for the PTFE samples. This process would continue iteratively until a change in the sensitivity by 0.01 μV-cm^2/mW and a change in the contact resistance by 0.01 K/W had no effect on the RMS error.

The resulting value for the sensitivity is 6.87 μV-cm^2/mW, which is sufficiently different than the manufacturer's calibration of 7.88 μV-cm^2/mW to warrant a recalibration. The value of the contact resistance was found to be 1.80 K/W, which again includes both interfaces. Comparisons of the measurements for several samples can be seen in Figure 3.9 and 3.10. Here are shown two examples from each material measured: the thick and thin PTFE samples and silicon samples. These are not chosen because they are the best or worst fitting examples, but because they represent a good mix of what was seen in the calibration. For each sample, the heat rates are shown on the left-hand side while the corresponding temperatures above and below the sample are shown on the right-hand side.

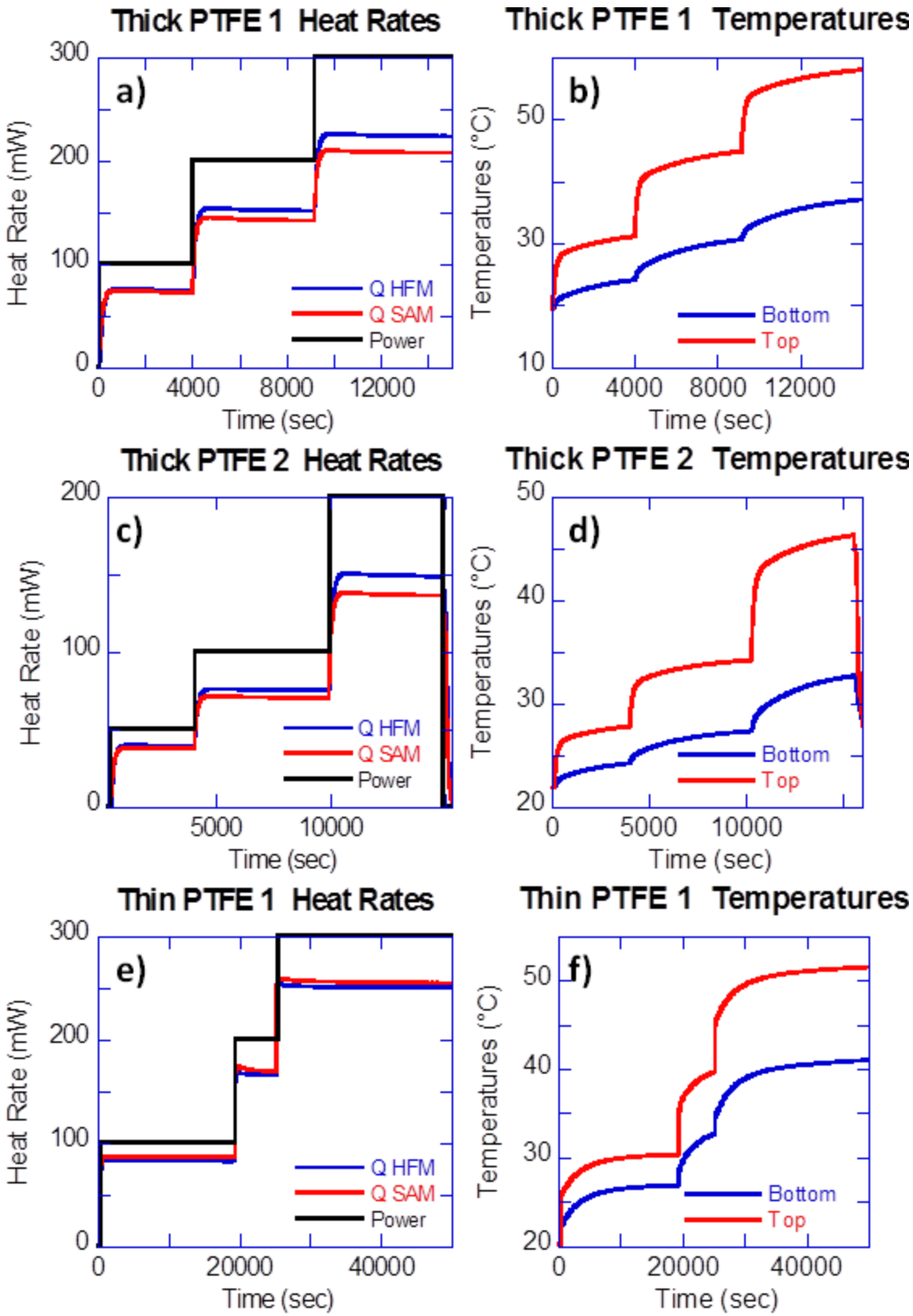

Figure 3.9. Heat rates and temperatures for three calibration measurements.

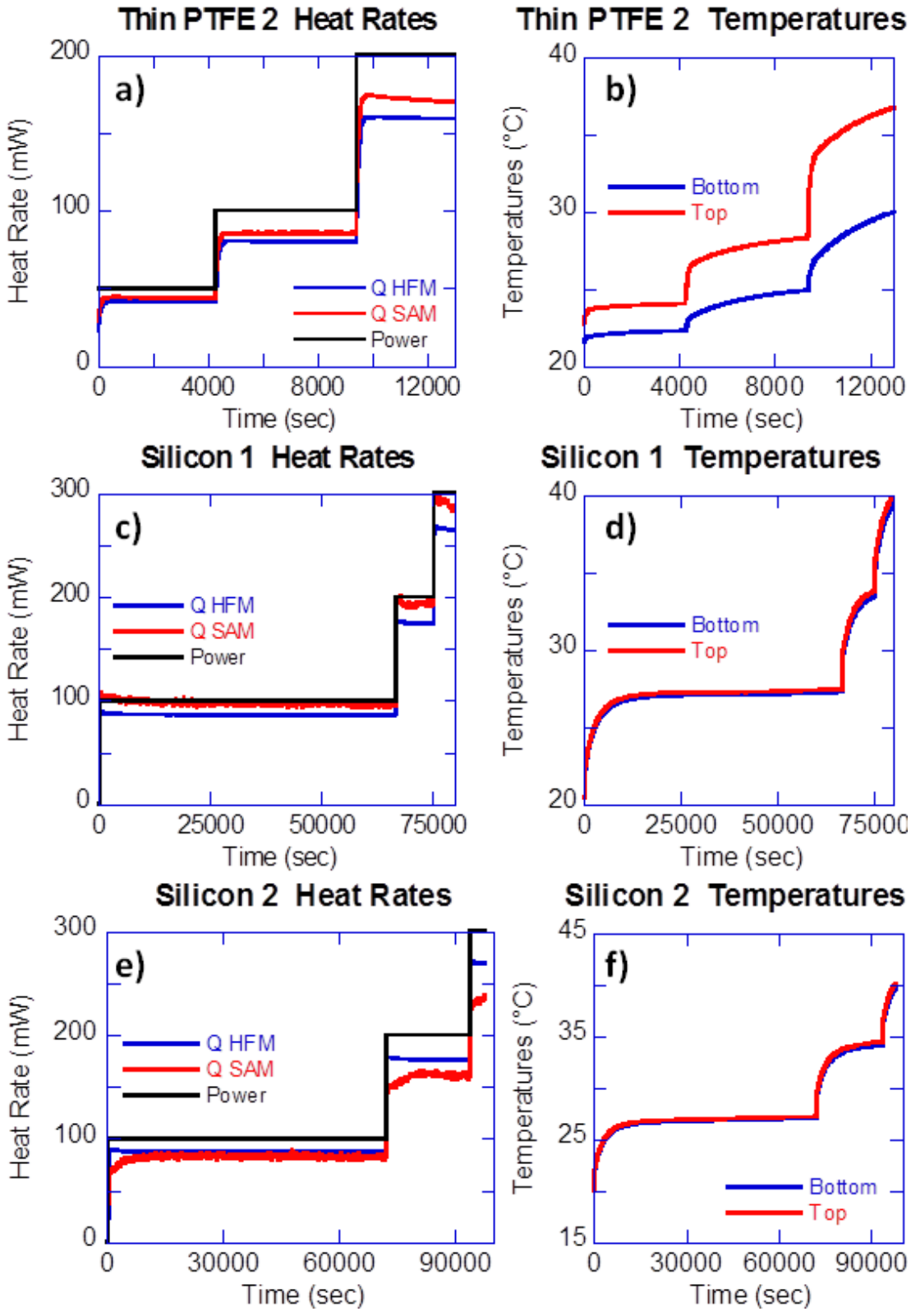

Figure 3.10. Heat rates and temperatures for three calibration measurements.

For the heat rate plots, both calculations for the heat rate are shown, with the heat rate using the HFM denoted by “Q HFM” and the heat rate using the temperature drop and thermal resistance denoted by “Q SAM”. Additionally, the input power is shown in black, and is always expected to larger than the measured heat rates, with this discrepancy growing larger as the temperatures increase. As can be seen in these figures a single set of sensitivity and contact resistance are able to cause the two readings to match very well. There is generally no trend in the error with temperature or sample thickness, and it seems that the discrepancies are largely random as desired. The total root-mean-squared error between the two heat fluxes for the PTFE samples is 8.5 mW versus the average heat rate of 130 mW. This RMS error includes uncertainties due to the contact resistance, and cannot be used directly for uncertainty calculations in the HFM sensitivity. It should be noted that the measurements of the silicon samples shown in Figure 3.10c-f do not agree as well as the PTFE samples, and this is likely due to the measurement of very small temperature drops.

The degree to which these measurements reached steady-state conditions can also be seen, despite the fact that none of the temperatures actually reached a constant value. There have been tests that allow this to happen, however the measurement time is typically several days, and the results are no different. This is because the entire base plate is allowed to heat with time. Because the thermal mass is so much larger than the sample and measurement components, the time for the system to fully reach steady state is very long. The temperature plots here all show a very steep rise immediately after the power is increased which corresponds to the thermal time constant of the sample and measurement equipment. Once the heat flux stabilizes the entire system temperature rises as a whole, and the heat rates should remain stable. One important note is that the heat rate does decrease slightly with increasing temperature. Since the thermal conductivity

remains fairly constant in these temperature ranges, it appears as though the total amount of heat passing through the sample is decreased due to side losses.

Though not shown here, these measurements are not the first set of calibration experiments. Earlier tests were made to calibrate similar heat flux meters, and the results were all similar to what is presented here. However, the heat flux meters calibrated were uninstalled either because of problems with the meters themselves, or surrounding components. Because of the nature of the epoxy used, these meters were unrecoverable. Furthermore, the sensitivities found for those meters were different by over 50%, and the results cannot be applied to these measurements.

3.2.5 Uncertainty Calculations

The validity of the analysis of the near-field heat transfer as measured in Chapter 6 depends on experimental analysis. Since no experiment is infinitely accurate or precise, is it necessary to quantify the errors and uncertainties. This section will outline the major pieces of equipment and give the associated uncertainties that pertain to the thermal measurements. The uncertainty of the sensitivity of the heat flux meter will also be determined. Since the uncertainties of the near-field measurements depend highly on the individual measurements of the gap spacing, temperatures, and heat rates, the uncertainty of the overall heat rates will be discussed in Section 6.3.

Table 3.1 gives a list of all of the equipment used that contains significant uncertainties, along with the stated uncertainties. It should be noted that unless otherwise mentioned, all uncertainties are combined uncertainties. This table does not include any uncertainties for the measurement of near-field radiation related to the samples, including vacuum gap spacing. The LakeShore DT-670 Silicon Diode thermistor was calibrated by the manufacturer and tested to be accurate within 37 mK in the temperature range used here. The Agilent 34401A digital multimeter used at the lowest DC voltage measurement range has a listed uncertainty [83] of 0.0050% of the reading + 0.035 μV from the range

setting, giving a maximum uncertainty of 0.2 μV. The micrometer used for thickness measurements and dial calipers for width measurements are from the Fowler Precision series, and the uncertainties are inferred from the measurements. The calipers have a smallest resolution of 0.0001" and should be precise to within half of that scale, so the uncertainty is estimated to be 0.0013 mm. The calipers have a minimum resolution of 0.001"; however difficulties in the sample geometries make this an unreliable number. Because most of the samples are not perfectly square, the overall uncertainty of any width is taken to be 0.005", or 0.13 mm.

Table 3.1. Uncertainties of all major equipment used in the heat flux meter calibration. Given is the instrument name used in the text as well as the manufacturer's make and model and the associated uncertainty. Uncertainties shown should be interpreted as combined uncertainties.

Instrument	Equipment Model	Uncertainty
Si Diode Thermistor	LakeShore DT-670 Silicon Diode thermistor	0.037°C
Duplexed Thermocouple	Omega 40AWG E-type	0.15°C
Multimeter	Agilent 34401A	0.0050% of reading + 0.0035% of range
Micrometer	Fowler Precision Micrometer	0.0013 mm
Calipers	Fowler Precision Dial Caliper	0.13 mm
Laser Flash	Netzsch LFA 467 Hyperflash	3% of reading
Differential Scanning Calorimeter	TA Q100 Differential Scanning Calorimeter	1% of reading
Heat Flux Meter	Captec Enterprises 1 cm^2 thermopile-type heat flux meter	4.4%

The thermocouples used are Omega 40AWG E-type thermocouples connected together as described in Section 3.2.3. Omega claims that the special limits of error for this type of thermocouple are the greater of 1.0°C or 0.4% [84], however much of this

error comes from the uncertainty of the lead temperatures, which this method eliminates. As such, an experiment was conducted to determine the accuracy of the thermocouples. A set of thermocouples was made for this experiment. 5 buckets were filled with approximately 50 liters of water, and four of these buckets had temperature-controlled water heaters, MGW Laudo Series MS E100. One bucket was kept at room temperature. Two platinum resistance thermometers, Burns Engineering Model 12001-A-12-6-2-A/LT14 resistance thermal detectors (RTD), were used to measure absolute temperatures of the room temperature bucket and the heated buckets. The thermocouples were wrapped around the two RTDs throughout the entire experiment. The junctions of the thermocouples were set to be as close to the RTD sensor element as possible, and were secured using electrical tape sufficiently far away from the junction. Since the rated uncertainty of the RTDs is only 0.006°C [85], it is assumed that any difference between the temperatures as measured by the RTDs and thermocouples must be due to uncertainties in the thermocouples.

The four heated baths were set in a range of temperatures, starting at 22°C, 34°C, 46°C, and 58°C, and were left to come to temperature for three hours, after which there were no visible changes in the heater readout. The cold junction of the thermocouple and the connected RTD were placed in the room temperature bucket, which varied between 20.5°C and 21.5°C over the course of the experiment. The other temperature sensors were submerged in the 22°C bucket and left for at least 5 minutes to come to temperature before the voltage and resistances were read. The thermocouple and RTD were moved to the second heated bucket, and the temperature of the first bucket was increased by 2°C. This process repeated for all four buckets, and then a measurement was made where both of the thermocouple junctions were submerged in the room temperature bucket to check for consistency. With all of the heated buckets increased by 2°C, measurements were

made in a similar manner, until the measured temperatures spanned 22°C to 70°C, which is more than the range expected in the vacuum chamber.

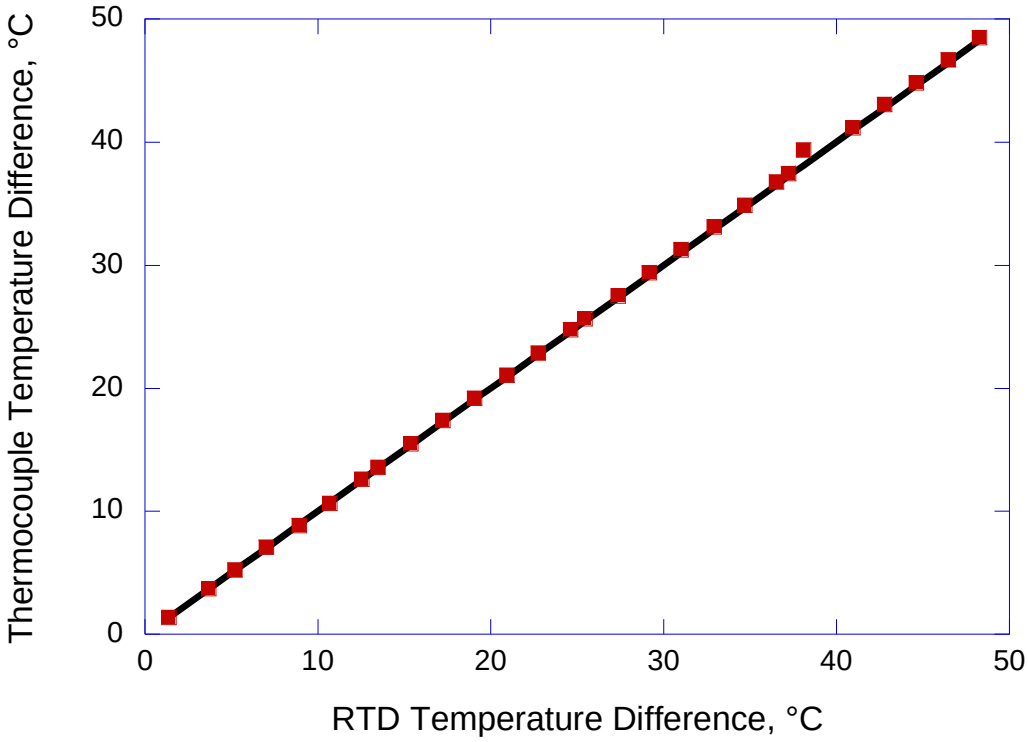

Figure 3.11. Results of thermocouple calibration experiment. The markers are experimental data, while the ideal response is shown in black.

As seen in Figure 3.11 the prediction from the thermocouples is very close to the RTD temperature difference. Shown in red markers are the temperature differences determined by the thermocouples, while the black line is the RTD temperature difference. Ideally these points lie exactly on this line, and only at one point near 60°C is there any significant difference. There are some small errors, and the standard error of estimate (SEE) is found to be 0.15°C, and this is taken to be the uncertainty in the thermocouple measurements.

As described in Section 3.2.4, the heat flux meter was calibrated, and this calibration has limits of uncertainty. The manufacturer specified a sensitivity of 7.88 μV-cm^2/mW with a 5% uncertainty, however the value found in this work is 6.87 μV-

cm^2/mW. The uncertainty of this value depends on the uncertainty of the equipment used to measure the sensitivity through the use of error propagation analysis (EPA). This relies on predicting the changes of a function based on small changes in the independent variables according to their uncertainties [86]. For a general function $y = f(x_1, x_2, ..., x_n)$, the changes in *y* can be determined using first-order Taylor series approximations to model changes in any x_i. This effectively yields an *n*-dimensional uncertainty vector with components in each of the *n* dimensions, and the magnitude of this vector gives the overall uncertainty in *y* about a point.

$$U_y = \sqrt{\left(\frac{\partial f}{\partial x_1} U_{x_1}\right)^2 + \left(\frac{\partial f}{\partial x_2} U_{x_2}\right)^2 + ... + \left(\frac{\partial f}{\partial x_n} U_{x_n}\right)^2} \tag{3.6}$$

The heat flux meter sensitivity depends on temperatures, heat flux meter voltage reading, and importantly, the PTFE sample resistance. In order to obtain the properties of the samples, the thermal conductivity was measured, and Equation 3.4 was used with the measurements of the density, thermal diffusivity, and specific heat. This procedure was explained in Section 3.2.4. The thermal diffusivity was measured using a Netzsch LFA 467 Hyperflash laser flash device with a given accuracy of 3% by the manufacturer's data sheets. The specific heat was measured using a TA Q100 Differential Scanning Calorimeter with an accuracy of 1% stated by a company representative.

The density was determined by measuring the mass of a small piece using a precision scale where the minimum resolution was 1 mg, thus the uncertainty was taken as 0.5 mg. A piece of thin PTFE and thick PTFE were cut and measured using the calipers and micrometer for area and thickness, respectively. Two measurements were made for each side of the piece and the results were averaged, changing the uncertainty in the width measurements by a factor of $1/\sqrt{2}$. The uncertainty of an average value can be found using Equation 3.6 and will reduce the uncertainty by $\sqrt{N}$ for *N* measured values.

Since the pieces were roughly square blocks, the volume was calculated, and the density was found. The uncertainty of the density was found using Equation 3.6 using the uncertainties of the length, width, thickness, and mass. The densities were very similar, with a value of 2.17 g/cm^3 for the thin piece and 2.16 g/cm^3 for the thick piece, with uncertainties of 9.0 mg/cm^3 and 12 mg/cm^3, respectively. Here the width and length measurements accounted for most of the uncertainty.

The uncertainty of the thermal conductivity was then calculated using these values and Equation 3.4 as the function for Equation 3.6. Since the thermal conductivity was different for the two thicknesses of PTFE as well as with the temperatures, the uncertainty was calculated at each temperature. It was found that the uncertainty is always proportional to the thermal conductivity, and when rounded to two significant digits, the value is 3.2% for both the thick and thin PTFE samples at all temperatures.

Finally, the uncertainties of the temperatures are required, though these are different than the instrument uncertainties. Since the temperature below the sample, $T_{\mathrm{L}} = T_0 + \Delta T_1$ is found using the measurements from the thermistor and thermocouple, the uncertainty must include both instruments. Because the uncertainty of the thermistor is so low, the uncertainty in the low temperature is the same as the thermocouple at 0.15°C. The temperature above the sample, $T_{\mathrm{H}} = T_{\mathrm{L}} + \Delta T_2$ relies on the absolute temperature below the sample and the temperature difference, the uncertainty of this value changes to 0.22°C.

Unfortunately, Equation 3.6 cannot be used directly to find the uncertainty of the heat flux meter sensitivity. A least-squares fitting was used to find the best fit of the sensitivity and the contact resistance to the data, so determining an algebraic equation is difficult. However, the partial derivatives can be approximated using a first-order Taylor series, similar to the method of finite difference.

$$\frac{\partial f}{\partial x_i} \simeq \frac{f(x_1,...,x_i+\Delta x_i,...,x_n)-f(x_1,...,x_i,...,x_n)}{\Delta x_i} \tag{3.7}$$

Here the partial derivative required for Equation 3.6 can be found by doing a recalculation with a change in one of the independent variables. This method can be used to forecast the behavior backwards by Δx_i as well for a central difference formulation. Finally, since the choice of a change in the variable is arbitrary, an obvious choice is to let the parameters vary by the uncertainty. Since the overall expression required is the partial derivative times the uncertainty, we can find the influence coefficient.

$$\frac{\partial f}{\partial x_i} U_{x_i} \simeq \frac{f(x_1,...,x_i+U_{x_i},...,x_n)-f(x_1,...,x_i-U_{x_i},...,x_n)}{2} \tag{3.8}$$

This method requires only that the sensitivity be re-optimized twice for each variable that has significant uncertainty. It is determined that six measured quantities are important: the temperatures above and below the sample, T_{H}, T_{L}, heat flux meter voltage V_{HFM}, and the PTFE properties including area A, thickness t, and thermal conductivity κ. The width of each sample is measured at four corners, and these are used to find the area. From this the area uncertainty is obtainable.

All of the calibration measurement data was adjusted slightly for each variable as per the uncertainty. For each direction of each variable, the heat flux meter sensitivity was changed until the RMS error was minimized again. In the original sensitivity fitting the contact resistance was allowed to vary to further minimize the RMS error; however this was foregone in the uncertainty analysis. Initially the error due to the contact resistance was minimized with each variable, but the trend was that the sensitivity would be resistant to changes from the uncertainty. This was true especially for uncertainties in the temperatures where the contact resistance absorbed most of this change. For this reason, the contact resistance was kept constant at 1.8 K/W. It should be noted that this

contact resistance will not be used for the near-field measurements, and only exists to aid in the calibration fitting.

Table 3.2. Results from the uncertainty analysis of the heat flux meter sensitivity. Shown are all of the values where uncertainty was considered along with the change in the sensitivity and the contribution to the overall uncertainty. The sensitivity found earlier is 6.87 μV-cm^2/mW, and the uncertainty found is 0.30 μV-cm^2/mW.

Variable x	T_L	T_H	V_{HFM}	t	A	κ
Sensitivity C	7.00	6.73	6.88	6.90	6.80	6.67
$\frac{\partial C}{\partial x}U_x$	0.105	0.155	0.005	0.01	0.08	0.22

Table 3.2 shows the results from this analysis. Note that each variable was adjusted in both directions of the uncertainty, but only the sensitivities from positive changes in uncertainty are shown. The influence coefficients still incorporate both directions, however. It is seen here that the voltage, thickness, and area have almost no contribution to the total uncertainty of 0.30 μV-cm^2/mW. The high temperature above the sample contributes more than the lower temperature, and this is because the high temperature measurement depends on the low temperature measurement, thus the uncertainty is higher. It can be seen that with a more accurate measurement of the thermal conductivity the overall calibration uncertainty can be improved, however a more accurate temperature measurement would also need to be made before any real improvements could be seen.

With this known, it is valuable to find the uncertainty in the heat rate from the HFM, as this will be trusted as the heat rate measurement in the near-field experiments. The heat flux can be found from the voltage and sensitivity as $Q_{HFM} = V_{HFM} / C$. Applying Equation 3.6 to this yields:

$$U_{Q_{\mathrm{HFM}}} = \sqrt{\left(\frac{-V_{\mathrm{HFM}}}{C^2}U_C\right)^2 + \left(\frac{1}{C}U_{V_{\mathrm{HFM}}}\right)^2} = \frac{V_{\mathrm{HFM}}}{C^2}U_C = \frac{U_C}{C}Q_{\mathrm{HFM}} \qquad (3.9)$$

Here the contribution from the heat flux meter voltage is negligible, and the uncertainty can be solved in terms of the heat rate. With a constant sensitivity and uncertainty, the uncertainty in the heat rate is 4.4% of the measured heat rate. This value will be used in Chapter 6 when the uncertainties of the near-field radiation measurements are needed.

4: NEAR-FIELD TPV EMITTERS USING TUNGSTEN GRATINGS

This chapter describes the design and optimization of a NFTPV device using a periodic tungsten grating as the thermal emitter. By optimizing the geometry of the grating, a majority of the heat exchange can be tuned to be above the bandgap while enhancing the power output through photon tunneling. The emitting source is modeled as a one-dimensional high-temperature tungsten grating on a tungsten substrate. This will be compared to a baseline case where the emitter is a simple planar geometry. It can exchange heat to a room-temperature $In_{0.18}Ga_{0.82}Sb$ PV cell with a bandgap of 0.56 eV through a vacuum gap of several tens of nanometers. Using an exact method to analyze the radiative exchange, the electrical power output and conversion efficiency will be optimized. To do this, a parametric sweep of the height, period, and width of the emitter grating will be conducted over a large range of values, while maintaining realistic parameters. A phenomenological study of the trends with the geometry will reveal insights behind the performance enhancement, and an optimal emitter will be investigated to search for potential resonance phenomena that control or augment the thermal radiation. Through the use of advanced simulations and analysis, this work hopes to further the understanding the role of nanostructures for near-field radiation, and create a new avenue for TPV development.

4.1 Numerical Methods

The grating geometry is shown in Figure 4.1. Here, the tungsten emitter is comprised of a one-dimensional tungsten grating and a semi-infinite tungsten substrate. The tungsten emitter is separated from a semi-infinite $In_{0.18}Ga_{0.82}Sb$ receiver by a subwavelength vacuum gap d. The emitter and receiver extend infinitely in the x- and y-directions, with the emitter being periodic in the x-direction. The periodicity is governed by the grating period, P, the strip width is shown as w, and the grating height is H For

most of this work, the filling fraction $f=w/p$, which represents the relative size of the grating strip will be used.

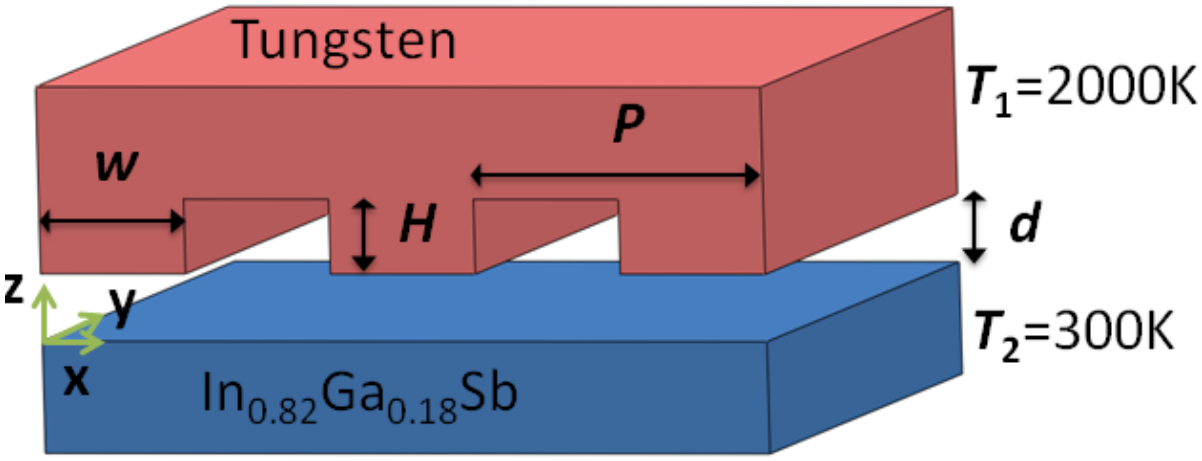

Figure 4.1. Schematic of the NFTPV device showing the coordinate axes, vacuum gap spacing d, and the geometric grating parameters: Ridge width w, grating height H, and period P. The temperatures of the emitter at $T_1$and receiver at T_2 are specified.

The radiative exchange between the emitter and receiver will occur over a temperature difference. The emitter temperature is prescribed as $T_1 = 2000\text{K}$, and the receiver temperature is $T_2 = 300\text{K}$ such that the peak thermal radiation wavelength will be 1.45 μm. The optical properties of tungsten are taken from Palik [37], while the optical properties of $In_{0.18}Ga_{0.82}Sb$ are obtained from [37, 87]. The near-field heat transfer can be obtained between the tungsten emitter and TPV cell through the framework of scattering theory [75, 76] as seen in Section 2.1.2.

$$Q = \frac{1}{8\pi^3}\int_0^\infty \left[\int_{-\infty}^{\infty}\int_{-\pi/P}^{\pi/P} \xi\left(\omega,k_x,k_y\right)dk_x dk_y\right]\left[\Theta\left(\omega,T_1\right)-\Theta\left(\omega,T_2\right)\right]d\omega \qquad (4.1)$$

Here, the function $\Theta\left(\omega,T\right)$ represents the average energy from Planck's oscillator at a given angular frequency and temperature, and $\xi\left(\omega,k_x,k_y\right)$ is the energy transmission coefficient. It should be noted that the energy transmission coefficient depends on the

geometry and material properties. In order to obtain the transmission coefficient, rigorous coupled-wave analysis (RCWA) is used; this is why the integration limits on k_x are restricted to the first Brillouin zone. The details of this method can be found in [77].

The computation of the transmission coefficient is a lengthy process prone to discretization errors, and the parameters used are outlined here. RCWA is used to find the reflection matrixes of dimension $2(2N+1)$ for both the emitter and receiver. Here N is the maximum diffraction order considered in the calculation, and 35 orders were used in this work. The angular frequency ω was logarithmically spaced with 80 values over a range from 2.3×10^{14} to 4.5×10^{15} rad/s. The wavevectors k_x and k_y were evenly spaced with 43 values for k_x and 71 values for k_y. The maximum value of k_y was initially set to $5k_0$, where $k_0 = \omega / c_0$ is the magnitude of the wavevector in vacuum. This limit was increased and recalculated if any transmission coefficient was not sufficiently small at this maximum wavevector, to ensure a robust convergence. Using these parameters the calculation time on a dual eight-core XEON E5-2687 W workstation is just over two hours. A convergence study was performed whereby the number of diffraction orders, frequencies, or wavevectors was allowed to increase by 10%. The overall heat rate was compared between the base parameters, and the increased parameters, and only the number of frequencies evaluated made any impact, changing the heat rate by 1% as the number of frequencies changed from 80 to 88. Every other parameter change affected the heat rate by less than 0.1%, thus the numerical accuracy is believed to be within 1%.

Since the geometries of the emitter substrate and TPV cell receiver are semi-infinite, it is assumed that all of the radiative energy exchanged is absorbed by the receiver and each absorbed photon can excite an electron-hole pair as long as the photon energy exceeds the $In_{0.18}Ga_{0.82}Sb$ cell bandgap of 0.56 eV. Furthermore, surface and bulk recombination is neglected, such that 100% quantum efficiency is assumed. While this is

expected to over-predict the actual near-field TPV performance [88], the intent of this work is to optimize the tungsten grating emitter, and TPV cell performance serves mainly as a metric for comparison of the relative performance. The maximum electrical power output is evaluated by $P_{el} = J_{sc} V_{oc} FF,$ where the short circuit current J_{sc} can be found from [89].

$$J_{sc} = \frac{e}{hc_0} \int_0^{\lambda_g} \lambda q_\lambda d\lambda \tag{4.2}$$

Here the spectral heat flux q_λ can be found from equation 1, and is integrated up to the band gap energy, 2.2 μm. The open circuit voltage V_{oc} and fill factor FF are functions of the carrier concentrations, diffusivities, and lifetimes, and can be found for $In_{0.18}Ga_{0.82}Sb$ from [88]. Finally, the conversion efficiency can be found as the ratio of electrical power to total heat exchange, $\eta = P_{el} / Q$.

4.2 Results and Discussion

To identify the best grating performances, a parametric sweep was performed for the grating height *H*, period *P*, and volume filling fraction *f=w/p* with a fixed gap thickness *d* = 20 nm. This gap spacing is chosen to illustrate the behavior in the very near-field where nearly all wavelengths are able to tunnel effectively, and all calculations will be at this value unless otherwise noted. *H* was allowed to vary between 10 nm to 1000 nm, *P* varied between 10 nm and 2000 nm, and *f* varied between 0.1 and 0.9, for approximately 400 unique grating geometries. Shown in Figure 4.2 are surface images of the maximum power output and efficiency over a large range of geometric parameters. Here, for each point *H* and *P* shown, only the value of *f* with the highest maximum power output (Figure 4.2a) and conversion efficiency (Figure 4.2b) are shown. Thus, these figures can be

interpreted as being optimized in the *f*-axis. Please note that the filling fraction *f* is generally different for points on either plot.

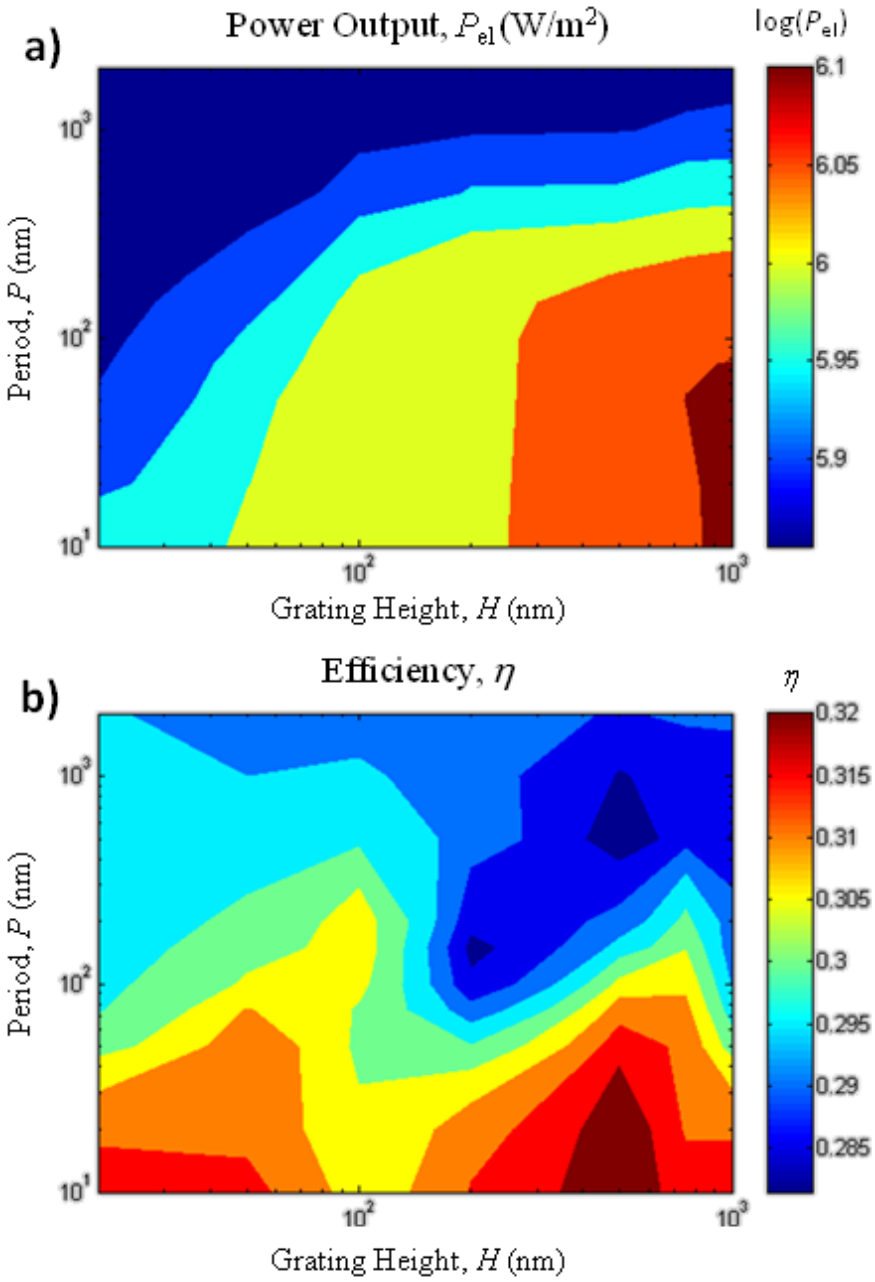

Figure 4.2. a) Electrical power output in log scale versus period and grating height. Values shown only at the filling fraction with the highest power. b) Conversion efficiency versus period and grating height. Values shown only at the filling fraction with the highest efficiency. Note that all calculations are at a gap spacing of 20 nm.

Figure 4.2a demonstrates a very clear trend towards grating geometries with very low periods and very high grating heights. Although it would appear that the parametric study should continue in this direction, these geometries represent a class of gratings that are extremely difficult to fabricate, with sub-nanometer minimum feature sizes at aspect ratios verging on 1000. It is still important to note the trend, and importantly the steep gradient seen at higher grating heights. Figure 4.2b illustrates a more complicated topology when only looking at the efficiencies. It is important to note that the values of the filling fraction are different at each point in Figure 4.2a versus Figure 4.2b, so comparison is difficult between the two plots. However, it can be seen that there are potentially promising areas to investigate that do not have extremely difficult dimensions. Regardless, the area with maximum efficiency does coincide with the area of maximum power, though the location of the gradient is important. This illustrates the importance of the grating height, in that the maximum possible power typically increases with the grating height, though there may be a lack in efficiency.

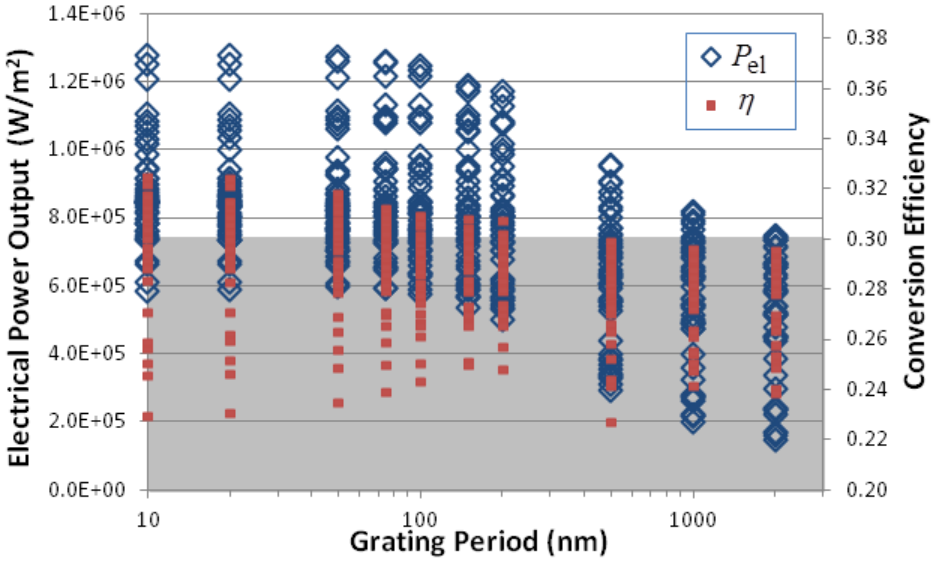

Figure 4.3. Electrical power output and conversion efficiency versus grating period. The gray section highlighted represents the performance versus a flat tungsten emitter.

For each permutation of parameters, the TPV electrical power output P_{el} and energy conversion efficiency η were compared to the baseline case of a planar tungsten substrate. This is shown in Figure 4.3 for all of the geometries calculated. Here, the performance of a planar tungsten emitter is compared to all of the grating geometries. The earlier trend of increasing power and efficiency with decreasing period is very apparent, however when compared against the baseline case, this is even more important. Using standard photolithography techniques, a minimum feature size, i.e. the smaller of the strip width, *w*, or *P*-*w*, can be as low as 1 μm. As seen here, none of these calculations place the efficiency better than the planar tungsten emitter under that constraint. While fabrication technologies exist that can create grating geometries much smaller than 1 μm, care must be taken to maintain realistic parameters.

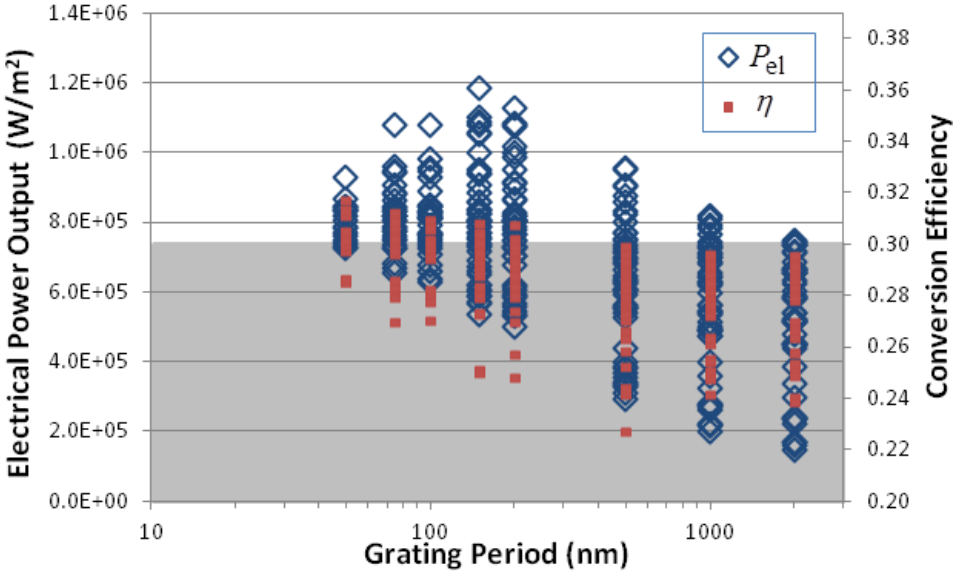

Figure 4.4. Electrical power output and conversion efficiency versus grating period only for geometries with a minimum feature size greater than 10 nm and an aspect ratio less than 35. The gray section highlighted represents the performance versus a flat tungsten emitter.

Shown above in Figure 4.4 the useful points have been reduced. Here, the calculations are limited to geometries with a minimum feature size of 10 nm, which is possible to fabricate using existing technologies, e.g. electron beam lithography, and a

maximum aspect ratio of 35. Here the aspect ratio is defined to be the ratio of the grating height to the minimum feature size, and represents a value achievable by either deep reactive ion etching (RIE), or inductively coupled plasma RIE. This limits the field greatly, however, there are still many promising geometries. Qualitative analysis of the spectral energy distribution absorbed by the receiver was also used to identify successful emitter geometries. A selection of grating geometries with good performance is shown in Table 4.1.

Table 4.1. A sample of high-performing grating geometries from the parametric sweep with the power output and efficiency at a gap spacing d = 20 nm. The performance of a planar tungsten emitter is also shown.

Height H (nm)	Period P (nm)	Filling fraction f	Power Output P_{el} (kW/m^2)	Efficiency η (%)
500	50	0.8	1060	31.8
750	75	0.5	833	31.1
750	150	0.7	1000	30.0
100	200	0.9	1000	30.8
Planar Emitter			768	30.1

The results for a planar tungsten substrate are already fairly high with a power output P_{el} of 768 kW/m^2 and efficiency η of 30% at 20 nm gap spacing, and a majority of the grating geometries were not able to outperform the baseline case in both power and efficiency. Many of the structures analyzed were able to exceed the electrical power output, but at the cost of a reduced efficiency. Furthermore, a majority of the structures that had an efficiency exceeding the planar tungsten case require feature sizes of a few nanometers. Though Table 4.1 shows several promising candidates, we choose to focus on a grating with the best combination of power and efficiency, with a height H = 500

nm, period P = 50 nm and filling fraction f = 0.8 for the majority of this work unless otherwise noted. It should be noted that geometries with lower periods and higher filling fractions may outperform this combination by up to 20%; however, they are too challenging to fabricate using current techniques. The performance of this grating is shown in Figure 4.5 with planar tungsten for comparison.

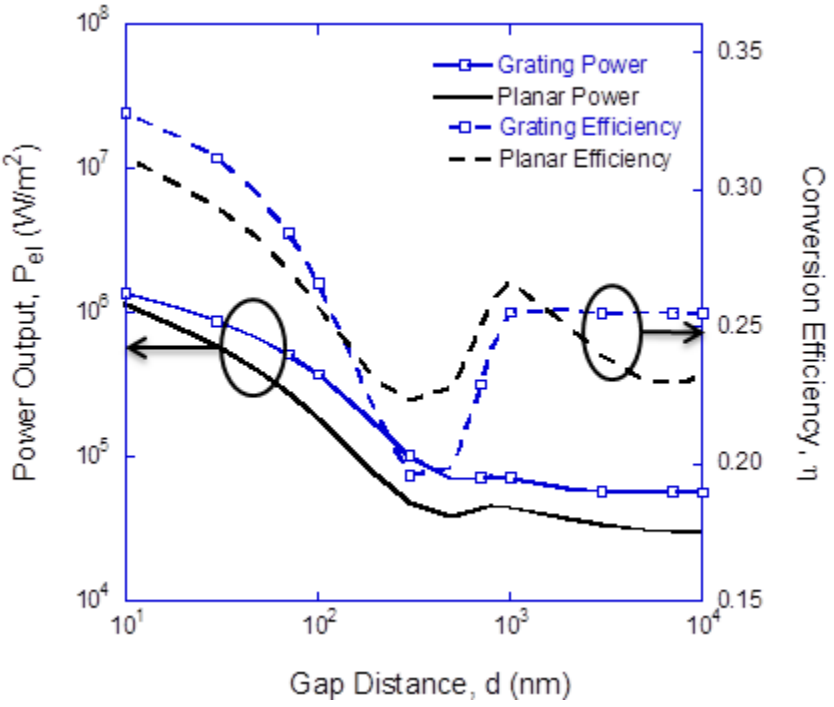

Figure 4.5. Power output (solid lines) and conversion efficiency (dashed lines) for the selected grating (shown with markers) and for a planar tungsten slab (no markers).

Here the power and efficiency can be compared between the planar tungsten and the optimized grating over a large range of gap spacings. It is seen that the grating has a higher power output over all gap spacings; nearly double at 100 nm. This improvement decreases until the planar case exceeds the grating power below 10 nm. The efficiency of the grating is only improved below 200 nm, and the improvement increases with decreasing gap spacing. At 20 nm, the grating has a modest improvement in both power and efficiency. Here the efficiency is 31.8% and the power is 1.06 MW/m^2; a 40% improvement in power while still gaining a slight efficiency advantage over the planar

case. Even at a more modest gap spacing of 100 nm the power output is almost double the planar case (375 kW/m^2 versus 188 kW/m^2) with a slight advantage in efficiency, though the absolute value is only around 25%.

It should be noted that even though this grating has been chosen to have a higher efficiency than planar tungsten, this is not the case for all gap spacings. As the spacing increases, the grating actually underperforms the flat tungsten in efficiency. In this intermediate region seen in Figure 4.5, wave interference effects in the vacuum gap increase the power and efficiency near 1 μm and decrease near 500 nm. Here constructive and destructive interference modulate the transmission near the bandgap frequency. This affects higher energy photons as well as deconstructive interference in the vacuum at one frequency necessarily means constructive interference at twice that frequency, leading to extra thermalization and causing lower efficiency. Since the grating is optimized for higher frequency transmission, this is a larger problem in the grating, causing the efficiency gap compared with the planar emitter. For gaps larger than approximately 2 μm the grating behaves as a selective far-field emitter. For the remainder of this work, all calculations will be at a gap spacing of 20 nm, as this shows a high heat flux while being in a region where the radiative power is monotonically increasing with decreasing d.

It is important to try to understand mechanisms behind the enhancement, or lack thereof, for this and similar microstructures. To get a good understanding of the geometric effects, the power output and conversion efficiency are shown in Figure 4.66 for a variety of related geometries. Here the geometries include the optimized grating with one parameter free to vary over the range of the initial parametric sweep.

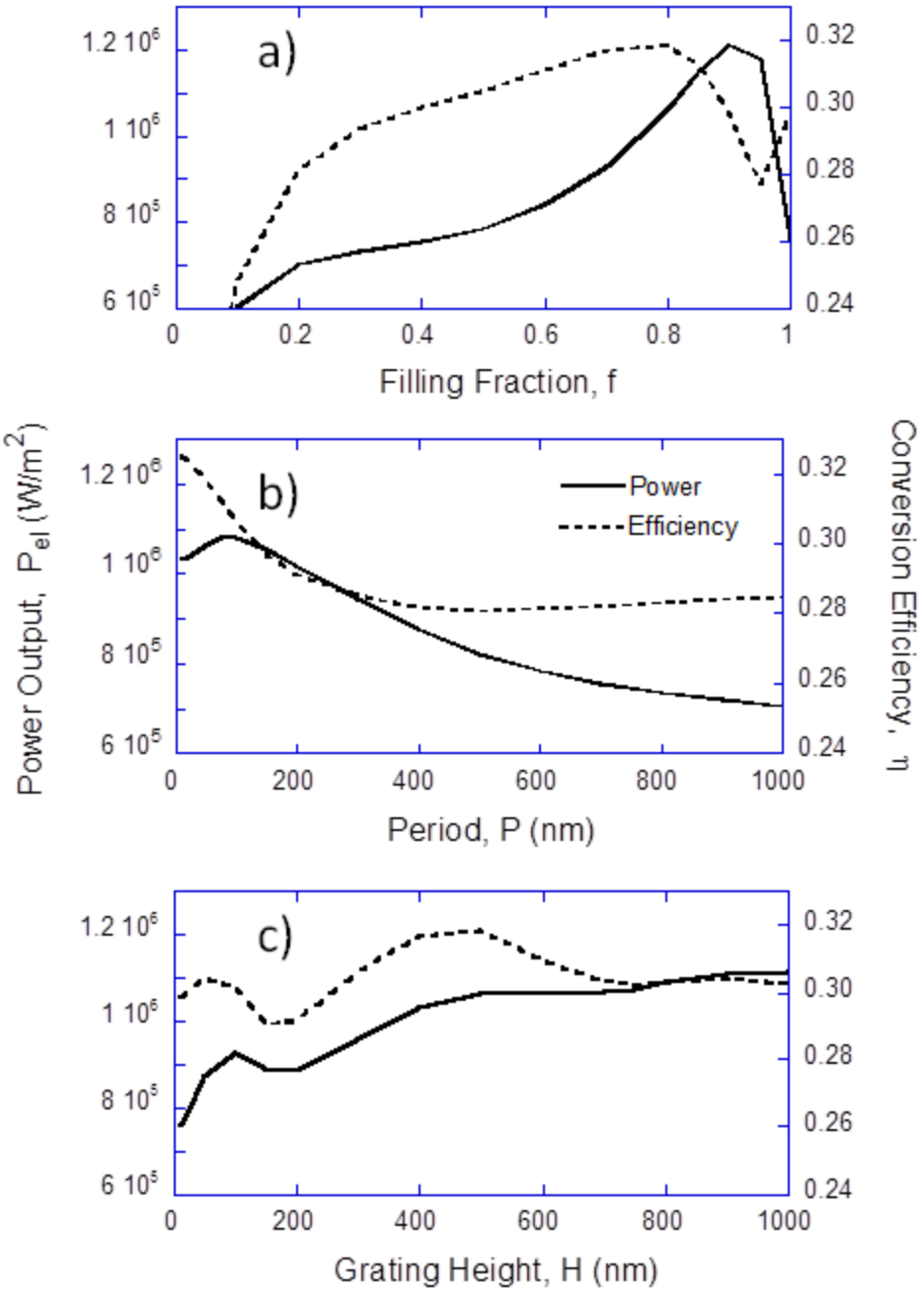

Figure 4.6. Performance comparison for a grating with $H = 500$ nm, $P = 50$ nm, $f = 0.8$ by varying a single geometric parameter: a) filling fraction, b) period, c) grating height.

In Figure 4.6a the efficiency reaches a maximum at f = 0.8 while the power increases a bit further before both converge to the planar performances at f = 1. As the filling fraction decreases both the power and efficiency drop, indicating that the narrowness of the grating slit plays a key role in the enhanced performance. Figure 4.6b

shows a very clear trend of decreasing efficiency with period at low periods, however with many of these periods the extremely small geometries, especially the slit widths, may be unrealizable. Towards larger periods the power decreases while the efficiency actually increases slightly. In Figure 4.6c a clear maximum in efficiency can be seen at a grating height of 500 nm while the power continues to increase with deeper gratings.

It should be noted that similar trends are seen in other grating geometries. Performance, especially efficiency, is typically very good for geometries with low periods; however, larger periods show greatly reduced performance as the grating period approaches the micron range. When the period is large enough, approaching the characteristic wavelength of radiation, the effects of the grating vanish, and the heat flux tends towards an average of the radiation from the top and bottom of the grating [90]. Another interesting trend is how the power tends to increase with grating height, suggesting that deep-grating cavity resonance modes may play a part in the enhancement. This also supports trends of increased performance at high filling fractions, as the slit width becomes very narrow. In the case of a deep grating with a narrow slit, cavity resonance modes can be excited [8], and may increase the energy throughput.

To better understand the mechanisms for the enhancement of using a grating over the planar tungsten case, the spectral response is analyzed. The transmission coefficient $\xi(\omega, k_x, k_y)$ for both the grating and the planar tungsten when $k_y = 0$ is shown in Figure 4.7a and 4.7b. It should be noted that the wavevector k_x is normalized by π / P for convenience in both plots, and the light line $k_x = k_0 = \omega / c_0$ is also shown.

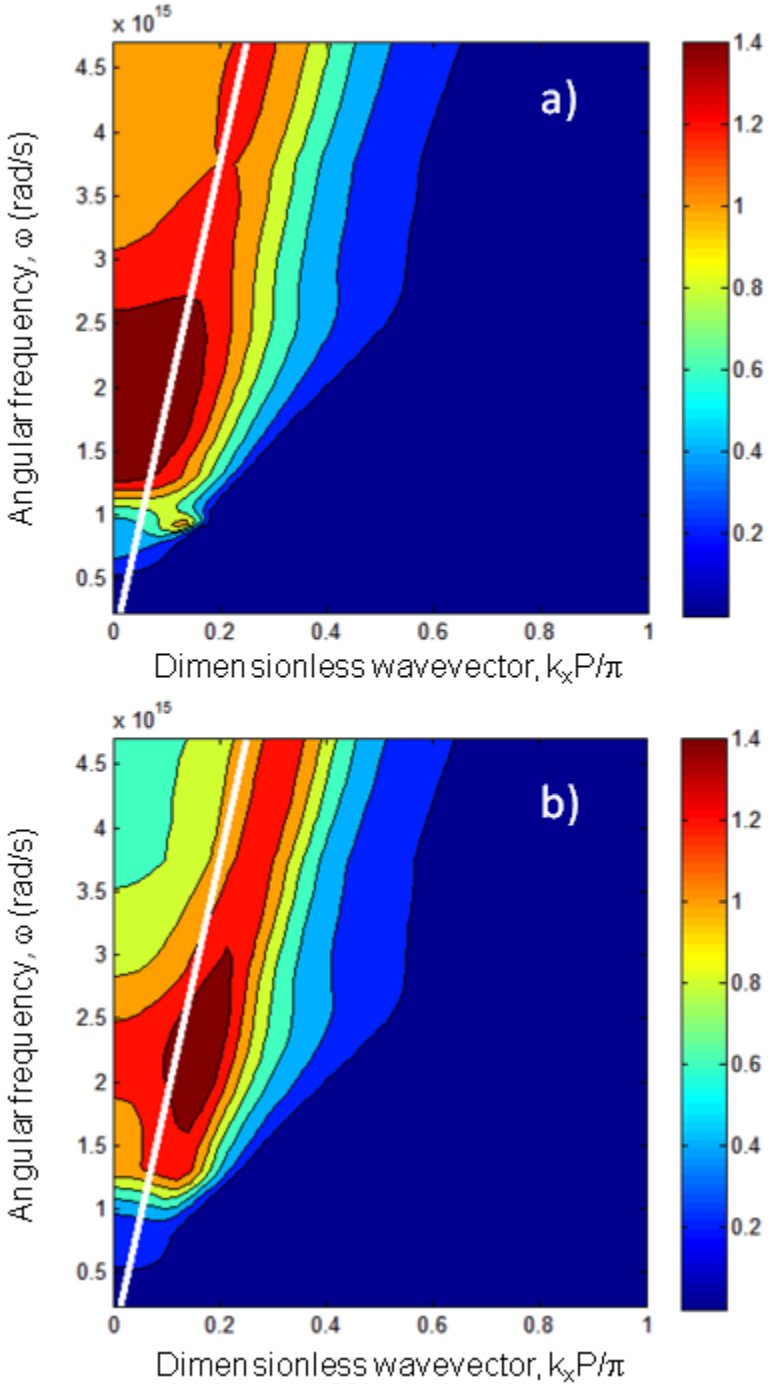

Figure 4.7. Transmission coefficient at $k_y = 0$ for a) tungsten grating with $H = 500$ nm, $P = 50$ nm, $f = 0.8$, and b) planar tungsten. The light line is shown here in white.

This shows a clear picture of the enhancement mechanisms that give higher performance to the grating. The contour plots are both invariant to temperature, as the Planck distributions Θ_1, Θ_2 do not contribute until after the frequency integration in equation 1, however, both geometries show a concentration of high transmission in the relevant frequency interval. For $In_{0.18}Ga_{0.82}Sb$ the bandgap is 0.56 eV (8.4×10^{14} rad/s), and only photons with a higher frequency will be converted to electron-hole pairs. Both structures have a majority of the high transmission above this frequency, which explains why it is difficult to outperform tungsten. Planar tungsten has a fairly optimized spectral response for this type of NFTPV cell naturally, so improvements due to structuring the emitter are not as drastic as desired.

Tungsten performs well for this application because of the ability to excite a surface plasmon polariton (SPP) in the relevant frequency range. The SPP dispersion can be predicted at the tungsten-vacuum interface via [67].

$$k_{SPP} = \frac{\omega}{c_0}\sqrt{\frac{\varepsilon_1\varepsilon_2}{\varepsilon_1+\varepsilon_2}} \tag{4.3}$$

where ε_1 is the complex dielectric function for tungsten while $\varepsilon_2 = 1$ for vacuum. Since the real part of the dielectric function for tungsten is -1 at 1.96×10^{15} rad/s, a strong evanescent wave can be excited [91]. This is the reason for the maxima seen in Figure 4.7a and 4.7b, though the feature is broader in the grating, giving a higher power and better efficiency. In the planar case, the SPP resonance extends more towards the high-frequency range, and though this still can excite electron-hole pairs, the efficiency is not as good due to thermalization of the energy exceeding the bandgap.

To fully understand the energy transmission and the resulting impact on efficiency, Figure 4.8 shows the transmission coefficient integrated over all wavevectors shown versus angular frequency

$$\xi_\omega = \frac{1}{4\pi^2}\iint \xi(\omega,k_x,k_y)dk_x dk_y \tag{4.4}$$

This clearly shows the advantage that the grating structure has over the planar tungsten structure as the energy transmission is not only higher, but also pushed closer to the TPV bandgap of 8.4×10^{14} rad/s. It is worth noting that the spectral transmission coefficient for the grating has a shoulder near 1×10^{15} rad/s, which corresponds to the low-frequency bump seen in Figure 4.7a. This feature is stronger with larger grating heights and narrow grating slits, so it is possible that cavity resonance is the reason for this enhancement [8]. However, based on predictions from the LC circuit model [7] there should be no magnetic polariton resonance near this frequency.

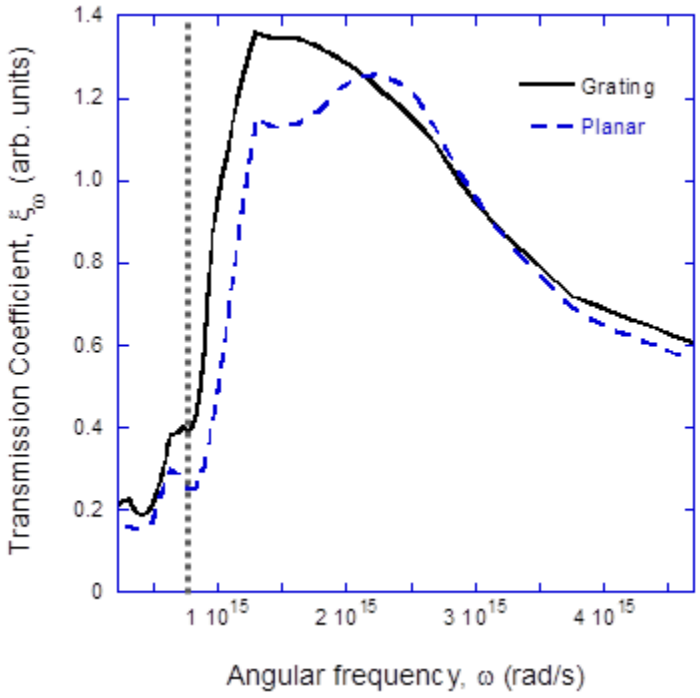

Figure 4.8. Spectral energy transmission coefficient for grating and planar geometries. The bandgap of 8.4×10^{14} rad/s is shown with a dotted line.

Upon comparison between Figure 4.7 and 4.8, a discrepancy occurs. Figure 4.7 clearly shows that SPP resonance should be the main mode of energy transmission, and the peak of the spectral distribution should occur at or near this frequency, corresponding

to 2.2×10^{15} rad/s. This is true for the planar case, but the grating has a maximum at 1.2×10^{15} rad/s. In order to understand this peak, the transmission coefficient at non-zero k_y values must be explored. This is shown in Figure 4.9 where the transmission coefficient integrated over k_x only, $\xi_{\omega y}(\omega,k_y)$, is shown versus the angular frequency and non-dimensional wavevector in the *y*-direction for the grating geometry. At $k_y=0$, there is good agreement with Figure 4.7a, but the maximum transmission coefficient tends towards lower frequencies as the wavevector increases.

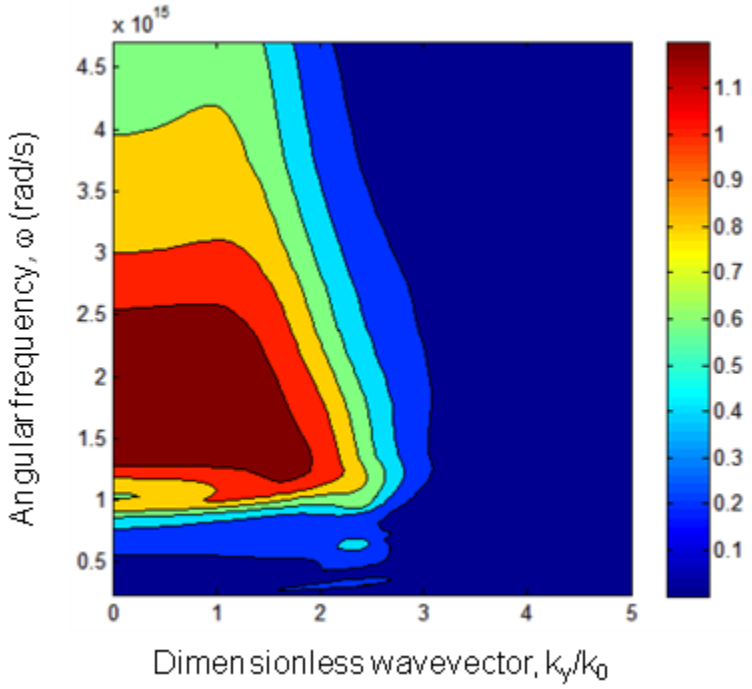

Figure 4.9. Transmission coefficient $\xi_{\omega y}(\omega,k_y)$ versus angular frequency and reduced *y*-dimension wavevector for the grating geometry.

This is typically not an expected behavior, as the direction of k_y will typically not have any resonance behavior associated with it. Since the grating is perpendicular to the k_x wavevector, it is expected that the transmission coefficient in the k_y direction should merely decay. This is shown in Figure 4.10.

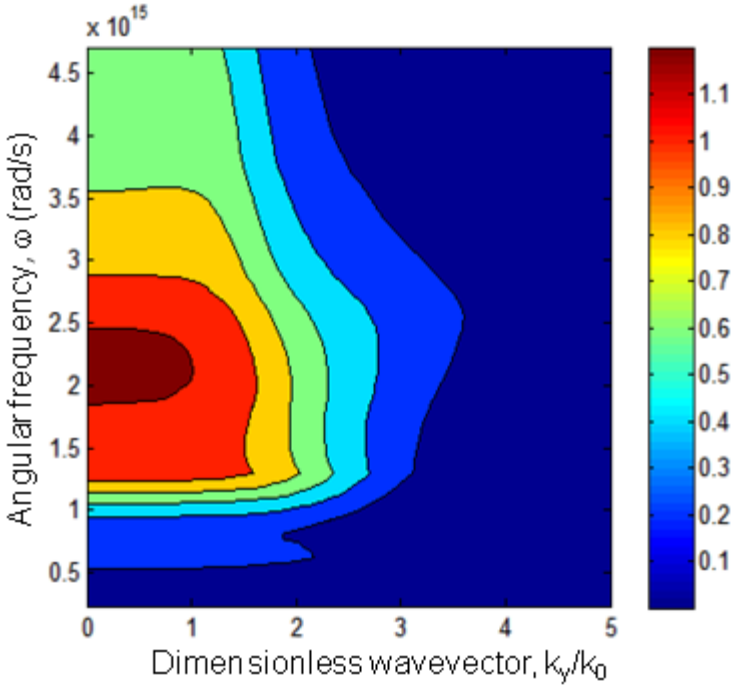

Figure 4.10. Transmission coefficient $\xi_{\omega y}(\omega, k_y)$ versus angular frequency and reduced y-dimension wavevector for the planar tungsten emitter.

In this case, the SPP resonance maintains the same frequency and dies out towards larger wavevectors. This can be seen over nearly all frequencies that the transmission coefficient decreases with increasing k_y wavevector. Larger wavevectors have a higher density of states, and can transfer more energy [74], thus have a higher weight in Figure 4.8. The shifted SPP resonance of the grating extends further, which is why the peak for the grating is so much higher than in the planar case, and since the lower frequency is closer to the TPV bandgap of 8.4×10^{14} rad/s, the conversion efficiency rises. Though it is not clear why this resonance shifts, it may be due to coupling with the low-frequency resonance seen in Figure 4.7a.

4.3 Conclusions

Using the exact scattering matrix approach combined with RCWA, we have been able to simulate the near-field radiative exchange between a tungsten grating and an

$In_{0.18}Ga_{0.82}Sb$ photovoltaic cell. The power output and conversion efficiency of the near-field TPV cell have been found by assuming 100% quantum efficiency, and compared with an unstructured planar tungsten case. Through a parametric study of grating geometries, it was found that improvements over an unstructured emitter are difficult, though possible, and a suitable emitter was found to outperform the baseline case. The electrical output power was 1.06×10^6 W/m^2 with a conversion efficiency of 31.8%, showing an improvement over the planar case by 40% and 6% for power and efficiency, respectively. The mechanisms for enhancement were investigated, and it has been shown that surface plasmon polariton resonance is responsible for the exceptional performance for the planar tungsten grating. The grating geometry is further enhanced as a separate resonance phenomenon shifts this SPP mode towards higher wavevectors and lower frequencies, increasing both the power and efficiency. It is through this work that we have shown simulations a powerful and efficient nanostructured near-field thermophotovoltaic device, and have gained insights into near-field radiation in one-dimensional grating structures.

5: INFRARED OPTICAL CONSTANTS THIN FILM TUNGSTEN

In this chapter the morphological and optical properties of thin tungsten films are investigated. Four films were deposited on silicon substrates using DC magnetron sputtering with or without annealing. X-ray diffraction, Rutherford backscattering, X-ray photoelectron spectroscopy, scanning electron microscopy, and atomic force microscopy were used to characterize the sample phases and morphology. The transmittance and reflectance of the samples were measured from 1 to 20 μm wavelengths. The dielectric function of each sample was obtained by fitting the measured radiative properties using the Drude-Lorentz dispersion with adjustable parameters. The Hall effect and sheet resistance of one of the samples were also measured to compare the transport properties with the optical parameters in the Drude model. From this investigation, the complex refractive index was accurately determined for all samples, and insights into the penetration depths and hemispherical emissivities are made.

5.1 Sample Fabrication and Characterization

Four samples were deposited with DC magnetron sputtering under the same conditions but with different combinations of pre- and post-deposition treatments. The samples were deposited in an Ar gas flow rate of 25 sccm and a power of 50 W. The substrates were maintained at a constant temperature of 350°C with a tungsten filament lamp, and monitored with a calibrated radiation thermometer throughout the deposition process. The deposition time was 4 min to achieve a nominal film thickness of 70 nm. The substrates were square (110) silicon wafers with a diagonal of 20 mm. The wafers were 770 μm thick measured with a micrometer, double side polished, with a resistivity of approximately 100 Ω·cm. Prior to deposition, two of the silicon wafers were ion-cleaned to remove any native oxide layer. This was done to investigate the possibility of diffusion of tungsten into the silicon layer. While there was no evidence of interfacial

diffusion, an effect on the growth of the tungsten film was observed and will be discussed in more detail. Two of the samples were annealed for one hour at 800°C in vacuum at 1.3×10^{-6} Pa (9.8×10^{-9} torr) to prevent any unintentional oxidation. The results show a drastic change in properties between annealed and unannealed samples. Table 5.1 shows the treatments performed on each sample, as well as the crystal phases and other parameters to be discussed in subsequent sections.

Table 5.1. List of samples used with the different pre- and post-deposition treatments indicated. Annealing was performed at 800°C for 1h in vacuum. The native oxide on the Si substrate was removed by ion-cleaning.

Sample number	W01	W02	W03	W04
Pre-treatment	Ion-cleaned	-	Ion-cleaned	-
Post-treatment	Annealed	Annealed	-	-

To identify the crystal phases of the samples, X-ray diffractometry was performed. A PANalytical X'Pert PRO Alpha-1 using a Cu K-α source was used for the measurements. Because of the low thickness of the films, grazing incidence X-ray diffraction (GIXRD) was used at a fixed inclination angle of 8°. Figure 5.1 shows the GIXRD measurements for all four films. Peaks are marked according to their phase identifications from ICDD PDF cards (04-001-0110 for α-W; 00-047-1319 for β-W; 01-088-2339 for γ-W) [92]. The two annealed samples (W01 and W02) show peaks corresponding to the stable α-W phase. W03 matches the β phase while W04 matches the γ phase. Neither of these samples were annealed, but W03 was ion-cleaned for complete oxide removal prior to deposition, and W04 was not. Others have reported changes in the growth mode of tungsten films on silicon substrates with and without the native oxide layer [93]; however, further investigation is needed to confirm the relationship between film structure and the presence of the oxidized silicon layer.

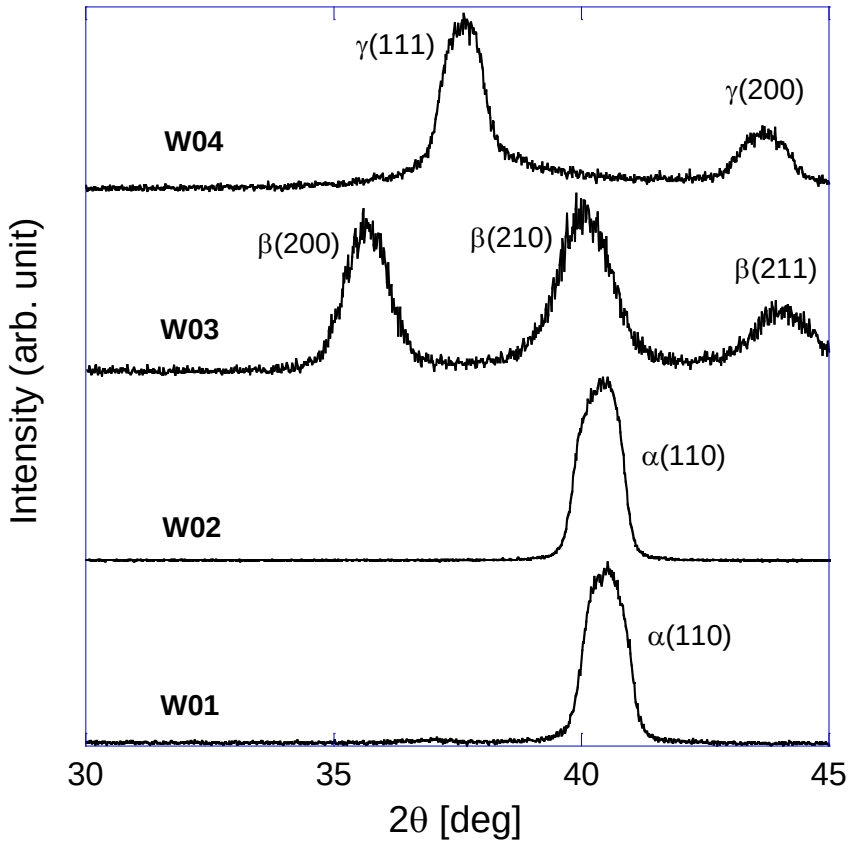

Figure 5.1. GIXRD profiles for all four samples with the phase and crystal orientation denoted. Note that samples W01 and W02 were both annealed and present the same crystal phase.

It should be noted that the GIXRD measurements are inconclusive for the β-W and γ-W phases. This is because β-W has an identical crystal structure as W_3O [49] and γ-W has an identical crystal structure as W_2N [94]. Since the formation of tungsten oxide or nitride is not unrealistic, neither of these compounds can be automatically ruled out. Additional measurements are needed to identify the film stoichiometry.

Rutherford backscattering (RBS) was performed on W02, W03, and W04. He^+ ions with energies of 2 MeV and a backscattering angle of 150° bombarded the samples. Details of this technique are described in [95]. This measurement not only reports the chemical composition of the films but also the thickness. The chemical analysis confirmed the identification of the phase of W03 as being β-W, since oxygen was not

present in a high enough content to form W_3O. Results for W04 were inconclusive because the backscattering energy of nitrogen overlaps with that of the silicon substrate [96], obscuring any presence of nitrogen in the film. X-ray photoelectron spectroscopy (XPS) was performed using a Surface Science Instruments M-Probe XPS. Results showed that not enough nitrogen exists for a nitride film, and thus the GIXRD measurement can only be explained with the γ-W phase for sample W04.

In addition to the chemical characterization of the samples, RBS can also help determine the film thickness based on the bandwidth of backscattered energies. The tungsten in these samples backscatters at a characteristic energy level, but due to volumetric electric field interaction, this energy will be attenuated proportional to the depth of each backscattering event [97]. The thicknesses obtained by this method were consistently (72±5) nm for all three samples, based on the bulk α-W density value of 19.256 g/cm^3 [21], however, this thickness cannot explain the spectroscopic measurements. The consistency in the RBS thicknesses suggests that a similar amount of material was sputtered for each sample, and the film thicknesses are found through analysis of the transmittance and reflectance of each sample, to be discussed later. These thicknesses vary considerably between samples, suggesting that the films were deposited with different film densities.

GIXRD measurements show that the unannealed samples were deposited poly- or nanocrystalline due to the presence of multiple diffraction peaks, but the same conclusion cannot be drawn from the annealed samples as there is only one diffraction peak within this range. Using Scherrer's formula to estimate the crystallite size for the annealed samples gives grain sizes on the order of 10-20 nm. However, additional peak broadening is expected to occur [98], and this value cannot be trusted. To determine the crystallite sizes, scanning electron microscope (SEM) surface images were obtained for samples W01 and W04 using a Zeiss Ultra60 FESEM. These images are shown in Figure 5.2a and

5.2b, respectively. The grains were of random shape and orientation. The average grain size for W01 is found to be approximately 60 nm. The SEM image for W04 did not reveal any grains greater than 20 nm which is the minimum feature size of the machine. Therefore it is assumed that all samples are nanocrystalline.

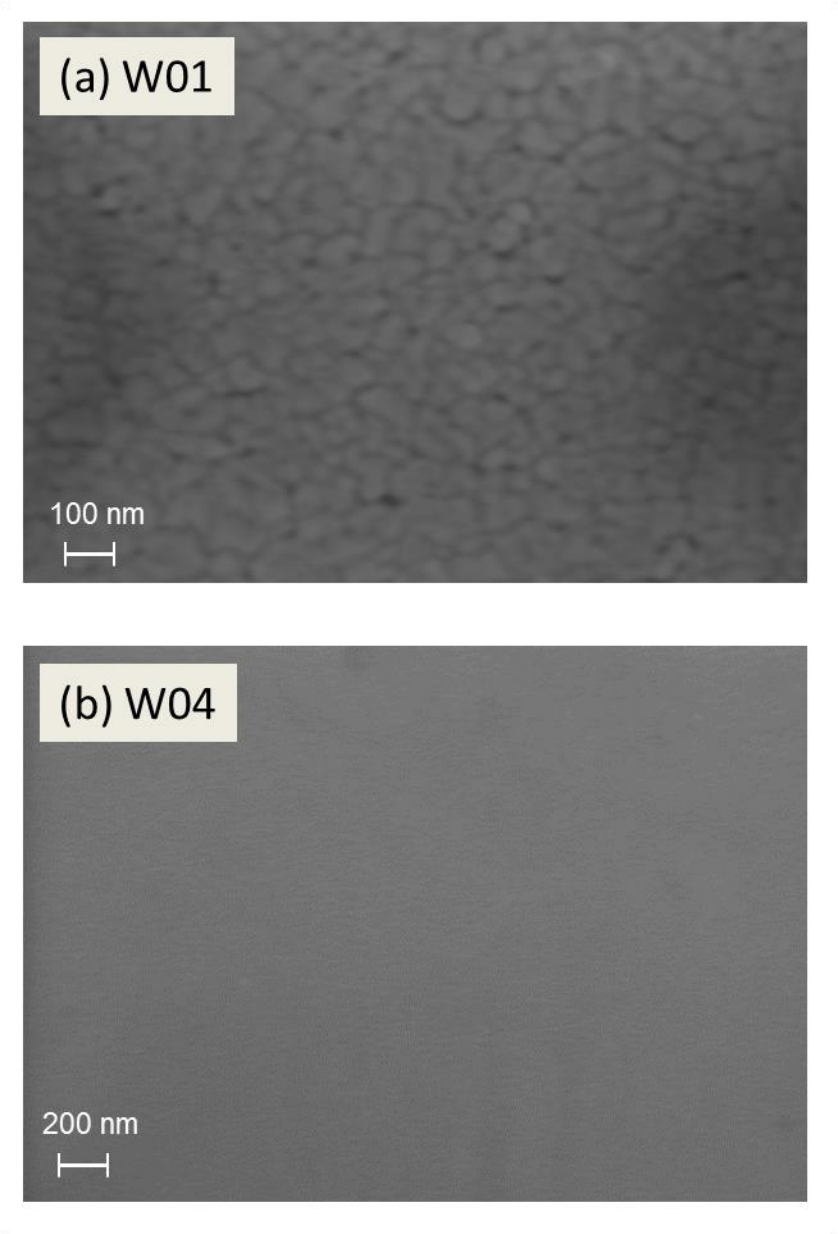

Figure 5.2. SEM images of the surface of (a) W01 with an average crystallite size of about 60 nm; and (b) W04 with undetectable features. Note that the scales are different.

Surface topography was measured for sample W01 using a Veeco Dimension 3100 AFM in tapping mode over a 2 μm × 2 μm scan area. The AFM probe was an uncoated *n*-type Si probe of 10 nm in radius. The results show that the root-mean-square (RMS) roughness is 10.7 nm. Note that the RMS roughness for a bare silicon substrate is 1-2 nm. It is expected that the rms roughness for the unannealed samples should be somewhere in between. This roughness should not affect the radiative properties of the samples, thus surface scattering losses are negligible in the transmittance and reflectance spectra from 1 to 20 μm. However, this roughness does affect the local film thickness, and the reported thicknesses should be interpreted as an average over a large area.

5.2 Radiative Properties and Dielectric Function Extraction

The focus of this work is to model the FTIR measurement results in order to develop suitable dielectric function models. It is assumed that the sample includes a thin W film (in which interference is considered) on a thick Si substrate (in which multiple reflections are considered by neglecting interference effects). The native oxide films in the samples without ion cleaning have negligible effects on the radiative properties in the infrared region. The formulation is similar to that used earlier and has been described previously [67, 79]. In essence, the transmittance and reflectance at normal incidence can be expressed in terms of the optical constants and thicknesses of the film and substrate at any given frequency.

$$T = T(\tilde{n}_{\mathrm{f}}, d_{\mathrm{f}}, \tilde{n}_{\mathrm{s}}, d_{\mathrm{s}}, \omega) \tag{5.1}$$

$$R_{\mathrm{f}} = R_{\mathrm{f}}(\tilde{n}_{\mathrm{f}}, d_{\mathrm{f}}, \tilde{n}_{\mathrm{s}}, d_{\mathrm{s}}, \omega) \tag{5.2}$$

$$R_{\mathrm{s}} = R_{\mathrm{s}}(\tilde{n}_{\mathrm{f}}, d_{\mathrm{f}}, \tilde{n}_{\mathrm{s}}, d_{\mathrm{s}}, \omega) \tag{5.3}$$

Here, the transmittance *T*, film-side reflectance R_{f}, and substrate-side reflectance R_{s} are functions of the complex refractive indices of the film and substrate $\tilde{n}_{\mathrm{f}}$ and $\tilde{n}_{\mathrm{s}}$

respectively, the thicknesses of the two layers, and the spectral variable (ω for angular frequency in rad/s). It should be noted that $\tilde{n}_f$ and $\tilde{n}_s$ are also frequency dependent. In the present study, the (angular) frequency is often expressed in terms of wavenumber and 1 cm^{-1} = 1.884 × 10^{11} rad/s. It can be shown that the reflectance at 10° incidence is essentially the same as that at normal incidence. Hence, the effect of polarization can be neglected.

The optical properties of (lightly doped) silicon can be obtained from Palik [37]. The calculated radiative properties were compared with the measurements for a bare silicon substrate and excellent agreement was obtained, except within a narrow band between 1000 and 1400 cm^{-1}. Here the extinction coefficient κ_s was modified to account for absorption due to interstitial oxygen, following a similar procedure described in [78, 99]. The thickness of the substrate is kept at d_s = 770 μm for all samples. The thickness of the tungsten films is also treated as an unknown to be determined along with the optical constants of the film.

One way to extract the optical constants of the film is to evaluate the real and imaginary parts of the refractive index at discrete frequencies along with the film thickness. This gives rise to $2N + 1$ unknowns for N measured data points. According to Equations 5.1 through 5.3, $3N$ equations are available and using a suitable regression method, the unknowns can be solved in principle. Not only is this method computationally intensive, but it is also highly affected by the measurement uncertainty. The resulting optical constants are discontinuous and may fluctuate due to the random noise in the experimental data. This is shown in Figure 5.3 for both the real and imaginary parts of the refractive index. Here, the refractive index was fit for sample W04 based on a minimization of the RMS error at each discrete wavenumber for the three spectral measurements. There are both local and absolute minima found, and the relative RMS error is shown by the color saturation, with the black points having a higher RMS,

representing a poorer fit to the data. This obviously creates several problems, one of which is that the refractive index does not necessarily form a continuous curve as expected. Thus, this method is not employed in the rest of this analysis.

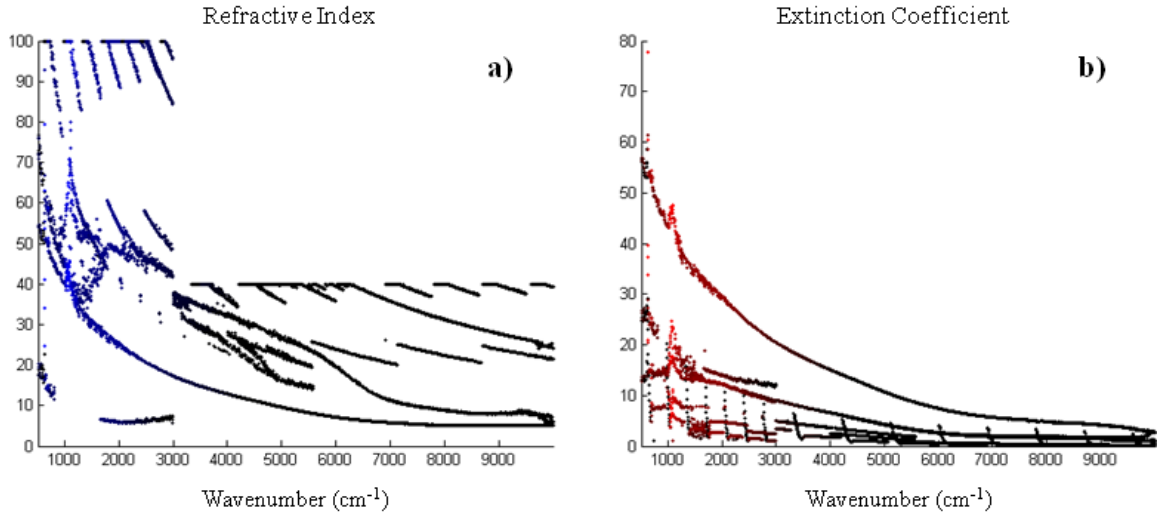

Figure 5.3. Results of the extracted refractive index for sample W04: a) real part of refractive index, b) imaginary part. Multiple local solutions are shown, and points with a higher color saturation have less RMS error.

A more common approach is to use a presumed dispersion model, which treats the refractive index or the dielectric function, $\tilde{\varepsilon} = \tilde{n}^2$, of the film as a smooth function of frequency. The combined Drude free-electron model and the Lorentz oscillator model, or the Drude-Lorentz model, appears to be appropriate in modeling the dielectric function of tungsten [33, 38]:

$$\tilde{\varepsilon}(\omega) = \varepsilon_1 + i\varepsilon_2 = \varepsilon_\infty - \frac{\Omega_p^2}{\omega^2 + i\Gamma\omega} + \sum_{j=1}^{M} \frac{\omega_{p,j}^2}{\omega_j^2 - \omega^2 - i\gamma_j\omega} \tag{5.4}$$

where ε_1 and ε_2 are the real and imaginary parts of $\tilde{\varepsilon}$. The first term on the right is a constant that accounts for high-frequency electron transitions. These transitions affect the dispersion in a narrow spectral region but reduce to a constant at shorter frequencies. Hence, ε_∞ describes the effect of all transitions from the ultraviolet to X-ray regions. The second term on the right represents the Drude term, where Ω_p is the plasma frequency

and Γ is the scattering rate. The last term is based on the classical Lorentz model, with *M* oscillators and each is characterized by a resonance frequency ω_j, damping coefficient γ_j, and plasma frequency $\omega_{\mathrm{p},j}$ [67]. The Drude model describes the contribution of free carriers or intraband transitions. The Lorentz model is used here to account for both the interband transitions and lattice vibrations (i.e., phonons). These parameters have significant implications not only on the shape of the dielectric function, but also on the physical characteristics of the material. For example, in the case of interband transitions, the energy bandgap is equal to the minimum photon energy required to excite an electron to a higher energy state, which roughly corresponds to the resonance frequency in the Lorentz term. While there exist other models that may describe bandgap absorption more precisely [38], the Lorentz model is chosen because of its simplicity.

Including the film thickness, there are a total of $3M + 4$ fitting parameters. Note that $M << N$, since there are thousands of data points in each measured spectrum. A steepest ascent hill climber algorithm [100] was used to fit these parameters based on the minimization of the figure of merit (*FOM*) defined as

$$FOM = \sqrt{\frac{\alpha_1 \sum \left(T_\mathrm{m} - T_\mathrm{c}\right)^2 + \alpha_2 \sum \left(R_\mathrm{f,m} - R_\mathrm{f,c}\right)^2 + \alpha_3 \sum \left(R_\mathrm{s,m} - R_\mathrm{s,c}\right)^2}{\left(\alpha_1 + \alpha_2 + \alpha_3\right) N}} \qquad (5.5)$$

which represents the weighted root-mean-squared error between the measurement points and the calculated points, subscripts m and c respectively, for all three spectral quantities *T*, R_f, and R_s. The measurements were interpolated to have N=1000 data points which were compared with the model described above at the same wavenumbers. Here, each coefficient α represents a weighting of one of the radiative properties, and the sum of these coefficients appears in the denominator to give the *FOM* the same order of magnitude as the experimental uncertainties.

Each sample was fit independently beginning with an initial trial of parameters from [33, 38] and a thickness of 72 nm (from RBS). Due to the complicated band structure of tungsten and the overlapping nature of the absorption phenomena in the spectrum, a single run of the algorithm will not result in the optimal solution, but a local minimum of the *FOM* which may have nonphysical parameters. As such, the algorithm was allowed to run for 100 iterations at which point the measurement and model curves were plotted. The minimum step in the algorithm was a 1% change in any parameter. The parameters could then be adjusted to match physical characteristics of films, and the individual weights could be adjusted to allow closer fitting to one curve. The algorithm would run again to fine tune these parameters. This procedure continued several times until the shapes of the models matched the shape of the measurements qualitatively and the maximum differences between the measurement and the model were within the specified uncertainties. The sensitivity and uncertainty of the fitting parameters can be tested by varying each parameter separately or as a group in some cases. The uncertainties are usually 10-15%.

5.3 Results

The results of this work will be broken into several subsections. Since the annealed samples and the unannealed samples show very different characteristics, as seen in the morphological studies in Section 5.1, the spectroscopic measurements will be analyzed separately, with the annealed samples discussed in 5.3.1 and the unannealed samples following in 5.3.2. Next, the spectrally-varying penetration depth will be discussed for all samples in Section 5.3.3. A Hall effect measurement of sample W01 will be used with the extracted plasma frequency to determine the effective carrier mass in Section 5.3.4, and finally the spectral normal emissivities of all samples will be examined in Section 5.3.5.

5.3.1 Analysis of the Annealed Samples

The annealed samples (W01 and W02) generally exhibit higher reflectance and lower transmittance, due to free-carrier contributions. The predicted and measured reflectance and transmittance spectra for W01 and W02 are shown in Figure 5.4. The two samples show very similar behavior. Excellent agreement between the model prediction and experiment is evident, particularly for W01. Note that the transmittance scale is from 0 to 0.1, and the maximum T is about 0.031 due to the metallic behavior of the α-W. It should be noted that R_s is more sensitive to the substrate absorption in the region from 500 to 1500 cm^{-1} [101]. These features also appear in the transmittance but are obscured due to the low T values. Furthermore, beyond 9000 cm^{-1}, bandgap absorption in silicon becomes important resulting in a significant drop in the transmittance at about 10000 cm^{-1}. The substrate-side reflectance also decreases to about 0.32, which is the reflectivity between the air and silicon interface as the substrate is almost opaque. It can be shown that the reduction in transmittance toward smaller wavenumbers below 6500 cm^{-1} is mainly due to the increase in the reflectance (R_f) rather than an increase in the film absorption. Further discussion will be given in Section 5.3.3.

The fitted parameters are listed in Table 5.2 along with optical and structural parameters for the remaining samples to be discussed in Section 5.3.2. The two annealed samples share very similar parameters. Note that the resonance frequencies can be identified as interband transitions [33-35]. The slightly lower transmittance in W02 may be attributed to the combination of somewhat larger thickness and lower scattering rate. The density of the film can be estimated based on the thickness obtained from fitting, using the bulk W density value and the nominal thickness of 72 nm obtained from the RBS. While the density of W01 was close to the bulk value (4% below), the density of W02 obtained this way appears to be relatively low at 16.5 g/cm^3. The plasma frequency Ω_p and scattering rate Γ for bulk tungsten obtained by Rakić et al. [38] were 48,400 and

516 cm^{-1}, respectively. The higher scattering rate in the film is usually expected due to the effect of microstructures.

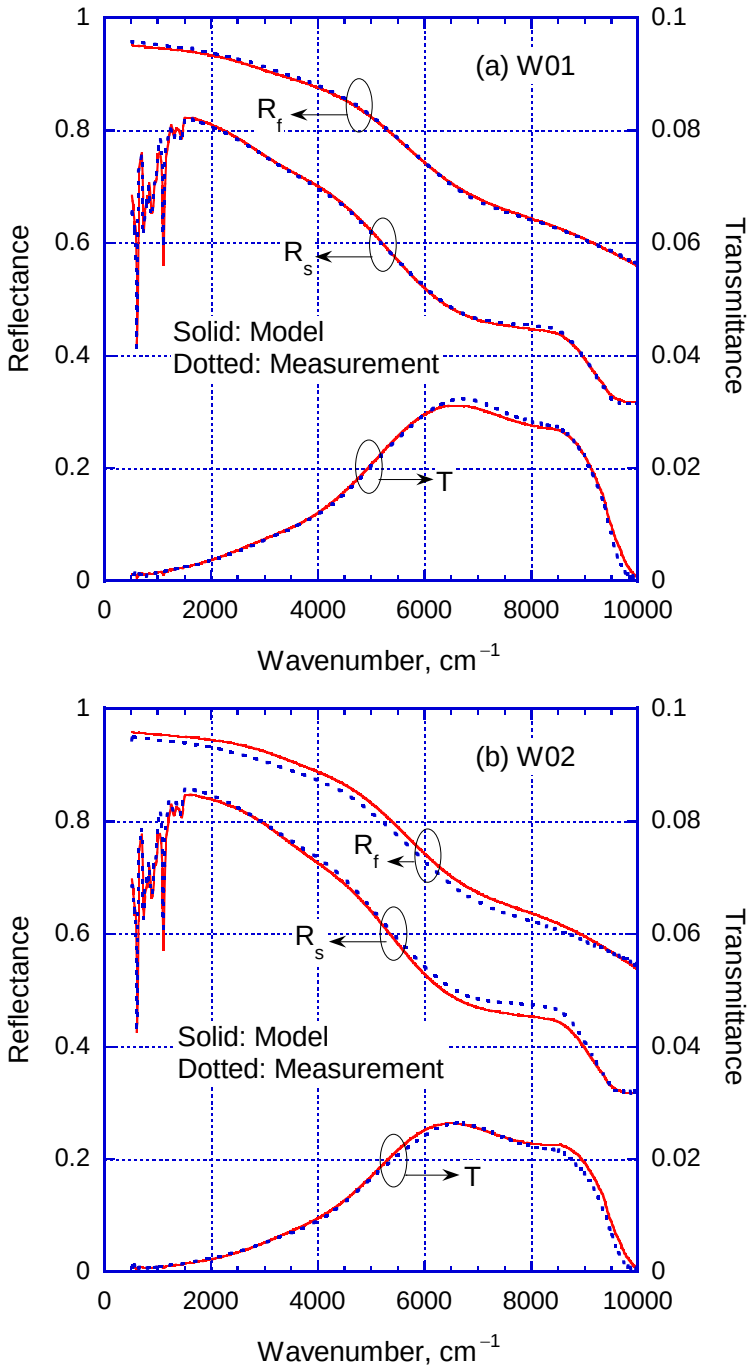

Figure 5.4. Measured and fitted spectral radiative properties for the two annealed samples: (a) W01 and (b) W02.

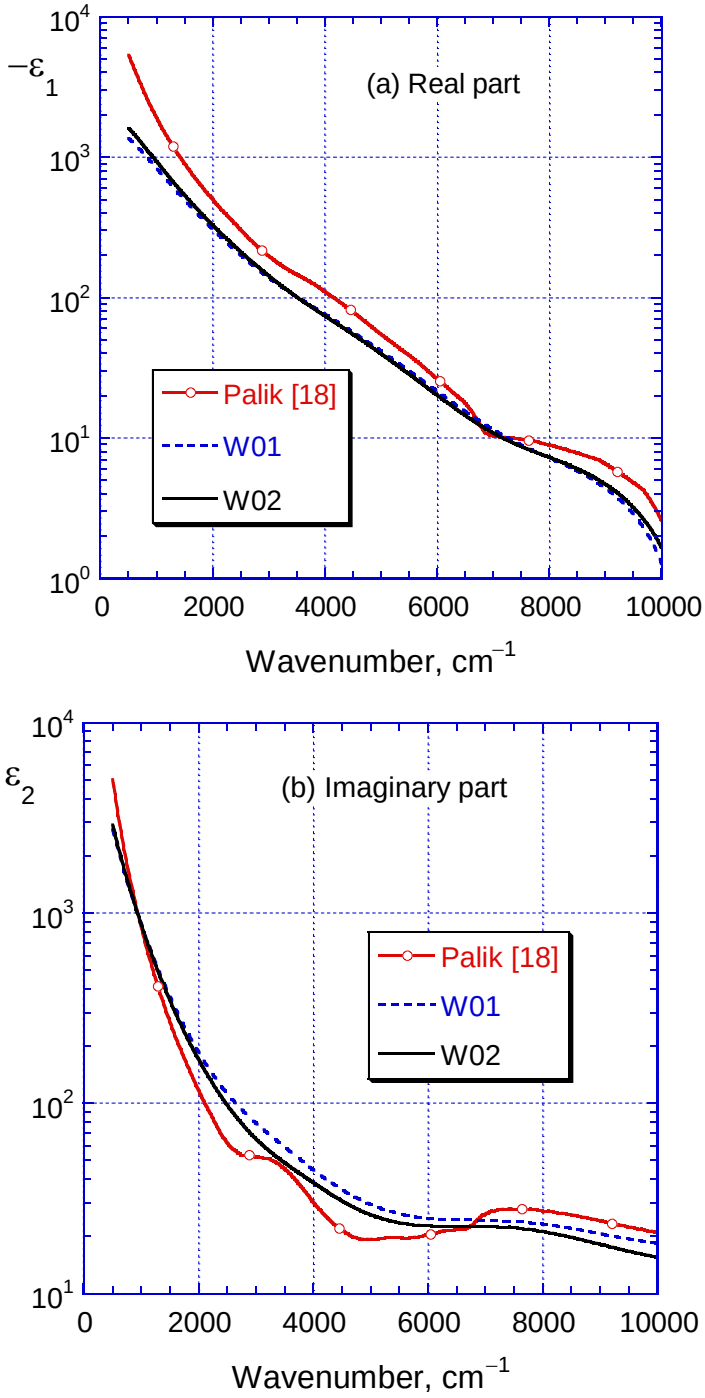

Figure 5.5. Dielectric function obtained for the two annealed samples: (a) Real part; (b) Imaginary part. The data from Palik [37] are shown for comparison. Note that ε_1 is negative in the spectral region of interest.

Figure 5.5 shows the dielectric functions for W01 and W02. The values for bulk tungsten from Palik [37] are also shown for comparison. Note that the real part ε_1 is always negative in the infrared, which is a typical metallic characteristic. Because $\varepsilon_1 = n^2 - \kappa^2$, where n and κ are the real and imaginary parts of the refractive index $\tilde{n}$, a negative ε_1 suggests that $\kappa > n$. It should be noted that the Drude term can be viewed as a Lorentz term with a zero resonance frequency. Hence, it dominates the optical behavior at lower frequencies, resulting in increased values of n and κ toward smaller wavenumbers. This can be seen from the increase of the imaginary part of the dielectric function since $\varepsilon_2 = 2n\kappa$. While the dielectric functions for W01 and W02 are close to each other, the deviation from the bulk values can be as high as 75% at certain frequencies. Interestingly, the curves for W01 and W02 are less structured than those for bulk tungsten. This is due to the large scattering rate in the Drude term, which tends to increase the effect of free carriers on the dielectric function at higher frequencies, effectively screening the interband absorption.

Table 5.2. Thickness and the Drude-Lorentz model parameters of each sample obtained from fitting. The different pre- and post-deposition treatments are also indicated. Annealing was performed at 800°C for 1h in vacuum. The native oxide on the Si substrate was removed by ion-cleaning.

Sample number	W01	W02	W03	W04
Pre-treatment	Ion-cleaned	-	Ion-cleaned	-
Post-treatment	Annealed	Annealed	-	-
Crystal phase	α-W	α-W	β-W	γ-W
Thickness [nm]	75	84	88	105
Density [g/cm^3]	18.5	16.5	15.8	13.2
ε_∞	8.47	12.9	10.3	6.81
Ω_p [cm^{-1}]	42000	42100	30500	20000
Γ [cm^{-1}]	1000	903	5720	8880
ω_1 [cm^{-1}]	3480	3850	5250	3730
$\omega_{p,1}$ [cm^{-1}]	12100	8880	9870	7590
γ_1 [cm^{-1}]	2730	2450	3730	4690
ω_2 [cm^{-1}]	8040	7880	7370	7780
$\omega_{p,2}$ [cm^{-1}]	24900	24000	22600	16700
γ_2 [cm^{-1}]	5860	5520	5330	8360
ω_3 [cm^{-1}]	16700	16500	15000	15000
$\omega_{p,3}$ [cm^{-1}]	58500	48300	61300	42900
γ_3 [cm^{-1}]	10900	12900	11900	10800
ω_4 [cm^{-1}]	-	-	663	663
$\omega_{p,4}$ [cm^{-1}]	-	-	1630	1480
γ_4 [cm^{-1}]	-	-	193	199

5.3.2 Analysis of the Unannealed Samples

The radiative properties of the unannealed samples are shown in Figure 5.6. The transmittance is much higher than those of the annealed samples, and the reflectance, particularly the film side reflectance, is much lower. The β-W (W03) and γ-W (W04) appears to be more dielectric and less metallic than the annealed samples. The unannealed samples have a much smaller plasma frequency and larger scattering rate, as can be seen from Table 5.2. As shown in Figure 5.7, ε_1 is always positive for both W03 and W04 due to the relatively weak Drude term. Furthermore, the two samples show distinct radiative properties due to different phases. W03 has a much higher plasma frequency than W04, resulting in a larger ε_2 (more absorption) and lower transmittance as compared with those of W04.

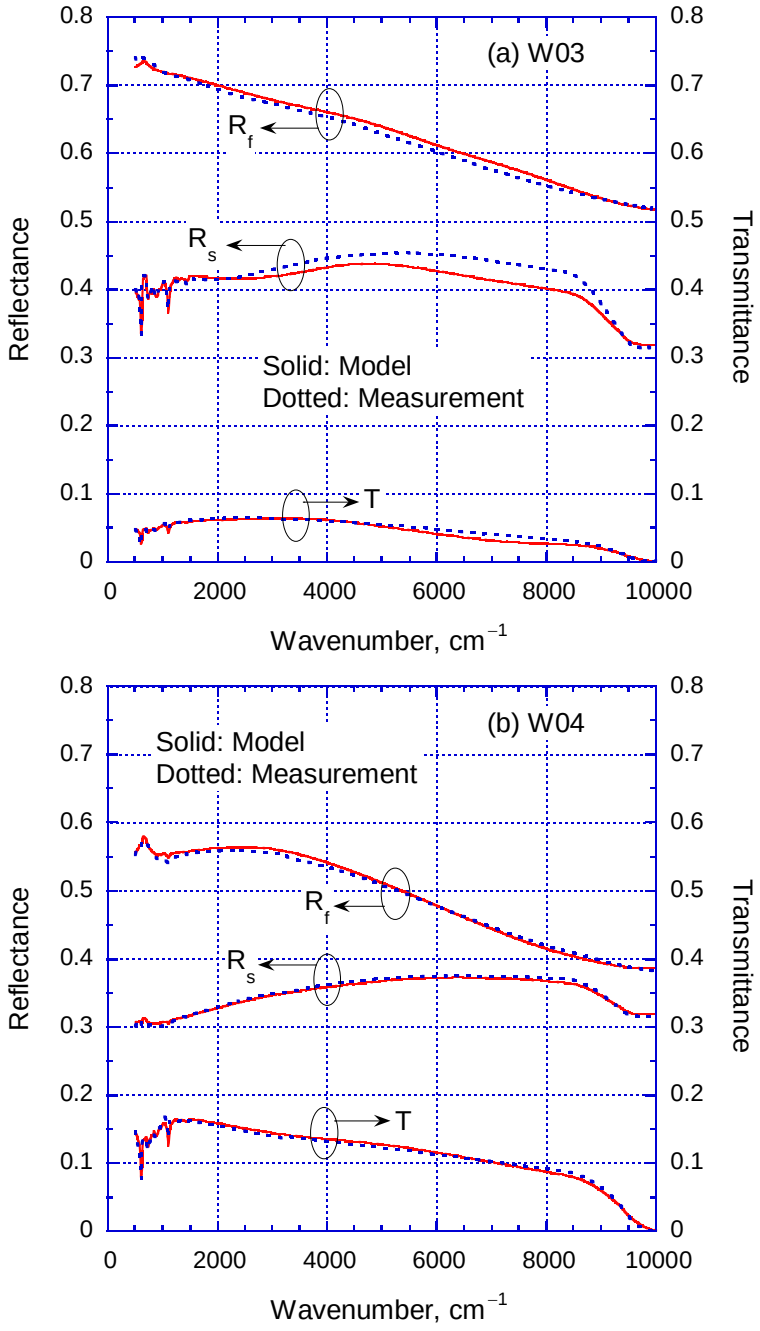

Figure 5.6. Measured and fitted spectral radiative properties for the two unannealed samples: (a) W03 (ion-cleaned) and (b) W04.

Unlike the annealed samples, a feature can be clearly seen in the radiative properties near 700 cm^{-1} in both W03 and W04. This may be due to phonons or an interband transition as tungsten has a very complicated electronic band structure. An

absorption peak near 630 cm^{-1} was also observed in an earlier study of single crystal tungsten and was attibuted to an interband transition [33]. While the exact mechanism is not clear, a low-energy oscillator at $\omega_4 = 690$ cm^{-1} was included in the dielectric function of W03 and W04 to best fit the transmittance and reflectance spectra. This feature might also exist in the annealed samples, but it is undetectable because the free-carrier contribution is much greater than the Lorentz term. While the parameters for the interband transitions are similar for W03 and W04, due to the large differences in the Drude parameters, these two samples possess very different dielectric functions as shown in Figure 5.7.

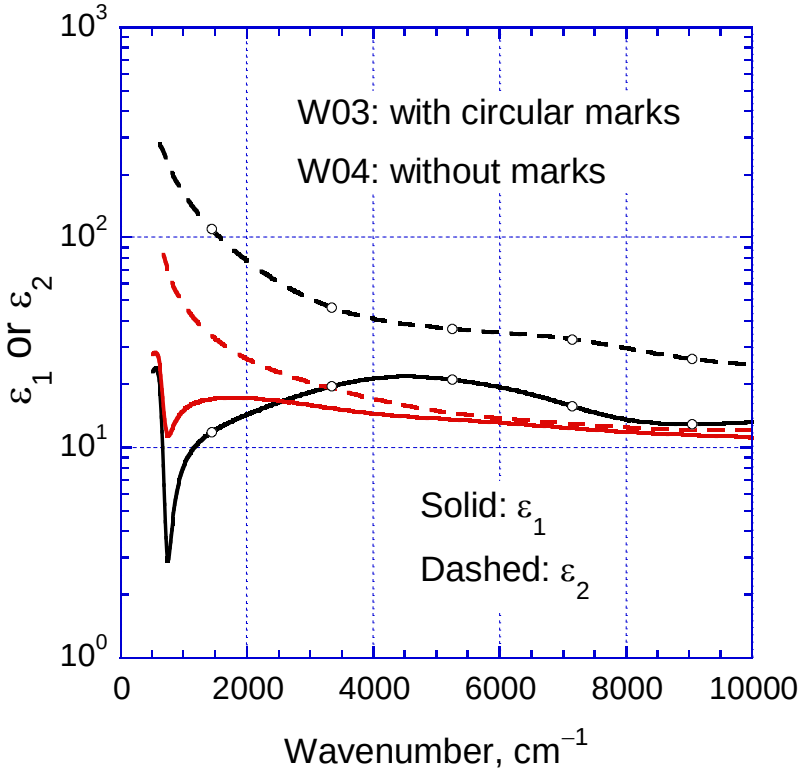

Figure 5.7. Real and imaginary parts of the dielectric function of the two unannealed samples.

Comparison of the fitted film thickness to the thickness found from RBS suggests that the density of the β-phase film is 15.8 g/cm^3, which agrees with other published values [44]. The sample W04, which contains fcc γ-W, shows the lowest film density of

all at 13.2 g/cm^3. It should be noted that the density of the β or γ phase based on lattice constants is not much lower than the bulk value, and cannot explain the thickness discrepancies. The variation in density must be attributed to the packing of grain boundaries in the polycrystalline films, and therefore represents an effective film density. It is interesting to note that the ion-cleaned films, W01 and W03, have higher densities than the uncleaned films. This could suggest that the presence of a native oxide layer promotes the growth of the less-dense γ-phase, which then anneals to a less dense α-phase film, however further research is needed to make this claim.

5.3.3 Penetration Depth

It is instructive to compare the photon penetration depth, $\delta = \lambda / (4\pi\kappa)$, where λ is the wavelength in vacuum. The penetration depths calculated for all samples as well as using the data from Palik [37] are as shown in Figure 5.8. It can be seen that the penetration depths for the annealed samples (W01 and W02) are similar to but greater than that of the bulk. On the other hand, the penetration depths of the unannealed samples are significantly greater. Even though the thickness of W04 is 20% greater than that of W03, the transmittance of W04 is about three times higher due to the much greater penetration depth. It is noted that the penetration depths for W01 and W02 do not change much and actually increase slightly with decreasing wavenumber below 2000 cm^{-1}. However, the transmittance drops significantly toward smaller wavenumbers as shown in Figure 5.4. Therefore, this is due to the increased reflectance rather than absorption toward longer wavelengths.

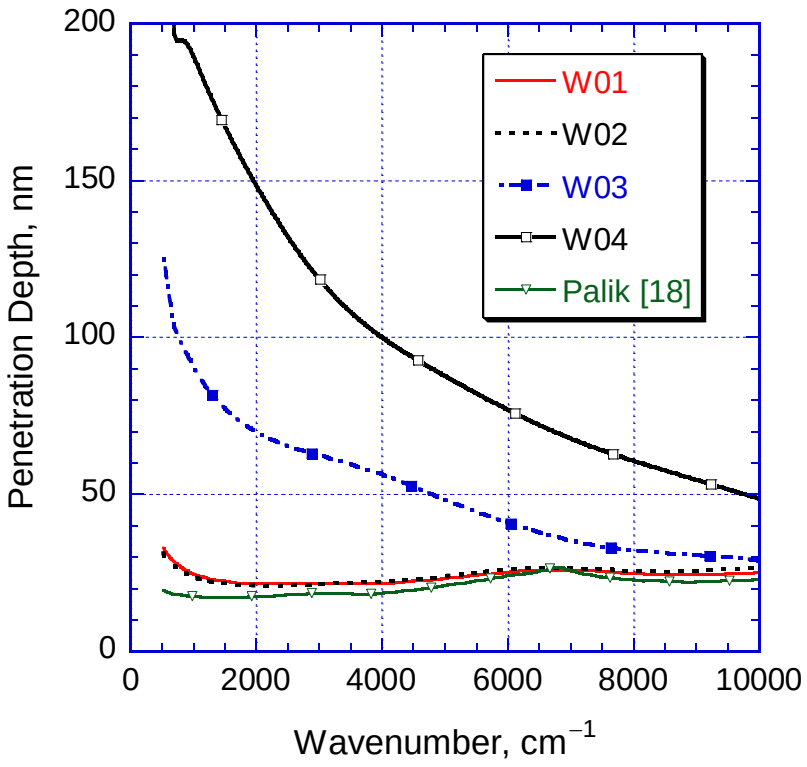

Figure 5.8. The penetration depths of all four samples calculated from the dielectric function models.

5.3.4 Hall Effect and Effective Mass

The electronic transport is important for electrical and thermal properties of the materials. Considering the importance of annealed films to future applications using tungsten films, sample W01 is characterized by measuring its sheet resistance and Hall effect using the van der Pauw method with an Ecopia Corporation HMS-3000. The applied magnetic field during the measurements was 0.556 T and the applied current ranged from 2 to 19 mA. The measurements showed a positive Hall coefficient of 1.2×10^{-4} cm^3/C, corresponding to a carrier concentration of $n_e = 5.2\times10^{22}$ cm^{-3}. These values are very close to the bulk Hall coefficient and carrier concentration [21]. The reason for the positively charged carriers is due to the fact that the band edge of the conduction band in tungsten lies very close to a plane of symmetry [89], and the carriers actually have a good probability of being decelerated instead of accelerated. This

effectively appears as if the electric field is being applied to a positive charge. The measured electrical resistivity is approximately 27 $\mu\Omega\cdot$cm, which is somewhat higher than reported values for tungsten films and much higher than that of bulk tungsten, which is 5.3-5.6 $\mu\Omega\cdot$cm [21].

Initially, it was thought that these two measurements would allow an evaluation of the Drude plasma frequency and scattering rate, however the free carriers do not behave ordinarily and the mass of the carriers becomes an unknown effective mass. The electrical resistivity can be related to the plasma frequency and scattering rate by [67]:

$$\rho = \frac{\Gamma}{\varepsilon_0 \Omega_p^{\ 2}} \tag{5.6}$$

where $\varepsilon_0 = 8.854\times10^{-12}\ \mathrm{C}^2\cdot\mathrm{N}^{-1}\cdot\mathrm{m}^{-2}$ is the vacuum permittivity. Based on the parameters obtained for W01, the calculated resistivity is 34 $\mu\Omega\cdot$cm, about 26% higher than the measured resistivity. On the other hand, when the plasma frequency and scattering rate obtained from Rakić et al. [38] is substituted in Equation 5.6, the calculated resistivity is 13.2 $\mu\Omega\cdot$cm, much higher than the bulk DC resistivity.

The ratio of the effective mass m^* to the electron rest mass m_e can be estimated from [67]

$$\frac{m^*}{m_e} = \frac{n_e e^2}{\varepsilon_0 m_e \Omega_p^2} \tag{5.7}$$

The above equation gives an effective mass of W01 to be $m^* = 2.6m_e$, compared to the bulk tungsten value of $m^* = 2.2m_e$ based on a free-carrier density of 5.8×10^{22} cm^{-3} and the plasma frequency obtained by Rakić et al. [38].

5.3.5 Normal Emissivity

As this material's primary use is as a thermal emitter, the emissivity is an appropriate radiative property to investigate. From the refractive indices obtained in Sections 5.3.1 and 5.3.2, the emissivity can be obtained. Using Kirchoff's law and the transmittance obtained in Section 2.3.1, the spectral normal emissivity can be obtained as $\varepsilon_\lambda = 1 - T$. Here, the reflectance is usually factored into this, however, the thickness of the film is of no importance, and the emissivity is calculated for a thick opaque slab of tungsten. It should be noted that while this is calculated only in the normal direction, the emissivity is typically a function of the polar and azimuthal angles off of the plane of incidence. For most metals, this is fairly invariant to direction except at grazing angles [68], and will not be discussed here.

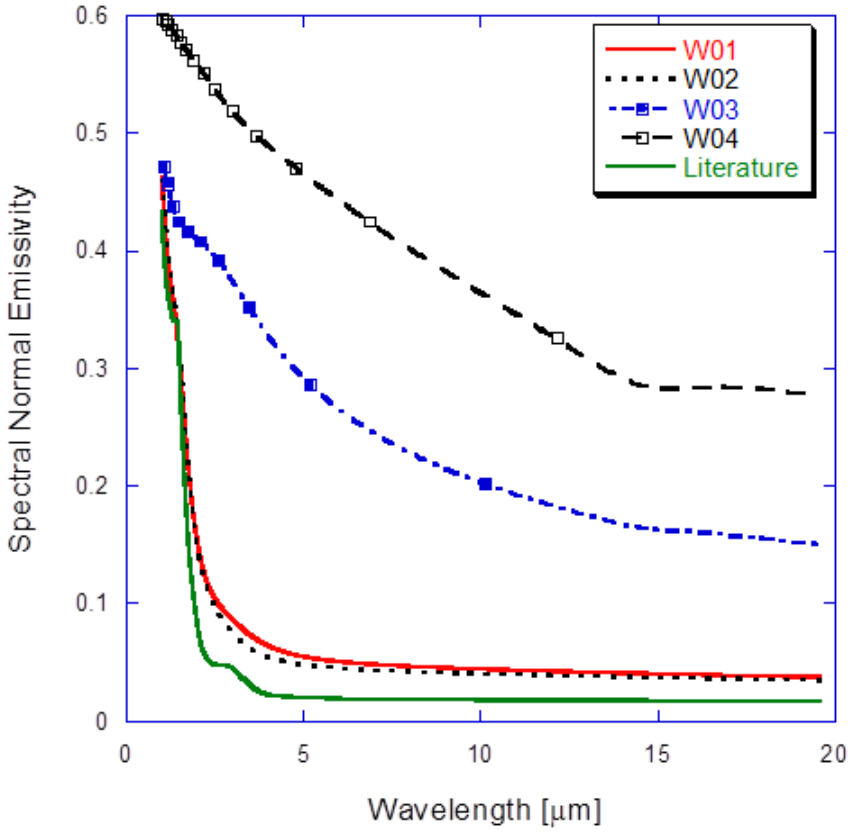

Figure 5.9 Spectral normal emissivity of all studied films and the literature value from Palik [37].

Figure 5.9 shows the spectral normal emissivity for all four of the extracted refractive indices as well as a comparison to the literature data [37]. It is here that an interesting phenomenon arises. While the vast amount of research on tungsten has been done on materials that exhibit the α-phase with highly metallic behavior, here it is seen that the divergence from this behavior gives strong emissive characteristics. For each sample the trend is towards lower emissivity at lower wavelengths, but it is only the unannealed samples that will have an appreciable emissive power at lower temperatures. Near room temperatures, most thermal radiation will be below 10 μm, and neither the single-crystal bulk tungsten nor the annealed tungsten films will have a very large emissivity. However, just like the penetration depth, the effect increases at decreased plasma frequencies, thus the refractive index obtained from W04 produces a highly emitting film.

This is an important note for researchers seeking to use tungsten thin films. If the film is to be used as a radiator for heat or a thermal emission source, the desired emittance should be high. Thus, for applications where the temperatures will be maintained well below 800°C, an unannealed film may prove more useful than a single-crystal or heat-treated film. For applications that will cover both above and below 800°C caution is advised as the emissive power may irreversibly drop by an order of magnitude upon crystallization, and should not be mistaken for oxidation. Lastly, it is important to note the differences between the annealed films and the bulk material, as it is difficult to obtain single-crystal tungsten films. It is clear that the plasma frequency and electron density will be lower in a polycrystalline film, and researchers should expect a significant increase in the emissive power.

5.4 Conclusions

Four samples of thin-film tungsten of equal mass were deposited on silicon substrates with different permutations of vacuum annealing and pre-deposition ion cleaning. XRD, XPS, and RBS measurements confirm that both annealed samples are bcc α-phase tungsten while unannealed films deposited on bare silicon and on a native oxide layer possess metastable A15 β-phase and fcc γ-phase tungsten, respectively. Film densities are found to be lower than single-crystal tungsten. It is found that the films that were not ion-cleaned show lower densities, and the annealed films have densities more comparable to the bulk density. The complex dielectric function is presented for all samples based on a dispersion model consisting of interband Lorentz oscillators and a Drude free-carrier term. The two annealed samples exhibit higher reflectance than the unannealed samples due to much stronger free-carrier contribution. On the other hand, interband transitions are relatively insensitive to differences in phase and film quality. An absorption feature was found in the low energy spectral region for the unannealed samples, possibly due to lattice vibration or an interband transition. This feature might also exist in the annealed samples but is obscured due to the strong free-carrier absorption.

The variation in the optical constants for the four films seen here illustrates a range of possibilities that may be expected in thin-film tungsten. Using bulk values for thin tungsten films may be insufficient, depending on the required accuracy. The annealed samples exhibit similar dielectric functions, but extra care must be taken if precise values are needed. However, there is large disagreement between the annealed and unannealed films, and researchers should be aware that a drastic change in the optical properties is to be expected upon heating the film above 800°C. With these elements in mind, further research may be conducted using thin-film tungsten in a nano/microstructured device for optical or thermal applications.

6: MEASUREMENT OF NEAR-FIELD RADIATION

This work describes a novel experiment for measuring near-field heat transfer between planar geometries at room temperatures. Vacuum gaps as low as 200 nm can be fabricated, and lead to an enhancement over blackbody radiation by as much as 1000%. Moreover, this separation can be maintained over a fairly large area, 1 cm^2, which demonstrates significant power throughput. This can be achieved repeatedly by using micro-fabrication techniques to create a sparse array of thermally insulating structures on an exceptionally flat wafer. This structure is mated to another wafer to create a vacuum gap. While this does create the problem of multiple modes of heat transfer, the periodicity and the thickness of the insulating supports can be tuned to demonstrate the maximum near-field heat transfer.

These samples are measured in a vacuum chamber near room temperature with multiple heat fluxes. Precise measurements of both the temperature difference and the heat transfer rate between the two surfaces are necessary to confirm the near-field heat transfer effects. A copper staging area has been designed and machined to control the flow of heat near the sample. Silicon diode thermistors, thermocouples, and heat flux meters will give accurate thermal measurements to describe the phenomena across the sample. Details of the experimental system, sample fabrication and characterization are discussed, and results showing near-field heat transfer with multiple samples covering a range of vacuum gaps from 200 nm to 800 nm are shown.

This chapter is organized into four sections. Section 6.1 illustrates a rough overview of the design of the measurement and the components. This outlines the spectrometry procedures and design of the heat transfer apparatus, though the details have been discussed in Chapter 3. Section 6.2 is focused on the design and fabrication of the samples used in this work. This will cover the design of the spacers to develop a near-field vacuum gap, choice of materials, and procedure for fabrication of the samples.

Measurements validating the properties and fabrication will also be shown. Section 6.3 will detail the measurement procedure and show the results of this work. The results for each sample successfully measured will be shown, and the uncertainties of these results will be discussed. Finally 6.4 will emphasize the major contributions from this work, and will discuss future avenues for the continuation of this research.

6.1 Design Methodology

The design of this system consists of two parts: the experimental apparatus to measure heat transfer under high-vacuum, and the sample which creates controllable gap spacing, *d*. The sample consists of two 1 cm^2 doped-silicon pieces with a sparse array of SiO_2 nanopillars. These pillars are fabricated on one side of the sample and support the other piece, providing the necessary gap spacing. These pillars are made as thin as possible using ultraviolet photolithography, with as few as feasible to minimize the conduction heat transfer. Once fabricated, the gap spacing is verified using FTIR spectrometry to accurately determine the gap between the two pieces, and the sample is installed into the experimental apparatus. The flow of heat will be adjusted, and the temperature drop over the sample as well as the heat flux is measured, allowing the determination of the radiative heat flux and heat transfer coefficient.

The near-field heat transfer can be calculated using the formulation used in [13] with dyadic Green's functions to predict the spectral Poynting vector at varying depths, and the details have been shown in Section 2.1.3. It is important to note that the formulation used in Section 2.1.1 will not suffice here, as the assumption of semi-infinite media may not hold. Undoped silicon performs very well in semi-infinite cases, but the transparency in the mid-infrared (MIR) range leads to low heat rates with wafer thicknesses of 500 μm. Doped silicon (d-Si) can be opaque in the MIR if the doping concentration is high enough, and will be used in this work. To predict the heat transfer the system modeled will consist of 5 layers: semi-infinite vacuum, d-Si, vacuum, d-Si,

and semi-infinite vacuum. The SiO_2 nanopillar layer between the two d-Si pieces is so sparsely filled that it does not contribute to an effective medium dielectric function, and thus is not considered for the radiative heat transfer. Conduction heat transfer through the nanopillar array is still considered using a simple one-dimensional conduction model for each pillar. Here, the conduction heat rate can be found as $Q_c = N_P \kappa A_p \Delta T / d$ where N and A are the number and areas of the nanopillars each having thermal conductivity κ =1.4 W/m-K [102]. The diameter of the nanopillars is 1 μm and the spacing between pillars varies between 200 and 500 μm, such that the conduction contribution is minimized.

An ABB FTLA-2000 FTIR is used to measure the reflectance in the spectral range from 500 to 10000 cm^{-1}, as discussed in Section 3.1.2. Here, with a parallel air spacing between the two d-Si pieces, interference fringes present in the reflectance according to $\Delta\nu = (2nd)^{-1}$ where n = 1 for air and $\Delta\nu$ is the free spectral range [67]. Much of this range is obscured by the spectrally varying properties of d-Si [78], and must be carefully matched to the calculated reflectance using the multilayer matrix formulation [67]. It is here than an undesirable tradeoff in the material selection occurs: higher doping concentrations typically increase the radiative heat transfer, but make the d-Si less transparent in the higher-frequency regions measured by the FTIR, making determination of the gap spacing impossible. However, a doping concentration of 2×10^{18} cm^{-3} achieves near-maximal heat transfer, while leaving nearly half of the FTIR spectral range transparent. Details of the material selection will be discussed in Section 6.2.2.

A room temperature high-vacuum heat transfer experiment has been designed for the purpose of measuring these samples, as has been discussed in Section 3.2. Once the sample is installed into the heat transfer apparatus, a resistance heater above the sample adjusts the heat through the system. The total thermal resistance is measured by recording the temperature drop across the sample using thermocouples, and the heat flux is measured using a heat flux meter. From this, the contribution from conduction is

removed and the radiative heat transfer coefficient is found. It should be noted that high-vacuum conditions are necessary in this experiment as the conduction through air at nanoscale distances is significantly stronger than the radiative heat transfer. However, the low-pressure effective thermal conductivity in the free molecular regime decreases proportionally to the pressure [80], so measurements need to be under 0.1 Pa to effectively ignore gas conduction. All of the experiments presented here are operated at or below 3×10^{-4} Pa.

6.2 Sample Design and Fabrication

The main objective of this work is to experimentally demonstrate near-field radiation heat transfer at submicron distances with planar geometries. This is accomplished through the measurement of a sample designed to maximize near-field radiation between two silicon pieces while simultaneously minimizing conduction heat transfer. Additionally, this sample needs to be transparent in the mid-infrared to allow FTIR determination of the gap spacing for photon tunneling, and must have as much mechanical stability as possible. This section describes the methodology and design choices that went into achieving these goals, and shows the results of the fabrication.

6.2.1 Spacer Design

As described in Section 2.1, the strength of near-field photon tunneling can vary as strongly as with d^{-3} [56], where decreasing the distance d between two plates can significantly increase the radiation heat transfer. The medium of this gap is not restricted to vacuum, though experimental validation through any other medium is very challenging. While the strength of thermal radiation increases by orders of magnitude at gap spacings approaching the nanometer range, radiation is still a very weak form of heat transfer, and great care must be taken to minimize both conduction and convection heat transfer.

Should the near-field heat transfer take place in air under atmospheric pressure, the detection of radiation heat transfer would be impossible. Even if the contribution from solid conduction through the sample was removed, conduction through the air would greatly overpower the radiation. At length scales approaching 200 nm, there would be little if any convection currents in the air, and heat transfer would occur through conduction in the gas. The thermal conductivity of air at room temperature and pressure is approximately 0.025 W/m-K[102], and the heat transfer coefficient can be found $h = \kappa_{\text{air}} / d$, which gives 125 kW/m^2-K. The heat transfer coefficient that will arise from the near-field radiation will be less than 100 W/m^2-K, so a reduction of the gaseous conduction by a factor of at least 10^5 is necessary.

This is accomplished by running the experiment under vacuum conditions. Unfortunately, a perfect vacuum cannot be maintained, and some gas particles will exist in the gap and continue to conduct heat. However, the method of conduction changes from diffusion to ballistic conduction when the pressure drops. With a change in pressure, the total number of molecules of gas will decrease, and the mean free path will change accordingly. From this, the effective thermal conductivity of the gas within the gap can be predicted following treatment from Zhang [67]

$$\kappa_{\text{eff}} = \kappa_{\text{atm}} \left(1 + \text{Kn} \frac{2 - \alpha_T}{\alpha_T} \frac{9\gamma - 5}{\gamma + 1} \right)^{-1} \tag{6.1}$$

Here the effective thermal conductivity can be found as being proportional to the atmospheric thermal conductivity. Note that the variation in the gas temperature between the boundaries is neglected in this formulation. In this, the specific heat ratio γ is a constant 1.4 for air, and the thermal accommodation coefficient α_T is chosen to be 1. This value represents the temperature drop at the two solid-gas interfaces, and when this is set to unity, the heat transfer between the gas and each wall is perfect. While this is typically not unity, this will result in an overprediction of the heat transfer contribution

from the gas. The Knudsen number can be found as the ratio of the mean free path to the length scale $\mathrm{Kn}=\Lambda / d$.

When the pressure decreases, the number of moles of gas decreases and affects the mean free path. If the air behaves like an ideal gas, then the mean free path can be found from

$$\Lambda = \frac{k_B T}{\sqrt{2}\pi a^2 P} \tag{6.2}$$

where k_B is Boltzmann's constant, a is the diameter of a particle of gas, and P is the pressure. If the temperature remains constant, then the product ΛP is constant. Here we can use the mean free path at atmospheric pressure and to define Λ_0 as 67.0 nm at a pressure P_0 of 101.3 kPa [103]. Equation 6.1 can then be recast as

$$\kappa_{\mathrm{eff}} = \kappa_{\mathrm{atm}} \left(1 + \frac{\Lambda_0 P_0}{dP} \frac{9\gamma - 5}{\gamma + 1} \right)^{-1} \tag{6.3}$$

Here the thermal conductivity of air at any pressure can be found. More importantly, the heat transfer coefficient can be found and compared to the minimum value expected for near-field radiation.

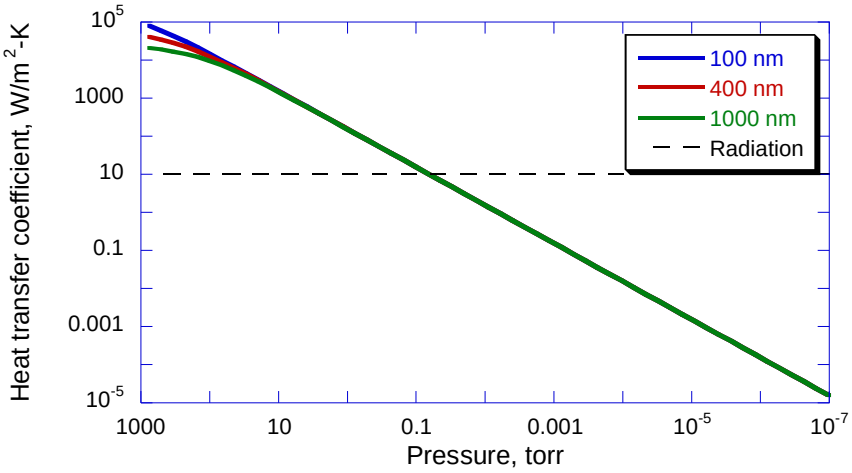

Figure 6.1. Heat transfer coefficient for gaseous conduction for different gap spacings at various vacuum pressures. The minimum radiation heat transfer coefficient is shown for comparison.

From Figure 6.1 it is clear that the conduction due to gasses can be neglected at even moderate vacuum levels. Since the size of the gap spacing is small, the Knudsen number becomes very large even when the pressure is not very low, and the size of the gap is not important. The minimum heat transfer coefficient expected for near-field radiation is conservatively 10 W/m^2-K, and the gas conduction contribution decreases below this threshold at around 600 mtorr (80 Pa). All of the measurements take place at pressures below 2×10^{-6} torr, so the maximum heat transfer coefficient will be 1.5×10^{-4} W/m^2-K.

It is possible to create a vacuum gap between heated plates with no solid medium between them by attaching one plate to a moving fixture. Ottens [64] demonstrated this by using a stepper motor to control the position of a sapphire plate. Conducted in vacuum, this technique should only have heat transfer from near-field radiation. Unfortunately, very small gap distances are difficult to reliably achieve with this technique. With a 1 cm wide piece to achieve 100 nm gap spacing, the angle of the piece cannot be off by more than 6×10^{-4} degrees, otherwise there would be contact between the top and bottom plates.

An alternative approach to creating a gap is to use solid support structures between the plates. Here the height of the support spacers determines the gap, so long as perfect contact can be maintained. Another important aspect of this technique is that the samples can be created and mated together in a clean environment. This is important for sub-micron gaps because a single particle of dust will make small gap spacings impossible. The typical size of a piece of dust is anywhere between 0.5 and 3 μm, with larger particles easily visible and removable. Certainly a single particle of dust between the plates will make a gap spacing of hundreds of nanometers impossible. Since the plates can be put together in a fume hood within a cleanroom, mitigation of this dust is possible.

This is especially important because dust can accumulate on a surface very rapidly. Indoor dust concentrations for PM2.5 (particulate matter smaller than 2.5 μm) vary by location and ventilation, but typically range between 10-40 $\mu g/m^3$ [104, 105]. The deposition velocity of particles of this size ranges between 5×10^{-5} m/s [106] to 2×10^{-4} m/s [107]. With an average particle mass density of 1 g/cm^3 [104] the flux of particle with an average size of 1 μm (assumed to be spherical) can be between 950 and 15000 $1/m^2$-s. Assuming that attempts are made to minimize dust, the lower range of this implies a piece of dust should land on a 1 cm^2 sample once every 10 seconds on average. Since the careful installation of a sample can take several minutes, an unprotected sample is not feasible. When samples are created inside a fume hood in a dust-free environment the likelihood of dust entering the gap is minimized. Once the samples are together the size constraints of the gap naturally prevent particulate matter from entering.

The design of a spacer pattern is a tradeoff between mechanical stability and minimization of thermal conductivity. Ideally a thin film would be employed and the mechanical stability would be ensured; however, much like the effect of gas conduction, the heat transfer coefficient from any solid layer would be orders of magnitude higher than the radiation heat transfer. Thus a sparse array of posts has been designed to provide support to the top plate while minimizing the thermal conductivity.

This begins with the choice of materials for the spacer. While certain polymers can have low thermal conductivities, the mechanical strengths are typically very poor. Furthermore, vacuum compatibility and ease of fabrication are important factors. An oxide is a natural choice, having good strength with relatively low thermal conductivities, and ultimately silicon dioxide was chosen because of the ease of fabrication on top of this. The thermal conductivity for bulk silicon dioxide is generally taken as 1.4 W/m-K [102], however for thin films of SiO_2 deposited with chemical vapor deposition (CVD), values between 1.5 and 1.3 W/m-K have been reported [108, 109]. In this work the value

of 1.4 W/m-K will be used, however uncertainties in the conduction heat transfer will be considered.

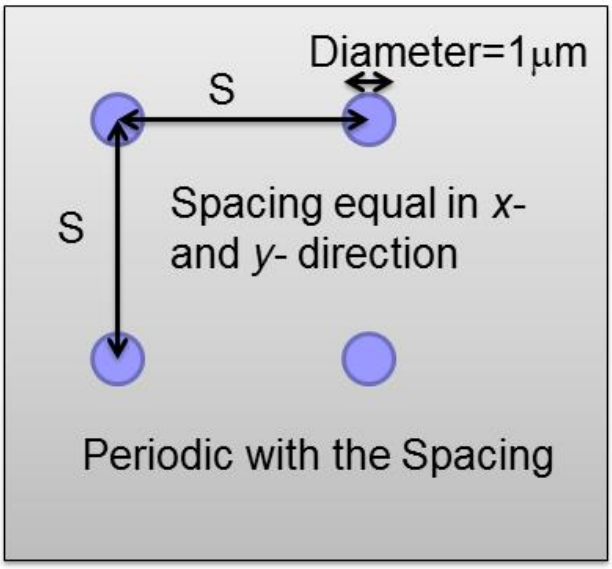

Figure 6.2. Layout of the sample pattern with SiO_2 posts shown in blue on a silicon substrate. The spacing *S* is demonstrated.

Figure 6.2 shows a layout of the pattern chosen. Here circular oxide spacers will be deposited on a substrate. The height of these posts can be controlled during the deposition process to control the gap spacing between the top and bottom plates. The diameter of the oxide posts is chosen to be 1 μm, as this is the smallest feature able to be easily fabricated using ultraviolet photolithography. The spacing between posts *S* is illustrated here. This number is chosen to be as large as possible with the post diameter as small as feasible to minimize the conduction while maintaining support. Electron-beam lithography was considered to control the size of posts down to the 100 nm, allowing the supports to be much more tightly arrayed, however this technique was not used because of the prohibitively high cost.

The spacing between posts was originally chosen to be between 10 μm and 1000 μm. Several wafers were patterned with these patterns, and images showing the 10 μm pattern will be presented later in this work. Unfortunately, much of this was not useful, as

it was determined that the mechanical stability for the 1 mm pattern was poor, and the contribution of conduction was too high in the smaller spacings. As such, the patterns made were changed to vary between 200 μm and 500 μm. There still exists a tradeoff between these values, so samples were created using multiple spacings. A photolithography mask was created that had patterns consisting of 200, 300, 400, and 500 μm spacings. Using this geometry, the conduction heat rate can be determined.

The heat rate due to conduction is calculated as simple one-dimensional conduction through a rod of length d. Since the thermal resistance associated with crossing the vacuum gap is so much larger than the lateral resistance in the silicon plates, the temperature is assumed to be completely uniform. Through this, the total conduction heat rate can be found from

$$Q_{\mathrm{c}} = N_{\mathrm{P}} \frac{\kappa A_{\mathrm{P}} \Delta T}{d} \tag{6.4}$$

where the conduction through each post is found from the thermal conductivity and cross sectional post area A_{P}. Since there is one full post in a unit cell of area S^2, so the number of these areas in the total sample gives the number of posts $N_{\mathrm{P}} = 1\mathrm{cm}^2 / S^2$.

Due to the extremely small size of these posts, is it reasonable to consider the potential of reduced effective thermal conductivity due to increased phonon-boundary scattering. The thermal conductivity in an insulator due to lattice vibrations can be found as from kinetic theory as [67]

$$\kappa = \frac{1}{3} C_v \nu_{\mathrm{a}} \Lambda_{\mathrm{ph}} \tag{6.5}$$

Here the volumetric specific heat C_v, propagation velocity of acoustic waves ν_{a}, and the phonon mean free path Λ_{ph} all contribute to the thermal conductivity. Matthiessen's rule

states that the mean free path may be reduced due to the increased phonon-boundary scattering seen with small structures.

$$\frac{1}{\Lambda_{ph,\,eff}} = \frac{1}{\Lambda_{ph}} + \frac{1}{\Lambda_{ph\text{-}b}} \tag{6.6}$$

The effective mean free path can then be used in Equation 6.5 to determine the reduced thermal conductivity. However, the phonon mean free path for silicon dioxide is only 9.7 nm [110]. The minimum boundary scattering mean free path can be interpreted as the smallest feature size of the posts. Using the smallest post height of 200 nm for this value, the effective mean free path changes to 9.3 nm, and the thermal conductivity could be reduced down to 1.34 W/m-K. However, this is a generous approximation of the size effect since only the height is considered. In this fashion, the effect from the post diameter is only a change in the thermal conductivity to 1.39 W/m-K. Furthermore, the scattering at the silicon-SiO_2 interface is not total, since the heat transfer requires some lattice energy pass this interface. As such, the effects of reduced thermal conductivity due to the size of the posts will not be explicitly considered, as the uncertainty for the thermal conductivity more than makes up for any potential changes.

The heat rate from conduction is shown below in Figure 6.3, shown as a percentage of near-field radiation to the total heat rate. Here, the conduction heat rate has been calculated and compared to the expected contribution from near-field thermal radiation. This has been calculated for doped-silicon using optical properties extracted from FTIR measurements to be discussed later. It can be seen that the 200 μm spacing is still fairly difficult to use at lower gap spacings, since roughly 70% of the heat rate is from conduction. This improves at larger gap spacings because of the hyperbolic nature of the conduction to the gap spacing. Near-field radiation increases with decreasing radiation; however, for light and medium doping levels, this effect is less pronounced due to the weaker effects from plasmonic resonance modes. The strength of radiation

eventually outpaces conduction at extremely small gap spacings, but this requires a gap spacing of at most 50 nm.

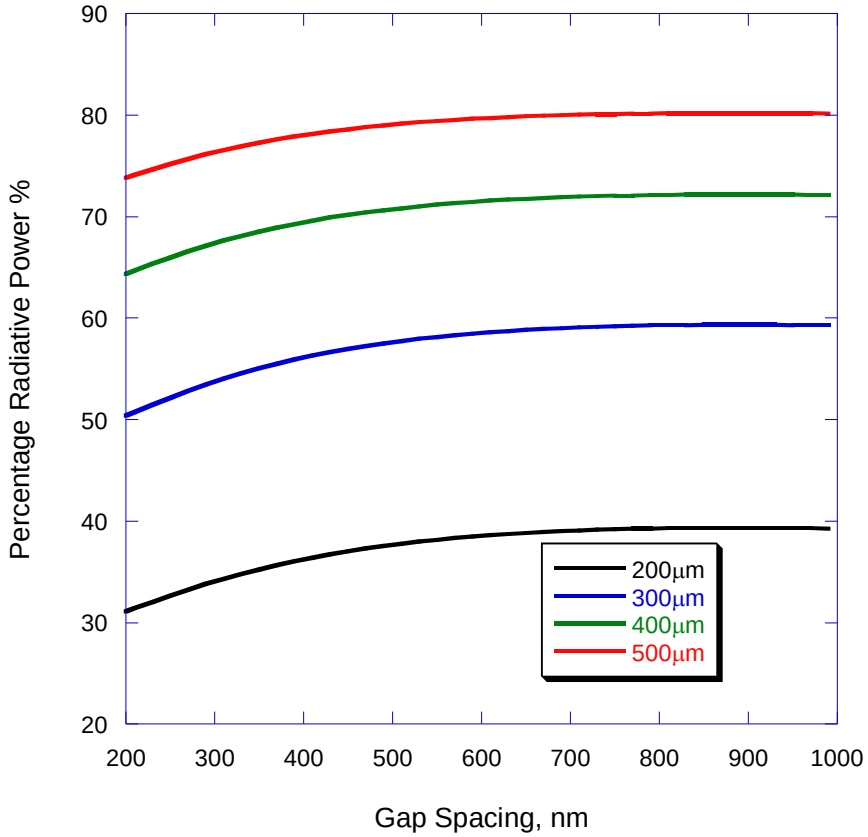

Figure 6.3. Percentage of radiation to total heat transfer in samples versus gap spacing. Results are shown for all four pattern spacings. The temperature drop used is 20K.

Thus, it is desired that only the very sparse patterns be used, especially for very low gap spacings. Unfortunately, the mechanical stability becomes a problem with such sparse supports. An immediate effect is that for the 500 μm spacing, roughly one part in 25000 of the area is supported. Thus, a very modest amount of force applied to the sample can be devastating to the posts. Furthermore, with so much of the silicon unsupported, deflection in the wafer may become a large problem.

To analyze these concerns, a finite-element simulation using COMSOL was created. Here, a single unit cell of the sample was created, with one-quarter of a post at each corner. The bottom surface of the bottom silicon plate was fixed, and the boundary

conditions on all of the exposed side faces was that there was no deflection in the normal direction, since the next unit cell face would be continuous on that face. A uniformly applied pressure was imposed on the top surface of the top silicon. This was calculated such that an applied weight in grams would be distributed over the entire structure, so the force on a single unit cell is proportionally less. Both the height of the posts and the spacing between the posts were varied, and the stresses and deflections in the silicon and the oxide posts were recorded. The thickness of the silicon plates was 500 μm. The elastic moduli for silicon and silicon dioxide were taken from the COMSOL reference library as 70 GPa and 131 GPa, respectively.

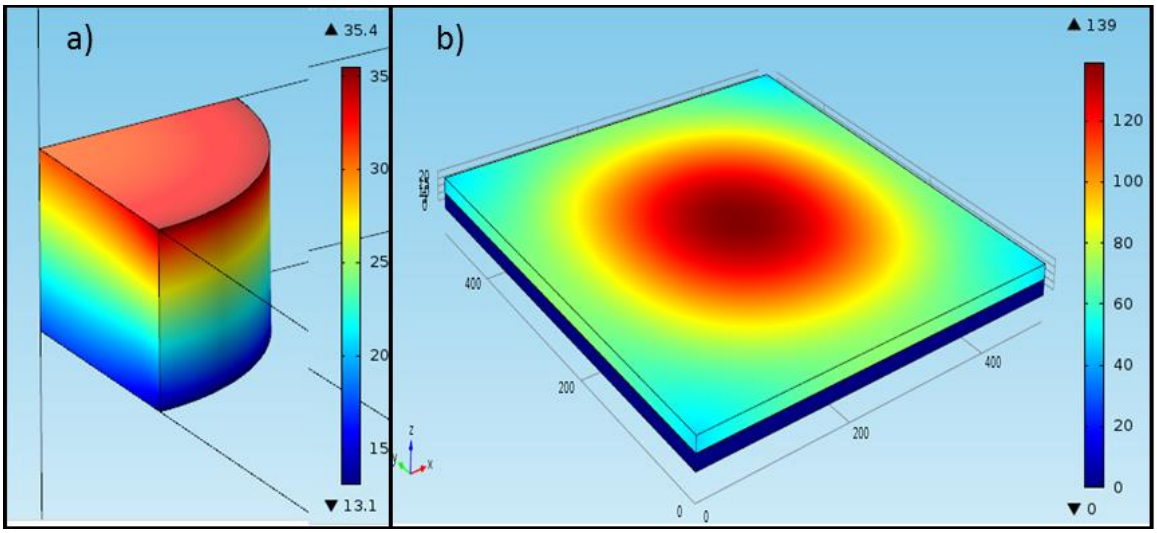

Figure 6.4. Finite element simulation of one unit cell of the silicon samples with 100 grams of load; a) deflection in the post, b) deflection in the silicon. The deflection is shown in nm. The sample geometry shown is a 500 μm spacing with 400 nm post height.

The salient results of this are shown in Figure 6.4 with the deflection in the post and silicon plates. This is for a post height of 400 nm and a spacing of 500 μm. A simulated weight of 100 grams is applied over the whole sample, though proportionally less is distributed over this single unit cell. As can be seen in Figure 6.4a, the deflection in the post is minimal. The bottom silicon plate compressed by nearly 15 nm in total, showing a total compression of about 20 nm in the post. This compression scales linearly

with the post height, so a maximum compression of 5% can be predicted, however this amount of load will not be reached in experiments. 100 grams is used here to reach the maximum compressive strength of the silicon dioxide posts. Unfortunately, the values for the maximum compressive strength of silicon dioxide vary. A 100 gram load shown here is able to create a maximum stress on the top edge of the post exceeding the maximum compressive strength of 8.4 GPa [111]. However, compressive strengths as low as 810 MPa have been reported as well [112], so loading this heavy should be avoided.

Figure 6.4b shows the deflection in the silicon pieces, and demonstrates a much larger deflection. It should be mentioned that the scale of the *z*-axis is altered to show the whole unit cell, and the piece is actually just as tall as it is wide. The maximum deflection in the center of the plate is approximately 80 nm. Regardless of the stress in the system, a deflection of 80 nm can be devastating to the gap spacing of 200 nm, so spacings larger than 500 μm cannot be used.

6.2.2 Choice of Materials

With the convection and conduction heat rates optimized, the near-field heat transfer must be maximized. This can be done by decreasing the gap spacing, as will be attempted, and also by carefully selecting the materials. An ideal candidate for near-field heat transfer has a very high refractive index at wavelengths near 10 μm where radiation is highest at room temperatures, or a material that has plasmonic resonance near this wavelength.

While this allows for a choice between a wide array of materials, a majority are disqualified because determination of the gap spacing from FTIR becomes difficult or impossible. Most metals have very high refractive indices in the mid-far infrared, and this allows for effective phonon tunneling, despite the fact that far-field emissivities are typically very low. This is because the wavevectors of propagating modes in the metal

can be very high, since a photon with a wavevector of up to $n^2 k_0$ is propagating within the medium. At the air or vacuum interface, only wavevectors up to k_0 can be propagating modes in the optically rarer medium, thus the amount of energy leaving the metal is low. In near-field radiation, those extra modes can tunnel across a small gap and the heat transfer can be very large. Unfortunately, metals are highly reflective with a low penetration depth, so almost none of the radiation incident on the sample from the FTIR would be able to reach the vacuum gap.

Polar materials are another potential candidate, as the impact of surface phonon polaritons (SPhP) can enhance near-field heat transfer in materials like silicon carbide [113]. In this, the effects of a strong Lorentz oscillator due to a phonon can create strong evanescent waves at the surface of a material, and these waves are able to tunnel across a small gap. A similar phenomenon occurs in metals with surface plasmon polaritons; however, this resonance typically occurs at much shorter wavelengths. Unfortunately, while polar materials they can be transparent in the spectral range of the FTIR, the reflectivity is usually low. This will be shown later for silicon dioxide, and the differences between the reflectance signals are too small to reliably distinguish.

Semiconductors represent a good balance between these two classes. Many materials are transparent in the near-mid IR while having a higher refractive index than insulators, giving higher near-field heat transfer rates. Furthermore, microfabrication is typically done on semiconductor substrates, so the compatibility of fabrication and availability of materials is also a boon. Furthermore, these materials can be doped to include extra free charges, giving some metallic behavior and increasing the radiation heat rate.

Silicon is a natural choice for this application. Not only is this material readily available, the refractive index allows for excellent FTIR determination. Silicon is transparent over a large range from approximately 1000 cm-1 to 9000 cm-1, giving a

large window for gap spacing determination. Furthermore, the near field heat rate can be good as seen below in Figure 6.5.

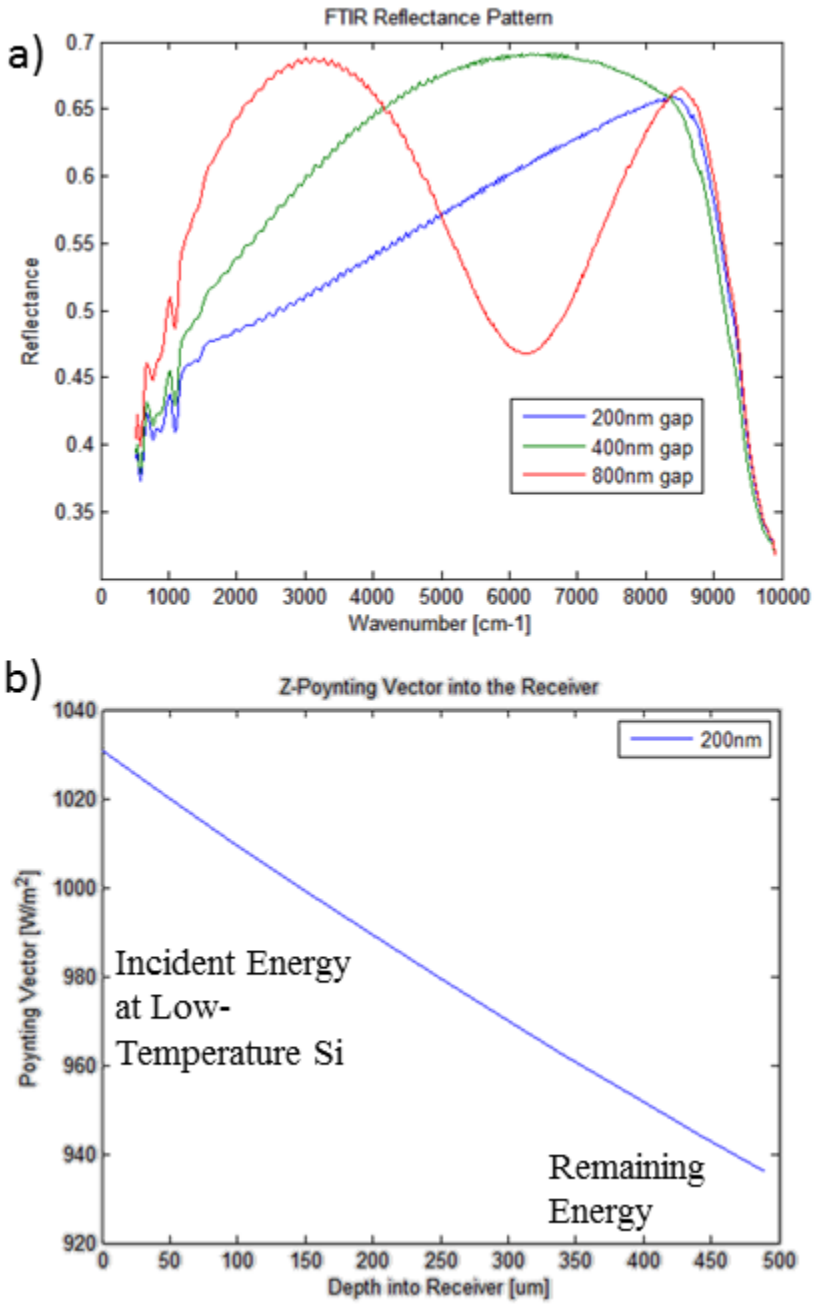

Figure 6.5. Performance of silicon as a sample material. a) FTIR simulations at various gap spacings, b) radiative heat flux into the low-temperature Si plate.

Contrast and spectral range available for FTIR determination seen in Figure 6.5a is very good, and clear distinctions can be seen between the simulations for different gap

spacings. Unfortunately, there is a problem as seen in Figure 6.5b. This is a simulation of the energy flux into the low-temperature silicon plate with a gap distance of 200 nm and a temperature difference of 20K. This formulation is for a two semi-infinite silicon plates, however the FIR absorptance is too low to be able to use the maximum performance. It is for this reason that the near-field heat rate must be calculated using the formulation in Section 2.1.3 instead of the considerably simpler formulation in Section 2.1.1. Here, the energy flux into the low-temperature silicon piece can be calculated at different depths into the material, and it is clear that a typical thickness of 500 μm is insufficient. Using undoped silicon, the transparency in the far-infrared where heat transfer occurs is too high, and none of the energy is properly absorbed. In fact, for this same reason, a vast amount of this energy is never even emitted when the high-temperature plate is a reasonable thickness, and the total heat transfer is only 100 W/m^2, leading to a heat transfer coefficient of only 5 W/m^2-K. Because a heat transfer coefficient near 100 W/m^2-K is desired at this small gap spacing, undoped silicon is not considered as the sample material.

This result clarifies the optimal parameters that the material should have: transparent below 10 μm for FTIR analysis and highly absorbing above 10 μm for heat transfer. Silicon dioxide is a good candidate for this, as it is transparent up to about 8 μm, and opaque at longer wavelengths due to phonon absorption. The FTIR comparisons and depth-resolved heat rates are shown in Figure 6.6. Here the heat rate through the sample in Figure 6.6b is much improved. Nearly all of the radiation is absorbed within the first 50 μm of material, and the overall energy rate is higher than any other material considered. Figure 6.6b shows the FTIR performance, and it should be noted that the discontinuity near 1000 cm-1 represents a SPhP where the reflectance should be close to unity. However, simulation of the reflectance at this pole requires special treatment and it is not important in this context.

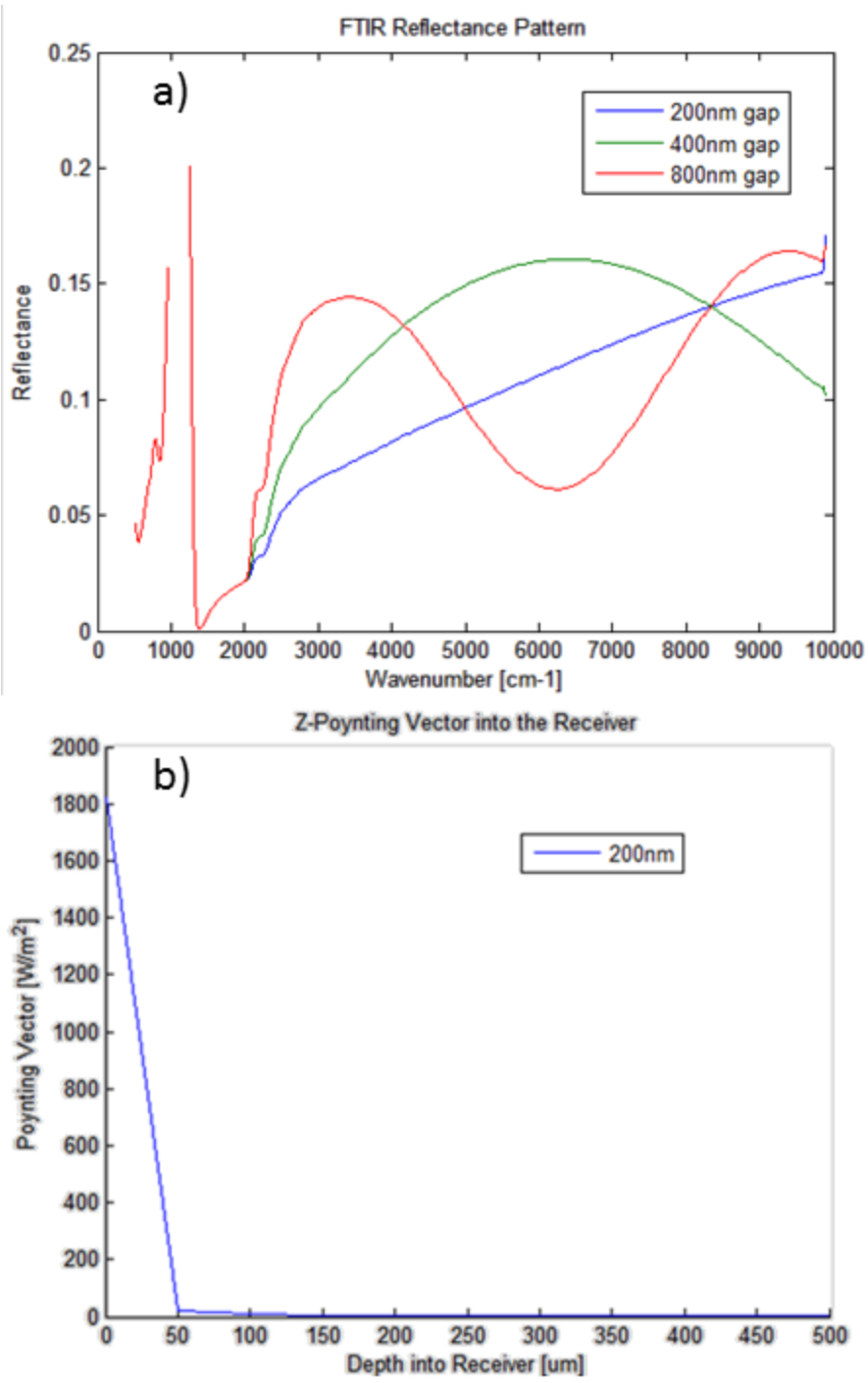

Figure 6.6. Performance of silicon dioxide as a sample material. a) FTIR simulations at various gap spacings, b) radiative heat flux into the low-temperature SiO_2 plate.

While Figure 6.6b appears to give adequate distinctions between the different vacuum gaps, the overall magnitudes of the reflectances are low. While these curves are

easily distinguishable, it is much harder to determine between differences of 20-40 nm as the peak locations do not vary significantly, and the value of the reflectance only changes by less than 0.01. Unfortunately, this renders silicon dioxide unusable for this experiment. While not shown here, silicon carbide is not considered for the same reason. There are methods to improve this, however, since the problem is only that the vacuum-SiO_2 interface has a low reflectance. A thin film of poly-silicon approximately 30 nm thick on the faces of each oxide piece can increase the FTIR contrast to values similar to Figure 6.5a, however the heat rate decreases by more than half.

Doped silicon is considered for the material, as implantation of low concentrations of elements that have a different valence number than silicon will cause an extra electron or hole to be freely conducting in the lattice. This increases the overall absorption, but just like the Drude model for free electrons seen in Chapter 5, the far-infrared absorption is affected more strongly than the shorter wavelengths. With the right amount of doping, the properties can be tuned such that the sample is opaque to thermal radiation while still maintaining a large transparent window in the near-mid IR range.

The results of Basu [78] are employed to model the complex dielectric function for doped silicon (d-Si) at room temperature. N-type dopants are chosen for this application, though p-type dopants behave very similarly. The doping element is irrelevant at the low concentrations used in this study, as only contributions from the free carriers are important. The presence of interstitial atoms in the silicon lattice does not have a significant effect on the optical or mechanical properties at such low volume concentrations. The thermal conductivity of the silicon may change with doping; however, the thermal resistance associated with heat transfer over the vacuum gap is orders of magnitude higher than thermal resistance in the silicon, so the effects will be unimportant.

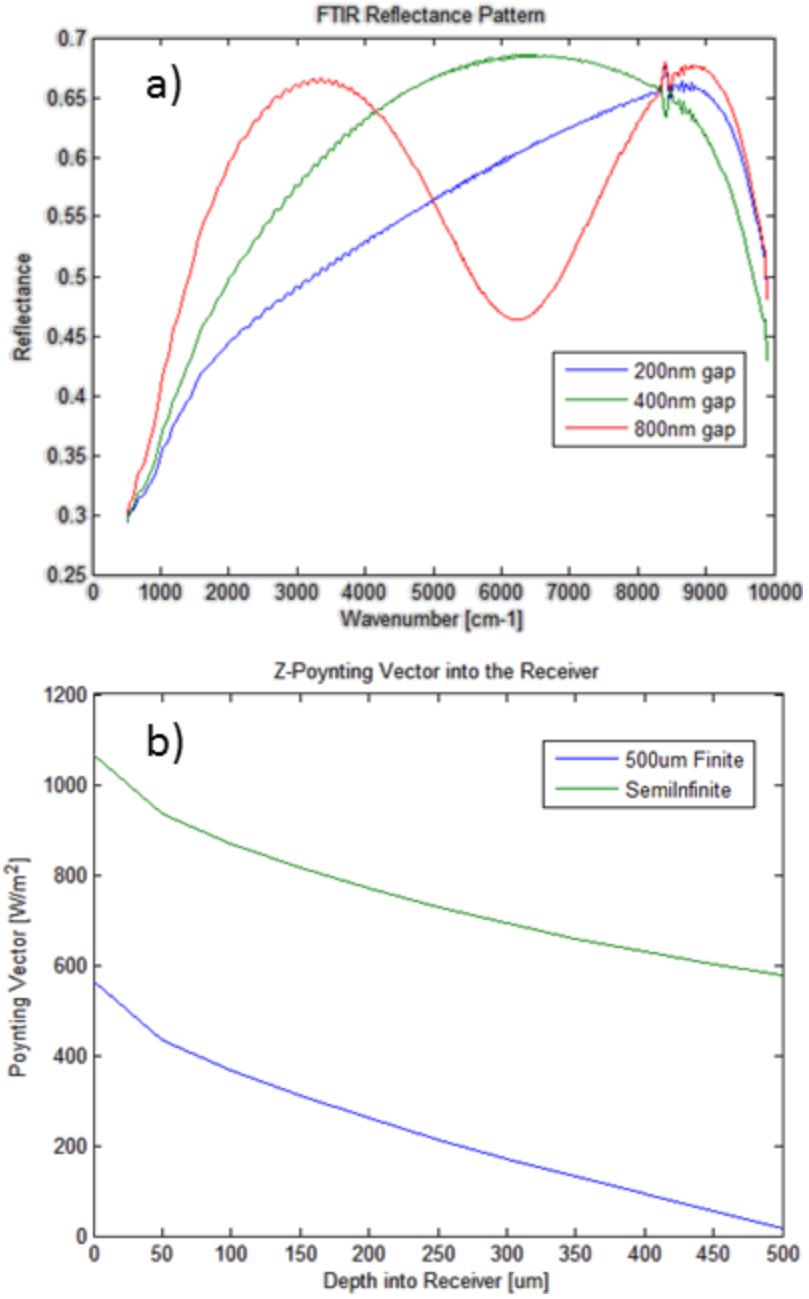

Figure 6.7. Performance of doped silicon at a doping concentration of 10^{17} cm^{-3} as a sample material. a) FTIR simulations at various gap spacings, b) radiative heat flux into the low-temperature d-Si plate compared with a semi-infinite thickness.

Light doping concentrations are considered first, as there will quickly be a tradeoff between being opaque enough for radiation heat transfer and too opaque for FTIR analysis. Figure 6.7 shows the FTIR spectra and the heat flux at a doping concentration of 10^{17} cm^{-3}, which is a very light doping. Figure 6.7a shows a slight

difference as compared to Figure 6.5a for undoped silicon. Here the phonon absorption below 1300 cm^{-1} is slightly suppressed, while the remainder of the spectrum is unchanged. Unfortunately, Figure 6.7b shows that the doping is not high enough for a 500 μm thick plate to be opaque. Two cases are shown here, the semi-infinite case where the doped silicon is infinitely thick on either side of the vacuum gap, and a finite case which models each plate as being 500 μm thick with a semi-infinite air layer at the ends. It can be seen here that the plate is only 50% as absorbing as required to be opaque.

When the doping concentration is increased, the sample becomes more opaque in both the FIR and MIR. This is shown in Figure 6.8 with a doping concentration of 10^{18} cm^{-3}, which is still a fairly low doping concentration. Here the transparent window for FTIR is visibly reduced in Figure 6.8a as the reflectances below 5000 cm^{-1} are significantly damped. In fact, the sample is completely opaque at 1000 cm^{-1} where the reflectances for all gap spacings converge. This is because the incident light either does not transmit to the vacuum gap, or is absorbed in the silicon after the reflection at this interface. Figure 6.8b shows that the opacity in the thermal wavelengths is very close to the maximum performance, as the curves for 500 μm thick plates and semi-infinite plates only have slight disagreements at the end of the plate. As this is just at the limit of being opaque enough for thermal radiation, this doping concentration is optimal for the purposes of this experiment.

It is interesting to compare Figure 6.8b with the semi-infinite calculation in Figure 6.7b. Here the maximum heat rate into the sample is slightly increased at a higher doping concentration. Therefore it is worthwhile to compare higher doping levels to see if an increased heat rate can be found while not impeding the FTIR analysis significantly more than is seen at a concentration of 10^{18} cm^{-3}.

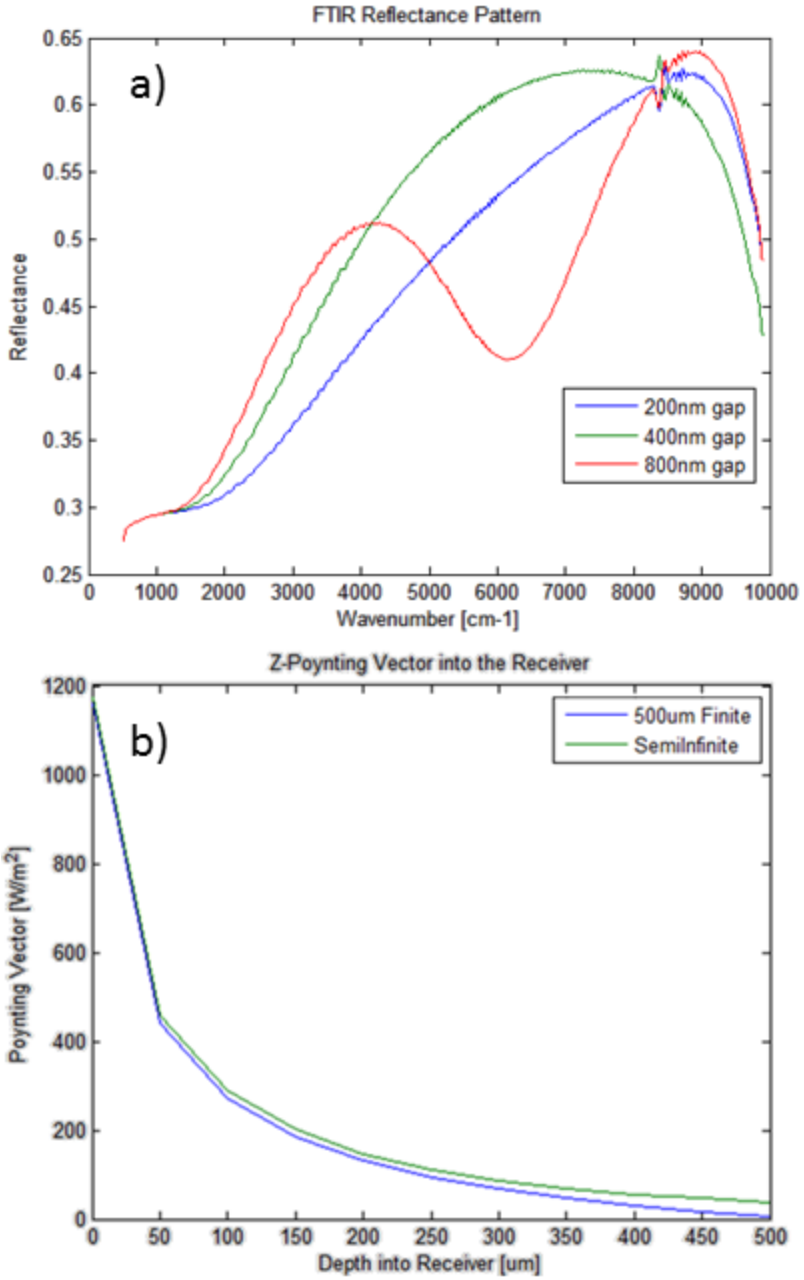

Figure 6.8. Performance of doped silicon at a doping concentration of 10^{18} cm^{-3} as a sample material. a) FTIR simulations at various gap spacings, b) radiative heat flux into the low-temperature d-Si plate compared with a semi-infinite thickness.

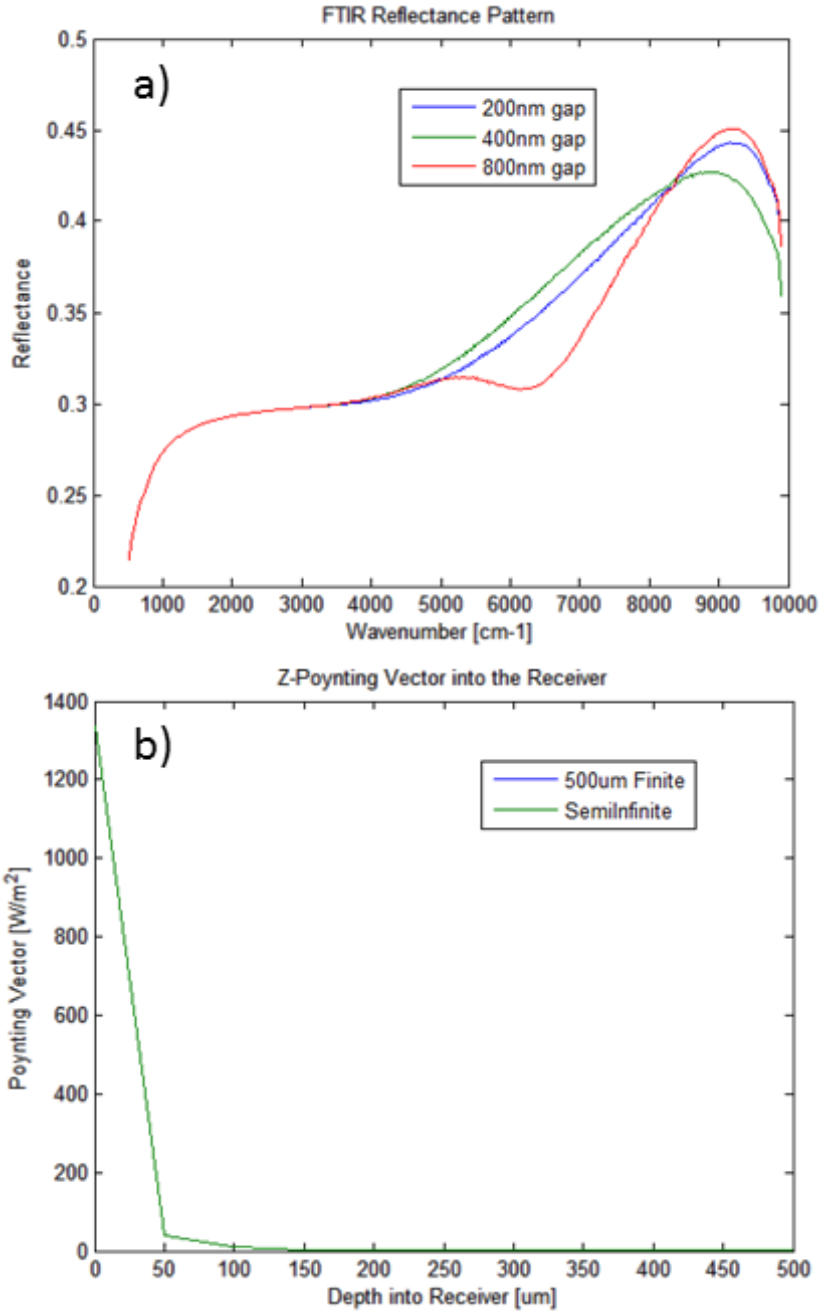

Figure 6.9. Performance of doped silicon at a doping concentration of 5×10^{18} cm^{-3} as a sample material. a) FTIR simulations at various gap spacings, b) radiative heat flux into the low-temperature d-Si plate compared with a semi-infinite thickness.

Figure 6.9 shows the performance for a doping concentration of 5×10^{18} cm^{-3}. While Figure 6.9b shows a slightly increased maximum heat rate, and the comparison between the finite thickness and semi-infinite plates shows that this is completely opaque

in the thermal radiation wavelengths, the transparency seen in Figure 6.9a is unacceptable. Here the interference patterns caused by multiple reflections in the vacuum gap are completely suppressed below 5000 cm^{-1}, reducing the available spectral range by half. As the gain in heat rate is only slight, this is determined to be too high of a concentration to use.

With this, wafers were purchased to be close to the concentration of 10^{18} cm^{-3} n-type dopant concentration. Because the sample require that the doping level be constant throughout the thickness, using ion implantation to precisely control the doping level on undoped wafers was impossible, as it is difficult to dope the wafer deeper than a few dozen microns. Furthermore, wafers were desired to be as flat as possible, with relatively little bow or warp, as will be discussed later. With this, wafers were purchased to have a resistivity between 0.012 Ω-cm and 0.027 Ω-cm with antimony as the n-type dopant. This corresponds to a doping concentration between 7×10^{17} to 3×10^{18} cm^{-3} [114]. A Signatone four point probe measurement system was used to measure the resistivity of the wafers, and the resistivity was found to be 0.016 Ω-cm averaged over four of the wafers. This gives a doping concentration of 2×10^{18}, which has an acceptable transparency window in the near-mid IR range while being completely opaque in the far IR.

Unfortunately, the predicted optical properties were unable to predict the transmittance and reflectance measured by the FTIR. All 25 wafers were measured between 500 cm^{-1} and 10000 cm^{-1} for both transmittance and reflectance on an ABB FTLA-2000 FTIR. Three measurements of the reflectance using a 10° reflectance accessory and two measurements of the transmittance were measured for each wafer, flipping the direction of the wafer in between measurements. Dry nitrogen was used to purge the chamber to remove gaseous absorption in the measurement. Each measurement had a resolution of 8 cm^{-1} and used 64 scans. The results for each wafer were very

similar, so an average of all of the measurements was used. The results are shown below in Figure 6.10 with a calculation from the optical properties for 2×10^{18} n-type silicon [78].

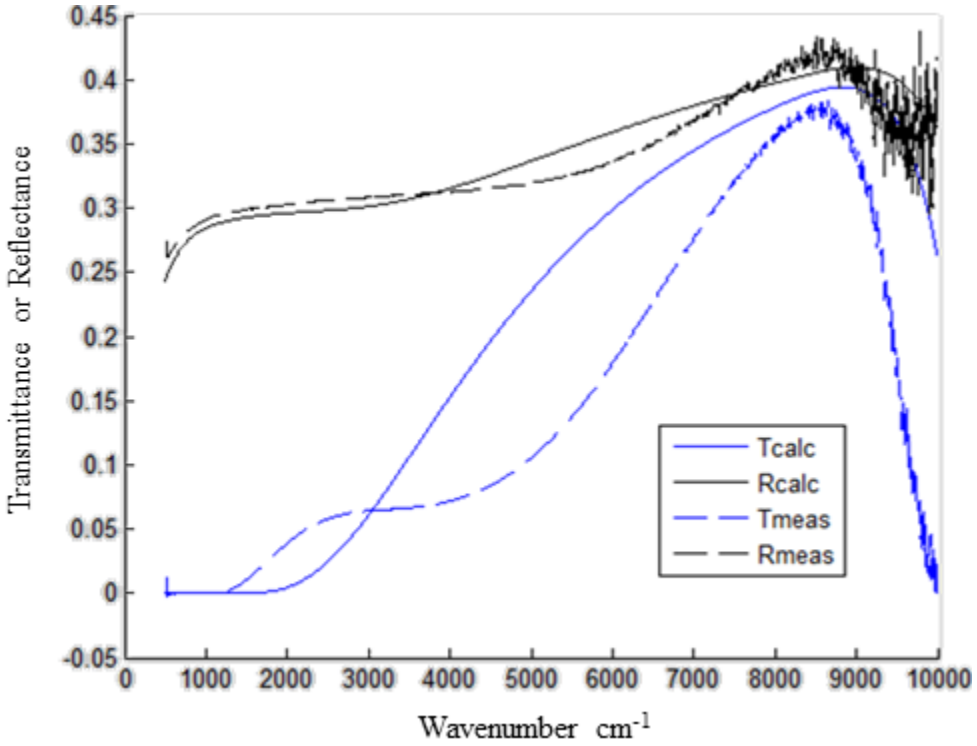

Figure 6.10. Measurement and prediction for the reflectance and transmittance for doped silicon wafers. Transmittance is shown in blue while reflectance is shown in black, and the measurements are shown using dashed lines.

Here a significant discrepancy can be seen in both the transmittance and reflectance spectra. Especially in the mid-IR the properties are completely unexplained. The shape of the transmittance measurement suggests that there is some absorption phenomenon that exists near 5000 cm^{-1}; however none of the literature suggests this. This could be because of impurities or defects in the lattice, though the properties should resemble undoped silicon with free carrier absorption increasing at lower wavenumbers.

As the optical properties are critical for predicting the vacuum gap spacing and the near-field heat rate, the refractive index was found for these wafers. Lessons learned from the optical property extraction in Chapter 5 were useful for this task. First a Drude

model was used to match the measurement spectra. The optical properties of undoped crystalline silicon from Palik [37] were used as a baseline, and a Drude model for free carrier absorption was added to this. The plasma frequency and scattering rate were adjusted, and results similar to Figure 6.10 were seen. Despite the parameters used, the drop in transmittance and reflectance near 5000 cm^{-1} could not be simulated; however the near-infrared transmittance was more closely matched between 9000 and 10000 cm^{-1}. This is not due to the Drude term, but results from more accurate silicon properties at shorter wavelengths than were considered in [78]. A Lorentz oscillator mode was added to this model to account for this. Along with the Drude terms, the resonance frequency, plasma frequency, and scattering rate of a single Lorentz oscillator were allowed to vary to match the measured spectra. No satisfying results were found, and are not presented here.

While an extra absorption mode can cause the transmittance to decrease in a certain range, the reflectance typically increases. Since the reflectance does not increase, and the transmittance depression causes a shoulder rather than a dip, it is believed that defects are the cause for this. This can be either impurities, dislocations, or voids in the lattice causing scattering in the volume of silicon. Attempts were made to test the stability of this with pressure and heat. Wafers were exposed to vacuum for roughly 10 hours and no change in the transmittance or reflectance was seen. A wafer was annealed at 950°C for two hours at atmospheric pressure and no change was measured. The same wafer was annealed again for four hours at 1100°C at atmospheric pressure, and an oxide layer formed on both surfaces. This caused the reflectance and transmittance to change, but the peculiar features in Figure 6.10 were unaffected.

With no useful dispersion model to aid in the property extraction, the refractive index and extinction coefficient, i.e. the real and imaginary components of the complex refractive index, were fit at each point. The thickness was measured using a micrometer,

and this value was fixed. Several guesses were made at each frequency, and the values of the reflectance and transmittance were found for each value of the complex refractive index. A value immediately above and immediately below this were calculated, and the value that corresponded to the lowest RMS error between measurement and prediction was chosen. This was repeated until no change was found. Multiple starting values were chosen to reduce the possibility of finding a local optimization rather than a global optimization. This process continued for all measured frequencies.

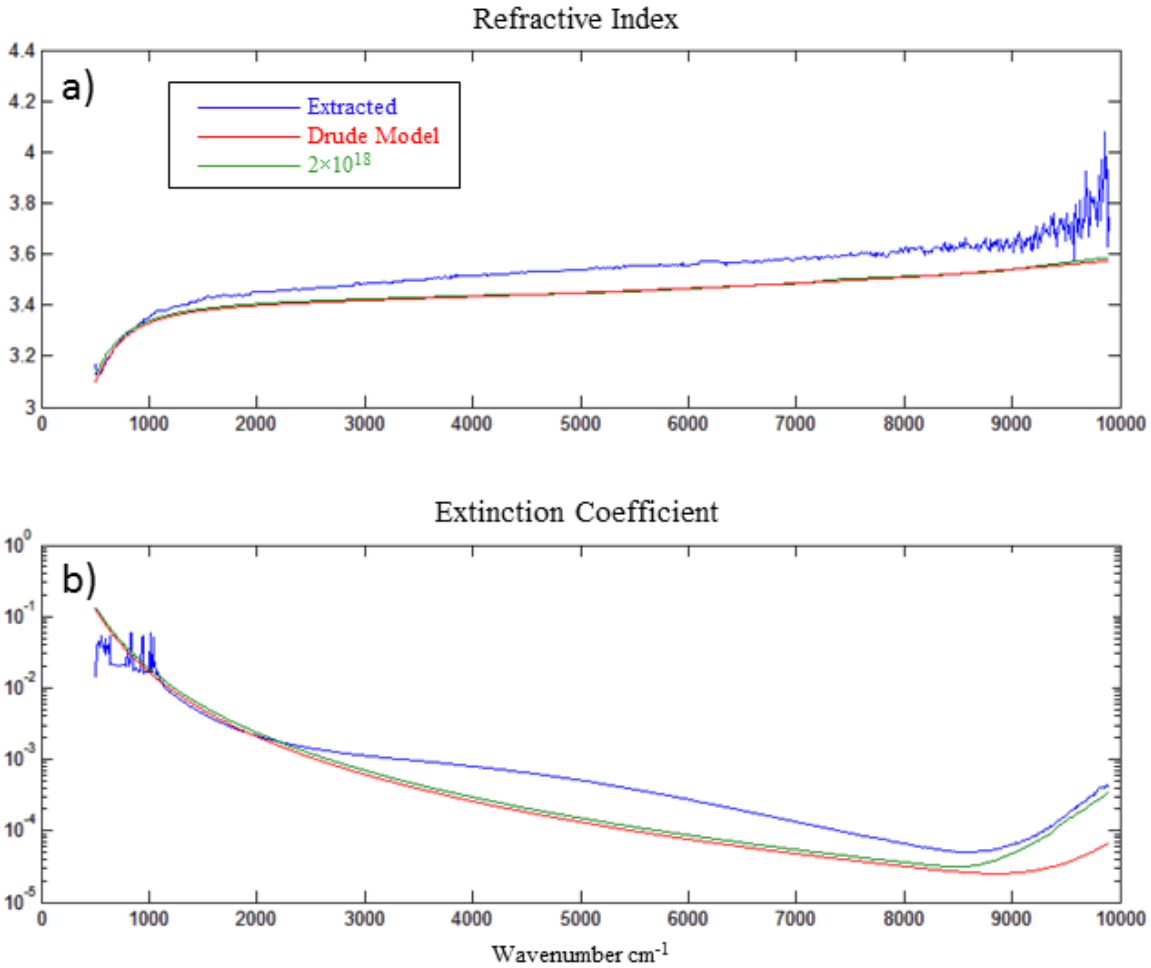

Figure 6.11. a) refractive index and b) extinction coefficient extracted for the doped silicon wafers. Shown are the values extracted using a point-by-point algorithm, as well as the predicted optical constants from Palik with an added Drude model, and from Basu at a doping level of 2×10^{18} cm^{-3}.

The results of this fitting are shown in Figure 6.11 along with the predictions discussed earlier. Though not shown, the extracted optical constants match the measurements almost exactly, while still maintaining a smooth curve through most of the spectral range. Only at the far ends of the spectrum are there problems with the continuity of the refractive index. This is due to noise in the measurement at the high wavenumber end and the opacity of the sample at the low wavenumber end. With a completely opaque sample, the transmittance becomes zero and the modelling of the extinction coefficient becomes very difficult.

It is clear that any single method shown in Figure 6.11 is insufficient to use in this work. The extracted optical constants are too imprecise to use in the near IR and do not extend past 10 μm. In order to model the heat rate, the optical properties must be known to at least 30 μm. However, the extracted optical constants represent the only way to model the mid-IR behavior for FTIR analysis. As such, the extracted constants were smoothed in the NIR and combined with the doped silicon predicted constants below 1000 cm^{-1}.

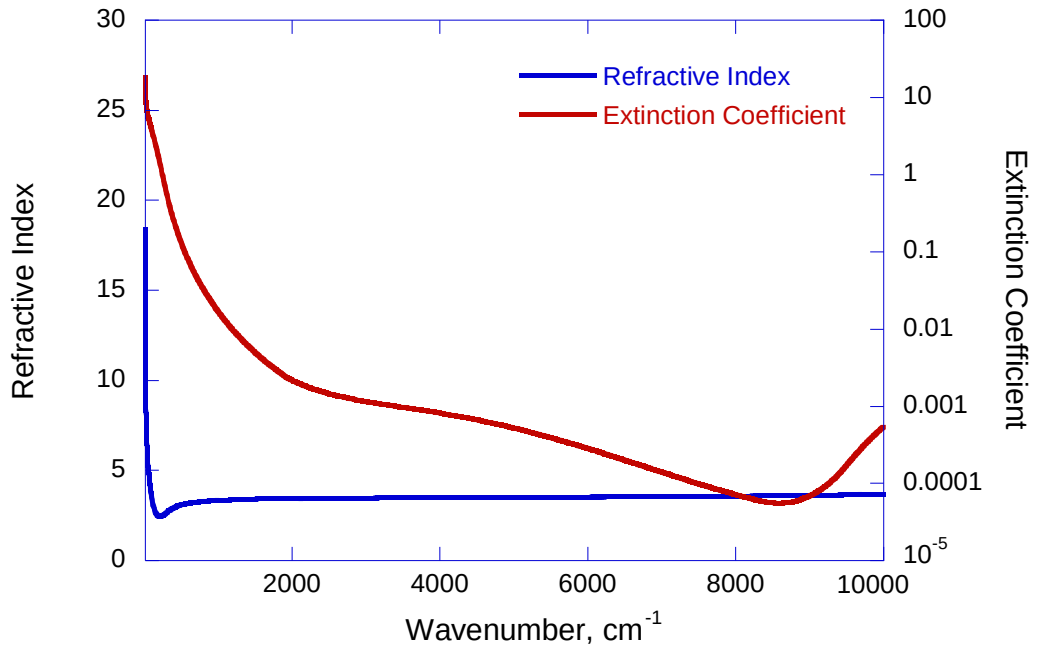

Figure 6.12. Refractive index and extinction coefficient shown between 100 cm^{-1} and 10000 cm^{-1} (1-100 μm)

As seen in Figure 6.12 the complex refractive index for the doped silicon wafers is shown to be continuous between 1 to 100 μm. The low wavenumber values were combined with the theoretical predictions at a value where there was crossover. The two curves were very close between 1500 cm-1 and 510 cm-1 where the measurements end, and below approximately 610 cm-1 where the theoretical curve and the extracted data overlapped, the theoretical curve was used. The high wavenumber optical properties did not match either the data from Palik or Basu well, so only the extracted data was smoothed in this range. This was done manually to remove the noise in the data shown in Figure 6.11. With this data, the radiative heat rates can be calculated. This is shown below in Figure 6.13, and also earlier in Figure 6.3 as a percentage of the total heat rate for all of the spacer patterns.

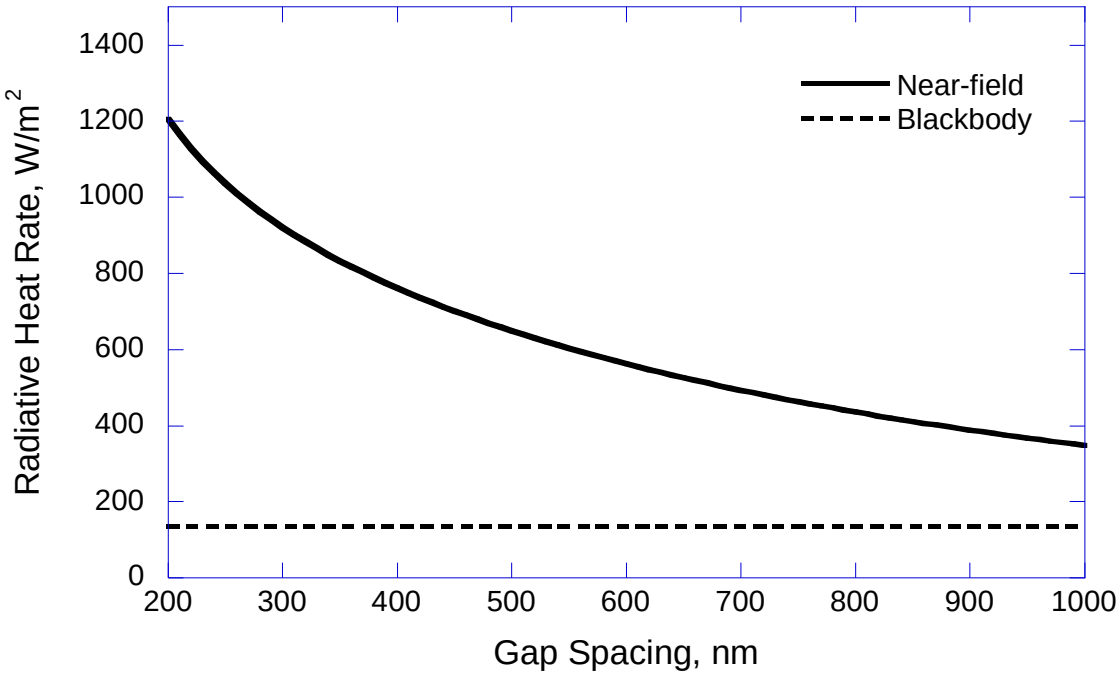

Figure 6.13. Radiative heat flux using doped silicon as a function of gap spacing. Calculations are done at a temperature difference of 20°C. The heat flux for blackbody radiation is also shown.

Here the heat flux is shown at a 20°C temperature difference, with the low temperature being 25°C. Blackbody radiation is also shown in this figure to show the improvement seen with this material. For a gap spacing of 500 nm, the improvement over blackbody is nearly 400%, with an increase of 800% at 200 nm. While this is just as expected from the earlier calculations of doped silicon at a doping concentration of 10^{18} cm^{-3} as was seen in Figure 6.8, the extra absorption in the MIR range decreases the usefulness of FTIR analysis.

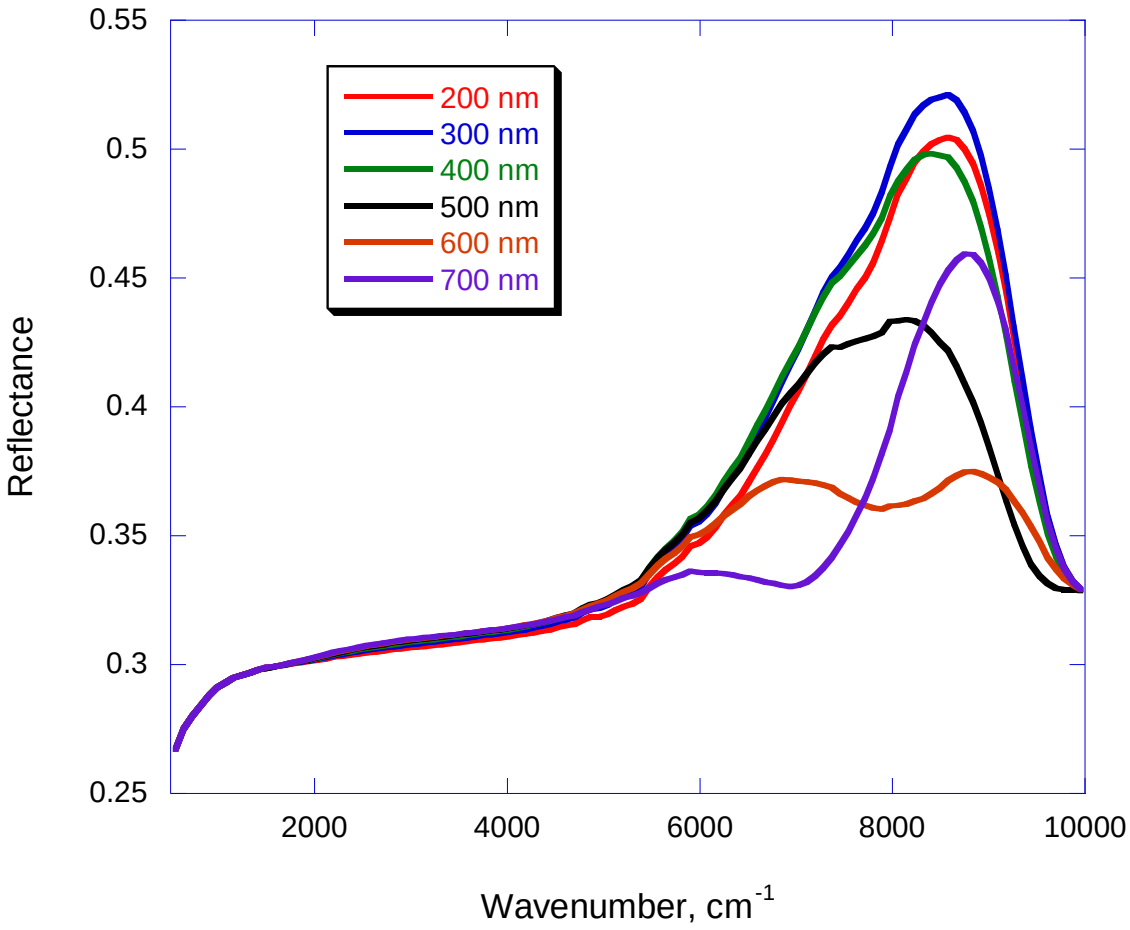

Figure 6.14. Calculation of the infrared reflectance of samples with different gap spacings shown in the range of FTIR measurements.

Figure 6.14 shows the computed spectra for gap spacings ranging from 200 nm to 700 nm. With this doping concentration, the sample should have exhibited a transparency window down to about 2000 cm-1, however reflectances lower than 5000 cm-1 are nearly opaque. This makes accurate distinction of the gap spacing a little more difficult, however it is still very manageable. Only for certain gap spacings are the curves difficult to distinguish, as the differences between the 500 nm, 600 nm, and 700 nm curves are easily identifiable. For this reason gap spacings larger than 700 nm were not shown in Figure 6.14. Lower gap spacings have less differences between curves, however it is still possible. Unfortunately, this will increase the uncertainty in the determination of the gap

spacing. As such, the error in the measured vacuum gap will be determined for each sample depending on how clearly identifiable the spectrum is.

6.2.3 Sample Fabrication and Characterization

Samples are created using ultraviolet photolithography to transfer the designed patterns into a plasma-enhanced chemical vapor deposition (PECVD) silicon dioxide layer. The thickness of this layer determines the gap spacing. The pattern is transferred over an entire 100 mm diameter wafer, then is diced into 1 cm^2 square pieces. One patterned piece and one bare piece are then cleaned and mated together in a fume hood. When everything works right, the Van der Waal's forces at the silicon-SiO2 interface are enough to hold the sample together and maintain the desired gap spacing through the FTIR measurements and near-field measurements.

6.2.3.1 Control of the wafer bowing

Before the samples are made, great care must go in to choosing the correct wafer. All of the wafers were measured for the optical properties, and there are no differences between any of the wafers. However, bowing throughout the wafer can be potentially disastrous. A typical wafer will have between 10-20 μm of total deflection between the center and the outside edge of a 4" silicon wafer. The profile is typically parabolic, and if a 1 cm long piece is cut from this wafer without reducing the bow, this piece can have a deflection between the edge and center of up to 150 nm. This can be seen below in Figure 6.15. Here the profile of the top and bottom of a silicon wafer were measured using a laser profilometer to show deflection. In Figure 6.15b this bow is enlarged and only 1 cm long segments are shown and recentered about their midpoint. This shows that deflections of up to 200 nm over a near-field sample are possible. It should be noted that Figure 6.15b is not a measurement of a diced sample.

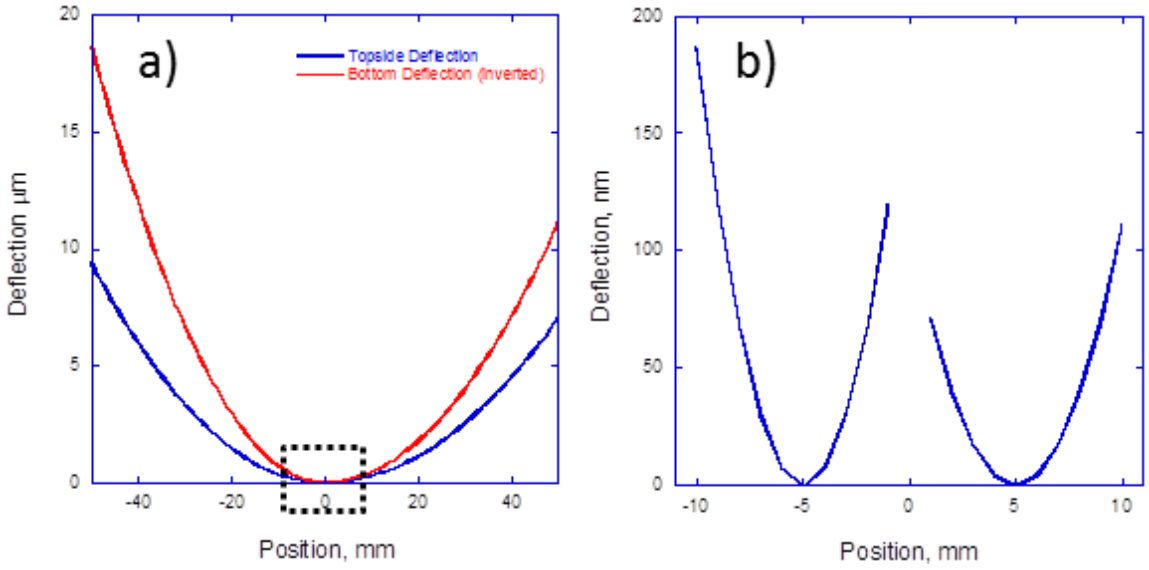

Figure 6.15. Bowing from a typical silicon wafer. a) measurement of the surface deflection of a 100 mm wafer. The bottom measurement is inverted for comparison. Boxed region is shown in b) where two 1 cm pieces detached and recentered to show individual bowing.

Wafers with low bowing or warping were purchased, however, tight specifications on this parameter are difficult. Not to be confused with the total thickness variation (TTV), the amount of surface deflection arises from intrinsic stresses within the crystal lattice of the silicon, and is only known once the wafer is cut to thickness. As such, great care needs to be taken before a wafer can be used in fabrication. All of the wafers purchased were measured for bowing. Here a Bowoptic 208 Stress measurement system is used to measure the surface profile of the top and bottom of each wafer. From this, a set of exceptionally low-bow wafers was chosen.

The surface profile measurement gives the radius of curvature, r, which can be used to find the bow from a 1 cm wide piece of diced silicon. Here the entire wafer is assumed to have an average circular curvature. From this a chord of length w is assumed to fit on this arc and the maximum distance between the chord and the arc can be found using the formula for the sagitta,

$$b = r - \sqrt{r^2 - \left(\frac{w}{2}\right)^2} \tag{6.7}$$

Using this formula, a curvature of 500 m results in a 25 nm maximum bow. This is shown below in Figure 6.16. Here the surfaces profiles on the top and bottom are shown for a wafer that has a radius of curvature of 900 m on the top surface and -90 m on the bottom. The negative curvature denotes that the surface is concave. Here the distance between the two surfaces does not correspond to the thickness of the wafer, and an arbitrary offset is chosen for comparison. Each surface was measured over at least three different directions to show the surface profile over the whole wafer. Note the cusp that appears at 40 mm, which is due to the stitching of multiple sections of the scan.

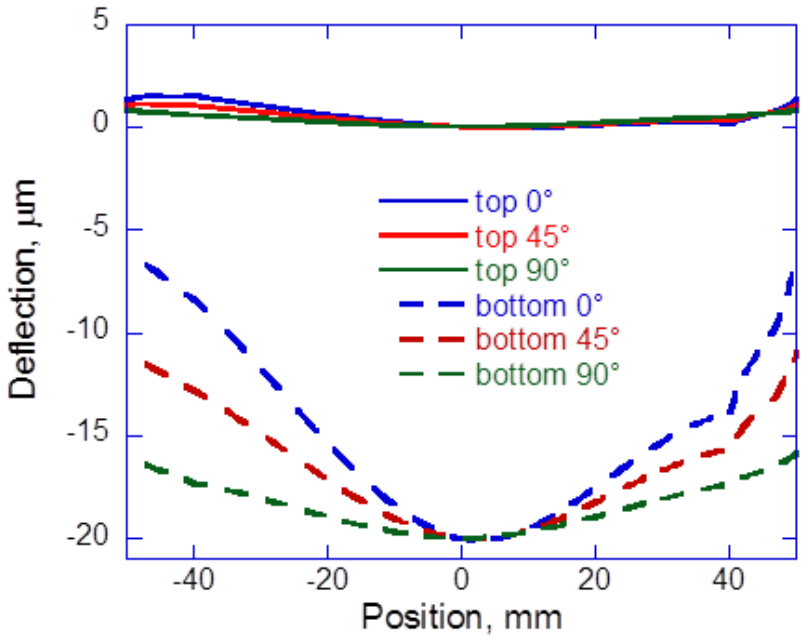

Figure 6.16. Deflection over a 100 mm wafer. Top and bottom surface profiles are shown at three angles each.

Here the top surface of Figure 6.16 could be used for fabrication, however it will not be presented in this work. As can be seen, this surface has a maximum deflection of approximately 1.75 µm, and Equation 6.7 predicts a deflection in a diced piece to be 14 nm. Results for wafers used will be given along with the results.

Unfortunately, not enough of the wafers had acceptable radii of curvature, and some wafers had to be debowed. Since the bow and warp arises from stresses within the

wafer, this can be controlled by applying a tensile stress on one surface of the wafers. This is accomplished by depositing a film of silicon dioxide on the backside of the wafer. Here, the deposition is done using PECVD using the same process as will be discussed later. Since the deposition occurs at 300°C, residual film stresses arise. The film is deposited stress free; however, when the silicon wafer cools to room temperature the mismatch in the coefficients of thermal expansion between the silicon and the oxide cause a tensile stress in the film. This causes the wafer to deflect away from the film. In this, a wafer that has a convex surface can have silicon dioxide deposited on the bottom to reduce the bow.

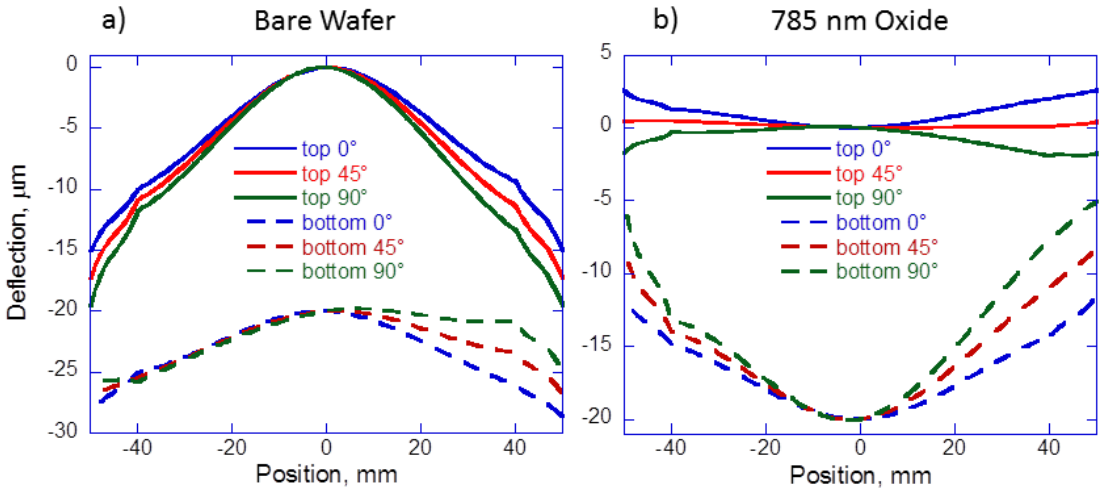

Figure 6.17. Surface profile of a wafer a) as purchased and b) after deposition of a 785 nm silicon dioxide film deposited on the bottom surface. The top and bottom profiles are offset, and multiple directions are shown for each profile.

Figure 6.17 shows the results of one such application of a debowing oxide. The top surface of the natural wafer is convex with fairly similar profiles at every angle shown in Figure 6.17a. This is important as the oxide layer will not generally fix any irregularities in the surface profile in the polar direction, so a saddle cannot be used. There is a linear relationship between the thickness of oxide and the change in the deflection of the wafer, though this is different for every wafer seen. As such, every debowed wafer needed to be tested with an arbitrary film thickness and the bow was

measured. From this, the correct amount of film thickness can be predicted and the film was removed either using reactive ion etching or wet etching in a bath of hydrofluoric acid. After the oxide was removed, the surface was retested to ensure additional film stresses were not introduced, and the correct oxide layer was deposited. As seen in Figure 6.17b, this reduced the surface curvature significantly. Here a 785 nm thick layer of oxide was deposited on the bottom of the wafer and the top side radius of curvature changed from -75 m to 507 m.

While the application of oxide to the wafer does not affect the heat transfer rates in any significant way, the measurement of the gap spacing with interferometry can be significantly affected. The introduction of a film on either side of the sample can create interference fringes due to coherence in the film when the film thickness is large enough. As is the case with the 785 nm thick film, there is a significant change in the reflectance versus what should result from Figure 6.14. However, this film thickness is constant and known for each wafer, so the measurement is not affected. The variable interference pattern created by the gap spacing is still present, though the total reflectance is notably different. Since the FTIR spectrum must be matched to a prediction of the reflectance at different gap spacings, quantitative analysis is still possible.

6.2.3.2 Sample fabrication

With all of the wafers measured for the appropriate bowing and optical properties, fabrication can occur. For this process two wafers must be used: one wafer, referred to as the patterned wafer, will have the pattern of silicon dioxide spacers, while the other wafer, referred to as the clean wafer, will have nothing on the surface. After dicing, these two samples will be mated together to form a sample. Ultraviolet photolithography is used to fabricate the patterns, and the process flow is shown below.

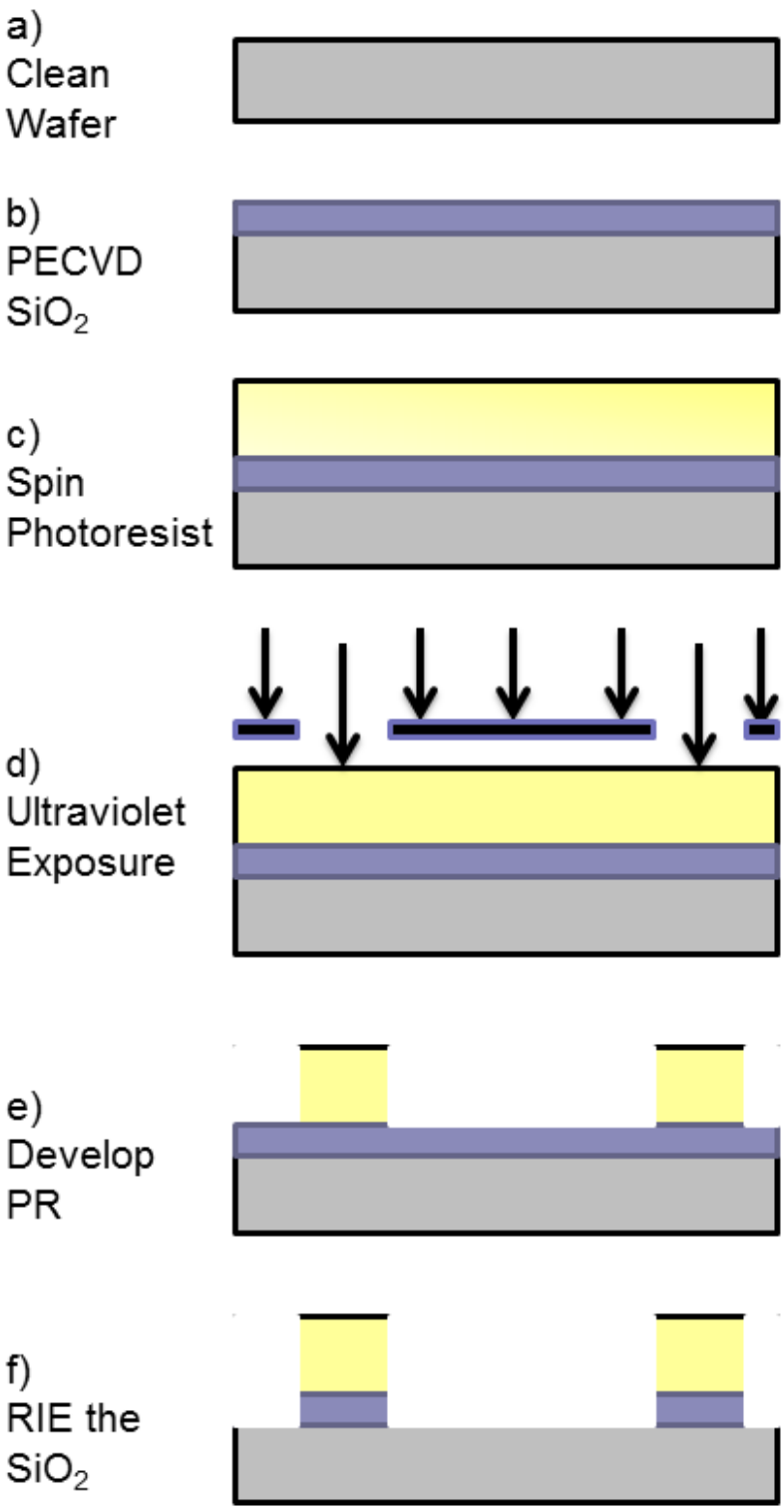

Figure 6.18. Process flow for creating samples. a) wafer cleaning, b) oxide deposition, c-g) pattern transfer through photolithography, h) dicing to 1 cm pieces, i) mating a patterned and cleaned piece.

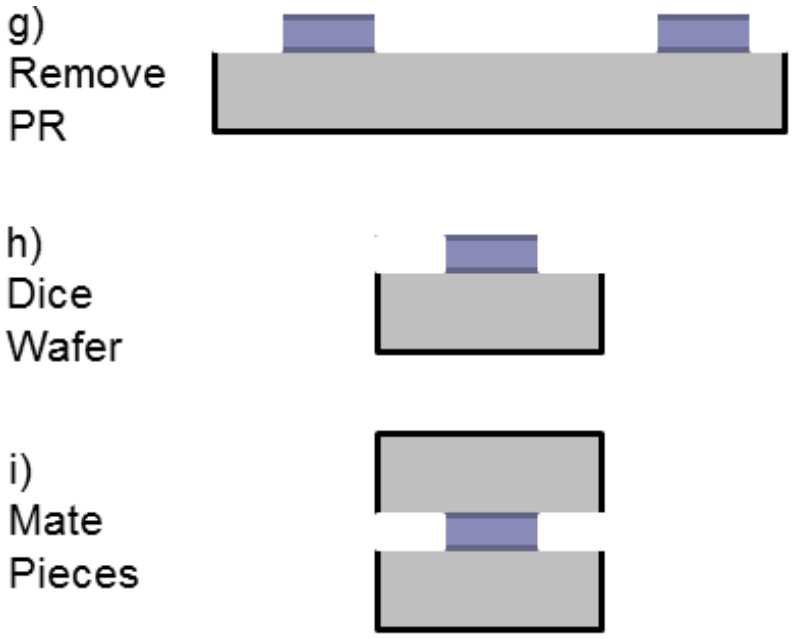

Figure 6.18 continued.

Figure 6.18 shows the complete process for fabricating samples used in this work. An important step in the process is cleaning, shown in Figure 6.18a. Wafers were cleaned using a heated piranha bath. This is a mixture of sulfuric acid and hydrogen peroxide in a ratio of between 5:1 to 10:1 to remove any organic contaminants. A bath was prepared and allowed to heat to 120°C, then the wafers were soaked for 10 minutes. Immediately afterwards, the acid was removed using a dump rinser with deionized (DI) water, and dried using a spin-rinse-dryer with dry nitrogen gas. As an extra precaution a dehydration bake was used, and the wafer was further dried in an oven for 30 minutes at 135°C to remove any adsorbed water or hydroxyl ions.

In Figure 6.18b, immediately after the dehydration bake the wafer was transferred to the PECVD machine, an Oxford Instruments Plasmalab 80 Plus. Here, gaseous precursors of silane, nitrous oxide, and nitrogen gas are added to the chamber at a pressure of 1000 mtorr while the temperature of the substrate is kept constant at 300°C. A radio-frequency source operating at 20 W reacts the gasses in an induced plasma to deposit a conformal layer of silicon dioxide on the sample. This machine has been tested

to deposit oxide at a reproducible rate of 62 nm/min. The films deposited are uniform to within 10 nm over the inside 8 cm of a 4" wafer. After the desired thickness of oxide is deposited, the thickness is checked with a Nanospec 3000 reflectometer. This machine measures the spectral response of the wafer in the visible range, and can deduce the thickness of a known film material by measuring the interference fringes.

The steps shown in Figure 6.18b are the exact same steps used to deposit silicon dioxide to the backside of the wafer. If this was deemed necessary for the wafer, the surface profile would be measured, and the oxide layer would be kept or discarded using either a heated HF bath, or RIE etching. Regardless, the cleaning step in Figure 6.18a would be repeated before continuing on in the process.

The next step is to deposit photoresist for photolithography, seen in Figure 6.18c. Futurrex NR71-3000P negative photoresist (PR) is chosen for this application because of the low sidewall profile after development. This process immediately proceeds the oxide deposition if possible; however if the oxide deposition occurred on a different day, then a piranha bath is used again. This is important because any adsorbed water in the film or the wafer can cause the photoresist to have poor stiction to the wafer. As an added precaution for the adhesion of the photoresist, a thin layer of hexamethyldisilizane (HMDS), Microposit P20 Primer, is applied to the film. The HMDS changes the surface of the SiO_2 to be hydrophobic, which makes a stronger bond with polymers.

Both of these chemicals are applied to the surface of the wafer using a Karl Suss RC8 spinner. The wafer was loaded onto the chuck and held in place using a vacuum. The wafer spun at 20 RPM while the chemical was applied with a pipette to the center of the wafer. Both chemicals were room temperature prior to spinning, though the photoresist is kept in a refrigerator for preservation. The HMDS was applied first, and the chuck was allowed to spin at 4000 RPM for 50 seconds with a ramp-up rate of 500 RPM/sec. This spreads a thin even layer of the chemical over the wafer. There is no

baking necessary for the HMDS. Next the photoresist is spun at a rate of 5000 RPM for 50 seconds with a ramp-up rate of 800 RPM/sec.

If the PR looked okay, i.e. not many visible dust or comets, an oven was used for the hard bake to solidify the film. Otherwise, the PR was removed with an AMI clean (acetone, methanol, then isopropanol) and the spinning process was repeated. Typically a hot plate can be used for baking processes, however the temperature variability can be as high as 20°C, leading to photoresist films that do not properly develop, or burn and are difficult to dissolve. This sensitivity to temperature has been seen to be a problem with this resist, and a slower bake in a convection oven is more easily controllable. The wafer was baked at 135°C for 20 minutes in an oven. The edge of the film was poked with tweezers to ensure that it had hardened sufficiently, and the film thickness was measured using the reflectometer. For this spinning recipe the film thickness varied between 2.5 μm and 3 μm.

A dark-field right-reading mask was made for the ultraviolet exposure seen in Figure 6.18d. This mask has four patterns of 1 μm diameter holes, as discussed in Section 6.2.1. Each pattern has a different spacing between the holes varying from 200 μm to 500 μm, and each section is a 3 cm square. Since these holes are too small to be visible to the naked eye, each 3 cm square is surrounded by a box pattern with markings on the outside to make the identification of the pattern simple. Prior to the exposure, the mask was cleaned using an AMI clean followed by a rinse in DI water and dried with N_2 gas. A Karl Suss MA6 mask aligner was used for the exposure. The light intensity was at a wavelength of 365 nm was measured before use and the exposure time was adjusted to correspond to a PR dosage of 21 mJ/cm^2/μm with a 15% overexposure. Vacuum contact was used to hold the mask and wafer together. This was followed by a post-exposure bake at 100°C for 20 minutes in the oven to promote cross-linking of the exposed PR.

Figure 6.18e shows the development of the photoresist. This was done in a bath of RD6 developer for approximately 30 seconds. With this, the exposed and cross-linked areas of PR are more resistant to being dissolved in the strong base, so the undeveloped areas rapidly dissipate. However, this needs to be carefully controlled as the etch rate for the developed photoresist is low, but not negligible, and overbaking of the undeveloped PR can cause the etch rate to decrease. As such, the wafer was submerged in the RD6 for 5 seconds longer than it took for the undeveloped photoresist to be look completely dissolved. If this time was longer than 45 seconds, the exposed photoresist was not reliable, and the wafer was not used. Immediately after the development, the wafer was submerged in DI water to remove all of the developer. It was then dried well using dry nitrogen.

The final step in the photolithography is using reactive ion etching (RIE) to transfer the pattern from the photoresist to the silicon dioxide layer, as shown in Figure 6.18f. Unfortunately, if the pattern is not correct and the oxide is etched, the wafer is unrecoverable. During etching, there is typically some damage done to the silicon at the edges of the patterned structures, and reverting to a smooth surface is impossible. If a bad pattern is caught before this, the photoresist can be removed and photolithography reattempted. The wafer can be cleaned using an AMI clean and a piranha bath to completely remove the photoresist without damaging the oxide layers. To check the pattern an Olympus LEXT 3D confocal microscope is used to take images of the pattern. This is shown below in Figure 6.19.

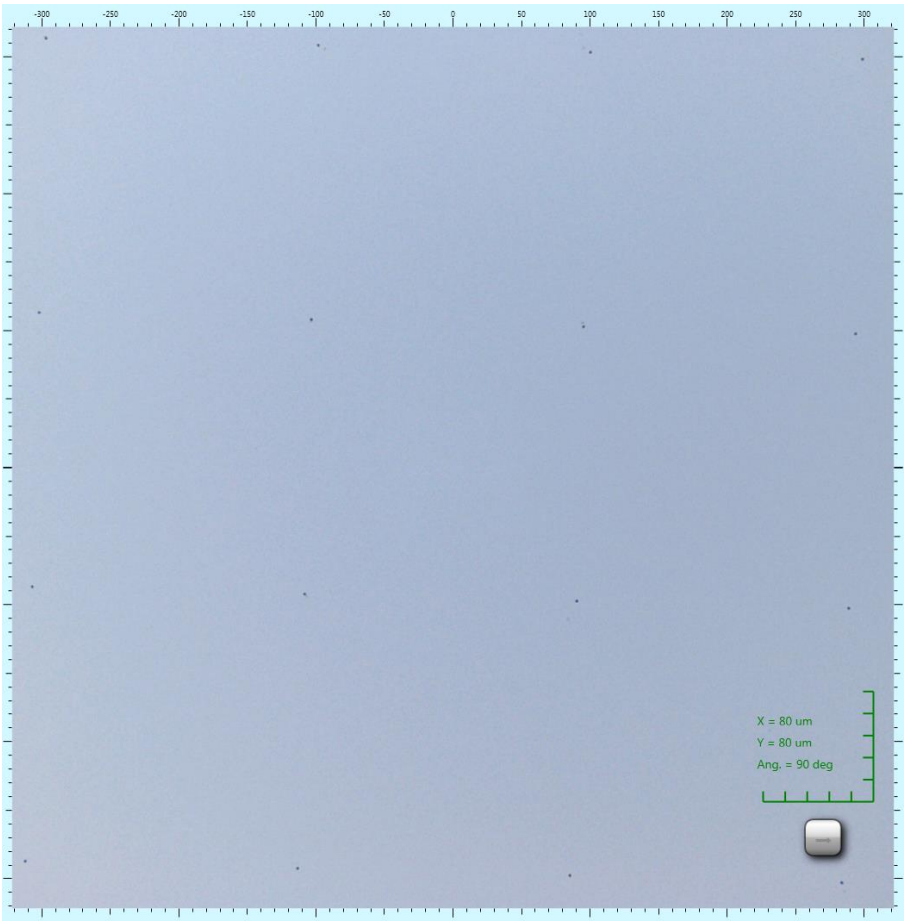

Figure 6.19. Confocal microscope image of a 200 μm pattern.

Though it is difficult to see, this area of the scan is able to see 16 posts with a spacing of 200 mm in both the *x* and *y* directions. A majority of the surface is briefly scanned to make sure that the pattern has transferred correctly, and results are typically that more than 95% of the surveyed area has the desired pattern. Note that this was not done for every wafer, and in many cases the correct pattern transfer was inferred from the state of the borders and markers transferred along with the posts.

A Vision 320 reactive ion etching machine is used to remove the silicon dioxide where it is not protected by the photoresist. CHF_3 and O2 gas is introduced to the etching chamber under low vacuum conditions, 40 mtorr. A radio-frequency power source operating at 250 W ionizes the precursor gasses which then react with the surface of the wafer. Since this occurs in vacuum, the ions can only etch the wafer anisotropically. Here

only the top surface can be etched, so everything protected by photoresist cannot be etched. This is the ideal situation, and some undercut does occur due to the nonzero pressure in the system. Since the trifluoromethane gas has a very low etch rate with the photoresist and the silicon, only the exposed oxide is removed. For this machine, a 30 second descum was used first, where only oxygen is in the chamber. This only etches the photoresist, but such a short etch does not fully dissolve the layer. This serves only to remove any corners or burrs that remain on the photoresist. The etch rate for the oxide etch was found to be approximately 26 nm/min measured using the reflectometer.

With this, the photoresist can be removed in Figure 6.18g. This is accomplished with an AMI clean to remove most of the photoresist, followed by a heated piranha bath to clean the residue and difficult to dissolve photoresist. In certain situations the photoresist would not release, and an extended soak in acetone at 45°C for 8 hours was necessary to fully remove the photoresist. In some rare cases no amount of chemical could remove the photoresist, and the wafer was discarded. This was thought to be the result of higher temperatures than desired during the baking processes or during the etching.

The samples are then diced as shown in Figure 6.18h. The sample is first covered in photoresist to protect the patterns. Because this is now not a critical step, the baking is done on a hot plate for 90 seconds at 150°C and the HMDS is not applied. Tape is applied to the bottom of the wafer to secure it during the dicing process. An Advanced Dicing Technologies 7100AD Precision Wafer Dicing Saw was used with a 3” nickel blade. The cuts were lined up with a camera to ensure correct dicing and alignment, and were spaced 10.15 mm apart to account for the kerf of the blade. Since each pattern was 3 cm by 3 cm, four complete pieces could be diced from each pattern without worrying about extremely precise alignment. Two initial cuts were made in the center of the wafer to easily separate the wafer into quarters after the dicing. Through these initial cuts the

angles and alignment of the cuts were made very precise and the area taken by the width of the blade was accounted for in the final cuts. Because of this, there is assumed to be no significant uncertainties associated with the area of the pieces.

The cleaned wafer was also diced during this time. Since there was no pattern to deposit, much of the process listed above was skipped. Only the cleaning was done for each wafer used, and some had CVD oxide on the back to debow. Afterwards a protective photoresist layer was applied and the wafer was cut. Here the wafer was cut in the center to align, then was cut to create as many 1 cm by 1 cm pieces as possible. This typically yielded approximately 30 pieces.

The final step is to put the patterned pieces together with the unpatterned pieces in Figure 6.18i. First the pieces were released from the dicing tape. The patterned wafer was cut into quarters so that there would be no confusion about the pattern on the piece, as these patterns are completely invisible to the naked eye due to the large spacing and small posts. The four pieces on tape were placed in acetone until they delaminated. The extra wafer pieces and tape were carefully removed without losing the orientation of the sample, as the front and back are indistinguishable. Inside a fume hood the pieces were cleaned individually with acetone, methanol, isopropyl alcohol (IPA), DI water, and finally IPA again. The piece was blown dry with dry nitrogen and placed on a cloth. All four pieces were cleaned in this way before being transferred to another fume hood with higher ventilation and less dust. The cleaned wafer was quartered and cleaned in the same manner before being transferred to the cleaner fume hood.

The pieces were re-cleaned again immediately before being put together. This was done with IPA first, then DI water. Since the silicon substrate is hydrophobic, the DI water should run off the piece immediately, unless a piece of dust or other impurity was present on the surface. If such a particle was detected, it was cleaned again. Finally the sample was rinsed in IPA again because of the superior drying properties and set aside.

The matching piece from the clean wafer was cleaned in a similar manner. Finally, the piece was placed on the patterned piece and light force was applied to the top by hand. Though it was not measured, the estimated force applied is between 100 grams and 200 grams. For nearly all samples, the pieces would hold together with some degree of Van der Waal's forces indicating a good mating. If this was not found after a few seconds more, then the sample was cleaned again. After a second try the sample was left as it was; however, these samples rarely survived the trip back to the near-field experiment.

6.2.3.3 Verification of post geometry

Aside from the FTIR and heat transfer measurements of the samples, plenty of other tests were made to ensure that the samples created were as desired. This included confocal microscopy as seen in Figure 6.19, AFM, and SEM to determine the size, shape, and distribution of the fabricated posts.

An additional confocal microscope image is shown below in Figure 6.20 to demonstrate the repeatability of pattern transfer. Shown is an older pattern with only 10 mm spacing between the posts, however the fabrication process is almost identical, and this image shows a much larger distribution of posts than in Figure 6.19. Here the pattern has been transferred in every spot; however some of the posts are irregularly shaped. It has been found that this is due to the photoresist posts falling over during the etching process due to poor adhesion to the oxide layer. The introduction of the HMDS layer prevents this phenomenon happening as much, but even shown here the effect is less than 2% of the posts having any irregularities. This microscope can also use a laser to find the focal point at different heights to build a three-dimensional image. The limits of this resolution are very much at their limit for this application, however the bottom of the Figure 6.20 shows the height profile of posts on the red line in the top image. This pattern was fabricated to be 400 nm tall with 10 μm spacing, which the microscope verifies, showing heights between 360 and 440 nm.

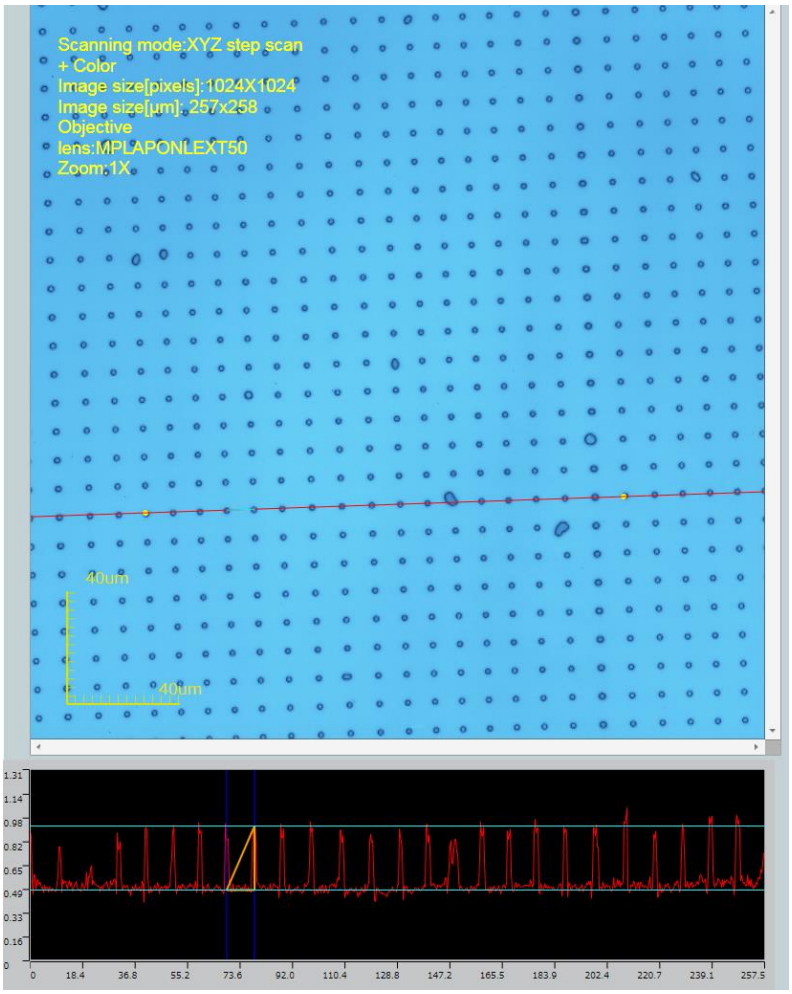

Figure 6.20. Confocal microscope image of a 10 μm pattern. The bottom segment shows the height distribution on the red line, consistently 400 nm.

SEM images were taken to show the detail of the individual posts. This is shown in Figure 6.21 with a Hitachi S4700 FESEM for an 800 nm post taken at 30° incidence. A post from a 400 nm pattern is shown from a Hitachi SU8230 FESEM in Figure 6.22. Both of these images show that the area at the top of the post is nearly ideal. The top of the post in Figure 6.21 appears elliptical, but this is only due to the angle of the image, and the eccentricity in Figure 6.22 only changes the area by less than 10%.

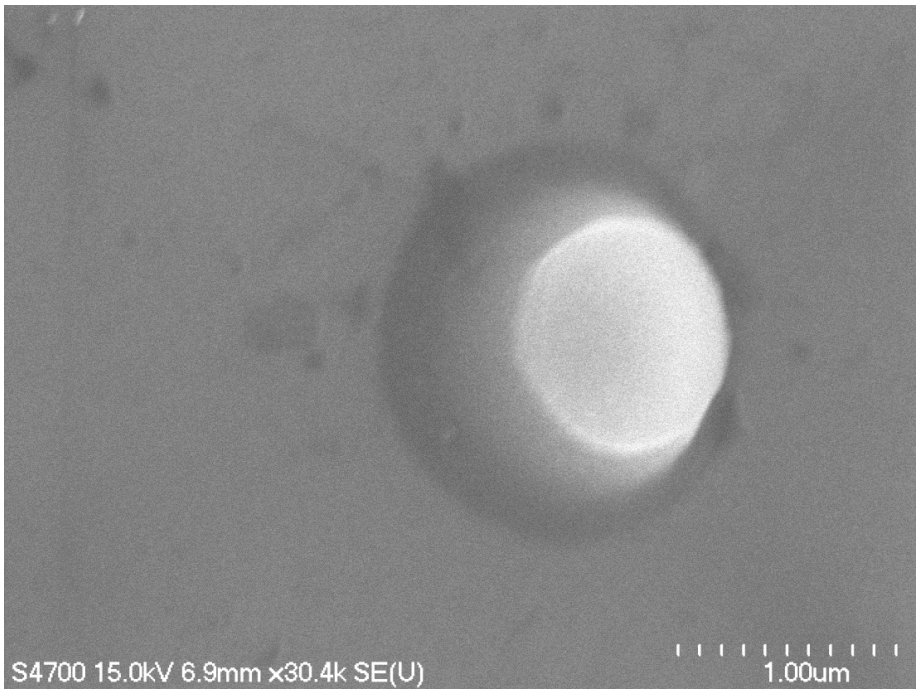

Figure 6.21. Scanning electron microscope image of a single post. This image is taken at a 30° angle to show the sidewall angles.

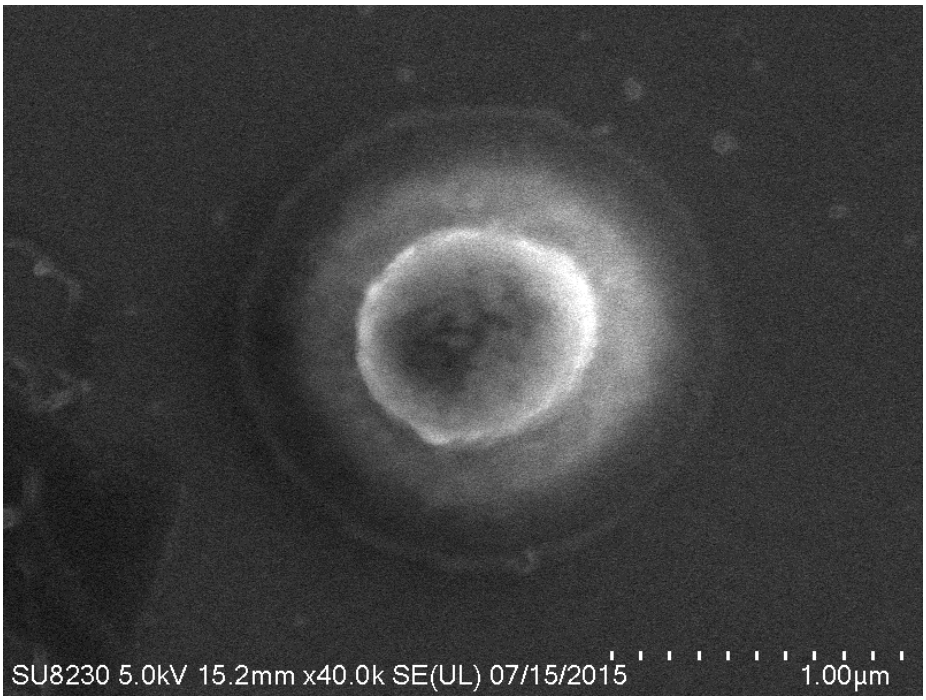

Figure 6.22. Scanning electron microscope of a single post.

Finally, an AFM image was taken from the same sample as from Figure 6.21. While the lateral resolution of this image shown in Figure 6.23 is less than ideal, the height measurement confirms the 800 nm height desired.

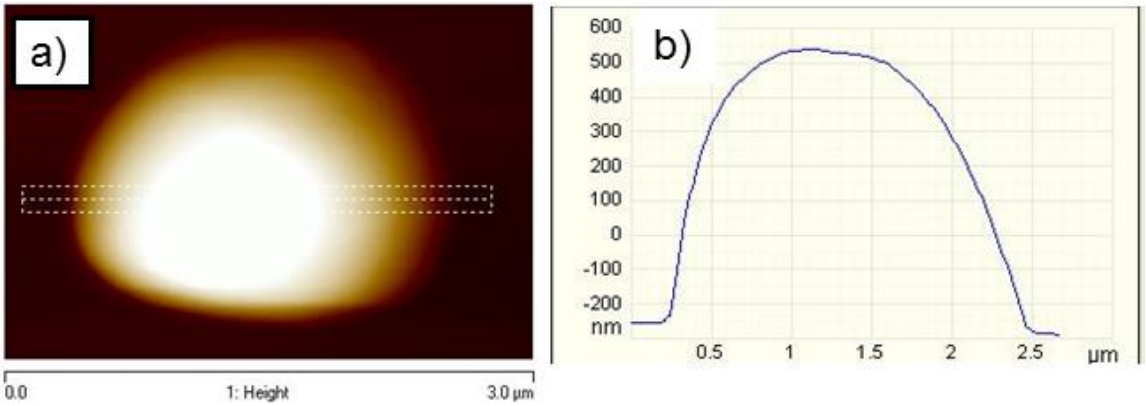

Figure 6.23. Atomic force microscope image of a single post. a) height distribution over a single post, b) quantitative measurement of the post height through the center.

Between all of these measurements, along with several more not presented, the pattern transfer of the posts is very reliable. Any defects in the geometry can affect the performance of the sample and must be detailed as uncertainty. As has been discussed along with the dicing, the total area of the diced pieces is nearly exact, and will not contribute to uncertainty. The area of the posts has been seen to have some variability, with nearly 2% of posts having a larger area in Figure 6.20 and the post area being lower than desired by 10% in Figure 6.22. Thus it is estimated that the uncertainty in the contact area for conduction heat transfer is 10%. Additionally errors in the post height and wafer bow may contribute; however, it will be shown that the uncertainty in the gap spacing can be found from the FTIR measurements.

6.3 Measurement Results

Through several fabrication attempts six wafers were successfully patterned to yield 96 samples. However, the yield on these samples is very low. Of these samples only 28 were tested in the near-field heat rate experiment. This is due to poor FTIR

measurements and fragile samples breaking before being placed in the dewar. Thus the yield on useful samples was less than 30% for the interferometry stage, and fewer still gave good results. Due to difficulties within the heat transfer experiment, only 6 of these samples gave good results. However, multiple measurements of certain samples were possible.

6.3.1 Measurement Procedure

This round of testing ran from June of 2015 until January of 2016, and the yield rose over the course of the testing, with four of the useable samples being measured within one month of each other. The two main reasons for samples to fail during testing were breaking and grease spillover. Because the samples have a very small area that is in contact, a very small shear force is enough to break the sample apart and introduce dust into the gap. Because this measurement requires a good thermal connection on the top and bottom of the sample, careful installation of the sample is critical, and the residual stresses in the lead wires for the heater and thermocouples was often enough to break the sample apart. This led to measurements where the temperature drop was much higher than predicted for the measured heat flux.

One method to combat this was to use more thermal compound at the interfaces between the sample and the thermocouple blocks. This ensures that there is a good thermal connection, and the viscous nature of the grease is able to absorb some of the stress. However, this led to issues with grease overflowing from the interface and entering the vacuum gap. The conduction heat transfer must be extremely small in the gap to show adequate near-field heat transfer, and a small amount of grease can act as a thermal short in the experiment. Cases where this was present showed a very small temperature drop versus the prediction for the measured heat rate.

The installation of the samples became one of the most critical parts of the experiment, and great care was taken to reduce the lateral forces on the sample. To install

a sample, a layer of thermal grease was applied to the lower thermocouple block and the sample was gently laid on top. Another layer of grease was spread over the bottom of the top thermocouple block, and this was carefully placed on top of the sample. It was at this point that mechanical failure of the sample was most common.

Unfortunately, this method was unable to give a repeatable contact resistance as was the case during the calibration with an applied load. However, the contact resistance was measured at the end of every measurement. Because the high thermal resistance through the sample relies on there being vacuum, a measurement in ambient pressure should have no thermal resistance, as was discussed in Section 6.2.1. At the end of every experiment, the chamber was allowed to return to ambient pressure, and a significant reduction in the sample temperature difference was seen. This is then assumed to be completely due to the contact resistance through the sample interfaces, and was factored out of all of the measurements.

Each sample was first measured for the gap spacing using FTIR interferometry using the technique detailed in Section 3.1.2. For many samples the impact of an applied force was measured with regard to the change in the gap spacing, and this led to multiple measurements of samples with varying gap spacings. It is assumed that the results from applying force on the sample during the FTIR testing correspond to the same change in gap spacing during the near-field experiment. To adequately determine the correct gap spacing, a numerical comparison between the measured reflectance spectrum and the calculated spectrum was required. A database of different reflectances for varying gap spacings was compiled for each set of samples, as some samples had an extra silicon dioxide layer to correct bowing, and these curves were used in the determination.

While the height of the fabricated posts was well controlled, this does not necessarily give the gap spacing. It is typical that the gap spacing is higher than desired by 20%; however, larger deviations were found as well. The simulations of the stress and

deflection discussed earlier explain that the silicon between the posts can deflect significantly under moderate loading in one unit cell of the pattern. This effect can be greatly enhanced if there are posts that are not in direct contact with both pieces of silicon as deflections can propagate throughout the sample. There were also cases where the measured gap spacing was smaller than the fabricated post heights.

Proper determination of the gap spacing was compounded with measurement errors during the interferometry. While alignment issues and poor background measurement can contribute to measurement uncertainties, this is generally an error in magnitude. Here the shape of the curve and the location of the maxima and minima created by the interference pattern were given more weight. However, for measurements over a larger area, i.e. larger incident beam spot size, the gap distance is not always constant. This led to issues with partial decoherence, where the constructive and deconstructive interference within the gap shows the effects of multiple gap spacings simultaneously. This can allow the spectrum to exhibit reflectance peaks corresponding to two or more gap spacings. While attempts to quantify this phenomenon were attempted, confident reporting of non-parallel gap spacing was not possible, as the variation in gap spacing as well as the curve of the non-parallelism was required. For this reason, measurements using a smaller spot size were preferred to minimize the effect.

The measurement of the gap spacing is necessary for calculation of the near-field heat transfer rate, but is also important for the conduction. While a larger gap spacing contributes in a predictable way to the radiation heat transfer, the effects on the conduction are difficult to quantify. For a sample that has a significantly higher gap spacing than the post height, the only reasonable conclusion is that not all of the posts are in direct contact. As such, the total conduction heat rate needs to be modified to include only the posts that have good thermal contact. Unfortunately, the exact surface profiles of each piece are unknown, and the distribution of contacting posts cannot be determined.

Furthermore, this behavior changes with applied forces, so an accurate conduction heat rate as a function of gap spacing would be needed for each individual sample.

Several models were proposed in an attempt to model the conduction heat rate, but it is clear that a variable number of posts are involved in the heat transfer. For a sample that is presumably bowed out in the center, it could be imagined that only posts near the perimeter of the sample are in contact. Using this methodology the conduction heat rate drops by over an order of magnitude, as does not appear to be the case, and some amount of deformation in the oxide posts or silicon pieces is likely to contribute. However, surely the conduction heat rate should decrease with the gap spacing as this would represent less contact on the posts. With the functional form of this unknown and presumably unknowable without extensive measurements, it is assumed to behave as if the posts are in perfect contact with both silicon surfaces and that they exchange heat over the length of the gap spacing. This method is used in cases where the gap spacing is larger or smaller than the fabricated post height.

After the gap spacing of a sample is verified, it is installed into the near-field measurement and placed under vacuum conditions. The temperature drop over the sample is measured at various input heat rates. The heat flows unidirectionally and is measured using a calibrated heat flux meter, as described in Section 3.2.4. The ranges of input power settings varied by sample and were typically chosen as arbitrary values to cover a range of heat rates between 20 mW and 300 mW. The temperatures and heat rates are measured rapidly, though only the steady-state measurements are shown here. At the conclusion of the experiment the sample was often measured again with an applied force. In this, a spring was placed on the center of the top heater and a bar was slowly lowered until the desired deflection in the spring was reached and the force was known. The vacuum was engaged and left to sit for several hours before a new set of measurements began. The process of adding force was done as necessary. Upon conclusion of the series

of measurements, the sample was removed and the stage was cleaned. Because of the high viscosity of the thermal compound, almost every sample broke during removal. Only in very rare cases did the sample remain intact, and these samples were not used again.

After the measurement, data was collected under ambient pressure at an input power of 100 mW. The contact resistance was found through the measurement of the temperature drop and heat flux meter reading, though the calibration found earlier does not apply. The calibration was necessary for vacuum readings because the heat paths through the heat flux meter changed with the absence of convection, and this was no longer the case under ambient pressure. Here the sensitivity of the heat flux meter given by the manufacturer was used as 7.88 $\mu V/mW/cm^2$ with an accuracy of 5%. Because of the delicate installation of the sample, poor thermal contact was common, and values ranged between 8 and 17 K/W. This resistance was removed from the vacuum measurements to give a corrected temperature drop. The temperatures above and below the sample were adjusted evenly to remove this extra thermal resistance. The manufacturer's sensitivity is used only for this purpose and only serves to change the temperatures. The effect that a 5% uncertainty makes on this change is negligible compared to the 0.15°C uncertainty in the thermocouple measurements.

6.3.2 Uncertainty Analysis

Uncertainty analysis was conducted on all measurements presented. A similar process to what was used in Section 3.2.5 using Equations 3.6 and 3.8 to evaluate the contribution of the measurement uncertainties on the heat rates through a central difference formulation. This is shown in all plots as error bars. The measured heat rate has an uncertainty only from the heat flux meter as 4.4% of the measurement; however the measured and predicted near-field radiation heat rates depend on separate measurements.

As discussed in Section 3.2.5, the thermocouples used have uncertainties of 0.15°C. Neglecting the uncertainty of the thermistor, this gives an uncertainty in the low temperature, T_L, of 0.15°C. The high temperature, T_H, of the sample depends on a thermocouple measurement along with the measurement of T_L, giving a total uncertainty of 0.22°C. These uncertainties are dominant in low power measurements where the total temperature drop is only a few degrees, but this uncertainty does not contribute much when the heat rate increases.

Parameters associated with the conduction heat rate in Equation 6.4 have uncertainties as well. The thermal conductivity has been seen to vary in other studies [108, 109] and the effects of phonon-boundary scattering can affect the thermal conductivity as discussed previously. For these reasons, the thermal conductivity used is 1.4 W/m-K with an uncertainty of 0.1 W/m-K. The number of posts is assumed to have no uncertainties, although uncertainty is considered in the area of each individual post. From the scanning electron and confocal microscope images shown in Figure 6.20 to 6.22 it is clear that some irregularities occur. For this reason, a 10% uncertainty in the areas is considered. Between these two factors, a sizable uncertainty in the conduction arises, which has a strong impact on the measured near-field heat rate.

The gap spacing used in the radiation and conduction calculations is measured through FTIR spectrometry, and it is through this measurement that the uncertainty is determined. This is done individually for each sample depending on the confidence of the match with the prediction. The lowest value of the uncertainty is 20 nm as differences between reflectances with gap spacing differences lower than this are very small. Most samples show an uncertainty of 40 nm showing that there is clear determination; however the agreement may not be very good or the curves are difficult to distinguish. In cases where there is poor agreement the uncertainty is 60 nm. This is typically due to small amounts of non-parallelism in the sample causing the shape of the spectrum to change.

There is also a region between 260 nm and 340 nm where the reflectances are nearly indistinguishable. The numerical best fit is chosen for curves matching this case and the uncertainty is given as 60 nm.

6.3.3 Individual Sample Results

Though not all of the samples measured will be shown here, all of the successful measurements will be presented, and some measurements that do not agree with the predictions will be shown for additional insights. Each measurement will show the gap spacing determination and justify the uncertainty prescribed. One value for each power setting will be analyzed, and the results for the measured and predicted heat rates as well as the measured and predicted radiation heat rates will be shown with error bars for the uncertainties. The predicted conduction heat rate can be found with Equation 6.4, and the predicted radiation heat rate is found using Equation 2.32. Because of the opacity of the doped-silicon, the semi-infinite near-field formulation is used. These two components are added together to find the predicted heat rate. The measured heat rate is found from the heat flux meter readings, and the radiation component can be found by subtracting the predicted conduction component. After all of the samples are shown individually, the heat transfer coefficient as a function of gap spacing will be presented for all of the successful samples.

The results will be presented in chronological order starting with sample 400n1-300u4. The naming convention of these samples denotes the post height in nanometers preceding the ‘n’ with the number following representing the sequential number of the wafer. The number preceding the ‘u’ represents the post spacing in μm, with the number after representing the sample number, as four samples were made from each spacing pattern for each wafer.

6.3.3.1 400n1-300u4

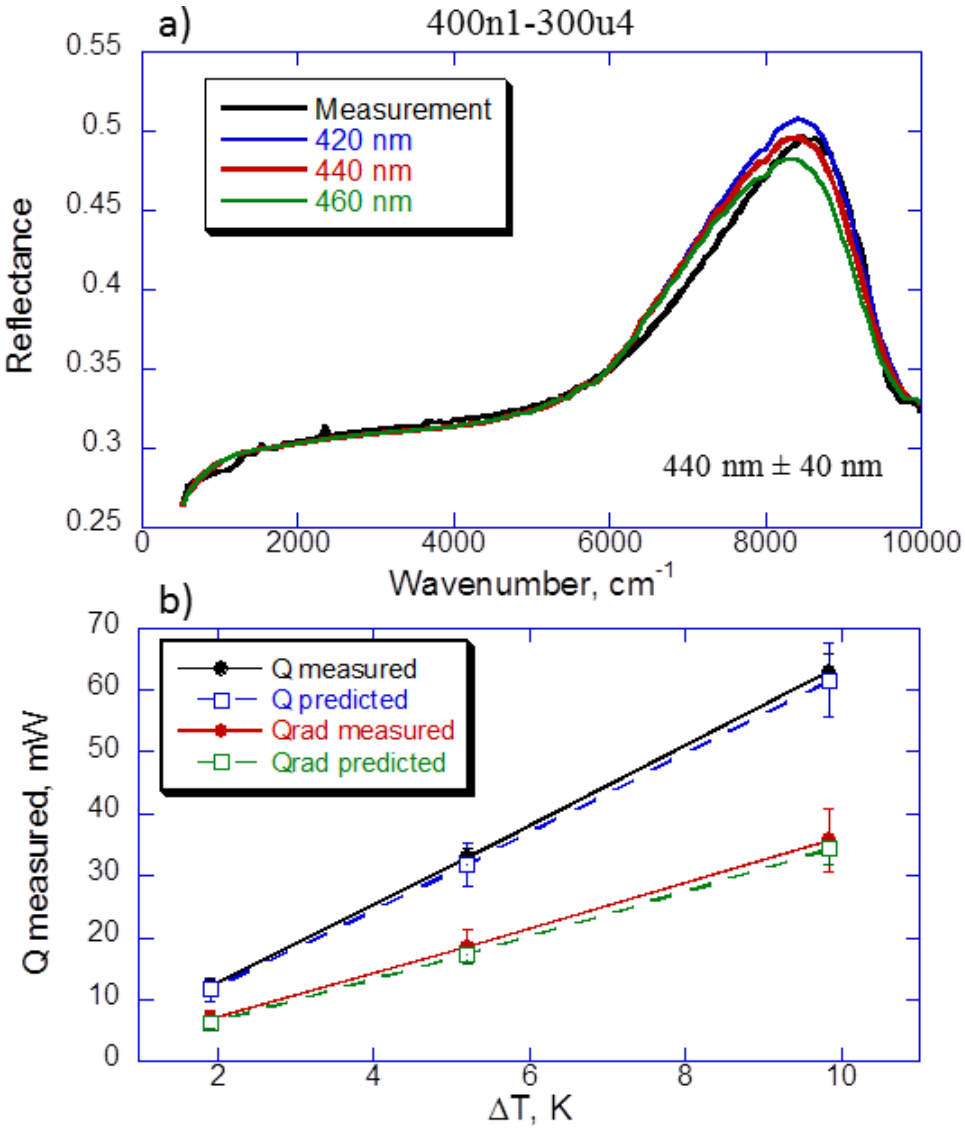

Figure 6.24. Measurement results for sample 400n1-300u4. a) FTIR results showing a gap spacing of 440 nm, b) near-field heat transfer results with excellent agreement.

The results for sample 400n1-300u4 are shown in Figure 6.24. This sample had posts fabricated to 400 nm height with 300 μm spacing. The two wafers had measured radii of curvature of 1900 m for the patterned wafer and 1300 m for the clean wafer, corresponding to maximum bowing of 6.6 nm and 9.8 nm, respectively. Figure 6.24a shows the results from the FTIR measurement, with the best fitting curve shown in red as

corresponding to 440 nm for the gap spacing. The two closest curves are also shown for comparison. While the choice of 440 nm is clear from this plot, there is some disagreement in the measurement. Here the peak reflectance is shifted and the reflectance is lower between 6000 cm^{-1} and 8000 cm^{-1}. For this reason, the uncertainty in the gap spacing is chosen to be 40 nm.

Figure 6.24b shows the comparison of the measured and predicted heat rates with the associated error bars. Here only three input power settings were measured, corresponding to 20 mW, 50 mW, and 100 mW. The uncertainty in the predicted heat rate is approximately 10%, coming largely from the conduction component, as conduction represents nearly 50% of the heat rate. The difference between the curves is approximately 4% for the total heat rates and 7% for the near-field radiation, and these differences are explained by the uncertainty, as seen with the error bars in Figure 6.24b.

6.3.3.2 400n1-500u4

Sample 400n1-500u4 is shown in Figure 6.25. This sample had a fabricated post height of 400 nm with a spacing of 500 μm. This sample was cut from the same set of wafers as the previous sample, and has the same expected bowing of 6.6 nm and 9.8 nm for the patterned and cleaned pieces, respectively. The FTIR results in Figure 6.25a show a slightly poorer agreement than is desired. This sample, along with the previous and the next sample were measured using a 9.5 mm spot size for the FTIR reflectance, and Figure 6.25a appears to have some degree of non-parallelism. The gap spacing is determined to be 500 nm as it is the closest match, and the uncertainty is 40 nm due to the apparent non-parallelism.

Figure 6.25b shows the measured and predicted heat rates. The power settings used were 20 mW, 50 mW, 100 mW, and 200 mW. It should be noted that this sample was measured twice, and this is the second measurement. The first measurement was very similar to these results, agreeing within 5%. After the conclusion of the first

measurement the contact resistance was very high, 30 K/W, and the sample was lightly pressed on the top to have better thermal contact at the interfaces. This dropped the contact resistance to a more manageable 17 K/W, though the repeatability of this measurement gives credibility to the process. The agreement with the predictions is very good, with an average difference of only 1% for the total and radiative heat rates. The uncertainties are approximately 7% and easily explain the differences.

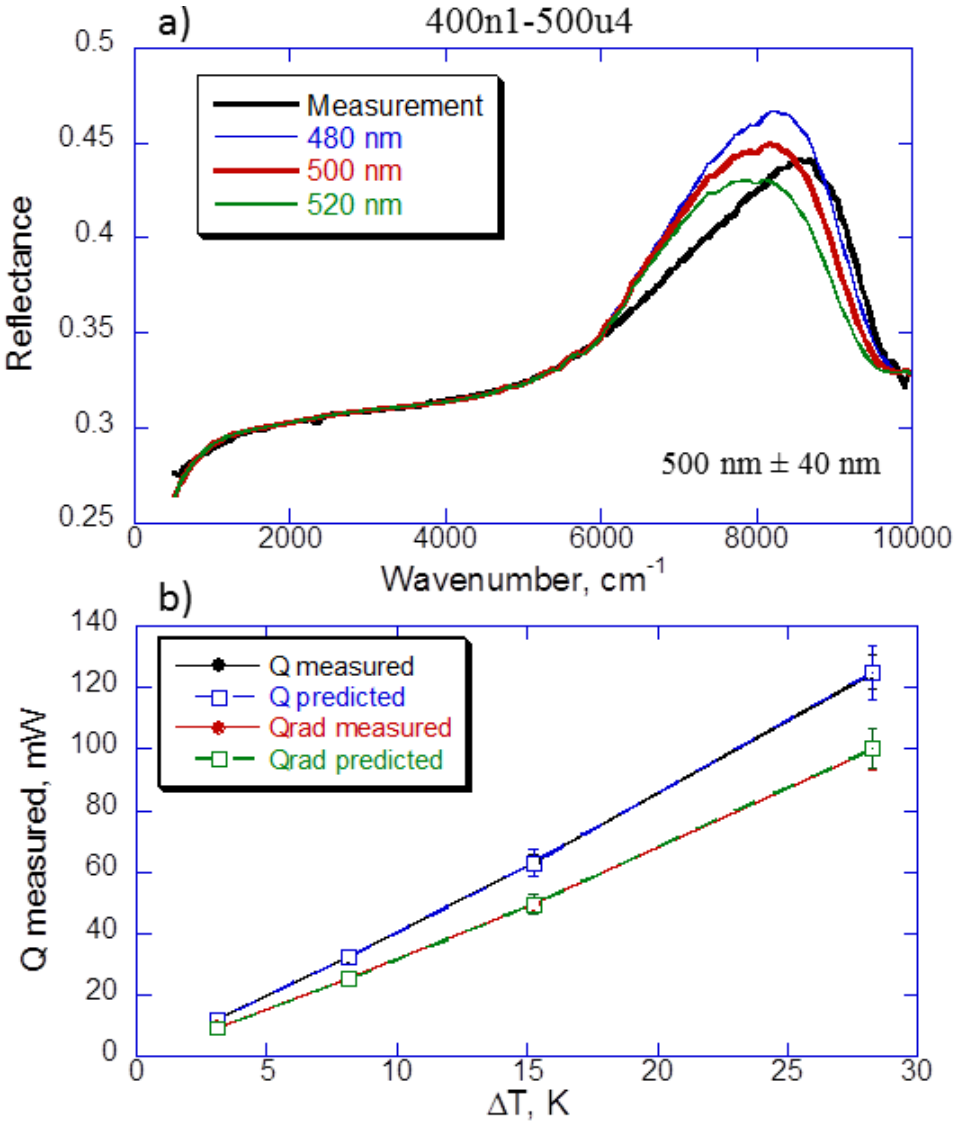

Figure 6.25. Measurement results for sample 400n1-500u4. a) FTIR results showing a gap spacing of 500 nm, b) near-field heat transfer results with excellent agreement.

6.3.3.3 200n1-400u2

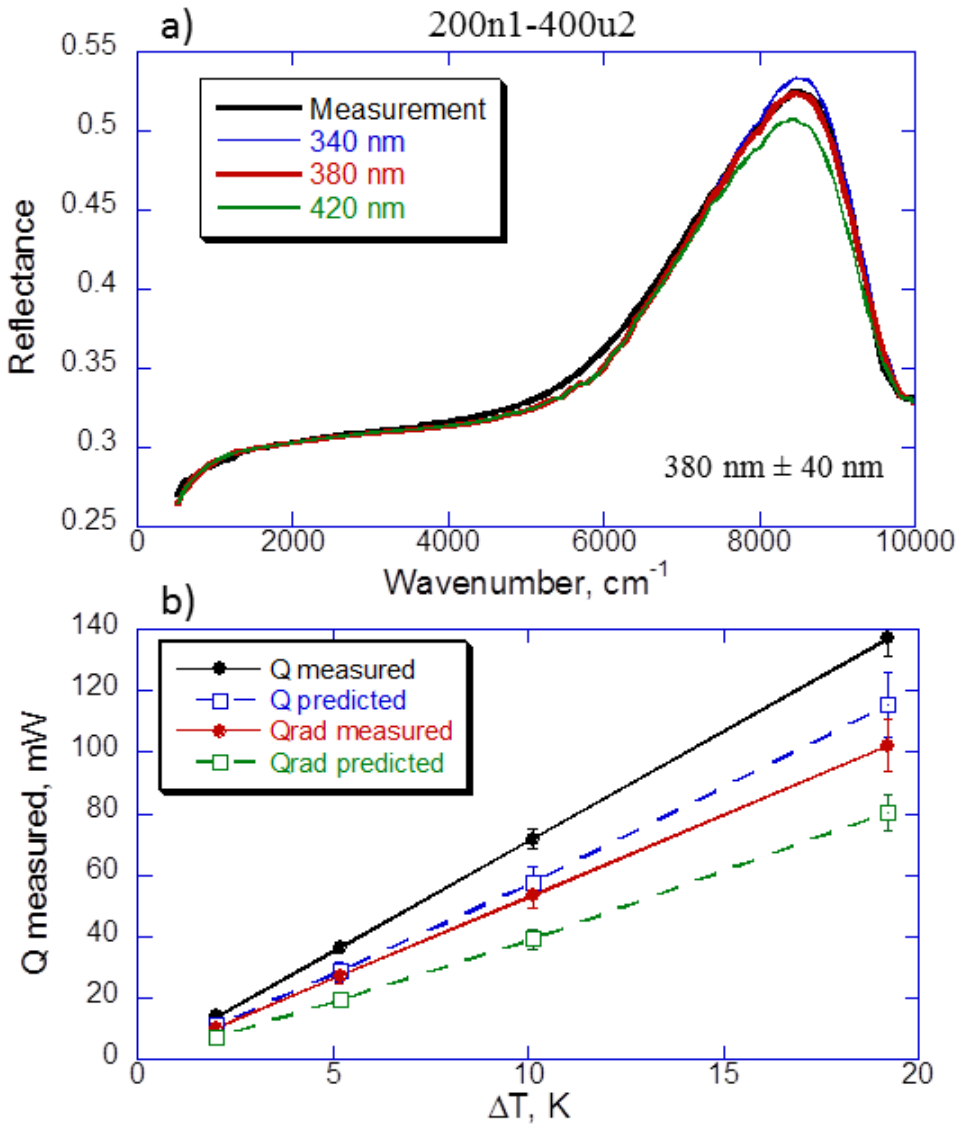

Figure 6.26. Measurement results for sample 200n1-400u2. a) FTIR results showing a gap spacing of 380 nm, b) near-field heat transfer results showing poor agreement.

The results for sample 200n1-400u2 are shown in Figure 6.26. The fabricated post height was 200 nm with a 400 μm post spacing. The radii of curvature for the patterned and cleaned pieces were -3600 m and 1700 m, corresponding to maximum bowing of 3.5 nm and 7.1 nm, respectively. The input power settings were 20 mW, 60 mW, 100 mW, and 200 mW. As seen in Figure 6.26b, the heat rate measurements do not match well with the predictions. While the uncertainties come out to be nearly 10%, the differences

between the curves exceeds 40% for the radiation. This may be due to poor identification of the gap spacing shown in Figure 6.26a.

For reflectance predictions between 260 nm and 340 nm the difference between the curves is very minimal, and this trend extends in either direction a bit. For this reason, Figure 6.26a shows comparisons with 40 nm of difference between the curves for clarity. However, the trend of the curves is increasing with decreasing gap spacing. This reaches a peak value at 300 nm and then continues to decline. This gives rise to an issue where the difference between the curves corresponding to 240 nm and 360 nm is very close, with only a small shift in the frequency of the maximum reflectance. If the heat rates are recalculated using a gap spacing of 240 nm, the difference is within 15% and the uncertainties explain the difference.

Unfortunately, the nearly perfect agreement of the 380 nm gap spacing signal in Figure 6.26a cannot be ignored. The uncertainty is believed to be 40 nm because of the difficult differentiation between the curves. With this value, the difference between the curves is not explained by uncertainties; however the sample is presented here for comparison.

6.3.3.4 200n3-400u1

Sample 200n3-400u1 is shown in Figure 6.27. The input power settings were 20 mW, 50 mW, 100 mW, 156 mW, and 200 mW. This sample required both the cleaned wafer and the patterned wafer to have a backside oxide deposited to reduce the bow. The patterned wafer had 595 nm of oxide to reduce the radius of curvature from -98 m to 1400 m for a maximum bow over a 1 cm length of 8.9 nm. The cleaned wafer had 785 nm of silicon dioxide deposited on the back to change the radius of curvature from 140 m to 580 m causing a maximum bowing of 22 nm.

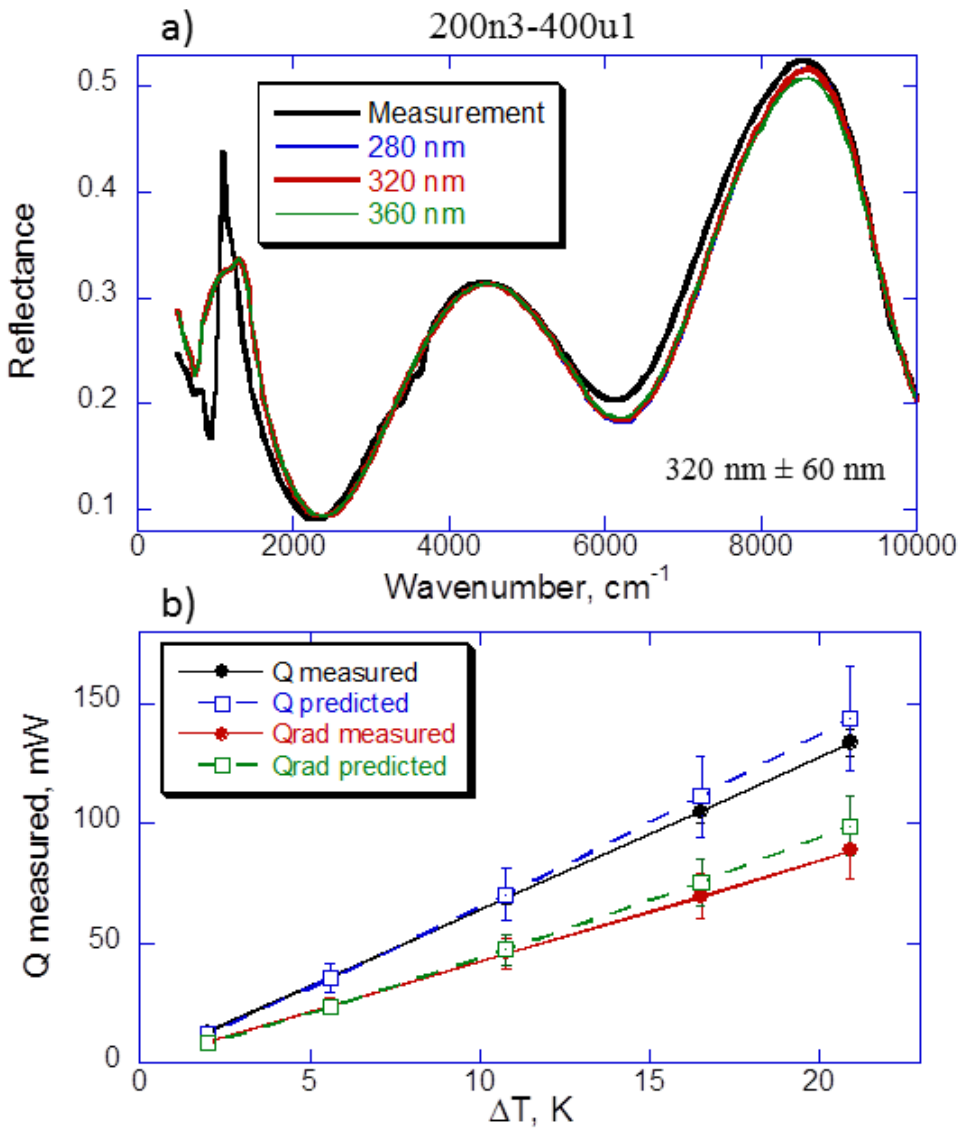

Figure 6.27. Measurement results for sample 200n3-400u1. a) FTIR results showing a gap spacing of 320 nm, b) near-field heat transfer results with good agreement.

This oxide significantly changes the reflectance spectrum, as seen in Figure 6.27a. Here the cleaned piece has the beam incident, so the interference pattern through the 785 nm oxide film is very obvious, while the oxide layer on the other side is very prominent due to absorption in the sample. The determination of the gap spacing is similar to a sample without any oxide film; however, this sample has a gap spacing very much so in the difficult to determine region mentioned earlier. The curve corresponding to 320 nm

fits the measurement the best, and a 60 nm uncertainty is added to account for the closeness of the curves.

Figure 6.27b shows the heat rate performance. The uncertainties shown here are up to 15%, largely due to the uncertainty in the gap spacing, and this does explain the differences between the curves, which is around 7% for the heat rate and 10% for the radiation heat rate.

This sample was measured using the custom-designed reflectance accessory described in Section 3.1.2, and the response of the change in gap spacing with applied force was measured. For this sample, an application of a spring force on the center of the sample changed the gap spacing between 340 nm unloaded and 180 nm with 20-30 grams of applied force, and the extracted gap spacings were repeatable upon unloading the sample. A force of 20 grams was tested in the near-field experiment, and the results are shown in Figure 6.28.

Here the gap spacing determination is simpler because of the larger difference between predicted curves. While none of the curves fit exactly, the closest fit in both magnitude and shape is 180 nm. The differences between the measurement and calculation appear to be differences in scale, which is expected for FTIR measurements. Note that the disagreement seen at 1000 cm^{-1} is due to the spectral averaging algorithm used for the predictions and the resolution is unable to match sharp peaks. Because of the disagreement, the uncertainty of this gap spacing is determined to be 40 nm.

The heat transfer results are shown in Figure 6.28b. The input power settings were 20 mW, 50 mW, 100 mW, 200 mW, and 265 mW. Here the agreement between the prediction and the measurement is within 10% for the heat rate and 15% for the radiation heat rate. Because of the low gap spacing, the sensitivity to the uncertainty is very large, and the uncertainties shown here are up to 20%, explaining the difference. With a

maximum measured near-field radiation heat rate of 128 mW, this represents the largest measurement of near-field radiation at submicron distances to date.

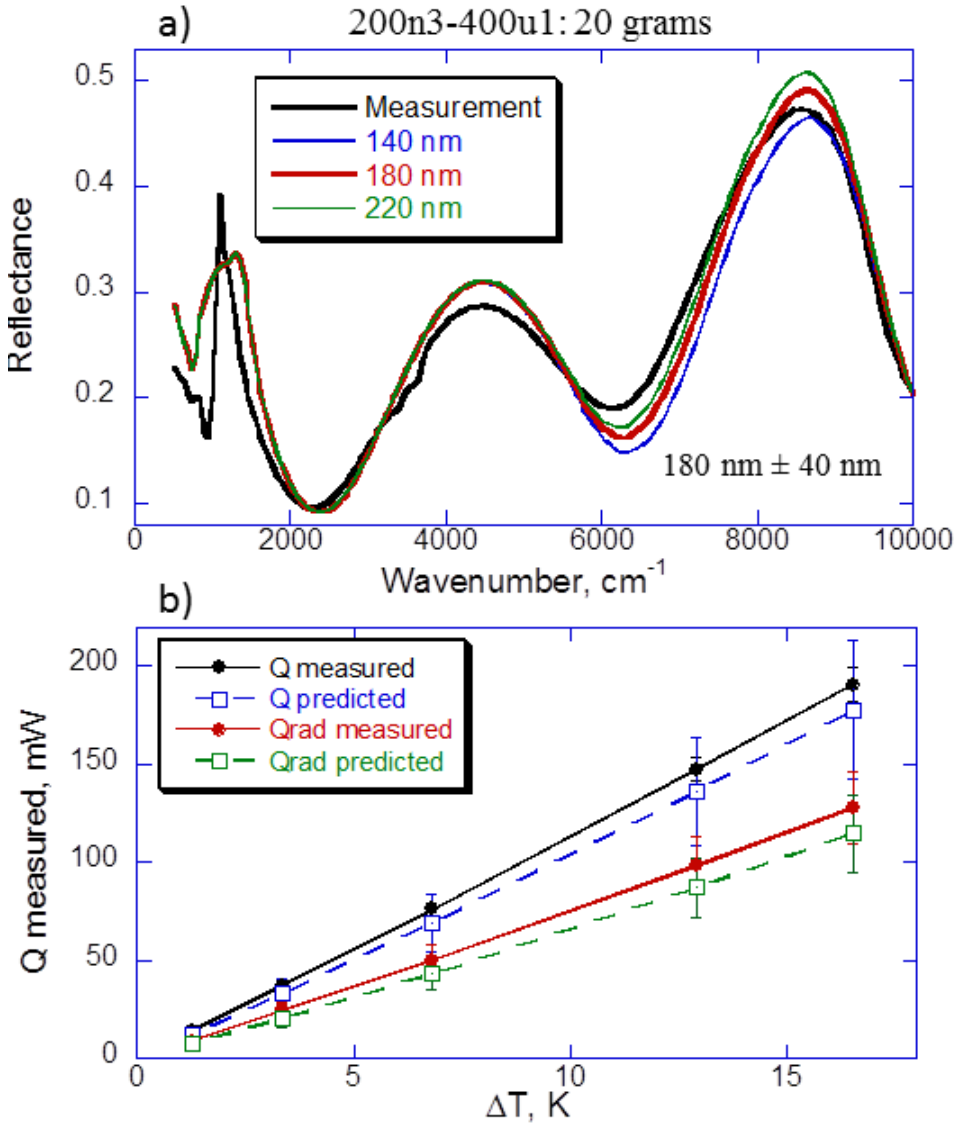

Figure 6.28. Measurement results for sample 200n3-400u1 loaded with 20 grams. a) FTIR results showing a gap spacing of 180 nm, b) near-field heat transfer results with good agreement.

6.3.3.4 600n1-500u1

Results for sample 600n1-500u1 are shown in Figure 6.29. This sample has fabricated post heights of 600 nm, with 500 μm spacing between them. The patterned wafer had a radius of curvature of 18000 m corresponding to a maximum bow of less than 1 nm. The cleaned wafer was the same as used in the 400n1 series and had a

maximum bow of 9.8 nm. The input power settings were 20 mW, 50 mW, 86 mW, 100 mW, and 200 mW. The FTIR match was very good, showing clear determination of a 740 nm gap spacing as shown in Figure 6.29a. Because of the excellent fit, the uncertainty is prescribed as 20 nm.

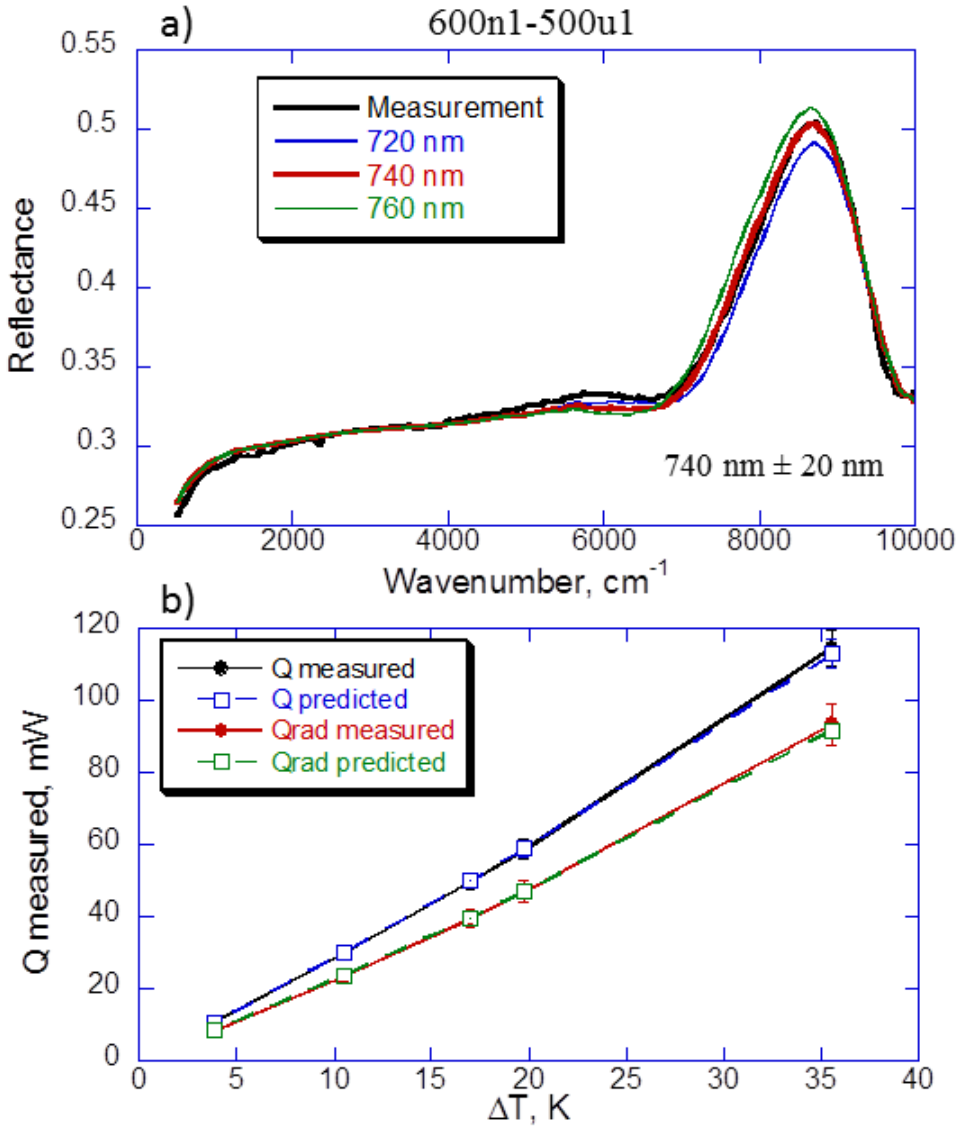

Figure 6.29. Measurement results for sample 600n1-500u1. a) FTIR results showing a gap spacing of 740 nm, b) near-field heat transfer results with excellent agreement.

The heat rates for this sample as seen in Figure 6.29b align very well with the predictions, with both the total and radiative heat rates agreeing within 2%. The

uncertainties found are fairly low, at only 4%, but manage to easily explain the differences.

This sample was also measured at different forces. The FTIR results showed that the gap spacing changed between 740 nm unloaded to 500 nm at 25 grams of force. A measurement of the near field heat rate was made at 12 grams, and the results are shown in Figure 6.30.

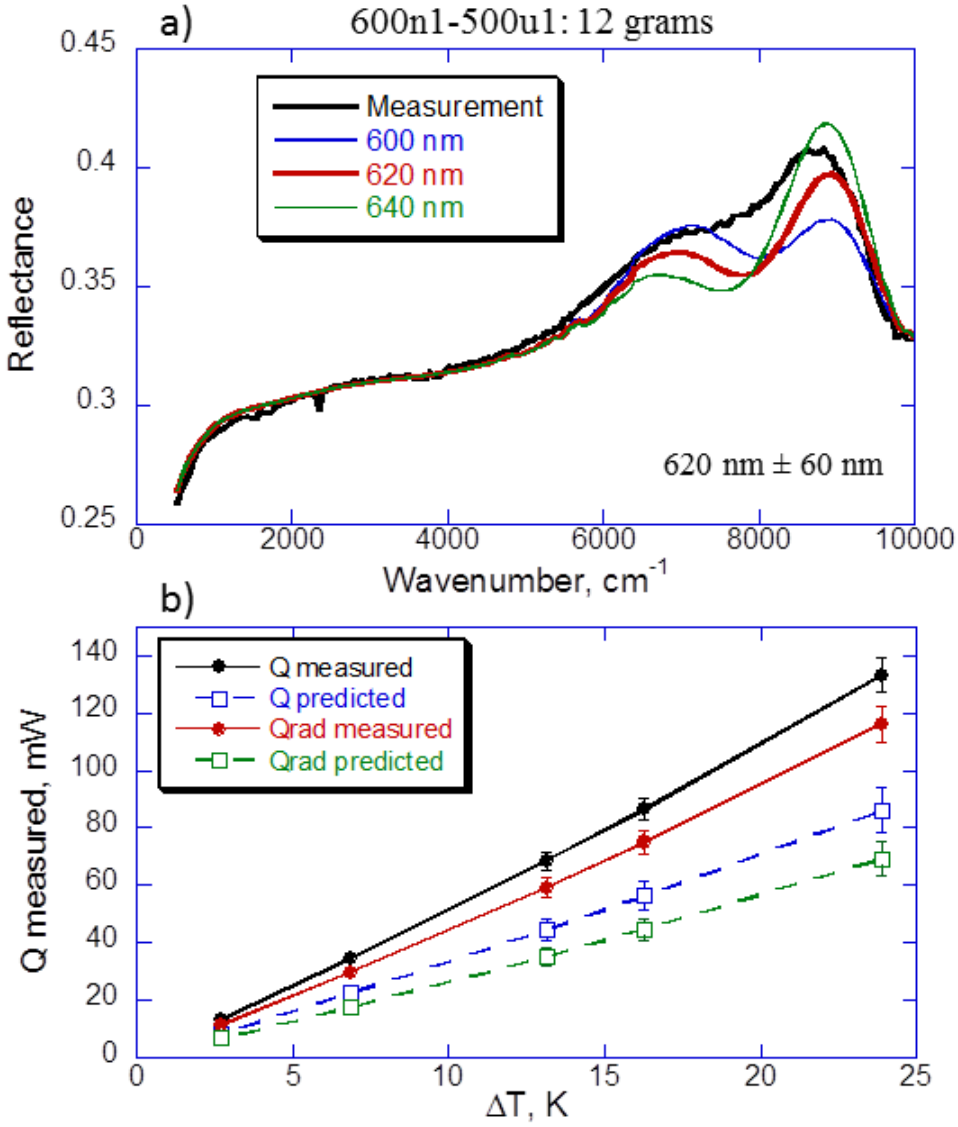

Figure 6.30. Measurement results for sample 600n1-500u1 loaded with 12 grams. a) FTIR results showing a gap spacing of 620 nm, b) near-field heat transfer results with terrible agreement.

Here the FTIR pattern shows clear evidence of non-parallelism. The curves near 600 nm all have a clear pattern of peaks, but the measurement only shows a shoulder. This is believed to be because part of the measurement area is 640 nm where the peak at 9000 cm^{-1} is strong, while part of the area must be 600 nm or lower where the peak at 7000 cm^{-1} is dominant. An intermediate value of 620 nm is chosen for this sample while the uncertainty is generously prescribed as 60 nm. However, this is not important, as the mismatch in the heat rates is extreme. As seen in Figure 6.30b, the differences between the measurement and the prediction are greater than the differences between the radiation and total heat rates. Though the uncertainties allow for a 10% difference, the disagreement between the measurement and the model is up to 65%. This type of performance was typical with samples that broke during measurement.

6.3.3.5 800n1-500u3

Sample 800n1-500u3 was fabricated to have 800 nm tall posts at a spacing of 500 μm apart. Both the patterned wafer and the cleaned wafer had a backside oxide to reduce the bow. The cleaned wafer was the same as the one used in the 200n3 series, and has a maximum bow of 22 nm after a 785 nm oxide layer was deposited. The patterned wafer had 730 nm of oxide deposited on the back side to reduce the radius of curvature from 100 m to 8000 m, reducing the maximum bow from 125 nm to less than 1 nm.

Figure 6.31a shows the FTIR results of the gap spacing determination. Here, the curves are not an exact match; however the agreement is clear. It is determined that the gap spacing is 780 nm with an uncertainty of 40 nm because of the mismatch near 7000 cm^{-1}. The heat rates shown in Figure 6.31b do not match very well. The applied input power settings used here were 20 mW, 50 mW, 100 mW, and 200 mW. The uncertainties for the heat rates are fairly low, approximately 7%. Because the high gap spacing causes the conduction terms to be less important, the uncertainties that affect the conduction do not affect the heat rate much. Unfortunately, this does not explain the differences

between the measurement and predictions, which is as high as 22% for the radiation and 18% for the total heat rate.

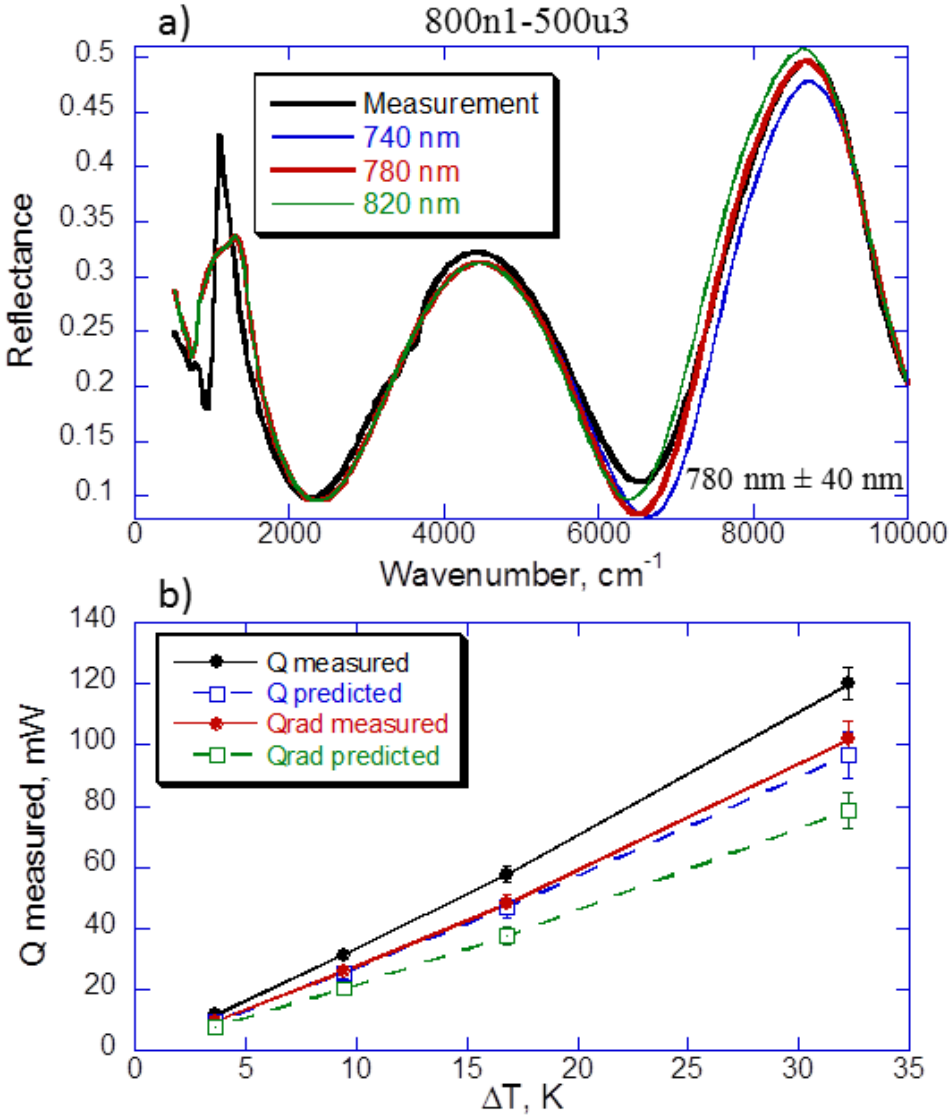

Figure 6.31. Measurement results for sample 800n1-500u3. a) FTIR results showing a gap spacing of 780 nm, b) near-field heat transfer results with poor agreement.

This sample was measured at multiple applied forces as well, and was found to be very sensitive to changes in the force. From the FTIR measurements, the gap spacing changed from 780 nm to 600 nm over a change in the force of only 8 grams. It is estimated that the uncertainty in setting the force on the sample is less than 2 grams in Section 3.2.1. By prescribing a linear relationship between the gap spacing and the force

for this sample the FTIR measurements state that a change in the force of 2 grams could change the gap spacing by up to 90 nm. In this case, the uncertainties would explain the measurement error in Figure 6.31, however this is speculative. The results from 800n1-500u3 without any applied force will be included in the final results with uncertainties pertaining to 40 nm for the gap spacing.

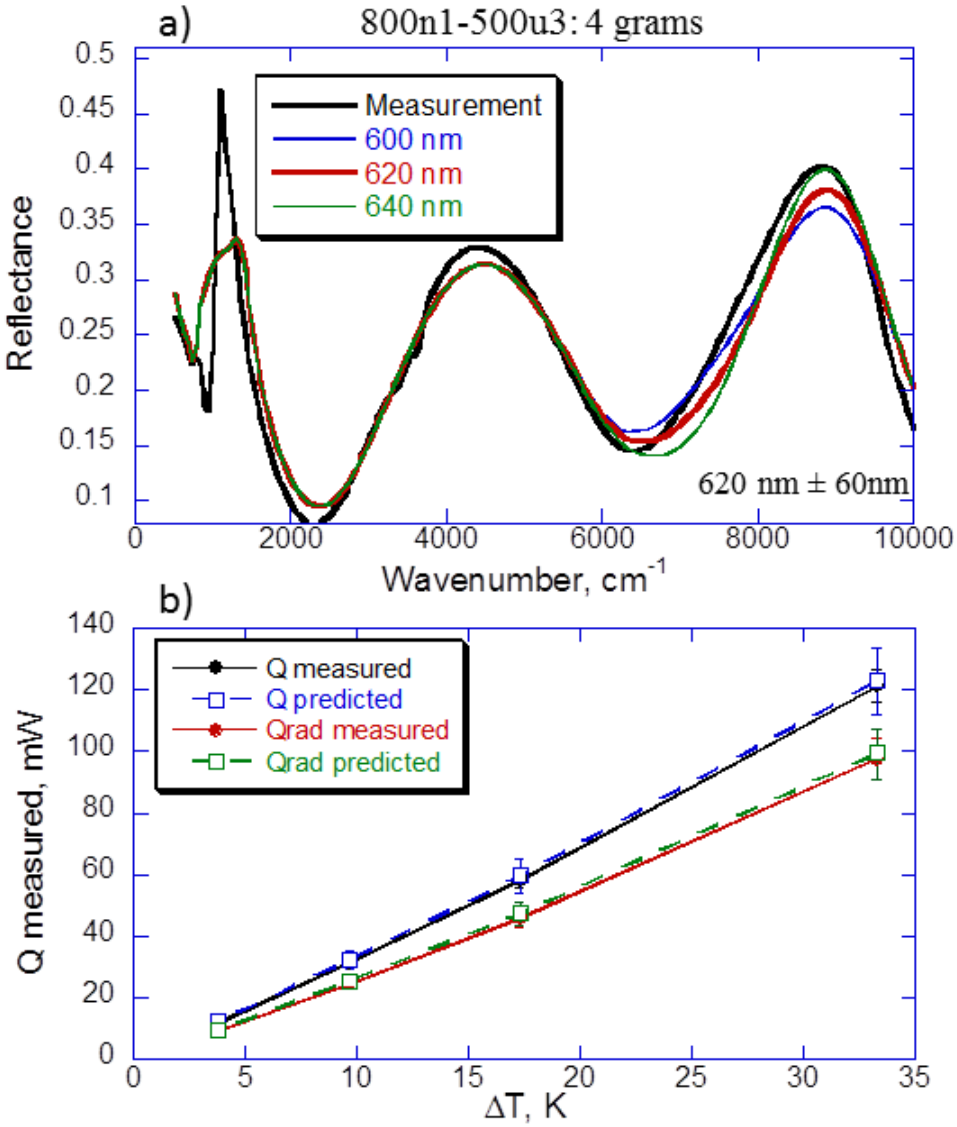

Figure 6.32. Measurement results for sample 800n1-500u3 loaded with 4 grams. a) FTIR results showing a gap spacing of 620 nm, b) near-field heat transfer results with excellent agreement.

The results for sample 800n1-500u3 with an applied load of 4 grams are shown in Figure 6.32. The FTIR results suggest that the best fit for the gap spacing at this loading

is 620 nm, though the match is poor and the uncertainty is estimated at 60 nm. The range of input power settings was 20 mW, 50 mW, 100 mW, and 200 mW. The agreement between the predictions and the measurement is much better, with an average disagreement of only 3%. The uncertainties are approximately 9%, showing great agreement.

6.3.3.6 200n3-400u4

Sample 200n3-400u4 was fabricated to have 200 nm tall posts with 400 μm of separation. Since this is from the 200n3 series, the maximum bowing has been shown to be 8.9 nm and 22 nm in the patterned and cleaned pieces, respectively. A 785 nm oxide layer was deposited on the back of the clean piece, while a 595 nm oxide layer was deposited on the patterned side to achieve these curvatures. This sample is unique in this experiment as it was measured multiple times in the near-field experiment with loads varying from 0 to 12 grams. Measurements corresponding to gap spacings between 520 and 340 nm are found to have good agreement between the measurement and the prediction. Measurements of the gap spacing were taken all at the same time, while measurements of the near-field radiation were taken on successive days, allowing for measurements of the contact resistance after each measurement, and adequate time was allowed for the vacuum pressure to stabilize.

The results for sample 200n3-400u4 without any applied load are shown in Figure 6.33. The gap spacing is easily identified here as 520 nm, and the large difference between close curves gives an uncertainty of 20 nm. The input power settings for the heat transfer experiment were 20 mW, 50 mW, 100 mW, and 200 mW. As can be seen in Figure 6.33b, there is an overlap in the error bars, indicating that the differences in the measurement and prediction are explained. Here the uncertainties are approximately 9%, while the differences in the heat rates are 10% and 15% for the radiation heat rates.

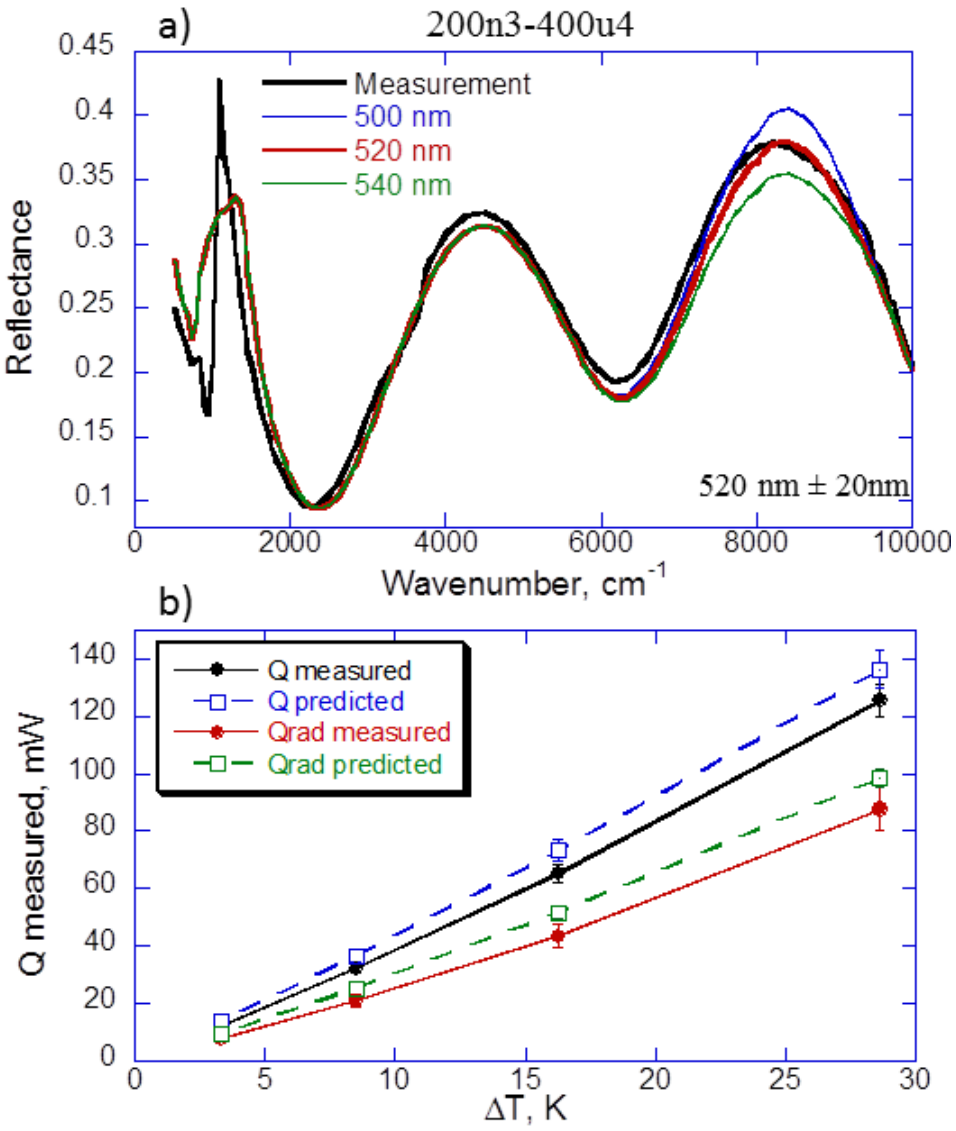

Figure 6.33. Measurement results for sample 200n3-400u4. a) FTIR results showing a gap spacing of 520 nm, b) near-field heat transfer results with good agreement.

After this measurement, 4 grams of force was placed on the sample and remeasured, and the results are shown in Figure 6.34. The gap spacing at this load is found to be 480 nm, and the agreement coupled with the large variation between curves places the uncertainty at 20 nm. With this gap spacing, the heat rates agree very well between the measurement and prediction. The heat rates were measured using input power settings of 20 mW, 50 mW, 100 mW, 118 mW, and 200 mW. The setting at 118 mW is meant to create a measurement whereby the temperature drop is near 16 K so that

the heat transfer coefficients between samples are more readily comparable. Similarly odd power settings are present in other measurement. The uncertainties are around 7% while the disagreement between the heat rates is less than 2%, and the difference between the radiation heat rates is less than 2.5%.

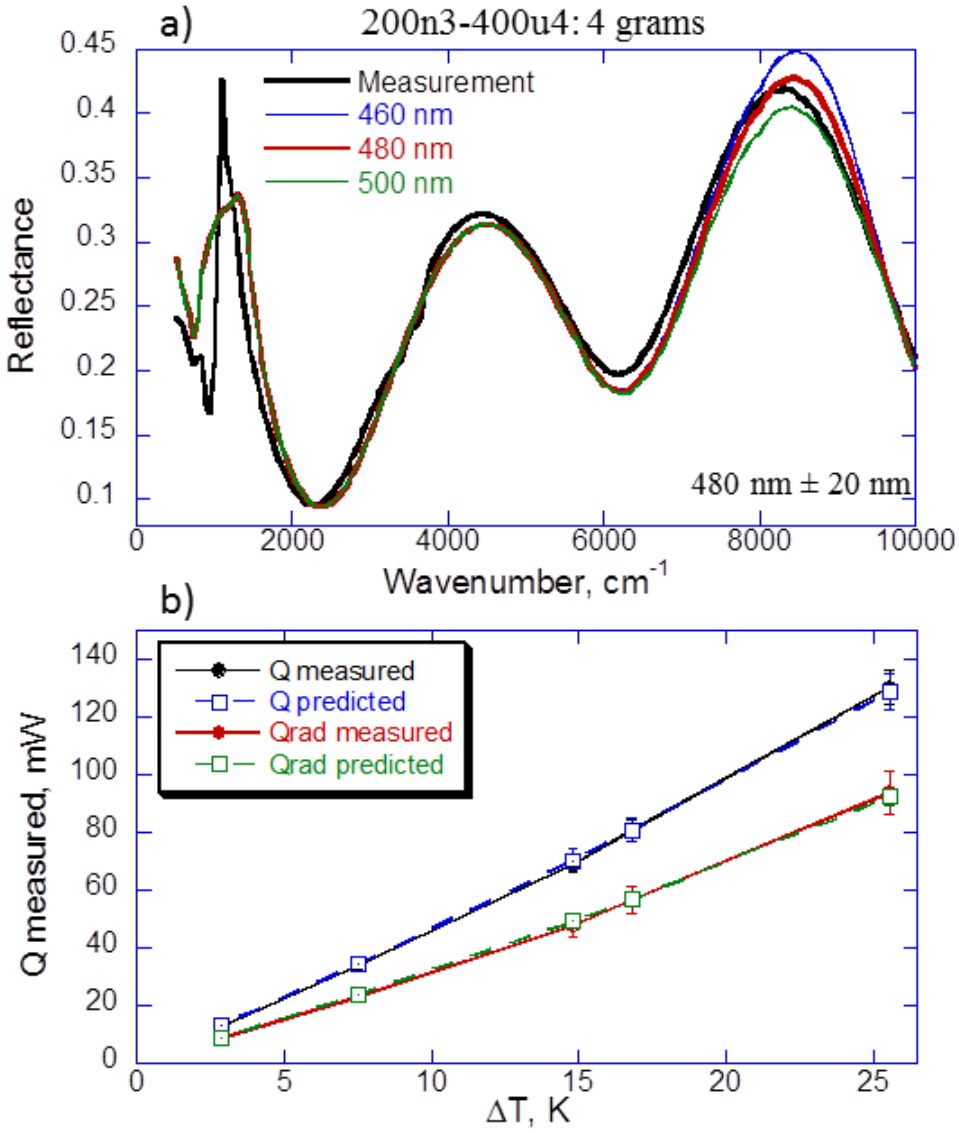

Figure 6.34. Measurement results for sample 200n3-400u4 loaded with 4 grams. a) FTIR results showing a gap spacing of 480 nm, b) near-field heat transfer results with excellent agreement.

Results with a load of 8 grams are shown below in Figure 6.35. Again the agreement seen in the FTIR spectrum shows a clear gap spacing of 420 nm with an uncertainty of 20 nm. The agreement between the measured and predicted heat rates is

not as exact, but is still very good. Here the heat rates only vary by about 7% while the radiative heat rates differ by approximately 10%. The uncertainties of this measurement were fairly low, typically around 5-6%. It is for this reason that the error bars make the agreement look fairly weak while the actual disagreement is relatively small.

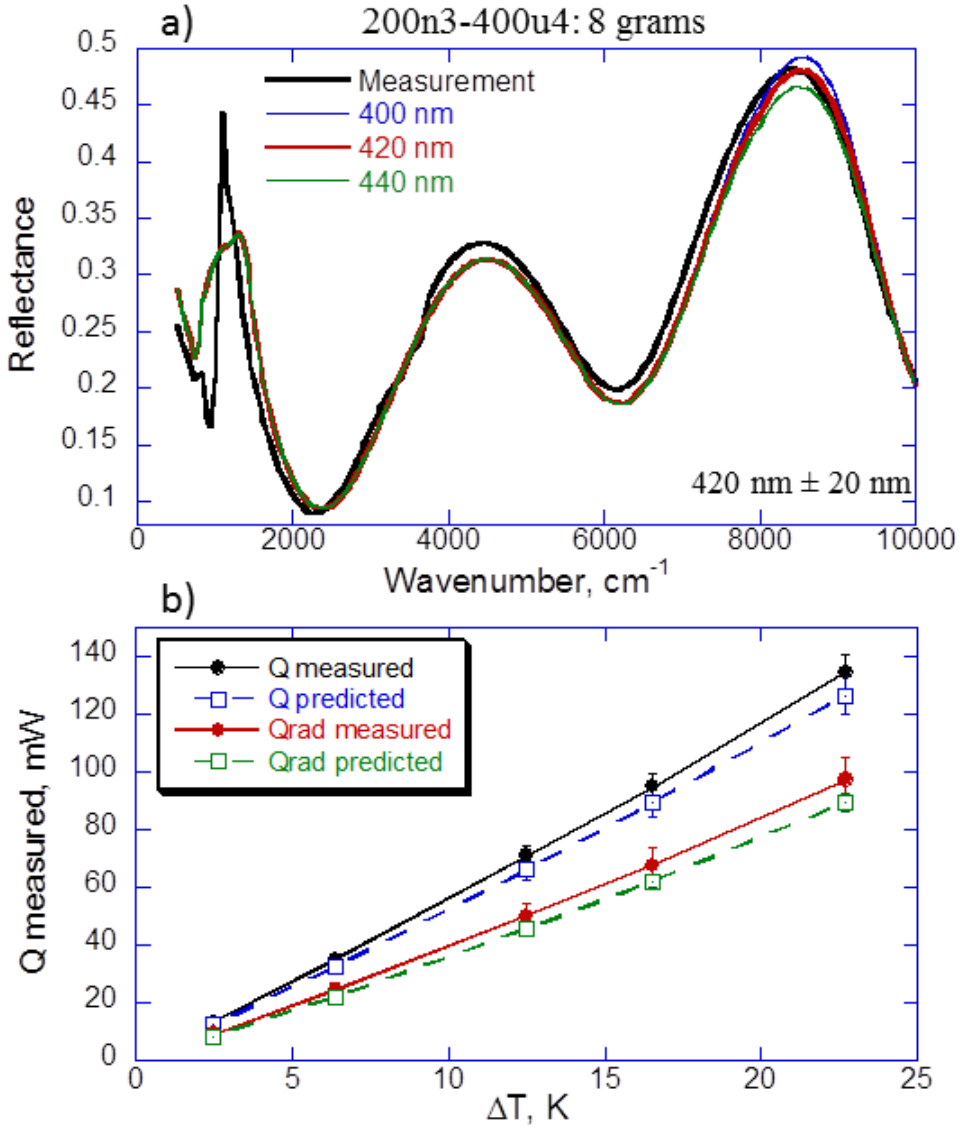

Figure 6.35. Measurement results for sample 200n3-400u4 loaded with 8 grams. a) FTIR results showing a gap spacing of 420 nm, b) near-field heat transfer results with good agreement.

The final measurement presented for sample 200n3-400u3 is with a load of 12 grams. This is seen in Figure 6.36. Because the gap spacing decreases with force, the interferometry must eventually have to distinguish curves between 240-360 nm. As was

discussed earlier, the difference between the reflectance spectra in this range is very small, and accurate determination is difficult. As seen in Figure 6.36a, the gap spacing enters this range, and it is difficult to determine the spacing. The best fit curve was found to be 340 nm, and the uncertainty is estimated at 60 nm to account for improper identification.

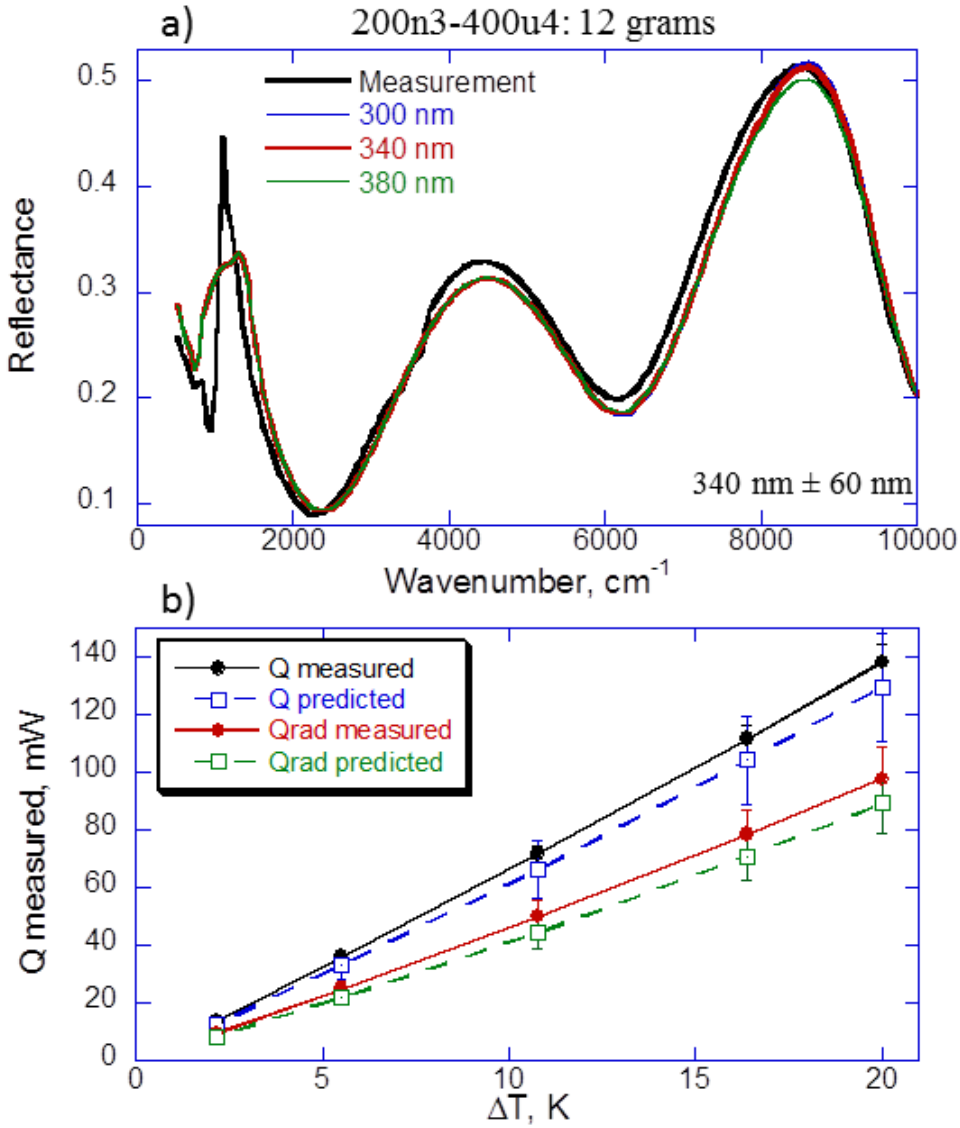

Figure 6.36. Measurement results for sample 200n3-400u4 loaded with 12 grams. a) FTIR results showing a gap spacing of 340 nm, b) near-field heat transfer results with excellent agreement.

The heat transfer results in Figure 6.36b are still in agreement with the predictions. Here the input power was set to 20 mW, 50 mW, 100 mW, 158 mW, and 200

mW. Because of the high uncertainty in the gap spacing, the uncertainty in the heat rate is as high as 15%. Regardless, the agreement between the measurement and prediction is still well within reason at 8% and 12% for the heat rates and radiative heat rates, respectively.

Further measurements on this sample were performed, though the details will not be presented here. Because of the magnitude of the gap spacing, as the force increased it was impossible to distinguish the change in the spacing. As such, the measured temperature drops for similar heat rates decreased as the force increased, as would be expected for decreasing gap spacing. However, since the FTIR measurements were lacking, these measurements are not presented.

6.3.4 Heat Transfer Coefficient

With 11 successful measurements of 6 different samples all at varying vacuum gap spacings, the trend of near-field thermal radiation can be clearly shown. Unfortunately, it is difficult to compare heat rates or heat fluxes because of the different parameters that affect these values. Therefore, it is useful to present the heat transfer coefficient, $h = q''/\Delta T$ given by the heat flux reduced by the temperature difference.

This still varies between samples, but to a much lesser degree. As can be seen from the previous section, the trend between the heat rate and the temperature difference is linear at a glance. This is not strictly true, and the relationship for blackbody radiation is well-known to vary with T^4. However, since the temperature differences are small, the effect of the temperature difference, as well as the absolute temperatures, is weak. Furthermore, attempts were made during testing to measure at a similar temperature drop. Except for the measurement of sample 400n1-300u4, all of the samples were measured near a temperature drop of 16°C. Only these points will be presented in this section, and the highest temperature difference of 9.8°C will be used for 400n1-300u4.

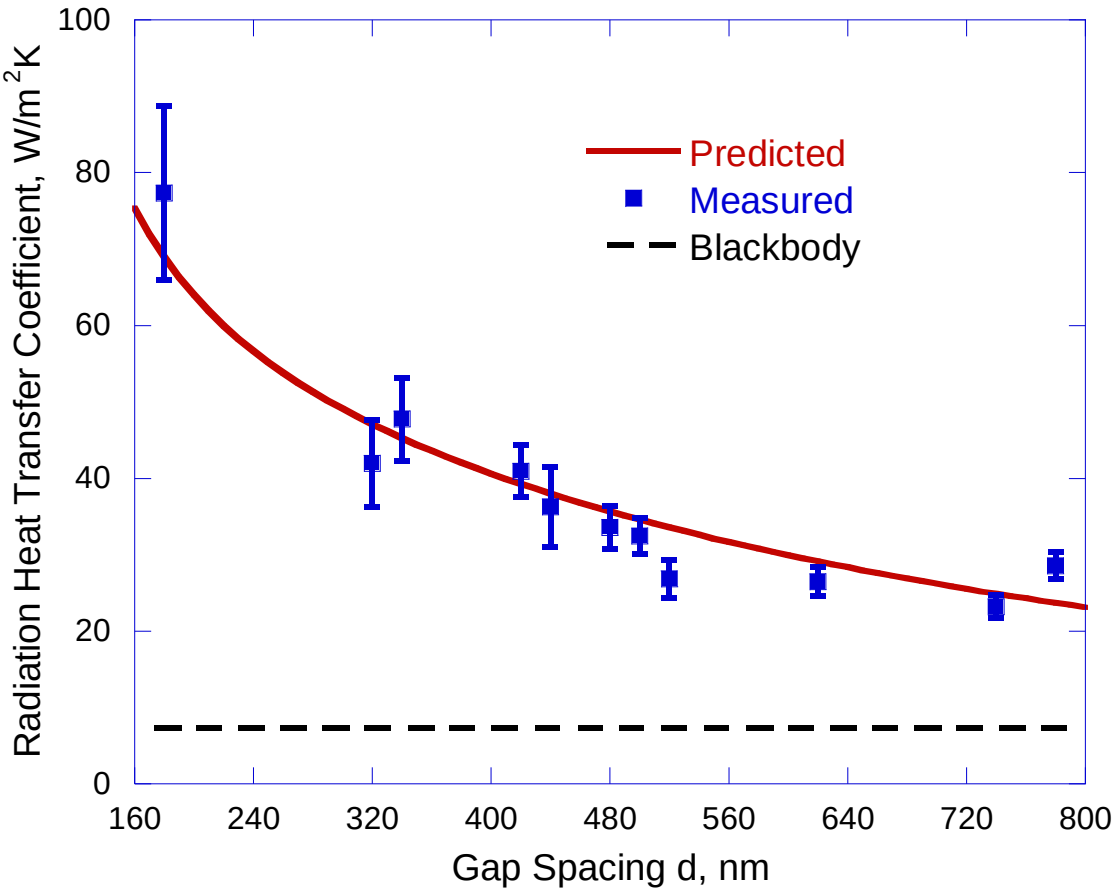

Figure 6.37. Near-field radiation heat transfer coefficient for all successful samples compared to a prediction versus the gap spacing and blackbody radiation. Error bars are shown for the measurements.

Figure 6.37 shows the results of all of the successful samples with the associated uncertainties as error bars. Here the prediction is for a temperature difference between 36°C and 52°C to be comparable to the sample conditions, as most samples had a lower temperature near this value. Aside from sample 400n1-300u4, the largest variation in temperature difference from 16°C was 1.5°C. The agreement between the measurements and the model is clear, and the error bars show that this is supported by the uncertainties in all but two cases. There are only two samples that are not explained by the uncertainty. Sample 200n3-400u4 without any force has a gap spacing of 520 nm and a lower than expected heat transfer coefficient. However, upon inspection of Figure 6.33, the

predictions do match with the measurement. The other sample that does not match is for sample 800n1-500u3 with no loading at 780 nm. As explained above, this is thought to be due to the extreme sensitivity of the gap spacing to the force.

6.4 Conclusions

This work shows strong evidence of near-field thermal radiation across planar geometries at incredible heat rates. The measurement systems have been tested, calibrated, and validated to give credibility to these measurements, and this work shows both the lowest vacuum gap in planar near-field radiation experiments as well as the highest total radiation heat rate at submicron distances to date.

A heat transfer experiment was designed and built to accurately measure the temperatures across and the heat rate through a sample with a cross-sectional area of 1 cm^2. The temperature sensors were calibrated to give accurate measurement of the temperature drop and the uncertainties were found to be less than 0.25°C. The heat rate was measured using a heat flux meter that has been individually calibrated and the uncertainty of the measured heat rate is found to be 4.4%. These experiments all took place under high-vacuum conditions, and the thermal contact resistance at the sample interfaces has been eliminated.

Samples were designed by separating doped-silicon pieces with silicon dioxide nanoposts to create a parallel vacuum gap with minimal conduction heat transfer and a maximal radiation heat rate. The choice of materials was optimized and the optical properties of the doped-silicon were measured using FTIR spectrometry. The effects of the stresses and heat rates through the nanoposts were simulated and informed the distribution and size of the spacers. Ultraviolet photolithography was used to fabricate the spacers with a minimum feature size of 1 μm, over a rectangular periodic array with

periods ranging between 200 μm and 500 μm. Measurements of the individual posts and the entire array pattern were made to justify correct pattern transfer onto the sample.

The nanoposts spacers created a nanoscale vacuum gap between the two doped-silicon pieces, but the values used were measured using FTIR spectrometry. Here the reflectance of the sample was compared to a model incorporating a thin coherent vacuum gap producing interference effects between the silicon pieces, and this technique was found to have a maximum uncertainty of 60 nm, though lower uncertainties were common. The parallelism of the gap was also measured, and attempts to control the innate bowing of the samples were made. The surface profiles of the doped-silicon wafers used was measured, and in some cases a silicon dioxide film was deposited to control the deflection. All of the samples used had a predicted sample bowing between 1 nm and 23 nm. Additionally, adding an applied force over the top of the sample was found to reduce the gap spacing, and a custom reflectance accessory was made for the spectroscopic measurements of this.

Through these techniques, 6 samples were successfully measured over 11 total measurements. The results show a clear trend in radiation heat rates at vacuum gaps ranging between 180 nm and 780 nm. Of these measurements, all but one are well explained by comparisons to theoretical predictions with the rigorous uncertainty analysis, concluding that these represent accurate results. Comparing these results to the blackbody limit for far field radiation at these temperature differences, these results show an increase over this limit by 960%. To date, these measurements show the highest total radiation heat rate through submicron gap spacings.

7: CONCLUSIONS AND RECOMMENDATIONS

This work has shown the promise of using TPV devices for energy harvesting applications while addressing technical issues. We have been able to simulate the near-field radiative exchange between a tungsten grating and an $In_{0.18}Ga_{0.82}Sb$ photovoltaic cell. Through a parametric study of grating geometries, a suitable emitter was found to outperform the baseline case. The electrical output power was 1.06×10^{6} W/m^2 with a conversion efficiency of 31.8%, showing an improvement over the planar case by 40% and 6% for power and efficiency, respectively. The mechanisms for enhancement were investigated, and it has been shown that SPP resonance that shifts towards higher wavevectors and lower frequencies is responsible for the exceptional performance of the tungsten grating. It is through this work that we have shown simulations of a powerful and efficient nanostructured near-field thermophotovoltaic device, and have gained insights into near-field radiation in one-dimensional grating structures.

The variation in the optical constants extracted for thin-film tungsten shows that using bulk values for thin tungsten films may be insufficient, depending on the required accuracy. The annealed samples exhibit similar dielectric functions, but extra care must be taken if precise values are needed. However, there is large disagreement between the annealed and unannealed films, and researchers should be aware that a drastic change in the optical properties is to be expected upon heating the film above 800°C. With these elements in mind, further research may be conducted using thin-film tungsten in a nano/microstructured device for optical or thermal applications.

Finally, an experiment to accurately measure near-field heat transfer has been developed. This includes an apparatus to accurately measure the temperature drop and heat rate across a 1 cm^2 sample. Through rigorous calibrations, the measured heat flux has shown to be accurate within 4.4%. Samples were designed, fabricated, and tested to deliver the maximum amount of near-field radiation while minimizing conduction and

convection heat transfer. The fabrication involved ultraviolet photolithography at the lowest resolution possible with this technique. Various microscopy techniques validated the correct application of this technique. The bowing of the samples was measured and controlled to within 25 nm. Force-resolved FTIR spectroscopy was used to measure the vacuum gap under applied loads to within 20%, though higher accuracies were common.

These samples were tested for the amount of near-field thermal radiation while accounting for the contact resistance in situ. The measurements of near field thermal radiation matched very well with predictions from theory, and these results are well supported through rigorous uncertainty analysis. Here, the uncertainties in the measured thermal radiation were less than 15%. Six samples were successfully measured over 11 experiments by adjusting the applied forces. From these measurements, strong evidence of near-field thermal radiation was shown, and the effects of the changing gap spacing were shown. Results are found for samples exhibiting vacuum gap spacings between 180 nm and 780 nm, showing an improvement over Planck's blackbody radiation limit by over 1000%. With the highest measurement of near-field radiation shown at 127 mW over a 1 cm^2 across a 180 nm gap, these results show both the lowest vacuum gap in planar near-field radiation experiments and the highest total radiation heat rate at submicron distances to date.

While this work now represents a completed state, further investigations are possible. While investigating one-dimensional grating emitters for NFTPV technologies, it is clear that improvements are possible, and further investigation of the role that near-field radiation has in nanostructured materials is necessary. Unlike periodic grating structures in the far-field, the control of emission bands is less controllable. This necessitates the investigation and simulation devices capable of tunable near-field radiation. This can be achieved through the simulation of periodic gratings with more metallic behavior than the tungsten gratings used to create sharper plasmonic resonance

modes, or gratings utilizing two-dimensional materials like graphene to excited other resonance modes. Additionally, the interactions of one-dimensional gratings in the near field needs more investigation to fully understand the impact that wavevectors parallel to the grating have on the excitation of resonance modes.

With great success in the development of this near-field radiation experiment, accurate measurements can be made of more exotic samples. Because of the fabrication methods used, the cleaned piece used in every sample can be switched with any number of interesting devices. This includes thermophotovoltaic devices, multilayered thin films showing hyperbolic dispersions, and periodic gratings. In this, the silicon dioxide spacer pattern can be deposited on the device directly, or kept as a separate piece and aligned to match any surface topology. Experiments of this nature have never been attempted before, and measurements of near-field radiation with micro/nanostructured materials will signify a breakthrough in the field.

REFERENCES

[1] Liu, X. L., Wang, L. P., and Zhang, Z. M., 2015, "Near-field thermal radiation: recent progress and outlook," Nanoscale and Microscale Thermophysical Engineering, 19(2), pp. 98-126.

[2] Basu, S., Chen, Y. B., and Zhang, Z. M., 2007, "Microscale radiation in thermophotovoltaic devices—A review," International Journal of Energy Research, 31(6-7), pp. 689-716.

[3] Yang, W. M., Chou, S. K., Shu, C., Xue, H., Li, Z. W., Li, D. T., and Pan, J. F., 2003, "Microscale combustion research for application to micro thermophotovoltaic systems," Energy Conversion and Management, 44(16), pp. 2625-2634.

[4] Bermel, P., Ghebrebrhan, M., Chan, W., Yeng, Y. X., Araghchini, M., Hamam, R., Marton, C. H., Jensen, K. F., Soljačić, M., Joannopoulos, J. D., Johnson, S. G., and Celanovic, I., 2010, "Design and global optimization of high-efficiency thermophotovoltaic systems," Optics Express, 18(S3), pp. A314-A334.

[5] Laroche, M., Carminati, R., and Greffet, J.-J., 2006, "Near-field thermophotovoltaic energy conversion," Journal of Applied Physics, 100(6), p. 063704.

[6] Bernardi, M. P., Dupré, O., Blandre, E., Chapuis, P.-O., Vaillon, R., and Francoeur, M., 2015, "Impacts of propagating, frustrated and surface modes on radiative, electrical and thermal losses in nanoscale-gap thermophotovoltaic power generators," Scientific Reports, 5, p. 11626.

[7] Wang, L. P., and Zhang, Z. M., 2012, "Wavelength-selective and diffuse emitter enhanced by magnetic polaritons for thermophotovoltaics," Applied Physics Letters, 100(6), p. 063902.

[8] Zhao, B., and Zhang, Z. M., 2014, "Study of magnetic polaritons in deep gratings for thermal emission control," Journal of Quantitative Spectroscopy and Radiative Transfer, 135, pp. 81-89.

[9] Lee, B. J., Chen, Y.-B., Han, S., Chiu, F.-C., and Lee, H. J., 2014, "Wavelength-selective solar thermal absorber with two-dimensional nickel gratings," Journal of Heat Transfer, 136(7), p. 072702.

[10] Zhao, B., Wang, L. P., Shuai, Y., and Zhang, Z. M., 2013, "Thermophotovoltaic emitters based on a two-dimensional grating/thin-film nanostructure," International Journal of Heat and Mass Transfer, 67, pp. 637-645.

[11] Rephaeli, E., and Fan, S., 2009, "Absorber and emitter for solar thermo-photovoltaic systems to achieve efficiency exceeding the Shockley-Queisser limit," Optics Express, 17(17), pp. 15145-15159.

[12] Kohiyama, A., Shimizu, M., Kobayashi, H., Iguchi, F., and Yugami, H., 2014, "Spectrally controlled thermal radiation based on surface microstructures for high-efficiency solar thermophotovoltaic system," Energy Procedia, 57, pp. 517-523.

[13] Bright, T. J., Wang, L. P., and Zhang, Z. M., 2014, "Performance of near-field thermophotovoltaic cells enhanced with a backside reflector," Journal of Heat Transfer, 136(6), p. 062701.

[14] Tong, J. K., Hsu, W.-C., Huang, Y., Boriskina, S. V., and Chen, G., 2015, "Thin-film 'thermal well' emitters and absorbers for high-efficiency thermophotovoltaics," Scientific Reports, 5, p. 10661.

[15] Messina, R., and Ben-Abdallah, P., 2013, "Graphene-based photovoltaic cells for near-field thermal energy conversion," Scientific Reports, 3, p. 1383.

[16] Ilic, O., Jablan, M., Joannopoulos, J. D., Celanovic, I., and Soljačić, M., 2012, "Overcoming the black body limit in plasmonic and graphene near-field thermophotovoltaic systems," Optics Express, 20(S3), pp. A366-A384.

[17] Chang, J.-Y., Yang, Y., and Wang, L. P., 2015, "Tungsten nanowire based hyperbolic metamaterial emitters for near-field thermophotovoltaic applications," International Journal of Heat and Mass Transfer, 87, pp. 237-247.

[18] Hirashima, D., and Hanamura, K., "Spectral control of near-field radiation through surface plasmon polariton interference," Proc. ASME 2013 Heat Transfer Summer Conference collocated with the ASME 2013 7th International Conference on Energy Sustainability and the ASME 2013 11th International Conference on Fuel Cell Science, Engineering and Technology, American Society of Mechanical Engineers, p. V001T003A047.

[19] Guérout, R., Lussange, J., Rosa, F., Hugonin, J.-P., Dalvit, D., Greffet, J.-J., Lambrecht, A., and Reynaud, S., "Enhanced radiative heat transfer between nanostructured gold plates," Proc. Journal of Physics: Conference Series, IOP Publishing, p. 012154.

[20] Lussange, J., Guérout, R., Rosa, F. S. S., Greffet, J. J., Lambrecht, A., and Reynaud, S., 2012, "Radiative heat transfer between two dielectric nanogratings in the scattering approach," Physical Review B, 86(8), p. 085432.

[21] Lassner, E., and Schubert, W. D., 1999, Tungsten: Properties, Chemistry, Technology of the Elements, Alloys, and Chemical Compounds, Springer, New York.

[22] De Vos, J. C., 1954, "A new determination of the emissivity of tungsten ribbon," Physica, 20(7–12), pp. 690-714.

[23] Larrabee, R. D., 1957, "The spectral emissivity and optical properties of tungsten," Technical Report 328, Massachusetts Institute of Technology Research Laboratory of Electronics.

[24] Wojcik, L. A., Sievers, A. J., Graham, G. W., and Rhodin, T. N., 1980, "Total hemispherical emissivity of W(100)," Journal of the Optical Society of America, 70(4), pp. 443-450.

[25] Sai, H., Kanamori, Y., and Yugami, H., 2003, "High-temperature resistive surface grating for spectral control of thermal radiation," Applied Physics Letters, 82(11), pp. 1685-1687.

[26] Laroche, M., Arnold, C., Marquier, F., Carminati, R., Greffet, J. J., Collin, S., Bardou, N., and Pelouard, J. L., 2005, "Highly directional radiation generated by a tungsten thermal source," Optics Letters, 30(19), pp. 2623-2625.

[27] Chen, Y. B., and Zhang, Z. M., 2007, "Design of tungsten complex gratings for thermophotovoltaic radiators," Optics Communications, 269(2), pp. 411-417.

[28] Chen, Y. B., and Tan, K. H., 2010, "The profile optimization of periodic nano-structures for wavelength-selective thermophotovoltaic emitters," International Journal of Heat and Mass Transfer, 53(23–24), pp. 5542-5551.

[29] Lin, S. Y., Moreno, J., and Fleming, J. G., 2003, "Three-dimensional photonic-crystal emitter for thermal photovoltaic power generation," Applied Physics Letters, 83(2), pp. 380-382.

[30] Narayanaswamy, A., and Chen, G., 2004, "Thermal emission control with one-dimensional metallodielectric photonic crystals," Physical Review B, 70(12), p. 125101.

[31] Celanovic, I., Jovanovic, N., and Kassakian, J., 2008, "Two-dimensional tungsten photonic crystals as selective thermal emitters," Applied Physics Letters, 92(19), p. 193101.

[32] Roberts, S., 1959, "Optical Properties of Nickel and Tungsten and Their Interpretation According to Drude's Formula," Physical Review, 114(1), pp. 104-115.

[33] Nomerovannaya, L., Kirillova, M., and Noskov, M., 1971, "Optical properties of tungsten monocrystals," Soviet Journal of Experimental and Theoretical Physics, 33, p. 405.

[34] Mattheiss, L. F., 1965, "Fermi surface in tungsten," Physical Review, 139(6A), pp. A1893-A1904.

[35] Romaniello, P., de Boeij, P. L., Carbone, F., and van der Marel, D., 2006, "Optical properties of bcc transition metals in the range 0-40 eV," Physical Review B, 73(7), p. 075115.

[36] Weaver, J. H., Olson, C. G., and Lynch, D. W., 1975, "Optical properties of crystalline tungsten," Physical Review B, 12(4), pp. 1293-1297.

[37] Palik, E. D., 1998, Handbook of Optical Constants of Solids, Academic press, San Diego.

[38] Rakić, A. D., Djurišić, A. B., Elazar, J. M., and Majewski, M. L., 1998, "Optical properties of metallic films for vertical-cavity optoelectronic devices," Applied Optics, 37(22), pp. 5271-5283.

[39] Deineka, A. G., Tarasenko, A. A., Jastrabík, L., Chvostova, D., and Bousek, J., 1999, "An ellipsometric study of W thin films deposited on Si," Thin Solid Films, 339(1–2), pp. 216-219.

[40] Davazoglou, D., Pallis, G., Psycharis, V., Gioti, M., and Logothetidis, S., 1995, "Structure and optical properties of tungsten thin films deposited by pyrolysis of W(CO)6 at various temperatures," Journal of Applied Physics, 77(11), pp. 6070-6072.

[41] Gravier, P., Chassaing, G., and Sigrist, M., 1979, "Optical properties of thin films of b.c.c. transition metals," Thin Solid Films, 57(1), pp. 93-98.

[42] Nestell, J. E., Christy, R. W., Cohen, M. H., and Ruben, G. C., 1980, "Structure and optical properties of evaporated films of the Cr- and V-group metals," Journal of Applied Physics, 51(1), pp. 655-660.

[43] Nestell, J. E., and Christy, R. W., 1980, "Optical conductivity of bcc transition metals: V, Nb, Ta, Cr, Mo, W," Physical Review B, 21(8), pp. 3173-3179.

[44] Shen, Y. G., Mai, Y. W., Zhang, Q. C., McKenzie, D. R., McFall, W. D., and McBride, W. E., 2000, "Residual stress, microstructure, and structure of tungsten thin films deposited by magnetron sputtering," Journal of Applied Physics, 87(1), pp. 177-187.

[45] Choi, D., Wang, B., Chung, S., Liu, X., Darbal, A., Wise, A., Nuhfer, N. T., Barmak, K., Warren, A. P., Coffey, K. R., and Toney, M. F., 2011, "Phase, grain structure, stress, and resistivity of sputter-deposited tungsten films," Journal of Vacuum Science & Technology A, 29(5), p. 051512.

[46] Rossnagel, S. M., Noyan, I. C., and Cabral, C., 2002, "Phase transformation of thin sputter-deposited tungsten films at room temperature," Journal of Vacuum Science & Technology B, 20(5), pp. 2047-2051.

[47] Chen, G. S., Tian, H. S., Lin, C. K., Chen, G.-S., and Lee, H. Y., 2004, "Phase transformation of tungsten films deposited by diode and inductively coupled plasma magnetron sputtering," Journal of Vacuum Science & Technology A, 22(2), pp. 281-286.

[48] Itoh, M., Hori, M., and Nadahara, S., 1991, "The origin of stress in sputter-deposited tungsten films for x-ray masks," Journal of Vacuum Science & Technology B, 9(1), pp. 149-153.

[49] Masashi, A., and Isao, N., 1993, "Tungsten films with the A15 structure," Japanese Journal of Applied Physics, 32(4R), p. 1759.

[50] Djerdj, I., Tonejc, A. M., Tonejc, A., and Radić, N., 2005, "XRD line profile analysis of tungsten thin films," Vacuum, 80(1–3), pp. 151-158.

[51] Morcom, W. R., Worrell, W. L., Sell, H. G., and Kaplan, H. I., 1974, "The preparation and characterization of beta-tungsten, a metastable tungsten phase," Metallurgical Transactions, 5(1), pp. 155-161.

[52] Chopra, K. L., Randlett, M. R., and Duff, R. H., 1966, "Face-centered-cubic tungsten films obtained by," Applied Physics Letters, 9(11), pp. 402-405.

[53] Gasgnier, M., Nevot, L., Baillif, P., and Bardolle, J., 1983, "Characterization and crystalline structures of tungsten thin films," Physica Status Solidi A, 79(2), pp. 531-542.

[54] Chopra, K. L., Randlett, M. R., and Duff, R. H., 1967, "Face-centred cubic modification in sputtered films of tantalum, molybdenum, tungsten, rhenium, hafnium and zirconium," Philosophical Magazine, 16(140), pp. 261-273.

[55] Weerasekera, I. A., Shah, S. I., Baxter, D. V., and Unruh, K. M., 1994, "Structure and stability of sputter deposited beta-tungsten thin films," Applied Physics Letters, 64(24), pp. 3231-3233.

[56] Basu, S., Zhang, Z. M., and Fu, C. J., 2009, "Review of near-field thermal radiation and its application to energy conversion," International Journal of Energy Research, 33(13), pp. 1203-1232.

[57] Betzig, E., and Trautman, J. K., 1992, "Near-field optics: microscopy, spectroscopy, and surface modification beyond the diffraction limit," Science, 257(5067), pp. 189-195.

[58] Guha, B., Otey, C., Poitras, C. B., Fan, S., and Lipson, M., 2012, "Near-field radiative cooling of nanostructures," Nano Letters, 12(9), pp. 4546-4550.

[59] Wang, L. P., and Zhang, Z. M., 2013, "Thermal rectification enabled by near-field radiative heat transfer between intrinsic silicon and a dissimilar material," Nanoscale and Microscale Thermophysical Engineering, 17(4), pp. 337-348.

[60] Kittel, A., Müller-Hirsch, W., Parisi, J., Biehs, S.-A., Reddig, D., and Holthaus, M., 2005, "Near-field heat transfer in a scanning thermal microscope," Physical Review Letters, 95(22), p. 224301.

[61] van Zwol, P. J., Ranno, L., and Chevrier, J., 2012, "Tuning near field radiative heat flux through surface excitations with a metal insulator transition," Physical Review Letters, 108(23), p. 234301.

[62] Shi, J., Li, P., Liu, B., and Shen, S., 2013, "Tuning near field radiation by doped silicon," Applied Physics Letters, 102(18), p. 183114.

[63] Hu, L., Narayanaswamy, A., Chen, X., and Chen, G., 2008, "Near-field thermal radiation between two closely spaced glass plates exceeding Planck's blackbody radiation law," Applied Physics Letters, 92(13), p. 133106.

[64] Ottens, R. S., Quetschke, V., Wise, S., Alemi, A. A., Lundock, R., Mueller, G., Reitze, D. H., Tanner, D. B., and Whiting, B. F., 2011, "Near-field radiative heat transfer between macroscopic planar surfaces," Physical Review Letters, 107(1), p. 014301.

[65] Ito, K., Miura, A., Iizuka, H., and Toshiyoshi, H., 2015, "Parallel-plate submicron gap formed by micromachined low-density pillars for near-field radiative heat transfer," Applied Physics Letters, 106(8), p. 083504.

[66] Lim, M., Lee, S. S., and Lee, B. J., 2015, "Near-field thermal radiation between doped silicon plates at nanoscale gaps," Physical Review B, 91(19), p. 195136.

[67] Zhang, Z. M., 2007, Nano/Microscale Heat Transfer, McGraw-Hill, New York.

[68] Modest, M. F., 2003, Radiative Heat Transfer, Academic Press.

[69] Francoeur, M., and Pinar Mengüç, M., 2008, "Role of fluctuational electrodynamics in near-field radiative heat transfer," Journal of Quantitative Spectroscopy and Radiative Transfer, 109(2), pp. 280-293.

[70] Rytov, S. M., Kravt͡sov, I. U. A., and Tatarskiĭ, V. I., 1989, Principles of Statistical Radiophysics: Elements of random fields, Springer-Verlag.

[71] Sipe, J. E., 1987, "New Green-function formalism for surface optics," Journal of the Optical Society of America B, 4(4), pp. 481-489.

[72] Francoeur, M., Pinar Mengüç, M., and Vaillon, R., 2009, "Solution of near-field thermal radiation in one-dimensional layered media using dyadic Green's functions and the scattering matrix method," Journal of Quantitative Spectroscopy and Radiative Transfer, 110(18), pp. 2002-2018.

[73] Polder, D., and Van Hove, M., 1971, "Theory of radiative heat transfer between closely spaced bodies," Physical Review B, 4(10), pp. 3303-3314.

[74] Joulain, K., Mulet, J.-P., Marquier, F., Carminati, R., and Greffet, J.-J., 2005, "Surface electromagnetic waves thermally excited: Radiative heat transfer, coherence properties and Casimir forces revisited in the near field," Surface Science Reports, 57(3–4), pp. 59-112.

[75] Guérout, R., Lussange, J., Chan, H. B., Lambrecht, A., and Reynaud, S., 2013, "Thermal Casimir force between nanostructured surfaces," Physical Review A, 87(5), p. 052514.

[76] Guérout, R., Lussange, J., Rosa, F. S. S., Hugonin, J. P., Dalvit, D. A. R., Greffet, J. J., Lambrecht, A., and Reynaud, S., 2012, "Enhanced radiative heat transfer between nanostructured gold plates," Physical Review B, 85(18), p. 180301.

[77] Lambrecht, A., and Marachevsky, V. N., 2008, "Casimir interaction of dielectric gratings," Physical Review Letters, 101(16), p. 160403.

[78] Basu, S., Lee, B. J., and Zhang, Z. M., 2010, "Infrared radiative properties of heavily doped silicon at room temperature," Journal of Heat Transfer, 132(2), p. 023301.

[79] Wang, L. P., Lee, B. J., Wang, X. J., and Zhang, Z. M., 2009, "Spatial and temporal coherence of thermal radiation in asymmetric Fabry–Perot resonance cavities," International Journal of Heat and Mass Transfer, 52(13–14), pp. 3024-3031.

[80] Tsien, H.-S., 1946, "Superaerodynamics, mechanics of rarefied gases," Journal of the Aeronautical Sciences, 13(12), pp. 653-664.

[81] Kommandur, S., Mahdavifar, A., Hesketh, P. J., and Yee, S., 2015, "A microbridge heater for low power gas sensing based on the 3-Omega technique," Sensors and Actuators A: Physical, 233, pp. 231-238.

[82] Brown, E. N., and Dattelbaum, D. M., 2005, "The role of crystalline phase on fracture and microstructure evolution of polytetrafluoroethylene (PTFE)," Polymer, 46(9), pp. 3056-3068.

[83] Agilent Technologies Inc., 2013, "Agilent 34401A Multimeter Data Sheet ".

[84] Omega Engineering, 1995, "Revised Thermocouple Reference Tables Type E," N. I. S. T. Monograph, 175(ITS-90), p. Z206.

[85] Burns Engineering, 2004, "Report of Calibration, Calibration Report Number 60275".

[86] Doebelin, E. O., 2004, Measurement Systems: Application and Design, McGraw-Hill, New York.

[87] González-Cuevas, J. A., Refaat, T. F., Abedin, M. N., and Elsayed-Ali, H. E., 2006, "Modeling of the temperature-dependent spectral response of In1−χGaχSb infrared photodetectors," Optical Engineering, 45(4), pp. 044001-044008.

[88] Park, K., Basu, S., King, W. P., and Zhang, Z. M., 2008, "Performance analysis of near-field thermophotovoltaic devices considering absorption distribution," Journal of Quantitative Spectroscopy and Radiative Transfer, 109(2), pp. 305-316.

[89] Ashcroft, N. W., and Mermin, N. D., 1976, Solid State Physics, Holt, Rinehart and Winston, New York.

[90] Liu, X. L., Zhao, B., and Zhang, Z. M., 2015, "Enhanced near-field thermal radiation and reduced Casimir stiction between doped-Si gratings," Physical Review A, 91(6), p. 062510.

[91] Lee, B. J., and Zhang, Z. M., 2008, "Lateral shifts in near-field thermal radiation with surface phonon polaritons," Nanoscale and Microscale Thermophysical Engineering, 12(3), pp. 238-250.

[92] Powder Diffraction File, 2011, International Centre for Diffraction Data, PDF-4+, Newton Square, PA.

[93] Meyer, F., Bouchier, D., Benhocine, A., and Gautherin, G., 1991, "Effects of impurities on the interface of ion beam sputtered tungsten with silicon," Applied Surface Science, 53, pp. 82-86.

[94] Shen, Y. G., and Mai, Y. W., 2000, "Structural studies of amorphous and crystallized tungsten nitride thin films by EFED, XRD and TEM," Applied Surface Science, 167(1–2), pp. 59-68.

[95] Mi, B., Coronell, O., Mariñas, B. J., Watanabe, F., Cahill, D. G., and Petrov, I., 2006, "Physico-chemical characterization of NF/RO membrane active layers by Rutherford backscattering spectrometry," Journal of Membrane Science, 282(1–2), pp. 71-81.

[96] McKerracher, I. R., Fu, L., Tan, H. H., and Jagadish, C., "Impurity-free vacancy disordering of quantum heterostructures with SiOxNy encapsulants deposited by

magnetron sputtering," Proc. Proc. SPIE 7039, Nanoengineering: Fabrication, Properties, Optics, and Devices V, p. 70390U.

[97] Alford, T. L., Feldman, L. C., and Mayer, J. W., 2007, Fundamentals of Nanoscale Film Analysis, Springer Science & Business Media, New York.

[98] Langford, J. I., and Wilson, A. J. C., 1978, "Scherrer after sixty years: A survey and some new results in the determination of crystallite size," Journal of Applied Crystallography, 11(2), pp. 102-113.

[99] Bright, T. J., Watjen, J. I., Zhang, Z. M., Muratore, C., and Voevodin, A. A., 2012, "Optical properties of HfO2 thin films deposited by magnetron sputtering: From the visible to the far-infrared," Thin Solid Films, 520(22), pp. 6793-6802.

[100] Coppin, B., 2004, Artificial Intelligence Illuminated, Jones & Bartlett Learning.

[101] Bright, T. J., Watjen, J. I., Zhang, Z. M., Muratore, C., Voevodin, A. A., Koukis, D. I., Tanner, D. B., and Arenas, D. J., 2013, "Infrared optical properties of amorphous and nanocrystalline Ta2O5 thin films," Journal of Applied Physics, 114(8), p. 083515.

[102] Incropera, F. P., DeWitt, D. P., Bergman, T. L., and Lavine, A. S., 2006, Fundamentals of Heat and Mass Transfer, John Wiley & Sons, New York.

[103] Jennings, S. G., 1988, "The mean free path in air," Journal of Aerosol Science, 19(2), pp. 159-166.

[104] Nazaroff, W. W., 2004, "Indoor particle dynamics," Indoor Air, 14, pp. 175-183.

[105] Hänninen, O. O., Lebret, E., Ilacqua, V., Katsouyanni, K., Künzli, N., Srám, R. J., and Jantunen, M., 2004, "Infiltration of ambient PM2.5 and levels of indoor generated non-ETS PM2.5 in residences of four European cities," Atmospheric Environment, 38(37), pp. 6411-6423.

[106] Lai, A. C. K., 2002, "Particle deposition indoors: a review," Indoor Air, 12(4), pp. 211-214.

[107] Thatcher, T. L., and Layton, D. W., 1995, "Deposition, resuspension, and penetration of particles within a residence," Atmospheric Environment, 29(13), pp. 1487-1497.

[108] von Arx, M., Paul, O., and Baltes, H., 2000, "Process-dependent thin-film thermal conductivities for thermal CMOS MEMS," Microelectromechanical Systems, Journal of, 9(1), pp. 136-145.

[109] Kleiner, M. B., Kuhn, S. A., and Weber, W., 1996, "Thermal conductivity measurements of thin silicon dioxide films in integrated circuits," Electron Devices, IEEE Transactions on, 43(9), pp. 1602-1609.

[110] Burns, G., 2013, Solid State Physics, Elsevier Science.

[111] Han, S. M., Xie, C., and Cui, Y., 2010, "Microcompression of fused silica nanopillars synthesized using reactive ion etching," Nanoscience and Nanotechnology Letters, 2(4), pp. 344-347.

[112] Hatty, V., Kahn, H., and Heuer, A. H., 2008, "Fracture toughness, fracture strength, and stress corrosion cracking of silicon dioxide thin films," Microelectromechanical Systems, Journal of, 17(4), pp. 943-947.

[113] Francoeur, M., Mengüç, M. P., and Vaillon, R., 2010, "Spectral tuning of near-field radiative heat flux between two thin silicon carbide films," Journal of Physics D: Applied Physics, 43(7), p. 075501.

[114] Hull, R., and INSPEC, 1999, Properties of Crystalline Silicon, INSPEC, the Institution of Electrical Engineers.